THE SMALL-SCALE STRUCTURE OF PASSIVE SCALAR MIXING IN TURBULENT BOUNDARY LAYERS

A Thesis

Presented to

The Academic Faculty

by

Lakshmi Prasad Dasi

In Partial Fulfillment

of the Requirements for the Degree of

Doctor of Philosophy in Civil Engineering

School of Civil and Environmental Engineering

Georgia Institute of Technology, Atlanta GA

August 2004

THE SMALL-SCALE STRUCTURE OF PASSIVE SCALAR MIXING IN TURBULENT BOUNDARY LAYERS

Approved by:

Dr. Donald R. Webster, Advisor

Dr. Predrag Cvitanovic

Dr. Phillip J. W. Roberts

Dr. Terry W. Sturm

Dr. Pui-Kuen Yeung

13th August 2004

To my daughter

Anoushka

Acknowledgement

I am extremely grateful to my advisor Dr. Donald R. Webster for his constant help and motivation during the past five years. He is truly a great mentor.

I would like to thank the committee members Dr. Predrag Cvitanovic, Dr. Phillip J. W. Roberts, Dr. Terry W. Sturm, and Dr. Pui-Kuen Yeung for their suggestions and comments during the oral defense and while writing of this thesis. I particularly note the sponsorship of National Science Foundation under Grant No. CTS-0303406

Special thanks to my wife Kiran and my daughter Anoushka for their constant support, inspiration, and love.

Finally, for the support and cheerfulness of Aranyak, Manu, Nayantara, Parikshit, Preeti, Shikha, and Sunit. I am truly thankful.

Table of Contents

List of Figures

List of Tables

List of Symbols

$\langle \cdot \rangle$	Ensemble averaging
∂_r^a	Partial derivative in the r direction operating at point a
A	Parameter dependent on flow geometry, or a set (if in chapter 5)
A_s	Nozzle cross-sectional area
$\alpha_g(\lambda)$	Scale-local area-volume density ratio exponent
$\alpha_\Omega(\lambda)$	Scale-cumulative area-volume ratio exponent
$B(i,j)$	Background image
C	Cantor set
$C(i,j)$	Cross-correlation of $F(i,j)$ and $G(i,j)$
c_k	Kolmogorov constant
C_N	N-point correlator
C_n	n^{th} order velocity structure function universal constant
$C_n^{'}$	Non universal constants
C_s	Obhukov-Corrsin constant
χ	Scalar variance dissipation rate
χ_r	Volume averaged scalar variance dissipation rate
d	Embedding dimension
D	Nozzle diameter
$D_A(\lambda)$	Coverage dimension of $A \subset \mathbb{R}^n$
$D_d(\lambda)$	Box-dimension or coverage dimension or fractal dimension
D_f	Fractal dimension
$\dim_H$	Hausdorff dimension
D_n	Universal constants on the velocity structure functions conditioned on volume averaged kinetic energy dissipation rate
d_t	Topological dimension
D_{ab}^{γ}	Symmetric tensor
D_n^{ε}	Generalized dimension of the multi-fractal nature of energy dissipation rate
$D_{Z_i \cap A}(\lambda)$	Coverage dimension of $Z_i \cap A$
δ_b	Bounding box size
e	Base of natural logarithm
ε'	One-dimensional surrogate of kinetic energy dissipation rate
ε	Kinetic energy dissipation rate

ε_r	Volume averaged kinetic energy dissipation rate
$E(k)$	Turbulence energy spectrum
η	Kolmogorov length scale
η_B	Batchelor length scale
η_{oc}	Obukhov-Corrsin length scale
$F(i, j)$	Interrogation region in first of PIV image pair
$\hat{F}$	Fast Fourier transform of $F(i, j)$
$f_d(\lambda)$	Largest empty box scale PDF (LEB-scale PDF)
$F_d(\lambda)$	Coverage fraction
$\hat{G}$	Fast Fourier transform of $G(i, j)$
$G(i, j)$	Interrogation region in second of image pair
$G(k)$	Scalar energy spectrum
$g_d(\lambda)$	Scale-local area-volume density ratio
γ	Intermittency factor of scalar field
H	Open channel flow depth
$\hat{H}$	$\hat{F}$ multiplied by the complex conjugate of $\hat{G}$
$H^s(A)$	s-dimensional Hausdorff measure of a set $A \subset \mathbb{R}^n$.
H_n	Universal constants in the n^{th} order scalar structure function
H_N	Hopf operator
$I(i, j)$	Raw image intensity
$I(i, j)_{corrected}$	Image intensity corrected for laser attenuation
I_N	In-homogeneous term in the evolution equation of multi-point correlators
$I_{new}(i, j)$	Conditioned image
k	Spectral wavenumber
κ	Molecular diffusivity
L	Integral length scale
$L(\lambda)$	Coverage length
$L_d(\lambda)$	Coverage length for an embedding dimension *d*
λ	Scale size or ruler size
$\Lambda(\lambda)$	Lacunarity
μ	Intermittency parameter of the kinetic energy dissipation rate
μ_m	Mean of mass-distribution function
n	Order of structure function
$N(\lambda)$	Coverage count
$N_A(\lambda)$	Coverage count of $A \subset \mathbb{R}^n$

$N_d(\lambda)$	Coverage count for an embedding dimension d
$N_{Z_i}(\lambda)$	coverage count of $Z_i \subset \mathbb{R}^n$
ν	Kinematic viscosity
$O(\,)$	Middle-thirds operation in the context of Cantor set
$\Omega_3(\lambda)$	Scale-cumulative area-volume ratio (embedding dimension is 3)
$\Omega_d(\lambda)$	Scale-cumulative area-volume ratio (embedding dimension is d)
$\Omega_{d,tot}$	Area-volume ratio at smallest scale ($\lambda \to 0$)
p	Fluctuating pressure
P	Pressure
Pe	Peclet number $= ReSc$
Ψ_{Δ}	Inertial-convective scaling exponent of longitudinal three-point correlation function
$\Psi_{\triangleright}$	Inertial-convective scaling exponent of vertical three-point correlation function
Q	Volumetric flow rate
r	Magnitude of separation vector
$r_1, r_2, \ldots, r_N$	Positions of N points
$\boldsymbol{R}$	Separation vector
Re_{λ}	Taylor-scale Reynolds number
Re	Reynolds number
$\mathbb{R}^d$	d-dimensional space
$\mathbb{R}^n$	n-dimensional space
$S_n^{\alpha_1\alpha_2\ldots\alpha_n}(\boldsymbol{R})$	Generalized n^{th} order structure function tensor
SO(3)	Spherical orthogonal rotation group in three-dimensional space
Sc	Schmidt number
σ_m^2	Variance of mass-distribution function
t	Time
t_η	Kolmogorov time scale
θ	Instantaneous scalar fluctuation from mean
$\langle \theta_1\theta_2\theta_3 \rangle_{\Delta}$	Longitudinal three-point correlation function
$\langle \theta_1\theta_2\theta_3 \rangle_{\triangleright}$	Vertical three point correlation function
$\Theta(\boldsymbol{x},t)$	Passive scalar field
$\langle \Theta^* \rangle$	Ensemble average of the local spatial average of scalar concentration
Θ_O	Source concentration
$\Theta_{th}(m)$	Concentration threshold level
u'	RMS streamwise velocity component
u^{α_1}	Velocity component in the i^{th} direction
u_i	Fluctuation of velocity component from mean

u_o	Large scale velocity
U_i	Mean velocity component
υ_n	Parabolic function of n
v_a	Velocity at points a
v_b	Velocity at points b
v_η	Kolmogorov velocity micro-scale
W_n	Constants in the conditioned scalar structure function
x	Longitudinal direction/displacement
x_i	Cartesian coordinate component
$\vec{x}_i$	Position vectors
ξ_x	Inertial-convective scaling exponent of longitudinal two-point correlation function
ξ_y	Inertial-convective scaling exponent of vertical two-point correlation function
y	Vertical direction/displacement
Z_i	Sequence of sets in $\mathbb{R}^n$
ζ^n	n^{th} order structure function scaling exponent
ζ_n	n^{th} order structure function scaling exponent
$\zeta_x^n(n)$	n^{th} order longitudinal structure function scaling exponent
$\zeta_y^n(n)$	n^{th} order vertical structure function scaling exponent

Summary

Small-scale structure of incompressible turbulent velocity and passive scalar fields has been a primary focus of turbulence research for decades. The objective of the current study is to contribute to several issues regarding the traditional view of the local structure of passive scalar fields: (1) the nature of the probability density function (PDF) of the fluctuating scalar concentration and scalar gradient, (2) the scaling behavior of the scalar power spectrum in the inertial-convective regime and the viscous-convective regime, (3) the anomalous scaling exponent of the passive scalar structure functions, and (4) the significance of correlation functions and multi-point correlators. In addition, the research provides a geometric description of two-dimensional transects of the passive scalar iso-surfaces using the tools of fractal geometry. The local structure is analyzed as a function of large-scale anisotropy, intermittency factor, Reynolds number, and initial condition of the scalar injection.

Experiments were performed in the bed boundary layer produced by a uniform depth open channel flow of water in a tilting flume for Re_λ = 63, 94, and 120. A small nozzle iso-kinetically delivers a passive scalar of high Schmidt number ($Sc \approx 1000$) at mid-depth to generate the turbulent scalar field. Three nozzle diameters (2.2 mm, 4.7 mm, and 9.4 mm) are used to study the effects of the injection length scale on the local structure of the scalar field generated downstream. A high-resolution planar laser induced fluorescence (PLIF) technique recorded long-time series of the concentration

along the nozzle centerline in a vertical plane parallel to the flow at six downstream distances.

The local structure is found to be far from isotropic and is influenced even at the smallest scales by large-scale anisotropy and the presence of the mean scalar gradient. The local structure is also influenced by the initial injection length scale and the Reynolds number of the flow. The PDF of the scalar fluctuations is found to be non-Gaussian and dependent on large-scale anisotropy. The PDF of scalar gradients show that the large-scale anisotropy of the scalar field influences the structure at the smallest scales. The spectrum of the scalar field is observed to deviate from the $k^{-5/3}$ prediction in the inertial convection regime due to large-scale anisotropy, external intermittency, and low Reynolds number. For the smallest injection length scale, a cascade bypass is observed with the inertial-convective regime scaling close to k^{-1}. In the viscous-convective regime, there is no evidence of Batchelor's k^{-1} scaling law. The downstream evolution of the scaling exponents of the even-ordered structure functions appears to be inversely correlated with the skewness and kurtosis of the scalar fluctuations. The saturation of the scaling exponents is stronger with presence of mean-gradients. Two-point correlation functions and three-point correlation functions also show scaling behavior in the inertial-convective regime with the exponents correlated with the variations in the structure function exponents.

The fractal geometry of the two dimensional transects of passive scalar iso-surfaces is dependent on Reynolds number, injection length scale, and concentration threshold of the

iso-surfaces. The iso-surfaces are found to possess scale-dependent geometric properties. The fractal dimension is 1.0 at the smallest length scale and increases in a universal manner to reach a local maximum at a scale around the Kolmogorov length scale. At larger scale the fractal dimension is eventually less than 1.0. The scale-local length-area ratio exponent indicates the presence of self-similarity in the inertial-convective regime. The coverage length underestimate is found to have universal behavior in the viscous-convective regime and hence is a useful tool for many mixing applications. The lacunarity of the iso-surface structure is introduced to show that the instantaneous scalar field is most in-homogenous around the Kolmogorov scale.

Chapter 1

Introduction

1.1 Introduction

Mixing and transport of passive scalars in incompressible turbulent shear flows is an important process occurring in many natural and engineered environments. Common examples include contaminant discharges in water bodies, smoke plumes in the atmosphere, and chemical mixing in reactors. Despite decades of research aimed at understanding the dynamics of turbulent transport, the scalar fields continue to defy accurate theoretical predictions. The lack of a general theory to predict the statistical nature of turbulent transport ultimately requires empirical tests to predict and optimize mixing efficiency in many practical situations.

This study focuses on several important aspects of the local structure of the passive scalar field transported in a turbulent shear flow. Theoretical aspects to be experimentally studied include: 1) the phenomenology of the local structure of the fluctuating passive scalar field, and 2) fractal geometry of the passive scalar iso-surfaces. These aspects of the small-scale passive scalar structure are studied with respect to the effects of large-scale anisotropy, such as mean gradients and intermittency factor. The local structure is also studied with respect to variation in Reynolds number and the initial size of the passive scalar filament prior to the onset of turbulent mixing.

1.2 Motivation

Phenomenology of the passive scalar field

Theoretical descriptions of turbulent velocity and passive scalar dynamics have evolved considerably in the past four decades. One prevalent modeling approach for the passive scalar field is a phenomenological model (refined similarity hypotheses as applied to passive scalar fields, RSHP), which bypasses the governing equations by employing a universal small-scale self-similar eddy picture for both the velocity and passive scalar fields. This model nearly predicts the scaling laws of the structure functions for the passive scalar fields. While these results are encouraging, problems with RSHP have been reported. For instance, the model shows that in the inertial-convective range the structure function scaling law is parameterized only by the dissipation rate of kinetic energy and the dissipation rate of scalar variance. By assuming a joint log-normal distribution characterizes the fluctuating behavior of the dissipation rates, the theory predicts that the scaling exponents of the structure functions are a function of the parameters of this distribution function. Some agreement has been observed between the theory and experimental data, but significant deviations have been observed in the scaling exponent of higher-order structure functions (see recent reviews by Sreenivasan & Antonia 1997, Warhaft, 2000).

RSHP is currently synonymous with passive scalar turbulence theory; however, we lack a complete understanding of the implications of the universal self-similar eddy picture. For instance, the influence of large-scale anisotropy in the scalar field on the local structure is not clearly understood. This study examines the applicability of RSHP on the small-scale

structure of a scalar field that possesses large-scale velocity and scalar gradients. It is important to examine the applicability of RSHP for realistic scalar fields with a small intermittency factor, moderate Reynolds numbers, significant mean gradients in the velocity and scalar fields, and varying initial conditions of the passive scalar field. Results from this study are significant for developing small-scale models for anisotropic passive scalar fields, and also highlights the distinction between naturally-occurring turbulence and that corresponding to a self-similar isotropic velocity field.

Fractal geometry of passive scalar iso-surfaces

Another important aspect of passive scalar transport in turbulent shear flows is the fractal geometry of interfaces (surfaces of constant temperature or concentration). Catrakis (2000) describes turbulent mixing and transport of passive scalars as a combination of folding and wrinkling processes. The effect of these processes can be studied by quantifying the geometric scale distributions of the convoluted structure of passive scalar interfaces within the fluid. Catrakis (2000) developed a framework to study the fractal properties of these interfaces and applied it specifically to turbulent jets. The motivation for the present study is to characterize the fractal nature of the passive scalar surfaces generated by iso-kinetic plumes in a boundary layer. The broader objective for this study is to better understand the relationship between structure functions and power spectra of the passive scalar field to the geometric characteristics of iso-surfaces at various scales.

The overall focus of this study is to characterize the small-scale dynamics of the passive scalar fields in a turbulent boundary layer flow. Fundamental turbulence research

continues to favor modeling of the structure at dissipative scales, thus the current experimental study will impact both modeling strategies and our understanding of the coupling between small-scale and large-scale behavior.

The thesis is organized as follows: Chapter 2 is a literature review of previous work relevant to this study; Chapter 3 describes the experiment, instrumentation, and flow characteristics; Chapter 4 presents the statistical view of the local structure of the passive scalar field under the influence of large-scale anisotropy for different Reynolds numbers and initial conditions; Chapter 5 describes the fractal geometry of two-dimensional transects of the passive scalar iso-surfaces; and Chapter 6 contains the summary and discussion with recommendations for extending this study.

Chapter 2

Literature Review

The difficult nature of fluid turbulence has made it a huge challenge for physicists, as well as engineers, for over a century. Starting with the development of the Navier-Stokes equations, most turbulence research has taken place during the past 150 years. In that period, tremendous contributions to understanding turbulence have been made through detailed experimental, theoretical and computational research. Nevertheless, turbulence remains "unsolved" due to a lack of either the correct approach or the necessary tools and most research is still aimed toward understanding turbulence. Here the term "unsolved" refers to the inability of turbulence theory to predict statistical quantities of interest (such as the mean velocity at a point in a well defined turbulent flow problem) with reasonable accuracy without the need for ensemble averaging simulated or experimental data, or modeling of turbulence.

This chapter is organized as a brief history containing a mixture of the "classical era" (until the 1960s) and the "modern era" of turbulence research with emphasis on research relevant to small-scale structure and fractal geometry of turbulent passive scalar fields. The classical era has mostly consisted of the statistical approach combined with the phenomenological model of local isotropy by Kolmogorov. Following this, many experimental observations revealed the limitations of this theory as it failed to statistically describe turbulence, even generally. The modern era consists of revisions made to Kolmogorov's local isotropy hypothesis and the search for a new approach for a rigorous

understanding of turbulence. As a result, the modern theory of turbulence is built on several amendments to Kolmogorov's hypothesis as an attempt to account for the intermittency phenomena and the anomalous scaling behavior of statistical quantities. Focusing on turbulence as a small-scale phenomenon left large-scale motions as a separate and poorly addressed problem. Nevertheless, some research focused on large-scale phenomena through the study of coherent structures, a phenomenon that still lacks a satisfactory explanation. A brief review of these developments and their implications on the research in passive scalar transport in turbulent flows is presented. Most recently, research toward developing a dynamical theory of turbulence is taking shape with the premise that every turbulent flow problem is unique and that statistical measures is purely a function of the phase-space topology of a flow problem. Such an approach is beyond the scope of this study and therefore is not discussed.

2.1 Theory of fluctuating velocity in a turbulent flow field

The statistical theory was started by Reynolds (1883, 1894) and consists of analyzing the flow variables decomposed into their mean and fluctuating parts. For example, the following is the governing equation for the mean velocity field, derived by first decomposing the variables in the incompressible Navier-Stokes equations: $U_i = < U_i > + u_i$ and $P = < P > + p$, followed by ensemble averaging.

$$\frac{\partial < U_i >}{\partial t} + < U_j > \frac{\partial < U_i >}{\partial x_j} = -\frac{1}{\rho}\frac{\partial < P >}{\partial x_i} + \frac{\partial}{\partial x_j}\left(\nu \frac{\partial < U_i >}{\partial x_j} - < u_i u_j > \right) \qquad 2.1$$

The above equation contains the second order moment, $< u_i u_j >$, that appears as an additional stress acting on the mean flow (named the Reynolds stress). Equation 2.1 combined with the continuity equation for the mean incompressible flow (i.e. $\partial < U_i > / \partial x_i = 0$) forms an unclosed system of equations owing to the presence of the unknown Reynolds stress. Moreover, an equation derived for the Reynolds stress itself includes unknowns of higher order moments. This demonstrates the so called "closure problem" where evolution equations derived for a given moment always contain higher order moments as additional unknowns thereby compounding the problem.

Most of the research until the 1960s was dedicated to using statistical assumptions and models to address the closure problem. One such statistical assumption was that the turbulent fluctuations of any flow variable follow a Gaussian distribution that is completely characterized by the first two moments. Models were developed to relate higher order moments to those of lower order to obtain a closed system of equations. These early approaches failed to formulate the fundamental problem of turbulence in the sense that they lacked a rigorous treatment and confidence of the solutions they obtained. Solutions to the closed system of equations often failed the realizability criteria (Sreenivasan 1999). A model is said to be realizable if it guarantees a positive kinetic energy in the flow domain for all time and also satisfies the Cauchy-Schwartz inequality for the fluctuating velocity field (for example $< u_1 u_2 > \leq \sqrt{< u_1^2 >} \sqrt{< u_2^2 >}$). However, despite producing unrealizable flow fields, these models proved to be useful for solving practical problems of modern technology faced by engineers. Being computationally approachable, they served as an excellent "quick-fix" to the increasing technological

demands from industries, namely chemical, automotive, aerospace etc. As far as the understanding of turbulence, the most significant progress came as a phenomenological model in 1941. This phenomenology of turbulence hasn't changed conceptually to the present day.

2.1.1 Phenomenological model – Kolmogorov's theory

The concept of isotropic and homogeneous turbulence was first introduced by Taylor (1935) to simplify the general problem of turbulence and also to facilitate a tractable analytical approach. Isotropy and homogeneity are purely theoretical and are generally not achievable in nature or in the laboratory. Based on these theoretical constructs, Kolmogorov (1941) postulated his theory (now called K41) and the results are useful to describe fundamental properties of small-scale turbulence. According to K41, small-scale turbulence is statistically isotropic and is independent of the production mechanism. This postulate is purely based on similarity arguments combined with dimensional analysis. Although this theory has had profound impact on turbulence research, its validity is often questioned due to strong discrepancies with experimental observations that were subsequently discovered.

Kolmogorov's phenomenological model starts with the view introduced by Richardson (1922) that turbulence consists of superposed eddy motions over a wide range of scales. Thus, the larger scale eddies have embedded smaller eddies and so on until a particular small scale. In this multi-fractal picture, the largest eddies have a size comparable to the flow geometry and a velocity comparable to the r.m.s. of the fluctuations. The effect of

viscosity does not play a dominant role in governing their motions as suggested by their high Reynolds number. On the other hand, the smallest eddies have a small Reynolds number for which viscous dissipation dominates their dynamics.

Following Richardson's eddy model, Kolmogorov (1941) introduced the concept of energy cascade to describe the eddy motions mathematically. In the energy cascade picture, the kinetic energy required to drive the small scales is fed by the immediate larger-scale eddies. Therefore the source of the energy to drive motions at all scales is the kinetic energy of the largest scale motion. This energy is transferred (and dissipated eventually) at a rate whose order of magnitude can be estimated as the characteristic kinetic energy per eddy turn over time, $\varepsilon = u'^2/(L/u') = u'^3/L$, where L is the integral length scale of the largest eddies and u' is the r.m.s. speed. Kolmogorov postulated that during the energy transfer from large to small scales, the directional basis of the anisotropic largest scales is lost. Since the directional basis is lost, he hypothesized that turbulence at small scales is statistically isotropic. The mathematical definition of local isotropy is that the turbulent fluctuations do not have any preferred orientation and possess the same statistical properties irrespective of rotation or reflection of the observer's coordinate system. Kolmogorov further postulated that information related to the flow geometry and boundary conditions is also lost during the energy cascade.

The consequence of these postulates is the first similarity hypothesis according to which all small-scale turbulent motion, irrespective of its source, has a universal form and is purely a function of ν and ε. Therefore, the characteristic length scale and velocity

scale of these small-scale turbulent motions must also be a function of ν and ε alone. By dimensional reasoning the smallest length scale (now called Kolmogorov length scale) scales as $\eta = \left(\nu^3/\varepsilon\right)^{1/4}$ and together with the corresponding time scale, $t_\eta = \left(\nu/\varepsilon\right)^{1/2}$ and velocity scale, $v_\eta = \left(\nu\varepsilon\right)^{1/4}$ characterize the motion at the lower end of the energy cascade.

A second similarity hypothesis was presented for very high Reynolds number flows. In this hypothesis, the range of scales of motion is so vast that there exists a sub-range ($\eta << r << L$) midway where both the viscous effects and the effects due to the anisotropic large scales are negligible. In this sub-range, the turbulent motion is also hypothesized to be universal and a function of ε alone. This range is called the "inertial sub-range". Following these arguments, the longitudinal velocity structure function, $<\Delta u_r^n> = <\left(u(x+r,t) - u(x,t)\right)^n>$, assumes the universal scaling law:

$$<\Delta u_r^n> = C_n\left(r\varepsilon\right)^{n/3} \qquad 2.2$$

where r is the separation distance of a magnitude that falls in the inertial sub-range, n is a positive integer, and C_n are universal constants. For n = 2, the Fourier transform of this structure function yields the spectral energy density function $E(k)$. This function mathematically defines the energy cascade as turbulent kinetic energy per unit wavenumber, k, and has the functional form $c_k\varepsilon^{2/3}k^{-5/3}$ where c_k is called the

Kolmogorov constant. The integral of the spectral energy density function over all wave numbers is defined as $\frac{1}{2} < u_i u_i >= \int_0^\infty E(k)dk$.

The prospect of finding the universal structure of small-scale motion in turbulent flows led many researchers to attempt to experimentally verify the K41 theory. Although there was good agreement on the existence of the universal scaling law for the first few moments, strong departures were observed for structure functions of higher order. These departures were subsequently explained as a result of non-benign interactions between the large and small scales, and indicated that the K41 theory rested on incorrect assumptions. Kolmogorov himself presented a refinement to his theory in 1962 following the suggestions of Obukhov (1962), later called the refined similarity hypotheses (RSH) or K62. According to Obukhov, the failure of K41 theory was attributed to the fluctuations of the dissipation rate due to intermittent changes in the large-scale processes. The refined similarity hypotheses are essentially a minor conceptual change to K41 theory. The refinement is that the statistics, while still locally isotropic and universal, are now a function of ε_r and ν, thereby replacing the mean dissipation rate, ε, by its local average, ε_r, calculated over a volume of dimension of the order of the dissipation scales. Kolmogorov further conjectured that the fluctuations of ε_r follow a log-normal distribution.

There is little doubt now that the K41 theory of a universal small-scale structure in turbulent flows has been the most significant step toward understanding turbulence.

However, the theory is purely grounded on similarity arguments and makes no connection with the Navier-Stokes equations for incompressible fluids. Furthermore, the deviations observed in higher order structure functions points to the fact that K41 is not a complete solution to understanding turbulence. This marked the end of the classical era of turbulence research. Turbulence theory research that followed this era mostly aimed to validate the refined similarity hypotheses that are still based on the concept of the energy cascade and multi-fractal eddies, but with non-universal small-scale motion.

2.1.2 Recent research in turbulence theory – Kolmogorov's legacy

By the end of the classical era of turbulence research it was clear that the energy dissipation rate fluctuated in time due to the fluctuations in the large-scale motion. Moreover it had strong variation in space due to the presence of intermittent structures at small-scales. These explanations seemed to address the observed deviations from the K41 prediction for statistical properties of third and higher orders. The refined similarity hypothesis (RSH) has proved to be a reasonable theory to the present day with some exceptions (Guvich & Yaglom 1967, Gibson et. al. 1972, Antonia et. al. 1982, Wang et. al. 1996, etc.). Over the years there has been general agreement on the description of small-scale statistics using longitudinal structure functions by RSH. More recently, simulations have shown deviations in the scaling exponents for higher order longitudinal structure functions ($n > 10$) (Wang 1996), and significant deviation in the transverse structure functions ($n > 5$) (Sreenivasan 1998). Since RSH does not predict any directional dependence for the scaling exponents these issues have become liabilities of the theory. Although several limitations of the experimental and computational

techniques have been identified, the confidence for a general turbulence theory based on the small-scale phenomenology is poor.

Kolmogorov (1962) proposed RSH to account for the spatial fluctuations of energy dissipation rate by employing the local volume average, ε_r. This averaged dissipation rate was then assumed to fluctuate in time following a log-normal distribution. Based on similarity arguments, the moments of Δu_r conditioned on ε_r were related to r, ν, and ε_r. This relation for the inertial sub-range was shown as $< \Delta u_r^n >\Big|_{\varepsilon_r} = D_n \left(r\varepsilon_r\right)^{n/3}$, where D_n are universal constants. Using the log-normal assumption for the fluctuating volume-averaged dissipation rate, Kolmogorov derived the structure function relation for the inertial sub-range as $< \Delta u_r^n >= C_n(A,L)\left\langle \varepsilon \right\rangle^{n/3} r^{\zeta_n}$ where C_n are a function of A, a constant that depends on the flow geometry, and L, the integral length scale. The log-normal assumption also implies that the scaling exponent, ζ_n, is non-linearly related to the order of the moment as $\zeta_n = \frac{1}{3}n - \frac{1}{18}\mu n(n-3)$, where μ is a universal constant known as the intermittency parameter calculated to be in the range 0.2 to 0.28 (Anselmet et al. 1984, Sreenivasan & Kailashnath 1993, Wang et al. 1996). This parameter appears directly in the relationship for variance of the logarithmic dissipation as $\sigma^2_{\ln \varepsilon_r} = A + \mu \ln \frac{L}{r}$. For n = 2, the intermittency parameter changes the $k^{-5/3}$ energy spectrum of K41 to $k^{-5/3-\mu/9}$ scaling law. Since μ is of order unity, the assumed log-normally fluctuating dissipation rate significantly affects only the higher order statistics (n > 3).

The refined similarity theory is currently accepted due to its reasonable agreement with observations for statistics up to the fifth order moments. However, several disagreements with the log-normal conjecture of the dissipation rate exist. Gurvich and Yaglom (1967) concluded on theoretical grounds that a log-normal distribution may be justified only for very high Reynolds number with an assumption of scale-similarity. Moreover, Norikov (1971) and Mandelbrot (1974) concluded that the conjecture was not valid as it cannot be proved for the given constraints. These researchers are only some of the many that either supported an alternate distribution or provided evidence against the log-normal distribution. Despite the disagreement in characterizing the dissipation fluctuations, the existence of a universal scaling exponent is still believed. These exponents can be determined by scaling structure functions of the form $< \Delta u_r^n > / u_o^n = C_n^{'} (r/L)^{\zeta_n}$, where the dissipation rate does not explicitly appear in the structure function relation by utilizing Obukhov's hypothesis, which states that the ratio $\varepsilon_r / \varepsilon$ is a fluctuating quantity dependent only on r/L. In this form, u_o is the large-scale velocity, $C_n^{'}$ are constant prefactors that are not universal, and ζ_n, although different from $n/3$, is presumed to be universal.

The most serious drawback of RSH, however, is the direct contradiction of local isotropy hypothesis recently observed experimentally. Chen et al. (1997) showed that the scaling of transverse structure functions had better correlation with locally averaged enstrophy (squared vorticity) than ε_r and reduced the anomaly in scaling exponents that deviated from the RSH prediction. They proposed a separate RSH theory for transverse structure functions as a bridge to explain the gap for anomalous scaling exponents for non-

longitudinal structure functions. This raises questions for structure functions at oblique directions. For now RSH has developed into two versions where energy dissipation characterizes the longitudinal structure functions while the enstrophy characterizes the transverse structure functions.

Several other problems of interest to turbulence theory were identified in light of RSH theory. These problems concern small-scale intermittency, namely dissipation intermittency and inertial range intermittency (Sreenivasan & Antonia 1997). Dissipation intermittency concerns the behavior of scaling exponents due to the effects of intermittent fluctuations in the dissipation rate. In particular, the focus is on Obukhov's hypothesis regarding the ratio of $\varepsilon_r / \varepsilon$. Scaling exponents for the dissipation rate is defined by the scaling law as $< \varepsilon_r^n > / < \varepsilon^n > \propto (r/L)^{-\upsilon_n}$. If Kolmogorov's log-normal conjecture is correct, then υ_n is a parabolic function of n. An assumption of multifractal structure of the dissipation rate with a generalized dimension D_n^ε (Mandelbrot 1974, Hentschel & Procaccia 1983) implies that υ_n and D_n^ε are related as $\upsilon_n = (n-1)(1-D_n^\varepsilon)$. Here D_n^ε can be experimentally obtained using the fractal scaling relationship for dissipation rate, defined as: $\sum (r\varepsilon_r)^q \propto r^{(q-1)D_q^\varepsilon}$, where the summation is over all the spatial intervals of size r. Inertial range intermittency concerns the deviation of the structure function relation predicted by RSH from measurements corresponding to separation distance r in the inertial sub-range. Inertial range intermittency manifests as a non-linear relationship between the scaling exponent, ζ_n, and n, as opposed to the non-intermittent K41 relation, $\zeta_n = \frac{n}{3}$. Meneveau and Sreenivasan (1987) showed that this non-linear

relationship could be related to the dissipation intermittency through the generalized dimension, D_n^{ε}, of the dissipation rate. Assuming RSH is correct, they showed that $\zeta_n = (\frac{n}{3} - 1)D_{n/3}^{\varepsilon} + 1$.

Although tremendous progress has been achieved through experiments and numerical simulations, it is worth noting the liabilities associated with some common practices. Most of the experimental studies on RSH are not accurate due to the use of Taylor's frozen turbulence hypothesis and the surrogacy issue (Sreenivasan 1999). Taylor's frozen turbulence hypothesis assumes that spatial variations of the velocity are fixed and simply advected by the mean flow and, thus, are analogous to temporal fluctuations at a point. Since the instantaneous velocity gradients in space cannot be easily measured it is common to calculate the spatial gradients from the time fluctuations and advection speed. Further, the volume average to calculate ε_r is indirectly computed from a longitudinal line average. The surrogacy issue involves the use of local isotropy assumption in order to calculate quantities such as dissipation rate. A "surrogate" instantaneous dissipation rate given by $\varepsilon' = 15\nu(\partial u_1 / \partial x_1)^2$ and is used for analysis because it can be conveniently measured with single point data. The effect of using the surrogate dissipation rate was studied by Wang et al. (1996) using high resolution DNS data for $Re_\lambda \sim 200$. The results indicate that the difference in scaling exponents is not severe. Also the universal constant, μ, previously calculated based on ε' was in good agreement with that calculated using the full dissipation rate. However, the low Reynolds number limitation of DNS has made it impossible to relate experimental findings to theoretical predictions with confidence. RSH studies require significantly higher Reynolds number flow

experiments and simulations than those corresponding to the state-of-the-art. Another drawback in the studies of RSH concerns the energy dissipation rate itself. Traditionally, the energy dissipation is believed to be independent of viscosity for high Reynolds number and a constant of order unity when non-dimensionalized with the integral length scale and the r.m.s. velocity. A recent investigation (Sreenivasan 1998) shows that this constant depends on the details for forcing used by DNS at low wave numbers to simulate a steady isotropic turbulence. Studies also indicated that the constant varied significantly in grid generated isotropic turbulence for different grids. These issues have raised questions about whether large-scale effects affect other aspects of small-scale turbulence.

Another fascinating area of recent research in turbulence theory has been large-scale coherent structures (Sreenivasan 1999). These structures are defined as organized motion within the random nature of fluid turbulence. Few studies have addressed these structures due to the preoccupied research on isotropic turbulence. However, research has gathered momentum since the studies of Liepmann (1952) and Favre et al. (1967), who measured correlation functions that established the existence of coherent structures. Recent emphasis on the importance of large-scale motions in the study of transport processes has led to increased focus on these structures. Consequently, several theories have been proposed to explain how these structures maintain coherence. One theory is that the structures result from instability of the mean Navier- Stokes equations. Although explaining their coherence in the midst of chaos has been a separate challenge, it has been more difficult to develop mathematical tools to lay a firm basis for the study. For now,

conditional averaging has proved to be an important tool in defining these structures objectively (Kovasnay et al. 1970). Other attempts have employed analytical description and models using low dimensional dynamical systems (Holmes et al. 1997). Research from the field of non-linear dynamical systems has shown that coherent structures are a generic phenomena and typical for systems with large degrees of freedom. These structures have been termed as solitons (Zabusky and Krustal, 1965), but a clear relation between solitons and coherent structures has yet to be proposed (Sreenivasan 1999).

There is little doubt that the phenomenological picture of small-scale motion in turbulent flows is an approximation and it has yet to establish itself as correct. Also, RSH was not derived from first principles (Meneveau et al 1990, Hosokowa 1991 etc.), thereby reinforcing the status of an approximate theory. The most important impact of this theory has been on developing simulations of complex flows by numerically solving the Navier-Stokes equations with a resolution greater than the smallest turbulent scales (so called Large Eddy Simulation or LES). The dynamical effect of small-scale motions is artificially modeled using RSH concepts to account for the reduced resolution. Such a practice reduces the necessary computational resources and time to simulate complex engineering flows. The "success" of the phenomenological model has also motivated the phenomenology of passive scalar transport in turbulent flows. Transport phenomenon of passive scalars in turbulent flows has been intractable owing to the nature of turbulence problem itself. A brief review of the progress achieved in the understanding of this problem is presented in Section 2.2.

2.1.3 Isotropic and anisotropic decomposition

In the past few years, the quest to explain the observed deviations from RSH predictions has taken a radical shift regarding the approach to addressing structure function scaling laws and their universal properties. Turbulence is now considered to be fundamentally anisotropic at all Reynolds numbers and only approaches Kolmogorov's local isotropy state as the Reynolds number approaches infinity. However, due to the symmetric properties of the Navier-Stokes equations it is possible to represent turbulent fluctuations as a sum of the isotropic and anisotropic contributions. Ariad et al. (1998, 1999), Kurien et al. (2000), Kurien & Sreenivasan (2001), Grossmann et al. (2000), and Biferale & Vergassola (2001) have successfully exploited this property to decompose structure function tensors into a sum of isotropic and anisotropic parts using the irreducible representation of SO(3) symmetry group.

To explain the SO(3) decomposition, the general n^{th} order structure function is defined in the full tensor form as:

$$S_n^{\alpha_1\alpha_2\ldots\alpha_n}(\boldsymbol{R}) = < \left(u^{\alpha_1}(\boldsymbol{r}+\mathbf{R}) - u^{\alpha_1}(\mathbf{r})\right)\left(u^{\alpha_2}(\mathbf{r}+\mathbf{R}) - u^{\alpha_2}(\mathbf{r})\right)\ldots\left(u^{\alpha_n}(\mathbf{r}+\mathbf{R}) - u^{\alpha_n}(\mathbf{r})\right) >$$

where the superscripts α_i indicate the velocity component in the i^{th} direction. In this equation, R is the separation vector and r is the position vector of the location associated with the structure function. Since the Navier-Stokes equation is invariant under symmetric operations of SO(3), it can be shown that the evolution equations derived for the structure function tensor also follow this property. Also, tensor fields

satisfying this property can be expressed as a linear combination of a suitable basis tensors which by construction separate the isotropic part from the rest with each basis component behaving in a different manner under coordinate rotation (i.e. the irreducible representation of the SO(3) group). Therefore, the structure function can be decomposed as:

$$S_n^{\alpha_1\alpha_2\ldots\alpha_n}(\boldsymbol{R}) = S_n^{\alpha_1\alpha_2\ldots\alpha_n}(\boldsymbol{R})\big|_{j=0} + S_n^{\alpha_1\alpha_2\ldots\alpha_n}(\boldsymbol{R})\big|_{j=1} + S_n^{\alpha_1\alpha_2\ldots\alpha_n}(\boldsymbol{R})\big|_{j=2} + \ldots$$

where $j = 0$ sector is the isotropic contribution while $j > 0$ are anisotropic contributions. Since each of these components satisfy the basic evolution equation of the structure function, the resulting set of equations is referred as "foliation" (Arad et al. 1999). Each of these structure function tensor components satisfy a different scaling law and the isotropic component is presumed to follow the K41 scaling.

Using the above decomposition, Arad et al. (1998) showed that the effect of anisotropy is more severe in the transverse components of the structure functions compared to the longitudinal components from turbulent velocity signals measured in the atmospheric surface layer ($Re_\lambda = 20{,}000$). An estimate for a universal exponent for the isotropic part of the second order structure function (i.e. $j = 0,\ n = 2$) was calculated to be 0.69. For $j = 2$ the exponent was 1.38 and 1.36, respectively, for two separate data sets corresponding to different probe separations. These results formed the first attempt to quantify the degree of anisotropy in turbulent flows.

Arad et al. (1999a) used the SO(3) decomposition analysis to further investigate a turbulent channel flow using DNS simulations at Re_λ = 70. Their main conclusion is that the isotropic scaling exponent is universal and independent of the measurement location, and that the j = 2 component of the structure function exhibits a scaling exponent that is comparable with the theoretical expectation. Following the successful and promising development of the idea of separating the isotropic and anisotropic contributions to statistical objects such as structure function tensors, Arad et al. (1999b) described a detailed general theory for analysis of correlation functions and structure functions in the context of SO(3) decomposition.

Kurien et al. (2000), using hot-wire velocity measurements in atmospheric surface layers, demonstrated that the scaling exponents of the three leading sectors (j = 0, 1, and 2) are different and universal (independent of probe location). The scaling exponents were estimated to be 0.68, 1.0 and 1.38. A theoretical argument based on Clebsch representation of the Euler equations predicts similar values of 2/3, 1 and 4/3, respectively. The authors note a high degree of uncertainty for $j \geq 3$ calculations.

Although these recent developments point to the monotonous decay of anisotropy with increasing Reynolds numbers, Shen and Warhaft (2000) presented observations in contradiction to these conclusions. For hot-wire measurements in a wind tunnel, the normalized 5^{th} order moments of the velocity increments were observed to be of order 10 and the 7^{th} order moments increased with Reynolds numbers. These trends indicate a non-monotonous behavior of anisotropy as a function of Reynolds numbers.

2.2 Statistical theory of passive scalars advected in turbulent flows

2.2.1 Background

Most of the research regarding passive scalar turbulence occurred in parallel to the developments in turbulence theory. Passive scalar turbulence refers to the dynamics of a passive scalar field, $\Theta(\boldsymbol{x},t)$, such as temperature or concentration of magnitude insufficient to induce buoyancy or any effect on the velocity field, that is transported by the velocity field given by the governing transport equation: $\partial\Theta/\partial t + U_i\,\partial\Theta/\partial x_i = \kappa\partial^2\Theta/\partial x_i\partial x_i$, where κ is the molecular diffusivity of the passive scalar. Substituting the Reynolds decomposition of the passive scalar ($\Theta = <\Theta> + \theta$) and velocity variables (see Section 2.1) in the transport equation, followed by ensemble averaging yields:

$$\frac{\partial <\Theta>}{\partial t} + <U_i>\frac{\partial <\Theta>}{\partial x_i} = \frac{\partial}{\partial x_i}\left(\kappa\frac{\partial <\Theta>}{\partial x_i} - <u_i\theta>\right) \qquad (2.3)$$

The correlation term between the velocity and scalar fluctuations, $<u_i\theta>$, reveals a familiar closure problem. A common model for the turbulent flux term is the eddy diffusivity model, in which $<u_i\theta>$ is directly proportional to the local mean scalar gradient, $\partial <\Theta>/\partial x_i$. The constant of proportionality is called the turbulent diffusivity coefficient, which has been estimated by several methods based on mixing length models. Although such models have very limited physical justification (i.e. turbulent mixing is

not a Fickian process) they are used extensively today in most industrial and environmental applications.

Concerning the small-scale passive scalar structures, a K41-type phenomenological model was developed to describe the statistics of small-scale structures of passive scalars in turbulent flows. This phenomenological model was based on similarity arguments for the passive scalar field and was introduced by Obukhov (1949) and Corrsin (1951) for high Reynolds number flows. Later, it came to be known as the Kolmogorov-Obukhov-Corrsin (KOC) argument. The multi-fractal picture of "eddy" structures for the passive scalars was assumed with a cascade of the scalar variance from large to small scales. According to this theory, small-scale statistics of the passive scalar are locally isotropic. However, the true nature of small-scale statistics of passive scalars is now accepted to be fundamentally anisotropic with only a possible approach to isotropy as Reynolds number tends to infinity. Most research concerning the small-scale passive scalar structures involved the implication of the KOC arguments and later its refinements on various mathematical descriptions of the turbulent scalar field such as the probability density functions, power spectra, structure functions, correlation functions, and fractal geometry.

2.2.2 Spectrum of the passive scalar field

The passive scalar spectrum depicts the cascade of scalar variance from the large scales to the smallest scales. The governing equation for scalar variance can be derived by Reynolds decomposition of the passive scalar transport equation and subtracting equation

2.3 to obtain the transport equation for θ. Multiplying this equation by θ followed by ensemble averaging results in the governing equation for scalar variance:

$$\frac{\partial <\theta^2>}{\partial t} + <U_i> \frac{\partial <\theta^2>}{\partial x_i} = \frac{\partial}{\partial x_i}\left(\kappa \frac{\partial <\theta^2>}{\partial x_i} - 2 <u_i \theta^2>\right) + \left(-2 <u_i \theta> \frac{\partial <\Theta>}{\partial x_i}\right) - \left(2\kappa < \frac{\partial \theta}{\partial x_i} \frac{\partial \theta}{\partial x_i} >\right) \tag{2.4}$$

The terms on the right hand side of equation 2.4 correspond to transport, production, and dissipation, respectively, of the scalar variance. The transport term is the rate of change of the scalar variance due to molecular and turbulent transport within the flow field. The production term increases the scalar variance due to velocity fluctuations acting across the mean scalar gradient. The dissipation term corresponds to the reduction of scalar variance due to "smearing" of scalar gradients by molecular diffusion. The scalar variance is thus produced at the large scales set by the mean scalar gradient and cascades down to the smallest allowable scale where dissipation takes place by molecular diffusion. Analogous to the velocity field where the energy cascade ends at a length scale corresponding to unit Reynolds number, Obukhov (1949) and Corrsin (1951) suggested that the cascade has a lower bound at a length scale corresponding to a unit Peclet number (Peclet number is defined as $Pe = UL/\kappa = ReSc$, where $Sc = \nu/\kappa$ is the Schmidt number). This length scale, called the Obukhov-Corrsin length scale, is given by $\eta_{oc} = \left(\kappa^3/\varepsilon\right)^{1/4}$. The effects of molecular diffusivity were assumed to play a dominant role in the dynamics for length scales smaller than η_{oc}. A similarity hypothesis analogous to Kolmogorov's hypothesis was presented using this new length scale along

with the Kolmogorov length scale for cases of low and high Schmidt numbers. According to these hypotheses there exists an inertial range ($\eta_{oc} << r << L$) (formally called the inertial-convective range in the context of passive scalar spectrum) where the turbulent structure of the passive scalar field is independent of the anisotropic large scales and the process of molecular diffusion. In this range the passive scalar structure is hypothesized to be a function of scalar dissipation rate χ and energy dissipation rate ε, only. In this range the energy spectrum takes the form $G(k) = C_s \chi \varepsilon^{-1/3} k^{-5/3}$, where C_s is the Obukhov-Corrsin universal constant and k is the wave number in the range $\frac{1}{L} << k << \frac{1}{\eta_{oc}}$.

Later, Batchelor (1959) showed that the cutoff length scale, η_{oc}, was appropriate only for low Schmidt number passive scalars (Sc << 1) and that the strain rate of the fluctuating velocity determines the cutoff length scale for scalars with high Schmidt numbers (Sc >> 1). Using dimensional reasoning, a new length scale for the cutoff point was put forward as $\eta_B = \left(\nu \kappa^2 / \varepsilon\right)^{1/4}$, which is now called the Batchelor scale. The Batchelor scale can also be expressed in terms of the Kolmogorov length scale as $\eta_B = \eta Sc^{-1/2}$. When the power spectrum of the velocity field has an inertial sub-range, several scaling regimes may exist for the high Schmidt number passive scalar spectrum. Inertial-convective range is defined as the range with negligible effects of large scale anisotropies, viscosity, and diffusivity (for the wavenumber interval $\frac{1}{L} << k << \frac{1}{\eta}$). The viscous-convective range is defined as the range where viscous effects start to play a role while molecular diffusivity does not ($\frac{1}{\eta} << k << \frac{1}{\eta_B}$). Finally the viscous-diffusive range is defined for the very high

wavenumbers corresponding to length scales of the order of or smaller than the Batchelor scale (i.e. $k > \frac{1}{\eta_B}$). Batchelor derived the behavior of the passive scalar spectrum for $k >> \frac{1}{\eta}$ as $G(k) = q < \chi > \left(\nu / < \varepsilon >\right)^{1/2} k^{-1} \exp\left(-q\left(k\eta_B\right)^2\right)$, where q is a dimensionless constant. Thus, the spectrum scales as k^{-1} in the viscous-convective range. Kraichnan (1968) modified this formula to take into account the stochastic nature of the fluctuating strain rate. The modified formula by Kraichnan also predicts k^{-1} scaling in the viscous-convective range, however it changes the constant in the exponential function. The modified formula is: $G(k) = q < \chi > \left(\nu / < \varepsilon >\right)^{1/2} \left(1 + k\eta_B \sqrt{6q}\right) k^{-1} \exp\left(-\sqrt{6q}\left(k\eta_B\right)^2\right)$.

Much of the research in the past three decades has focused on the validity of the above predictions. The validity of the $k^{-5/3}$ scaling in the inertial-convective regime of the scalar variance spectrum, the value of the Obhukov-Corrsin constant, the validity of the k^{-1} scaling in the viscous-convective regime, and Kraichnan's exponential viscous-diffusive spectral roll-off have been the primary areas of focus.

To summarize the current state of research on the inertial-convective regime, Sreenivasan (1996) compiled data for several Reynolds numbers for shear flows. The main conclusion was that the spectral slope was, in general, more flat and approached the -5/3 slope with increasing Reynolds number. Warhaft (2000) noted that the spectral slope was much closer to -5/3 in the case of shearless turbulent flows (Jayesh et al. 1994, Mydlarski & Warhaft 1998, and others). Sreenivasan (1996) estimated the Obhukov-Corrsin constant (for one-dimensional spectrum) to be between 0.3 and 0.5 using high Reynolds

number atmospheric data. Mydlarski & Warhaft (1998) estimated this constant to be in the range 0.45-0.55 over a large range of Reynolds numbers using an active grid turbulence generator in a wind tunnel. Yeung et al. (2002) obtained a -5/3 inertial convective scaling and estimated the Obhukov-Corrsin constant to equal 0.4 using direct numerical simulations of passive scalar turbulence with Schmidt numbers of 1/8 and 1 for Taylor-microscale Reynolds numbers of 140 and 240. Warhaft (2000) concluded that the scalar spectrum in the inertial-convective range is affected by boundary conditions as seen from the qualitatively different behavior between shear and shearless turbulent flows. Most recently Watanabe & Gotoh (2004) used direct numerical simulations to estimate the Obhukov-Corrsin constant for the full three-dimensional spectrum to equal 0.68. In general, the spectral slope is close to -5/3 (closer in the case of shearless flows) and appears to approach -5/3 with increasing Reynolds number.

Less agreement has been achieved regarding Batchelor's k^{-1} scaling prediction for the viscous-convective regime for the case of high Schmidt number passive scalars. Following the prediction in 1959, laboratory measurements by Gibson & Schwartz (1963) and measurements in the ocean by Grant et al. (1968) reported agreement with the k^{-1} scaling law. Yeung et al. (2002), using direct numerical simulation, also observed a k^{-1} scaling in agreement with Batchelor's prediction. Yeung et al. (2002) also verified Kraichnan's exponential roll-off in the viscous-diffusive range with a weak Schmidt number dependence of the exponential coefficient. In contrast to these observations, Gargett (1985) found no evidence of the -1 slope in measurements in the ocean. Komori et al. 1989 reached a similar conclusion for shear layers. Miller & Dimotakis (1991)

measured the scalar field in a turbulent jet and found no k^{-1} scaling behavior. Miller & Dimotakis (1996) again disputed the k^{-1} scaling law while paying close attention to signal-to-noise ratio issues that may have affected earlier measurements. They showed that a log-normal spectral decay was a better fit in the viscous-convective regime. Williams et al. (1997) showed in the case of magnetically forced two-dimensional turbulence that the scalar spectrum fell below the k^{-1} curve. In the review article, Warhaft (2000) argued that there is persuasive evidence for the existence of the k^{-1} scaling based on the theory of Kraichnan (1968) and Holzer & Siggia (1994) and that more careful experiments must be conducted to address this issue.

In an effort to provide a coherent explanation for the issues related to the -5/3 slope and the Batchelor scaling, Villermaux et al. (2001) suggested an alternative cascade picture based on the mixing time of a scalar blob. According to the mixing time argument the scalar spectrum was derived as: $G(k) \propto \chi\left(\varepsilon^{-1/3}k^{-5/3} + \frac{1}{2}(\nu/\varepsilon)^{1/2}k^{-1}\ln(Sc)\right)$. Here the spectrum is interpreted as an interpolation between the -5/3 and -1 scaling, thus accounting for the slopes less steep than -5/3 and the absence of Batchelor scaling in experiments. In addition to the interpolative spectrum, a cascade bypass was suggested for wavenumbers higher than the wavenumber at which the scalar blob is introduced. Due to the presence of a dominant stretching rate associated with the initial size of the scalar blob the deviation from the -5/3 behavior is more pronounced, and a k^{-1} scaling was shown to be a better scaling approximation.

The effect of large-scale intermittency (external intermittency) on the passive scalar spectrum has been addressed by a few investigators. Dowling & Dimotakis (1990) showed that the magnitude of the slope of the inertial range of the scalar variance spectrum increased with the radial distance from the centerline of an axisymmetric jet. The increase was attributed to a combined influence of the intermittency factor, γ, defined as the fraction of time for which the scalar field is turbulent, and the mean shear and scalar gradient, which also changed across the jet. The increase in slope magnitude was not attributed to the variation of Re_λ because a decrease in Re_λ would have caused a decrease in the slope according to previous findings (e.g. Sreenivasan 1996). Mi and Antonia (2001) studied the effects of external intermittency and mean shear on the scaling exponents in a turbulent jet. They found that the scaling exponents for the scalar fluctuation were more sensitive than those for the longitudinal velocity. Results for the slope of the scalar variance spectrum were found to be similar to that of Dowling & Dimotakis (1990).

2.2.3 Passive scalar structure functions and correlation functions

According to the KOC theory, the structure of the scalar field in the inertial-convective range can be fully determined by χ and ε alone. From dimensional arguments, the scalar structure function, $<\Delta\theta_r^n>=<\left(\theta(x+r,t)-\theta(x,t)\right)^n>$, assumes the form:

$$<\Delta\theta_r^n>=H_n\left(\chi^{1/2}\varepsilon^{-1/6}r^{1/3}\right)^n \qquad (2.5)$$

where H_n are universal constants. For n = 2, the Fourier transform of this structure function yields the scalar variance spectrum: $G(k) = C_s \chi \varepsilon^{-1/3} k^{-5/3}$, where C_s is the Obukhov-Corrsin universal constant, which is analytically related to H_2 (i.e. C_s = $0.4 H_2$).

Although the $k^{-5/3}$ scaling for the passive scalar spectrum in the inertial-convective regime has been observed (or approached) in many experiments (see previous Section), the phenomenological model for passive scalars suffers the same liabilities as K41 owing to the strong intermittent fluctuations of both χ and ε in space and time. These fluctuations helped explained the deviations observed in the scaling exponents of KOC prediction of $n/3$ for third order moments or higher. For these reasons, a refinement similar to the RSH theory was developed for the passive scalar phenomenology (Monin & Yaglom 1975). This theory is formally called the refined similarity hypotheses as applied to passive scalar fields (RSHP). Here the spatial fluctuations of χ and ε are accounted for by using the conditional volume averages χ_r and ε_r. The refinement also conjectures the probability distribution of (χ_r, ε_r) to be a joint log-normal distribution. Using the volume averages, RSHP relates moments of $\Delta\theta_r^n$ conditioned on χ_r and ε_r to a function of r, χ_r and ε_r only. The relation assumes the form: $< \Delta\theta_r^n > \Big|_{\chi_r, \varepsilon_r} = W_n \left(\chi_r^{1/2} \varepsilon_r^{-1/6} r^{1/3} \right)^n$.

Most current research has been preoccupied with predicting the scaling factor for various orders of statistical quantities to compare with the RSHP prediction. Until recently, the

scaling factors predicted by RSHP have been in good agreement with those measured experimentally (Warhaft 2000, Wang et al. 1999). However, these agreements are not considered to be a sensitive test of universality in small-scale structures. It is also believed that calculating conditional expectations masks departures from universality (Warhaft 2000).

The main drawback of RSHP is that the assumption of local isotropy itself does not have sound justification. The skewness (third moment) of the scalar derivative was observed to be of unit order even to the highest experimentally measured Reynolds number. Since the local-isotropy assumption implies zero skewness for the derivatives, the result questions the basis of small-scale phenomenology (Sreenivasan 1991, Sreenivasan & Antonia 1997, and Warhaft 2000). Ramp-cliff structures in scalar signals have been observed to affect the derivative skewness independent of Reynolds numbers. Such structures have been observed in numerical (e.g. Holzer & Siggia 1994) and experimental studies (e.g. Warhaft 2000). The general consensus is that the scalar field, even with an imposed constant mean scalar gradient in an isotropic velocity field, is fundamentally anisotropic.

New approaches to the study of passive scalars have now come into focus. As a result, multi-point correlators have become a useful tool to explore the fluctuating scalar field. Results from Shraiman & Siggia (1995, 1996) have motivated most of the research using multi-point correlators in experiments (Warhaft 2000).

Current research that does not follow the phenomenology of local isotropy is based on the early studies by Kraichnan (1968). Kraichnan theoretically studied scalar fields in a velocity field that has an infinitely rapid decorrelation time. Such velocity fields are hypothetical and are known as "white" or delta correlated in time. For such a field, Kraichnan showed that the velocity ensemble is fully specified by a two-point correlator for any points a and b separated by a distance r as:

$$< v_a(r,t)v_b(0,t') > - < v_a(0,t)v_b(0,t') >= D_{ab}^{\gamma}(r)\delta(t-t') \qquad (2.6)$$

where D_{ab}^{γ} is a symmetric tensor whose magnitude varies as $|r|^{2-\gamma}$ and the incompressibility constraint restricts $\partial_r^a D_{ab}^{\gamma}(r) = 0$ (where ∂_r^a is the partial derivative in the r direction operating at point a). In this model, the scaling index, γ, and the space dimension are the parameters that have analytical significance.

Using the above model, Kraichnan (1994) derived expressions for the scaling exponent based on an ansatz for the scalar dissipative term. Following this, recent years has seen an increase in the study of passive scalar fields using modeled velocity fields. Shraiman and Siggia (2000) stressed the importance of the multipoint correlator, which extracts useful information about the spatial structure of the scalar field in addition to the scaling usefulness. The multipoint correlator C_N is defined for simultaneous measurements of the scalar field at N points located at $r_1, r_2, \ldots, r_N$, as:

$$C_N = < \theta(r_1,t)\theta(r_2,t)...\theta(r_N,t) > \qquad (2.7)$$

Using Kraichnan's model for the velocity field, Shraiman & Siggia (2000) expressed the evolution equation for the multipoint correlator function as:

$$\frac{\partial}{\partial t} < \theta(r_1,t)\theta(r_2,t)...\theta(r_N,t) >= H_N < \theta(r_1,t)\theta(r_2,t)...\theta(r_N,t) > + I_N(r_1,...,r_N) \qquad (2.8)$$

where the H_N is the Hopf operator defined as,

$$H_N \equiv -\sum_{i \neq j} \left(D^{\gamma}_{ab}(r_i - r_j) + \kappa \delta_{ab} \right) \partial^a_i \partial^b_j \qquad (2.9)$$

and I_N is the inhomogeneous source term that is dependent only on lower order correlators. The equation is closed and has been solved for N = 2 (Kraichnan 1968). Physically, the Hopf operator generalizes Richardson's $r^{4/3}$ scaling law for relative diffusivity in a two-particle system to many particle pairs by following their Lagrangian trajectories. The Hopf operator also appears in the evolution equation governing a swarm of N particles in a random flow. A general solution for C_N is obtained by equating the left hand side of equation 2.8 to zero. This formulates the steady state solution, which corresponds to steady forcing, as a sum of the homogeneous and inhomogeneous solutions:

$$C_N = -H_N^{-1} I_N + \sum_j a_j \Psi_{N,j} \qquad (2.10)$$

The summation in equation 2.10 represents the homogenous solutions or zero modes given by $H_N \Psi = 0$. In the inertial range, each term in equation 2.10 can be expressed as a scaling function. The exponent for these scaling functions for the inhomogeneous solution, $H_N^{-1} I_N$, agrees with the KOC theory of local-isotropy, while the homogenous solution scaling exponents have a non-trivial solution and have to be determined by the nonlinear eigenvalues along $\Psi_{N,j}$.

The above model for multipoint correlators developed for a random velocity field provides a framework to study the anomalous scaling and has been used to account for the scalar fluctuation intermittency in real velocity fields. Perturbation expansion solutions of the multipoint correlator evolution equation are the focus of current research for three limits: (1) the diffusion limit ($2-\gamma << 1$ corresponding to a rough velocity field), (2) the large spatial dimension limit ($d >> 1$), and (3) the near Batchelor scale limit ($\gamma << 1$ corresponding to smooth velocity fields). It should be pointed out that real turbulent velocity fields are more complicated than the models used here. Predictions based on a model velocity field need to be validated with new experiments focused on multipoint statistics.

Another recent development is the application of the SO(3) decomposition to separate the isotropic and anisotropic properties of the velocity field to scalar fields (Kurien et al.

2001). The SO(3) decomposition for a scalar structure function simplifies into a spherical harmonic representation. The angular dependence of the odd moments of the scalar increments show that they cannot contain any isotropic part corresponding to $j = 0$ (or any even value of j). Thus, the lowest-order representation is $j = 1$, which is fundamentally anisotropic.

Due to the inherent anisotropy of scalars, the scaling laws for small-scale statistics predicted using a local-isotropy assumption are invalid. Given this, relevant research characterizing the behavior of small-scales has taken place only recently. Studies of the scalar field in modeled velocity fields have been the only accessible approach that hopes to appreciate the true behavior of scalars in turbulent flows. Moreover, the importance of multipoint correlators has been stressed as the "most important lesson" of the passive scalar problem (Shraiman & Siggia 2000). The new developments of the spherical harmonic representation of scalar structure functions offer new ground to study the small-scale behavior of scalar turbulence. For now, research on passive scalars in turbulent flows is at a juncture where several different and significant approaches may address the problem with equal competence.

2.2.4 Probability density functions (PDFs)

The nature of the probability density functions (PDFs) of scalar fluctuations, scalar differences, and spatial derivatives of scalar fluctuations have been of interest to the turbulence research community. The PDF of scalar fluctuations has attracted attention as it relates to the overall structure of the scalar field, and a controversy still exists regarding

their shape. The PDF of scalar differences has also gained considerable attention in light of intermittency effects on the scaling exponents of structure functions. The non-Gaussian nature of the PDF of fluctuating scalar derivatives has been extensively discussed and has been attributed to internal intermittency of the small-scale dynamics of scalar turbulence (Monin & Yaglom 1975).

2.2.4.1 PDF of scalar fluctuations

The PDF of the fluctuating passive scalar concentration measured at a point in a turbulent flow was initially thought to be Gaussian owing to analogy with the Gaussian velocity PDF. The Gaussian nature was supported by several studies (Tavoularis and Corrsin 1981, Eswaran and Pope 1988, and others). However, exponential tails were observed by Castaing (1989) with respect to high Rayleigh number convection experiments. Motivated by this result, Pumir et al. (1991) predicted, using a one-dimensional phenomenological model, exponential tails for the scalar PDF in the presence of a mean scalar gradient. This prediction is now called the PSS prediction (Warhaft 2000). The prediction was later confirmed via experiments (Jayesh and Warhaft 1991, 1992, Gollub et al. 1991). These experiments also showed that the tails of the passive scalar PDFs exhibited non-exponential characteristics in the absence of mean scalar gradients. They concluded that there exists a transitional Reynolds number (Re = 70 based on integral length scale) above which the tails change from Gaussian to exponential shape. On the other hand, nearly Gaussian PDFs have been observed by Thoroddsen (1992) in stratified flow, Overholt & Pope (1996) in numerical simulation of passive scalar turbulence with mean a gradient, and Ferchichi & Tavoularis (2002) in an experimental investigation of

temperature fluctuations in uniform sheared turbulence with a linear mean gradient. Warhaft (2000) attributed these Gaussian observations (excluding that in Ferchichi & Tavoularis 2002) to small computational domains, low Reynolds numbers, and wall effects due to the apparatus being less than eight integral length scales wide. However, Ferchichi & Tavoularis (2002) showed that this was not necessarily true with the ratio of wind tunnel height to integral length scales as high as 30 in their experiments.

The shape of the scalar PDF remains a point of controversy with the absence of a satisfactory explanation for the presence of exponential tails. However, it must be realized that the Gaussian or exponential shapes for the tails is most likely not an artifact of measurement error and therefore needs a unified explanation.

2.2.4.2 PDF of scalar differences

The effect of internal intermittency on the scaling exponents of structure functions has prompted many researchers to study the PDF of scalar differences (or scalar increments), expressed as $\Delta\theta_r = \theta(x+r) - \theta(x)$. The PDF of this variable is nearly Gaussian for separations of the order of the integral length scale and evolves exponential tails as r decreases towards the dissipative scales. Some of the early research observing stretched exponential tails was by Antonia et al. (1984) and Ould-Rouis et al. (1995). The non-zero values of the odd-order moments of this PDF for separations in the inertial range indicate a deviation from local isotropy. Also, the kurtosis of the PDF must be constant with respect to r in the inertial range in order to satisfy the local isotropy assumption. Comparable results from numerical simulations of Chen & Kraichnan (1998) using

white-noise velocity field and experiments by Mydlarski & Warhaft 1998) show a deviation from local isotropy using the skewness and kurtosis of the PDF of scalar differences. Celani et al. (2001), in a numerical simulation of passive scalar advection in a two dimensional Navier-Stokes velocity field, used the shape of these PDFs to depict the effect of scalar injection mechanism (random forcing of scalar fluctuations vs. scalar fluctuations produced by an imposed mean gradient) on the statistics of scalar increments. Here, although the shape of the PDF was considerably different, the scaling exponents of the structure function were shown to be unaffected. The main conclusion is that although the structure function itself cannot hold a universal form, the scaling exponents do not depend on the injection mechanics of the scalar fluctuations.

2.2.4.3 PDF of scalar gradients

The PDF of the scalar derivatives has received considerable attention due to the strong relationship between local anisotropy and various statistics of the scalar derivatives. In particular, the skewness of the streamwise scalar derivative is considered to be a measure of local anisotropy and its non-zero values are associated with the presence of the "ramp-cliff" structures in the instantaneous scalar field (Holzer & Siggia 1994). The kurtosis of the streamwise scalar derivative is also known to be greater than the kurtosis of the corresponding velocity derivatives and also has a stronger dependence on the Reynolds number (Sreenivasan & Antonia 1997). In general, the PDFs of scalar derivatives are far from Gaussian with tails broader than a corresponding Gaussian tail due to internal intermittency of the small scale structure (Monin & Yaglom 1975). Ferchichi & Tavoularis (2002) reported a nearly constant skewness value of -1.0 for the streamwise

scalar derivative for Re_λ between 184 and 253. Schumacher & Sreenivasan (2003) argued that the small-scale structure tends to be more isotropic with increasing Schmidt number by comparing the shape of the PDF of longitudinal scalar derivatives. Here the PDFs approached symmetry with increasing Schmidt number (from 1 to 64), which was associated with an increasingly "striated" appearance of the passive scalar field.

High values of the skewness and kurtosis of the PDF of the transverse scalar derivatives has also been observed (Mydlarski & Warhaft 1998, Tong & Warhaft 1994, Ferchichi & Tavoularis 2002). Non-zero values of the skewness were observed in these flows thereby providing more evidence to the violation of the local-isotropy assumption. The PDFs of scalar derivatives are asymmetric in the presence of a mean gradient with each tail approximated by an exponential decay. Ferchichi & Tavoularis (2002) report the value of skewness for the transverse scalar derivative to be 1.5, which is consistent with previous experiments (e.g. Sreenivasan 1977 and Mestayer 1982). The value of skewness for the transverse scalar derivative for the case of shearless turbulent flows is known to be higher and is associated with a strong correlation between the transverse velocity fluctuation and the scalar fluctuation (Tong & Warhaft 1994).

2.3 Fractal geometry of passive scalars

The ideas of self-similarity and fractal characteristics in turbulence, first introduced by Richardson (1922), have been the key principle in the development of similarity hypotheses for the turbulent velocity and passive scalar fields as discussed in previous sections. The concentration field can also be viewed as a spatial distribution with self-

similarity and fractal characteristics again relevant. From this perspective, the flow may appear as regions of clear and concentrate fluid (or unmixed and mixed fluid). The geometry of the surface dividing these regions has practical importance when studying applications, such a chemical and pollution mixing, because the rate of mixing depends on the interface size and shape.

Fundamental suggestions regarding the fractal nature of fluid interfaces were made by Welander (1955) and Mandelbrot (1975). Subsequently, fractal and multifractal scaling of the velocity and passive scalar fields have been used to describe fluid interfaces in turbulent flows. This section introduces basic definitions of fractal geometry and reviews previous fractal geometry descriptions of passive scalar iso-surfaces.

2.3.1 Introduction to fractal geometry

The concept of fractals arises from the challenge of measuring a peculiar kind of sets in a metric space. Construction of the cantor set and the tools developed to measure it will be described in order to introduce the basic idea of fractals. Consider the unit interval $[0,1]$ on the metric space given by the real line with the lebesgue measure. Let's define an operation, $O(\ )$, that deletes the middle third portion of any line segment contained in the set. Figure 2.1 shows the evolution of the unit interval after iterative operations on the unit interval, i.e. $O^M([0,1])$. From the figure it is clear that iterating ad infinitum leaves behind a dust of points on the unit interval. This set of points on the interval is called the middle-thirds cantor set, C. The most fascinating property of this set is that it

is self-similar meaning that the structure of the dust of points is the same at smaller scales therefore if one were to zoom in on the dust of points; the clusters of points will qualitatively look the same. Also, it can be proved that C has uncountably infinite number of points while having zero lebesgue measure. Therefore the dimension of C is neither zero nor one, i.e. it lies somewhere between a point and a line. Fractal geometry is essentially a set of mathematical tools developed to define measures and quantify geometry properties of such sets.

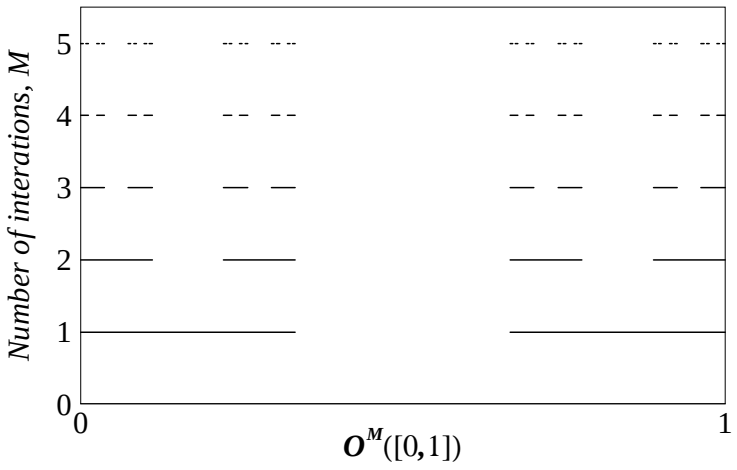

Figure 2.1 Construction of the middle-thirds cantor set on the interval $[0,1]$.

It is fairly easy to construct similar sets in higher dimensions with properties such as zero area and infinite length, or zero volume and infinite area. Such objects cannot be completely described by the tools developed in classical Euclidean geometry. Several mathematical tools were developed to generalize the concepts of measure and dimension in order to characterize any object in space in a manner consistent with common Euclidean objects (line, circle, cube, etc…).

The fractal dimension is a measure to describe the length-scaling behavior of the set. The length (or, in general, the measure) of a set is dependent on the length of the scale (or the ruler) that we use to measure the set. Suppose the length of the scale is λ, then we count the number of scales, $N(\lambda)$, that are required to cover the set and calculate the measure as $L(\lambda) = \lambda N(\lambda)$. Since this relationship is typically a power law for self-similar sets, i.e. $L(\lambda) \propto \lambda^{1-D_f}$, Mandelbrot (1967) coined the term fractal dimension to the exponent D_f. For the cantor set, the length scaling behavior is also a power law. After every operation (see Figure 2.1) the number of line segments that cover C doubles, i.e. 2^M line segments each of length $\frac{1}{3^M}$. It is trivial to show that for the cantor set shown the fractal dimension is $D_f = \frac{\ln 2}{\ln 3} = 0.630929...$, which lies between 0 and 1. However, most fractals are not exactly self-similar like the cantor set and exhibit scale dependent complexity. Thus, a power law description of the length-scaling behavior is insufficient and the fractal dimension is described as a function of scale. Here $1 - D_f$ is defined as the logarithmic derivative $\frac{d \ln L(\lambda)}{d \ln \lambda}$, which on integration yields the length scaling relationship: $L(\lambda) \propto \lambda \exp\left(\int_{\lambda}^{\infty} D_f(\tilde{\lambda}) d \ln \tilde{\lambda} \right)$. Catrakis (2000) suggested three levels of complexity for objects. Level 1 is for objects with complexity at single scale (e.g. Euclidean objects), Level 2 is for objects with power law measure-scaling behavior (e.g. self-similar objects), and Level 3 is for objects with scale dependent complexity. Objects with Level 3 complexity are also called multifractals.

The fractal dimension is typically a non-integer and always between the topological dimension, d_t, and the embedding dimension, d. The topological dimension is defined as the number of independent variables necessary to describe the neighborhood of any point in the object. Therefore the topological dimension is 0 for a collection of points (e.g. the set of natural numbers), 1 for curves (e.g. circle or helix), and 2 for surfaces (e.g. hollow sphere). The embedding dimension, d, is the smallest integer d, such that the object may be embedded in a d-dimensional space (i.e. $\mathbb{R}^d$) without intersecting itself. Therefore the embedding dimension is 1 for a collection of points on the unit interval, 2 for a circle, and 3 for a helix and a hollow sphere. For a thorough introduction to fractal and multifractal geometry concepts, please see the Master of Science thesis by Schuerg (2003).

2.3.2 Geometry of scalar iso-surfaces

In the context of passive scalars transported in turbulent flows, research has focused on using fractal and multifractal geometry to define iso-surfaces of concentration. Prasad and Sreenivasan (1990) showed that concentration filaments never detach. Instead the filaments elongate and deform due to the turbulent stretching and folding. They measured scalar fields in a turbulent round jet in two closely spaced planes using the LIF technique. A simple correlation scheme was used to describe the structure of the scalar field between the slices, and a three dimensional box counting algorithm calculated the fractal dimension of the scalar iso-surfaces to be 2.35 ± 0.04. Constantin and Procaccia (1991) presented a Lagrangian calculation of the area of iso-scalar surfaces in turbulent flows. They showed that such surfaces possess fractal properties and their theoretical

estimate of the fractal dimension agreed well with Prasad and Sreenivasan (1990). Similar estimates were obtained by Sreenivasan and Meneveau (1986) and Sreenivasan et al. (1989) and have been reviewed in detail by Sreenivasan (1991).

Miller and Dimotakis (1991) studied the fractal characteristics using streak images of scalar interfaces in turbulent jets ($1{,}000 < Re < 24{,}000$) and found that the fractal dimension depends on the spatial scale and concentration threshold. This result disagrees with previous experiments, which reported a constant fractal dimension over the inertial range scales. Frederiksen et al. (1996, 1997) showed that for one-dimensional transects, there existed a constant fractal dimension (estimated at 0.48) for the viscous-convective range while the dimension depends on scale for length scales larger than the Kolmogorov length scale. For the case of planar and three dimensional transects of the passive scalar iso-surfaces, there was no evidence of a constant fractal dimension.

Catrakis and Dimotakis (1996) introduced additional fractal measures, such as coverage fraction, scale distribution probability density function (PDF), and largest empty box (LEB) scale PDF, to describe the fractal geometry of passive scalar iso-surfaces in a turbulent jet. The fractal dimension was a function of scale for the data collected. Also, a Poisson or log-normal scale PDF was suggested as a model for the scale distribution PDF. Catrakis and Dimotakis (1998) introduced a dimensionless scale dependent area-volume fractal measure to describe the shape complexity of passive scalar iso-surfaces. Based on the LEB scale PDF, Catrakis (2000) characterized folding (large scale process) and wrinkling (small scale process) via dimensionless numbers for passive scalar iso-

surfaces in a turbulent jet. Catrakis et al. (2002) introduced additional area-volume properties of fluid interfaces, namely area-volume density and area-volume ratio. These measures were calculated for scalar iso-surfaces in a turbulent jet and were found to be scale dependent. However, they found that the area-volume density exhibited self-similarity with an exponent of 1.3.

Villermaux and Innocenti (1999) investigated the temporal evolution of the geometrical distributions of passive scalar injected continuously into a turbulent jet at scales smaller than the local integral length scale. The fractal dimension was found to depend on time, injection scale, and concentration threshold, in addition to being scale dependent.

2.4 Contributions of current research

The current study aims to report new data for the small-scale structure of a high Schmidt number passive scalar mixing in a turbulent boundary layer. This research addresses several open issues in the field of passive scalar turbulence as discussed in the previous sections. In particular, the focus is on passive scalar PDFs, spectrum (in the inertial-convective and viscous-convective regimes), anomalous scaling of structure functions, scaling behavior for two-point correlation functions and a three-point correlation function, and the fractal geometry of passive scalar iso-surfaces. The above characteristics are addressed in the context of the effects of Reynolds number, mean gradients, large-scale intermittency, and the scalar injection length scale.

The flow configuration is, perhaps, most similar to Villermaux & Innocenti (1999) where a high Schmidt number passive scalar was iso-kinetically injected into the far field of a turbulent jet. In the present study, the passive scalar is iso-kinetically injected with different initial length scales at mid-depth in a fully developed turbulent boundary layer of an open channel flow. The scalar field is measured in a rectangular area vertically aligned along the plume centerline. These measurements follow the evolution of the small-scale structure from the source to far downstream while the mixing of the scalar establishes a natural mean scalar gradient that produces the turbulent scalar fluctuations. The following Chapters discuss the experiment in detail, followed by statistical and fractal analysis of the small-scale structure.

Chapter 3

Experiment Description

3.1 Introduction

To meet the objectives of the study, the fluctuating scalar and velocity fields were measured downstream of a continuous iso-kinetic release of a high Schmidt number passive scalar into the inertial layer of a turbulent boundary layer. The resulting scalar field was statistically stationary in time and fundamentally anisotropic due to the presence of mean gradients of both the concentration and velocity fields. High-resolution measurements of the scalar and velocity fields were conducted in a vertical plane parallel to the flow using planar laser induced fluorescence (PLIF) and particle tracking velocimetry (PTV), respectively. This chapter provides an overview of the experimental apparatus, experiment procedures, and data processing methods. In addition, the experimental parameters and flow characteristics are described.

3.2 Flow facility – The tilting flume

A 24.4 m long and 1.07 m wide tilting flume with a smooth bed, located in the Environmental Fluid Mechanics Laboratory at Georgia Tech, was used to create open channel flows of water with uniform depth. The flume pivoted at the midpoint along the length and two screw jacks supported each ends. A single electric motor drove the jacks and a counting device indicated the number of rotations of the drive mechanism. Water was supplied to the flume head box from the laboratory constant head tank via a pipe system equipped with flow control valves. An *in situ* calibrated electro-magnetic flow

meter measured the flow rate (see Figure 3.1 for the flow meter calibration). During the experiments a submerged pump delivered water from the laboratory sump to the head tank to maintain the constant head. The pipe system culminated with a horizontal multi-port diffuser suspended in the flume head box. The diffuser distributed the flow laterally across the head box. The head box of the flume contained stilling devices (i.e. a wood baffle and two expanded metal screens covered with a synthetic fabric) downstream of the diffuser to further minimize large scale flow perturbations. The resulting flow entering the channel was laterally uniform with low turbulence intensity and minimal surface perturbation.

Experiments were conducted for three Reynolds numbers of 5000, 10,000, and 20,000. The Reynolds number was based on the flow depth and the mean channel velocity. The corresponding flow rates were 5.35×10^{-3}, 10.7×10^{-3}, and 21.4×10^{-3} m^3/s, respectively. For each case the bed slope and the height of the tailgate were adjusted to create a uniform open-channel flow of depth 100 mm. A point gauge mounted on a towing carriage was used to measure the flow depth between 8 m and 23 m downstream of the channel inlet. The resulting flow depth was uniform to within ±0.3 mm over 15 m of channel length.

Measurements of the passive scalar and velocity fields were conducted 23 m from the channel inlet. The walls of the channel at the measurement region were glass to provide optical access for the PLIF and PTV camera systems.

3.3 Description of experiments cases

The experiments described below provided time-series of planar velocity and scalar fields for a defined combination of Re, $\partial\langle\theta\rangle/\partial x$, $\partial\langle\theta\rangle/\partial y$, $\partial\langle U\rangle/\partial y$, and nozzle diameter, D. Keeping in mind that the concentration measurements resolve the smallest scale variations, the following experiments were performed to study the characteristics of the local structure of passive scalar turbulence with respect to large-scale anisotropies and the initial length scale of the scalar field:

Case I - Effect of $\partial\langle\theta\rangle/\partial x$ and $\partial\langle\theta\rangle/\partial y$

At Re = 10,000, the passive scalar was released iso-kinetically through a 4.7 mm diameter nozzle in the inertial layer at y = 50 mm. Long time-series of high-resolution two-dimensional measurements of the fluctuating scalar field were collected along the plume centerline in a vertical plane parallel to the flume at six downstream distances from the source (i.e. $1H$, $2.5H$, $5H$, $10H$, $20H$, and $40H$, where H = 100 mm is the flow depth). The mean scalar gradient varied among the six locations due to turbulent mixing.

Case II - Effect of Re

The measurements described in Case *I* were collected for Re equal to 20,000 and 5000. The purpose of these experiments was to study the influence of velocity characteristics on the local structure and mixing of the passive scalar.

Case III - Effect of length scale at which the scalar is introduced

The measurements described in Case *I* were collected for a nozzle diameter of 2.7 mm and 9.4 mm. The purpose of this case was to study the influence of the length scale of the passive scalar source, i.e. the length scale of the initial patch size, on the local structure downstream.

3.4 Velocity measurement system

The particle tracking velocimetry (PTV) technique was used to measure a time-series of the velocity field over the entire boundary layer for each of the Reynolds number cases. Measurements were collected at a single distance from the channel inlet because the flow was fully developed at the test section. The resulting velocity fields were used to characterize the turbulent boundary layer and determine the wall shear velocity. Profiles of the mean and fluctuating velocity components were presented to characterize the flow environment for the scalar field.

3.4.1 Overview

The basic principle of PTV is to illuminate a seeded flow (flow with suspended passive particles) with a planar laser sheet and record two consecutive images of the particle locations with a sufficiently small time delay. The PTV algorithm relied on an initial estimate of the velocity field provided by a PIV algorithm that is based on correlation methods. Using the velocity estimate generated from PIV analysis, the PTV algorithm tracked individual particles by matching particle pairs between the two consecutive

images. The individual particle displacements were converted to velocity using the image magnification and time delay information.

Due to dynamic range limitations, PIV/PTV data sets with two resolutions were collected for each Reynolds number. The low-resolution images covered 100 mm $\times$ 100 mm, and the high-resolution images covered 20 mm $\times$ 20 mm. The low-resolution case contained the instantaneous velocity measurements for the entire channel depth, while the high-resolution case contained velocity measurements close to the bed of the flume. The large velocity gradient near the bed necessitated this strategy to obtain reliable velocity data.

3.4.2 Data acquisition

The data collection system consisted of a laser, optics, a tracer particle delivery system, an electronic synchronization system, and an image acquisition system. Figure 3.2 showed a schematic of the experiment setup for velocity measurements.

3.4.2.1 Laser and optics

The illumination source consisted of a double head Nd:YAG laser mounted on a frame above the measurement area to produce a laser beam perpendicular to the flume bed. The laser light had a wave-length of 532 nm and the heads produce 125 mJ of energy per laser pulse. The beam had a $1/e^2$ beam diameter of 3.5 mm. A set of optics was used to create a thin laser sheet aligned with the centerline of the flume. The optic elements were a 0.5 m focal length symmetrical convex lens located 0.55 m above the flume bed and a -19 mm focal length planar-concave cylindrical lens. The result was a thin laser sheet in

the measurement region that covered the 100 mm × 100 mm image region. A clear 19 mm × 10 mm Plexiglas sheet was suspended just above the water surface with the lower surface wetted to allow the laser sheet to enter the measurement region without optical distortion due to small water surface perturbations. The Plexiglas sheet makes contact with the water surface only by surface tensile forces.

3.4.2.2 Tracer delivery system

Kaolin particles were used as the passive markers in water because they are small (< 5 μm diameter) enough to reliably track the fluid velocity and because they have good light reflective properties. The particles were delivered to the flume flow using a 4.7 mm diameter nozzle located 7 m upstream of the measurement area. The nozzle was pointed upstream (for maximum relative velocity) to release a high velocity jet of the suspended particles against the ambient flow at a flow rate of 4 GPH. Turbulent mixing of the particles in the resulting jet and subsequent mixing in the turbulent boundary layer created a nearly homogenous suspension of particles at the measurement location.

3.4.2.3 Synchronization and image acquisition system

A Berkeley Nucleonics 500D pulse generator was used to trigger the camera and synchronize the laser pulses with a preset time delay. A Kodak MegaPlus ES 1.0 camera (8-bit, 1018 × 1008 pixels) captured digital images of the illuminated particles. The camera was operated in the double frame mode and captured two images for each trigger signal received from the pulse generator. The camera viewed the illuminated measurement location from the side though the glass wall of the flume (Figure 3.2). A

Nikon MicroNikkor 200 mm focal length lens yielded images of approximately 20 mm × 20 mm and was used to capture the high resolution data (20 μm pixel^{-1}). The low resolution data was captured using a Nikon MicroNikkor 60 mm focal length lens that yielded images of approximately 100 mm × 100 mm (100 μm pixel^{-1}). An optical cut-off filter (Tiffen Green 11) on the camera lens blocked the ambient light while passing the reflected laser light from the particles to the camera sensor.

The camera was connected to a Windows 2000 computer through a Coreco image capture board. The images were stored in real time on the hard drive array using the Video Savant software (IO Industries). The images were stored in a binary format requiring approximately 1 MB hard disk space per image. A typical sample size for statistical convergence of the turbulence intensities was 4000 image pairs and was captured at a sampling rate of 10 Hz. Such a data set corresponded to 8000 consecutive images and 8 GB of hard disk memory.

3.4.3 Particle Image Velocimetry (PIV) algorithm

The PIV algorithm was based on previous algorithms developed by Cowen & Monismith (1997), Wereley & Meinhart (2001) and Gui & Wereley (2002). The first part of the algorithm was to condition the images to enhance the contrast. Two background images were created and stored on disk. The background image of an image series was defined as the lowest value attained by each pixel throughout the image series. The two images corresponded to the background of the odd numbered images and even numbered images,

respectively. Before further processing every image was rescaled using the following transformation:

$$I_{new}(i, j) = 255\frac{[I(i, j) - B(i, j)]}{255 - B(i, j)} \tag{3.1}$$

where $I_{new}(i, j)$ was the conditioned image with i and j as the pixel indices, $I(i, j)$ was the original 8-bit image, and $B(i, j)$ was the corresponding background image. In the unlikely event that $B(i, j)$ was equal to 255, then $I_{new}(i, j)$ was set as zero. To preserve the integrity of information in the original image data and to avoid effects due to integer round-off, the conditioned image $I_{new}(i, j)$ was defined as a floating point array.

The main PIV algorithm was performed using square interrogation windows of size 32 pixels. The algorithm yields a second-order accurate velocity measurement at the center of each 32 × 32 size bins of the image with no overlap, which corresponded to a maximum of 1024 vectors per image pair. The following steps outline the PIV algorithm to produce velocity information from one pair of images.

1. Create background images for even and odd numbered images, respectively.
2. Condition the images according to equation 3.1.
3. Divide the images into a regular 32 × 32 interrogation bins.
4. For each interrogation bin, perform a two-dimensional cross-correlation between the images. The technique employed the two-dimensional Real Fast Fourier Transform (FFT) routine provided by Press et al. (2002) to calculate the Fourier

transforms of the two interrogation windows and estimated the cross-correlation using the following equations:

$$\hat{F} = FFT\left(F(i, j)\right) \tag{3.2}$$

$$\hat{G} = FFT\left(G(i, j)\right) \tag{3.3}$$

$$\hat{H} = \hat{F}\hat{G}^{*} \tag{3.4}$$

$$C(i, j) = FFT^{-1}\left(\hat{H}\right) \tag{3.5}$$

where $F(i, j)$ and $G(i, j)$ are image intensity fields in the interrogation windows, $\hat{F}$ and $\hat{G}$ are their respective Fourier transforms, $\hat{H}$ is the product of $\hat{F}$ with the conjugate of $\hat{G}$, and $C(i, j)$ is the calculated cross-correlation between $F(i, j)$ and $G(i, j)$.

5. Estimate the integer displacement vector based on the location of the peak of the cross-correlation $C(i, j)$.
6. Perform a Gaussian peak fit analysis for the correlation peak to determine the displacement vector with sub-pixel accuracy.
7. Shift the original first interrogation bin against the displacement direction by a magnitude of half of the estimated displacement vector. A bilinear interpolation of the image was used for continuous window shifting in order to reduce the effects of pixel-locking (Gui & Wereley 2002).
8. Shift the original second interrogation bin in the displacement direction by a magnitude of half that of the estimated displacement vector using bilinear interpolation of the image.

9. Perform step 4 for the shifted interrogation bins and estimate a correction to the displacement vector and update the displacement vector. If the sum of the magnitude of corrections in the x and y directions is greater than or equal to 0.005 pixels then return to step 7, otherwise continue. If step 9 is repeated 20 times for the same interrogation bin, then flag the bin as a bad vector and begin processing the next interrogation bin.

3.4.3.1 PIV-data filtering

The resulting velocity fields may contain "bad" vectors that typically correspond to a false peak in the calculated cross-correlation function and may be attributed to noise present in the images or particles moving out of the plane between the laser pulses. The data filtering process identified and flags these bad vectors to avoid any erroneous contribution to the velocity statistical calculations. Filtering of the present data was based on the assumption that the velocity measured at a point fluctuates in time with a Gaussian distribution. Although this was not true near the wall of the boundary layer, such an assumption has been previously found to be sufficient for the purpose of removing stray vectors. The mean and standard deviation of the velocity was calculated for every bin. For each bin, a threshold deviation from the mean was estimated using a Gaussian distribution with the calculated mean and variance and the number of good vectors at the bin. Any vector with a deviation greater than the threshold deviation (typically 3 to 4 times the standard deviation) was flagged as a bad vector and was not included in the statistical estimations. This procedure was repeated until no additional stray vectors could be identified. For each iteration the mean was estimated using the

standard estimator ($\frac{1}{N}\sum n_i$) except for the first iteration in which the median was employed to minimize the influence of vectors with large deviations.

3.4.4 Particle Tracking Velocimetry (PTV) algorithm

The particle tracking algorithm was based on Cowen & Monismith (1997). The basic principle of the algorithm was to identify particles in an image pair and match particles using an initial guess of the displacement field. The following steps outline the algorithm used to produce velocity vectors corresponding to particle tracking between an image pair:

1. Condition both images according to equation 3.1.
2. Binarize each image using a threshold. "Threshold" is a parameter of the PTV algorithm to determine the cutoff intensity above the local average intensity associated with a particle. The local average was defined for every pixel row by calculating the mode of the intensities of pixels in the each row. The mode variation between the rows was smoothed by a six nearest-neighbor kernel to filter out the effects of noise. A pixel with an intensity that exceeds the local average plus the threshold was flagged with a "1", otherwise it's assigned a "0" value.
3. Identify and number each particles in each image. A pixel with a "1" was considered to be part of a particle. A pixel with a "1" that was adjacent either vertically or horizontally to another pixel with a "1" was considered to be part of the same particle. Particles were identified using this criteria and numbered

between 1 and the total number of particles identified. Particles that covered more than a threshold number of pixels were discarded because they were particles that are too large or multiple overlapping particles.

4. Calculate the center location of each particle with a Gaussian peak fit method with sub-pixel accuracy.
5. For each particle in the first image, estimate the local displacement vector by interpolation of the PIV velocity field. Identify a 9 × 9 pixel region in the second image centered on the projected (expected) location of the particle in the second image based on the interpolated velocity information.
6. Improve the local displacement estimate by performing a two-dimensional cross-correlation between a 9 × 9 pixel window centered on the particle location in the first image and a 9 × 9 pixel window centered on the identified particle in the second image.
7. Identify a 3 × 3 pixel window centered on the improved projected particle location in the second image.
8. Identify all particles in the second image that fall inside or touch the border of the 3 × 3 window. If one and only one particle is identified then go to step 9, otherwise start to process the next particle in the first image (i.e. go to step 5).
9. Calculate the displacement vector from the particle positions and assign to the location in the middle of the particle pair. The displacement was converted to velocity using the magnification and time delay between images.

3.4.4.1 PTV-data filtering

The PTV algorithm produced a non-uniform distribution of velocity vectors across the image area. The image area was divided into non-overlapping rectangular bins (1024 pixels wide and 8 pixels tall). For each bin, all vectors that fall in the bin were identified and filtered in the same manner as described above for filtering PIV data.

3.5 Planar laser induced fluorescence (PLIF) system

The passive scalar field was generated by iso-kinetically injecting a high Schmidt number dye ($Sc \sim 1000$), Rhodamine 6G, through a nozzle along the flume centerline. The high-resolution planar laser induced fluorescence (PLIF) technique was used to measure the resulting scalar field along the nozzle centerline at given downstream distances (see Section 3.3) in a vertical plane (covering approximately 18 mm $\times$ 13 mm) parallel to the flow direction. Since the flow was fully developed, the data corresponding to different downstream distances from the source were obtained by moving the plume source upstream of the measurement region. The data was post-processed to describe the statistical and fractal nature of the fields in order to understand the mixing dynamics involved.

3.5.1 Overview

The basic principle of PLIF is to capture a focused image of the light emitted by excited Rhodamine 6G dye solution, and convert the recorded intensity field to a concentration field using a calibration. The laser sheet created by scanning mirrors excited the

Rhodamine 6G present in the plane of the laser sheet. Rhodamine 6G has a peak absorption at 530 nm wavelength and a peak emission around 560 nm wavelength (Arcoumanis et al., 1990). The concentration field in the laser sheet thus appeared as yellow-orange light. Recording the instantaneous intensity field with an image acquisition system combined with a suitable calibration yielded the instantaneous concentration fields. The calibration was based on the fact that the fluorescence of the tracer was directly proportional to the incident laser power and the local tracer concentration.

The PLIF system consisted of an illumination system, plume delivery system, image acquisition system, and a calibration system. This system was designed with close attention to resolve the smallest spatial scales. A basic schematic of the PLIF system is shown in Figure 3.3.

3.5.2 Illumination system

The illumination system consisted of a laser with a combination of optics and a pair of scanning mirrors. These components were used to create a thin laser beam at the measurement plane, which was scanned across the plane during the exposure phase of the imaging sensor.

An Argon-ion laser (5 W, Coherent Innova 90) with a wavelength of 514 nm was used as the laser light source. A combination of a 6× beam expander and 2 m focal length symmetrical convex lens focused the beam to a Gaussian beam with a $1/e^2$ waist

diameter equal to 80 μm at an elevation of 50 mm above the flume bed (corresponding to the mid-depth of the flow). The Rayleigh length corresponding to this configuration was 20 mm which corresponds to the length within which the laser beam is of uniform waist diameter. Thus the beam waist is about 80 μm through the measurement region. Although the beam waist exceeds the Batchelor length scale it is confirmed via spectral analysis of the LIF images that the effects of noise dominate the spectral energy for higher wave-numbers while the middle of the viscous-convective regime is still resolved. A clear 19 mm × 10 mm Plexiglas sheet was suspended just above the water surface with the lower surface wetted to allow the laser beam to enter the measurement region without optical distortion due to small water surface perturbations. The Plexiglas sheet made contact with the water surface only by surface tensile forces.

The scanning mirror system consisted of two mirrors, each mounted on a galvanometer (Cambridge Technology) positioned above the water surface. The first mirror deflected the laser beam, which entered through the glass side wall, upstream along the flume centerline and parallel to the flume bed. The second mirror was positioned to deflect the beam downward and perpendicular to the flume bed. The position of the first mirror was always fixed, whereas the second mirror rotated in order to scan the beam through the measurement plane, which was parallel to the flow direction and perpendicular to the flume bed.

The voltage signal that controlled the mirror position was generated by a National Instruments multifunction input/output board controlled by a LABVIEW program. The

control voltage signal was periodic (See Figure 3.4) with a time period of 100 ms and was synchronized with the trigger signal to the imaging camera. Upon trigger, the scanning mirror moved the laser beam from a parking position (P) to the upstream side (US) of the measurement region. The voltage changed linearly with time causing the mirror to scan with a uniform angular velocity. The rate of change of voltage was such that the laser beam reached the downstream side (DS) of the measurement region in 3 milliseconds. The scan time of 3 ms ensured sufficient illumination of the tracer field while minimizing the horizontal distortion of the dye filaments due to advection to less than 3% for the fastest flow (Re = 20,000). The distortion was less for the slower flow cases with a maximum of 1.5% and 0.75% for Re = 10,000 and 5,000, respectively.

3.5.3 Plume delivery system

The plume delivery system included the nozzle (see Figure 3.5) attached to a towing carriage. Three brass nozzles were employed with inner orifice diameters of 2.2, 4.7, and 9.4 mm, respectively. Each nozzle was aligned independently with the centerline of the flume and pointed in the downstream direction parallel to the flume bed. The center of the each nozzle orifice was at an elevation of 50 mm above the flume bed. To minimize the wake perturbations each nozzle was custom built with a streamlined fairing. The minimal wake perturbation was confirmed by performing flow visualization with colored dye for the same experimental configuration as the PLIF experiments.

The tracer solution was pumped to the nozzle from a supply tank via a flow meter manifold. The flow meter manifold consisted of five rotameters (Dwyer Instruments) in

parallel. Four of the flow meters had a range of 0 - 30 cc/min, while the fifth flow meter had a range of 0 - 757 cc/min. Each of these flow meters was equipped with a valve facilitating fine control of the total flow in order to provide a nearly iso-kinetic release of the dye. Table 3.1 shows the tracer flow rates for each Reynolds number and nozzle diameter combination.

Table 3.1 Tracer injection flow rate, Q used to provide a near iso-kinetic release corresponding to the mean velocity at mid-depth. Subscripts on Q represent the nozzle diameter in mm. The mean velocity is estimated using the PTV boundary layer profile measurements discussed in Section 3.6.

Re	$<U>(y=50mm)$	$Q_{2.2}$ (cc/min)	$Q_{4.7}$ (cc/min)	$Q_{9.4}$ (cc/min)
	(mm/s)	$Q_{2.2}/A_s$ (mm/s)	$Q_{4.7}/A_s$ (mm/s)	$Q_{9.4}/A_s$ (mm/s)
5000	57.7	——	60	——
			57.6	
10,000	125.3	28.5	126.2	521.7
		125.0	121.2	125.3
20,000	222.6	——	231.8	——
			222.7	

The tracer solution was prepared using a pre-mixed Rhodamine 6G solution in filtered water with a concentration of 5×10^5 μg/l. This solution, after passing through activated charcoal and reverse osmosis (RO) filtration units, has zero chlorine content thereby

eliminating the bleaching effect and leaving the concentration unaltered over the experiment duration. The concentration of the plume source was adjusted for measurements at each downstream distance in order to maintain the concentrations in the measurement region within the calibration limits. Therefore, small volumes of the pre-mixed solution measured to an accuracy of $1/100^{th}$ of a milliliter were mixed in known volumes of the filtered water to create appropriate source concentrations for each distance. Table 3.2 shows the source concentrations for each case.

Table 3.2 Plume source concentrations used for each Reynolds number, Re, and nozzle diameter, D, combination.

Re, D	Θ_O (μg/l) (x/H=1.0)	Θ_O (μg/l) (x/H=2.5)	Θ_O (μg/l) (x/H=5.0)	Θ_O (μg/l) (x/H=10.0)	Θ_O (μg/l) (x/H=20.0)	Θ_O (μg/l) (x/H=40.0)
5000, 4.7	53.3	53.3	100.0	100.0	133.2	664.5
10000, 4.7	86.6	100.0	86.6	126.6	366.0	1652.9
20000, 4.7	66.6	66.6	133.2	133.2	664.4	2306.4
10000, 2.2	87.3	87.3	133.2	199.8	1324.5	2631.6
10000, 9.4	86.6	86.6	166.5	166.5	266.3	266.3

3.5.4 Synchronization and image acquisition system

The synchronization and image acquisition system consisted of the camera, synchronizing computer, image acquisition computer, and acquisition software.

The camera was a charged coupled device (CCD) camera called Imager Compact manufactured by LaVision Inc. The camera sensor was a rectangular array of CCD pixels of dimension 1392 × 1024. The camera used a 12-bit digitization of the pixel outputs to produce digital images with 4096 levels of gray. The experiments were conducted at a frame rate of 10 fps, although the maximum frame rate of the camera was 12 fps. The camera was connected to the imaging computer via an ethernet cable and a PCI interface card. The camera viewed the measurement region from the side of the flume with the flow from left to right of the imaging area (see Figure 3.3). A 200 mm Nikkon MicroNikkor macro lens was used to provide a magnification of approximately 13 μm/pixel. The lens and the CCD chip were protected by clear and standard hot mirror filters to block ultraviolet and infrared light. An additional long-pass optical filter (Tiffen Orange 21) with a cutoff wavelength of 560 nm was used to block the scattered laser light. This combination of filters passed only the fluoresced light and hence reduced the noise to signal ratio of the acquisition.

The synchronization computer was equipped with a National Instruments multifunction input/output board controlled via LABVIEW software. The LABVIEW program generated a TTL signal to trigger the camera and a synchronized scanning voltage signal to control the scanning mirror (Figure 3.4). An oscilloscope was used to verify synchronization between the signals during data acquisition.

The image acquisition computer was a Windows XP machine with 3.2 GHz Pentium processor and 1 GB RAM. The computer was equipped with two Serial ATA 250 GB

hard drives which together were capable of recording data at an average rate of 50 MB/s. Images were captured using the image acquisition and visualization software DaVis (provided by LaVision Inc.). Images were compressed (without loss of image integrity) and stored real-time-to-disk. For each case, a time series of 12,000 images was captured and stored.

3.5.5 Calibration system

A calibration of the PLIF system is necessary to convert raw images to concentration measurements. The measurement area was flooded with uniform concentrations ranging from 0 - 100 μg/l of Rhodamine 6G. A linear (Koochesfahani and Dimotakis, 1985) calibration equation was determined for each pixel via a least squares regression (Webster et al. 2003). .

A 2.54 mm diameter nozzle was used to inject the tracer solution of known concentration from the upstream side of the measurement region (see Figure 3.6). The nozzle was attached to the 4.7 mm plume delivery nozzle using expanding pipe fittings. A glass microscope slide was glued to the top of the nozzle in order to prevent spreading of the tracer above the measurement region for the purpose of laser attenuation calculations. The nozzle was pointed downstream and a jet of the tracer flooded the measurement area. Since the measurement area was less than one nozzle diameter in length and height and was immediately downstream of the nozzle opening, there was minimal entrainment of fresh water in the measurement region. Therefore, the measurement region was flooded with a known, uniform tracer concentration.

A series of 200 PLIF images was captured for each known tracer concentration in the range 0 - 100 μg/l. The average intensity was calculated for each pixel. A filtering algorithm was employed to remove samples with large deviations from the mean intensity. The algorithm ensured that large intensity deviations from the mean attributed to the occasional entrainment of ambient water into the tracer jet do not contribute to the average. These average images were then corrected for laser attenuation due to the presence of Rhodamine 6G (Ferrier et al. 1993). The corrected pixel intensities were calculated using the equation $I(i,j)_{corrected} = I(i,j)_{measured} \exp^{\{\alpha * c * L(i,j)\}}$, where I is the intensity (greyscale), c is the dye concentration (μg/l), $L(i,j)$ is the optical path (cm) of the laser beam. The attenuation coefficient, α, was assumed to be 0.00023 per μg/l per cm, as reported by Ferrier et al. (1993). The optical path was calculated as the distance from the glass slide to the pixel under consideration assuming that the angle between the laser beam and the glass slide was negligible.

A linear best fit was obtained via a least squares regression for the individual pixels between the concentration and corrected intensity. The regression forced the line to pass through the zero concentration data point. The slopes and intercepts of best fit lines for each pixel were saved as a binary file to be used by other data processing programs for statistical and fractal characterizations. Figure 3.7 shows a sample calibration curve for each of the Reynolds number and nozzle diameter cases.

The uncertainty in concentration measurement arises from errors in the concentration of the calibration fluid and the error due to digitization of the camera. The error in the calibration fluid is a function of the concentration of the fluid and is roughly ±2.5% on average. The error in the raw intensity measurement due to camera digitization is approximately $\pm(1/I)\times 100\%$, where I takes values from 1 through 4096 corresponding to the 12-bit grayscale. The worst case camera error corresponding to brightness at the lower end (i.e. around gray scale equal to 30) is ±3% . Combining these considerations yields an overall bound on the error for the concentration measurements of ±4%. As discussed in the next chapter, the uncertainty for the concentration fluctuations is less than this overall estimate.

3.5.6 PLIF image processing and data sets

The captured 12,000 images were analyzed using various statistical and fractal analysis programs. The specific methods used for the analysis are described in the following chapters. As described in Section 3.3, measurements were conducted at six downstream distances from the plume source along the plume centerline. Figure 3.8 shows a sketch of the measurement region with respect to the plume centerline. The shaded region at the bottom of the image (of dimension 512 × 512 pixels) contained a near uniform vertical gradient of the scalar field and was used to quantify the effects of scalar gradient on the small-scale characteristics.

3.6 Flow characteristics

A uniform open channel flow of depth 100 mm for Reynolds numbers of 5000, 10,000, and 20,000 was produced by adjusting the bed slope and tailgate position of the tilting flume for each flow condition. The flow conditions for the three cases were in the category of low Reynolds number open channel flows. Secondary currents due to the finite flume width were assumed negligible because the high aspect ratio (10.7) enabled a wide channel approximation (Webel and Schatzmann 1984) which requires the aspect ratio to be greater than 5.0. A summary of the flow conditions and important parameters is shown in Table 3.3

Table 3.3 Flow conditions and parameters.

$Re = UH/\nu$	$Fr = U/(gH)^{1/2}$	U (mm/s)	$<U_{max}>$ (mm/s)	Re_θ	u^* (mm/s)	$Re_\tau = u^*H/\nu$	$\delta^+ = u^*\delta/\nu$
5000	0.05	50	62.6	540	3.25	325	260
10,000	0.1	100	136.6	1200	6.4	640	550
20,000	0.2	200	238.0	1880	10.6	1060	860

Tachie et al. (2003) previously reported data for similar flow conditions in terms of flow depth and range of momentum thickness Reynolds number, Re_θ. Tachie et al. (2003) used laser Doppler velocimetry (LDV) to quantify the streamwise velocity characteristics and the current data will be compared to their results in the discussion below. Also, the

Froude number has been previously shown to have no effect on the boundary layer characteristics for the given range (Chow 1988).

Figure 3.9 shows the measured mean streamwise velocity profiles for each case. The velocity increased from zero at the bed to a maximum near the water surface. Data are not shown for $y > 90$ mm due to the difficulty of resolving the velocity near the water surface with optical measurement techniques. The free stream velocity is approximated as the maximum velocity for the respective profiles and is shown in Table 3.3.

The wall shear velocity, $u*$, for each profile was estimated by the Clauser plot technique, which assumes that a universal logarithmic profile exists in the inertial layer. The shear velocity was estimated to be 3.25, 6.4, and 10.4 mm/s for the boundary layer corresponding to Reynolds numbers of 5000, 10,000, and 20,000, respectively. Figure 3.10 shows the normalized mean streamwise velocity profile with respect to the inner variables along with the viscous sublayer and inertial (logarithmic) layer profiles. The mean velocity was normalized by the wall shear velocity, $u*$, while the distance variable was normalized by the viscous length, $\nu/u*$. The data show very good agreement with the law-of-the-wall profile in the viscous and inertial layers. Recent experiments for low Reynolds number open-channel boundary layers have suggested a power law formulation for the inertial layer profile (Bergstrom et al. 2001), but we have compared our data solely to the logarithmic layer formulation. Because the primary focus of this these experiments is the structure of the fluctuating scalar field, the debate regarding the best formulation of the inertial layer falls outside the scope of the present study.

Figure 3.11 shows the longitudinal turbulence intensity profile, namely the RMS of the fluctuating streamwise velocity component. The RMS profiles were fairly uniform for much of the channel depth with a significant peak near the bed. From the figure, it is clear that measurements in the viscous sublayer were achieved only for the lowest Reynolds number case owing to the appearance of the peak.

Figure 3.12 shows the normalized longitudinal turbulence intensity profile with respect to the inner variables. The three profiles collapse well close to the bed for $y^+ < 30$. The profiles also show a Reynolds number dependence for $y^+ > 30$ indicating that the Reynolds number affects higher order statistics deeper into the boundary layer compared to the mean velocity. The peak value is observed to be around 2.7 in the range of $13 < y^+ < 15$, which agrees well with the data of Nezu & Rodi (1986), Cowen & Monismith (1997), and Tachie et al. (2003). For $y^+ > 30$, u'^+ increases with increasing Re; with the profiles again closely agreeing with the profiles for similar Re_θ reported in Tachie et al. (2003).

Figure 3.13 shows the vertical turbulence intensity profile, namely the RMS of the fluctuating vertical velocity component. The profiles are similar to those of the vertical turbulence intensity profile for canonical turbulent boundary layers (Spalart 1988). Figure 3.14 show the same data normalized with inner variables. For Reynolds numbers of 5000 and 10,000, the normalized profiles reasonably collapse for $y^+ < 30$. The *Re* =

20,000 profile does not collapse for $y^+ < 30$, which reflects that fact that the fluctuation of the vertical velocity is very difficult to quantify. For $y^+ > 30$, v'^+ increases with increasing Re. Also the range of values of v'^+ agree well with previous experimental data presented by Nezu & Rodi (1986) and Cowen & Monismith (1997).

Figure 3.15 shows the Reynolds shear stress profiles. The profiles show a sharp increase from zero at the bed to a peak value. Above the peak location, the shear stress decreases to near zero at the water surface. Figure 3.16 shows the same data with inner variable scaling. The peak of the profiles is at $y^+ > 30$ and appears to shift to the right with increasing Reynolds number. Cowen & Monismith (1997) showed a peak with a similar non-dimensional value located at approximately $y^+ = 50$ for $Re_\theta = 1300$. For the current data, Reynolds number effects are evident for $y^+ > 30$ depicted by increasing shear stress for increasing Reynolds numbers.

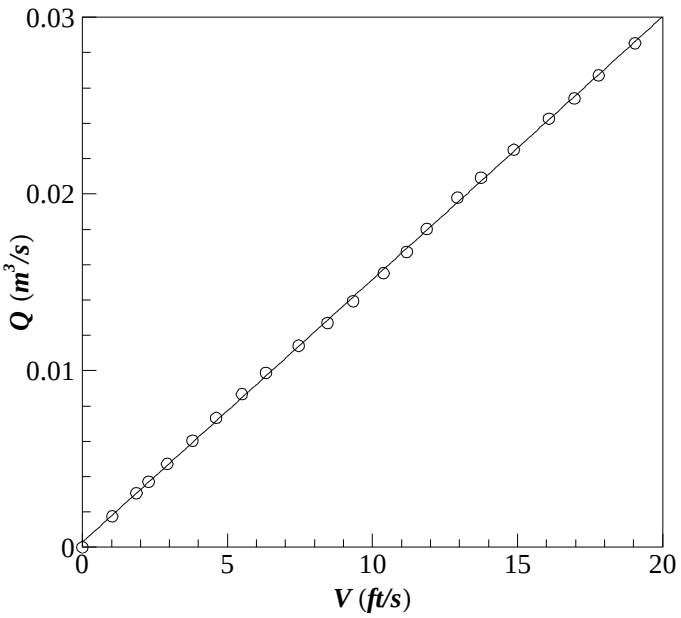

Figure 3.1 Electro-magnetic flow meter calibration data. The digital panel displays a velocity in ft/s and the actual flow rate, Q, was measured with a weigh barrel and stopwatch. Circles represent average data over 15 measurements. The straight line represents least-square best fit ($Q = 5.2522\times10^{-2}V + 1.0412\times10^{-2}$). In practice, the calibration curve is used to covert the displayed velocity to actually flow rate.

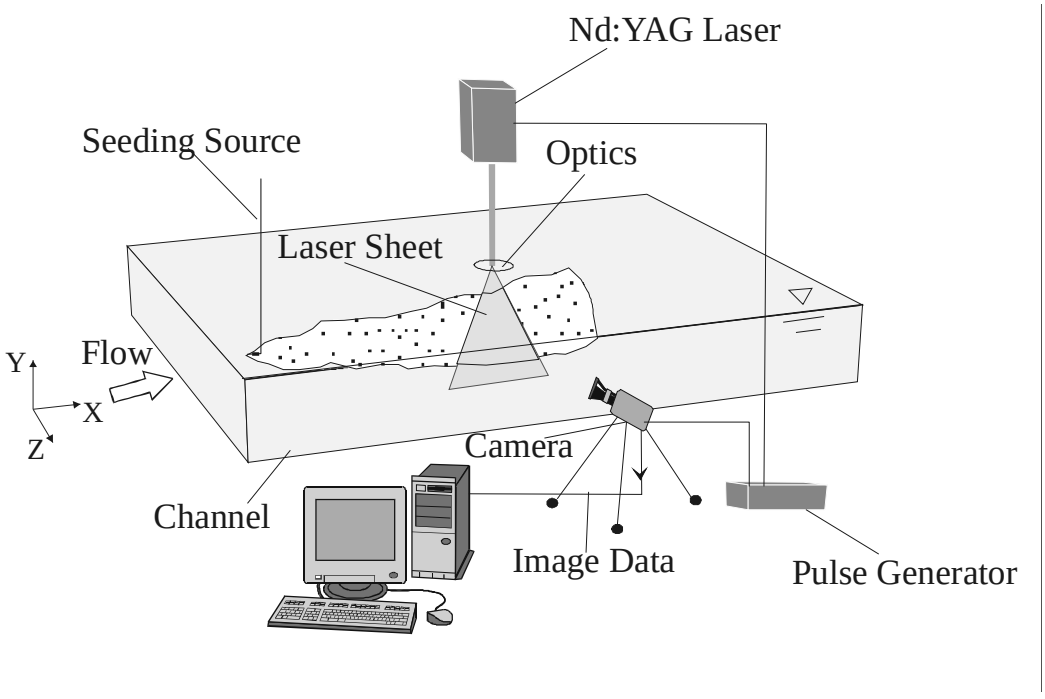

Figure 3.2 Schematic of the experiment setup for velocity measurement via PIV and PTV.

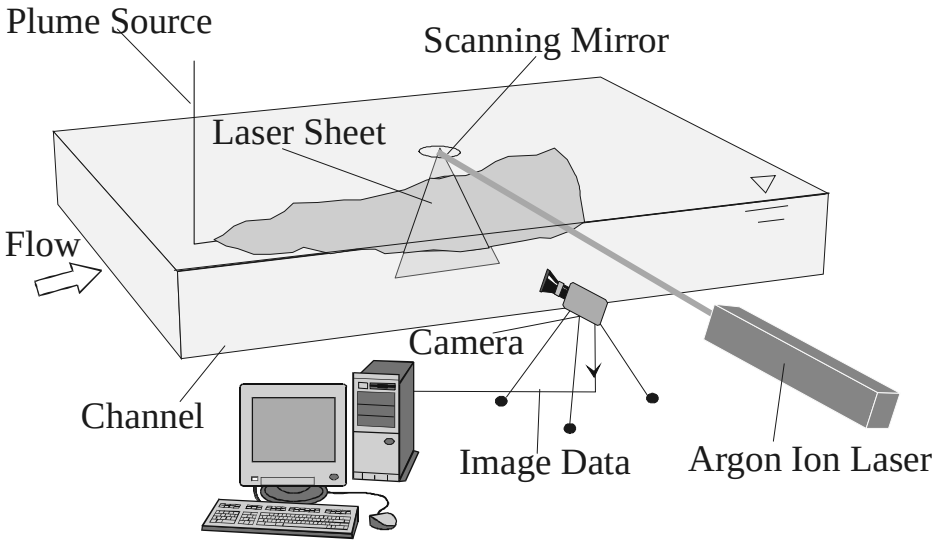

Figure 3.3 Schematic of the experiment setup concentration measurements via PLIF.

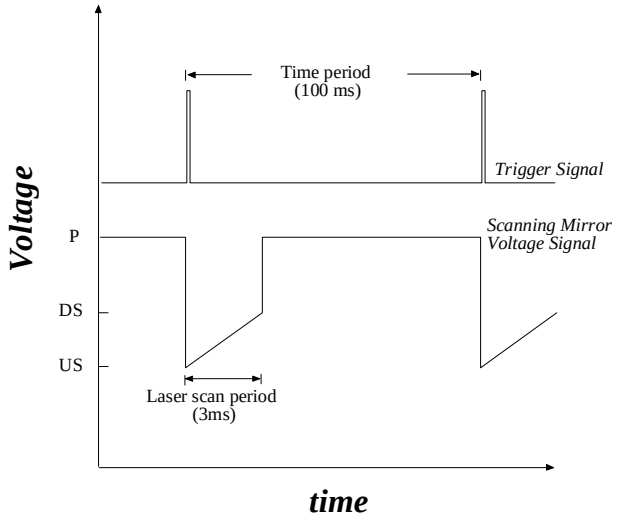

Figure 3.4 Synchronization between the camera trigger signal and the scanning mirror signal. The trigger signal is in arbitrary voltage units.

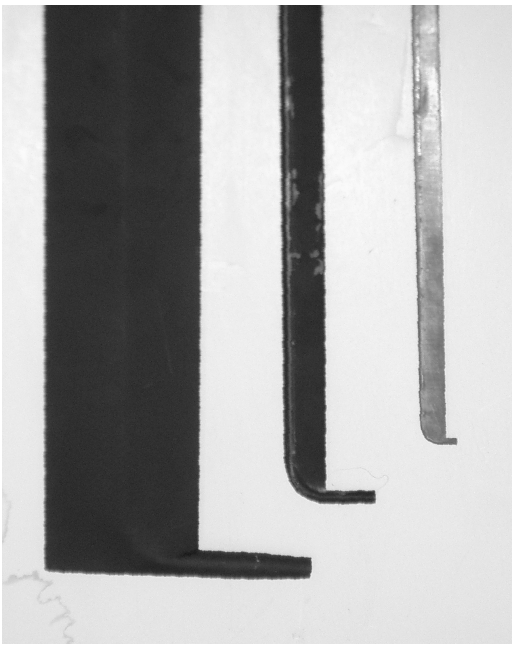

Figure 3.5 Photograph of the nozzles with diameter (from right to left) D **= 2.2, 4.7, and 9.4 mm.**

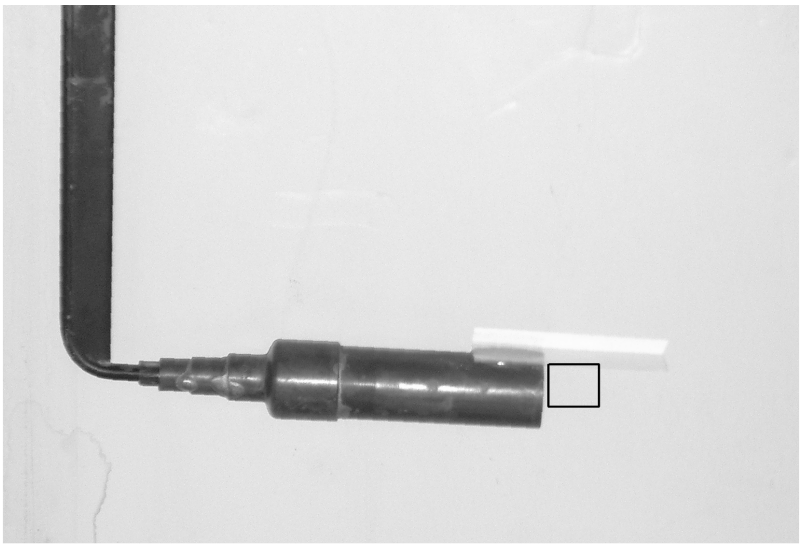

Figure 3.6 Photograph of the calibration nozzle attached to the 4.7 mm diameter plume delivery nozzle. The box shown represents the measurement region under the glass slide.

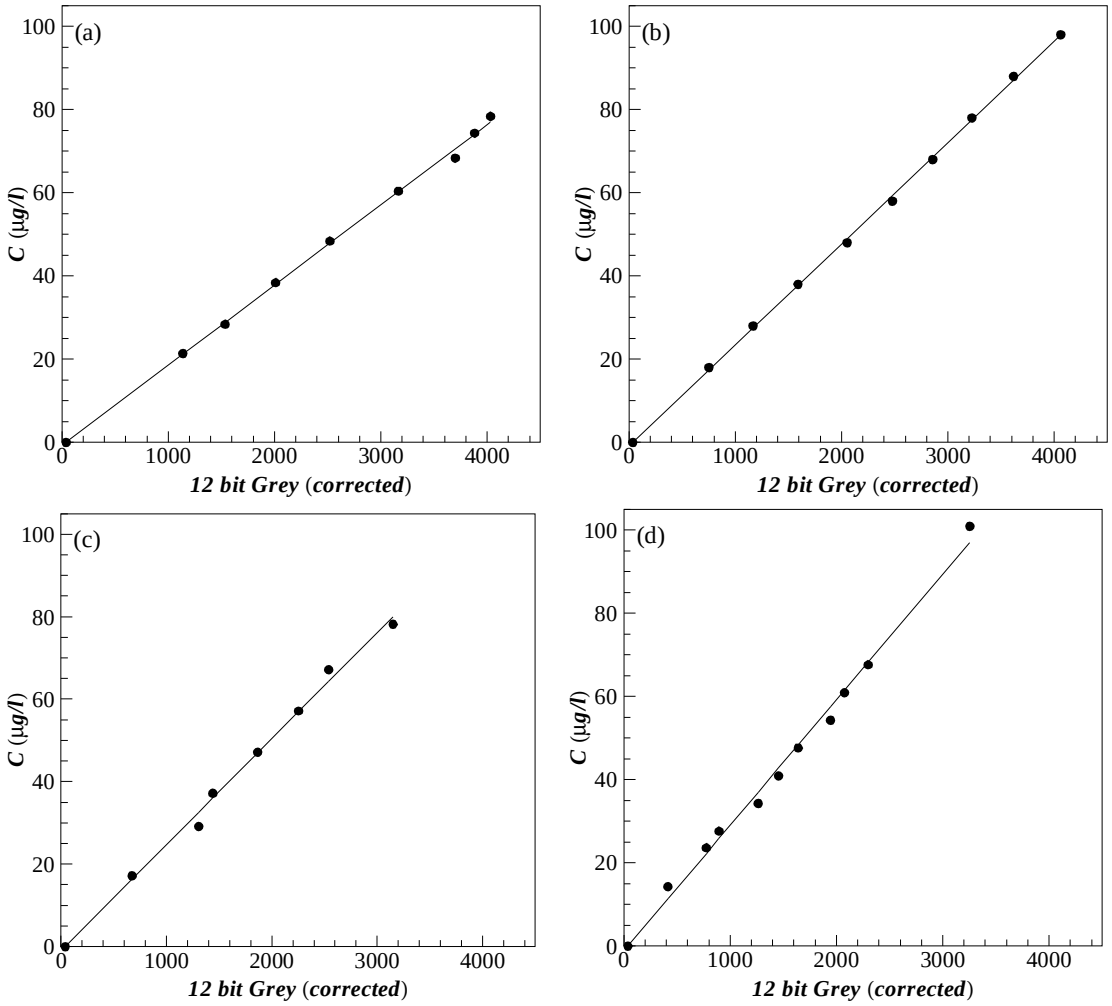

Figure 3.7 Sample calibration curves for a representative pixel for (a) Re **= 5,000 and** D **= 4.7 mm, (b)** Re **= 10,000 and** D **= 4.7 mm, (c)** Re **= 20,000 and** D **= 4.7 mm, and (d)** Re **= 10,000,** D **= 2.2 and 9.4 mm.**

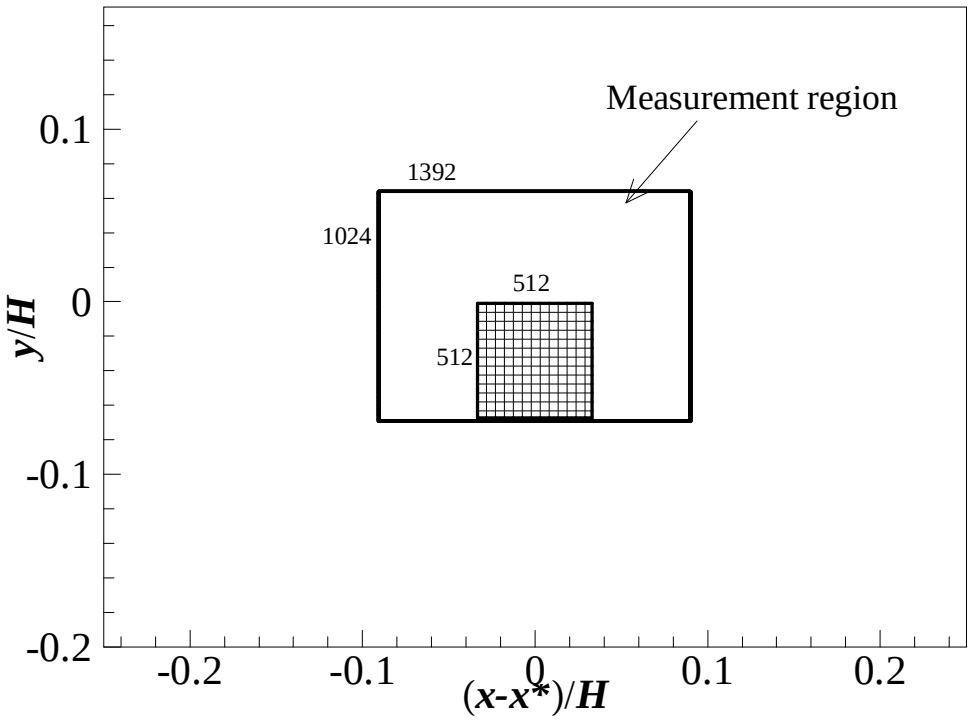

Figure 3.8 Sketch of the measurement regions for x^* = 0.1 m, 0.25 m, 0.5 m, 1 m, 2 m, and 4 m from the plume source. The shaded region represents the off-centerline region of interest used to quantifying the effects of the mean gradient.

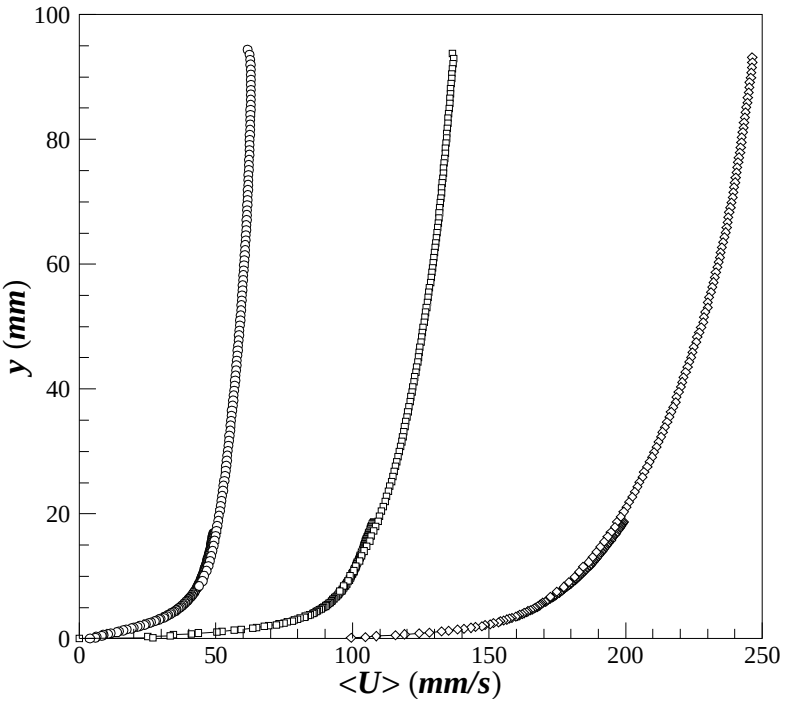

Figure 3.9 Mean streamwise velocity profiles for Re = 5000 (○), 10,000 (□), and 20,000 (◊).

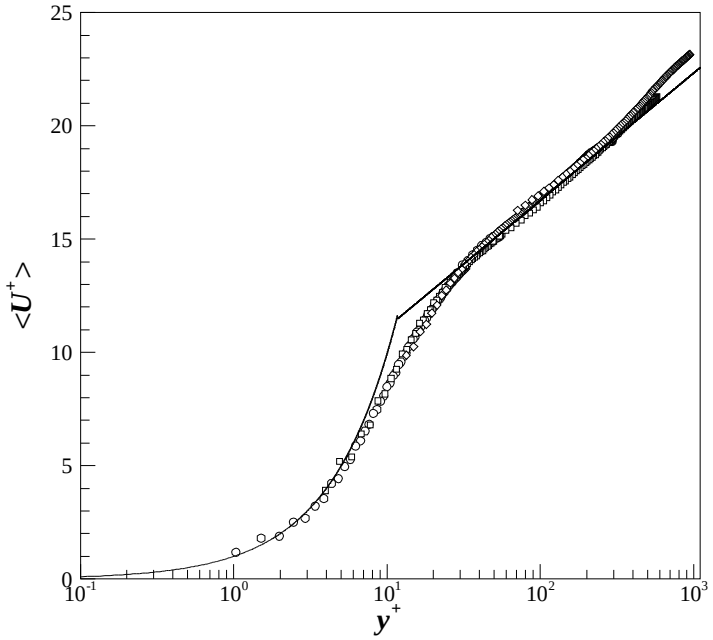

Figure 3.10 Normalized mean streamwise velocity profiles for Re = 5000 (○), 10,000 (□), and 20,000 (◊). The wall shear velocities, u^*, are 3.25, 6.4, and 10.6 mm/s, respectively. The solid line indicates the viscous sublayer ($u^+ = y^+$) and log layer ($u^+ = \frac{1}{\kappa}\ln y^+ + C$, κ = 0.41, C = 5.5) profiles.

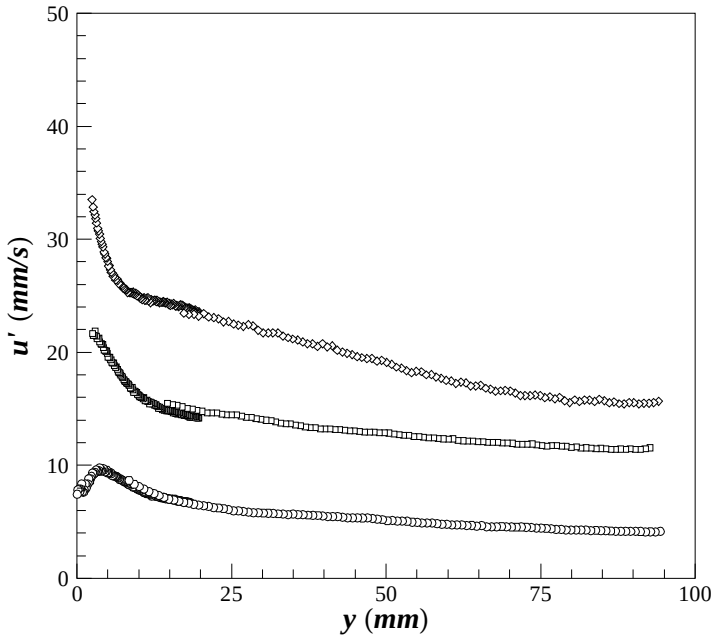

Figure 3.11 Profiles of RMS of the streamwise velocity, u', for Re = 5000 (○), 10,000 (□), 20,000 (◊).

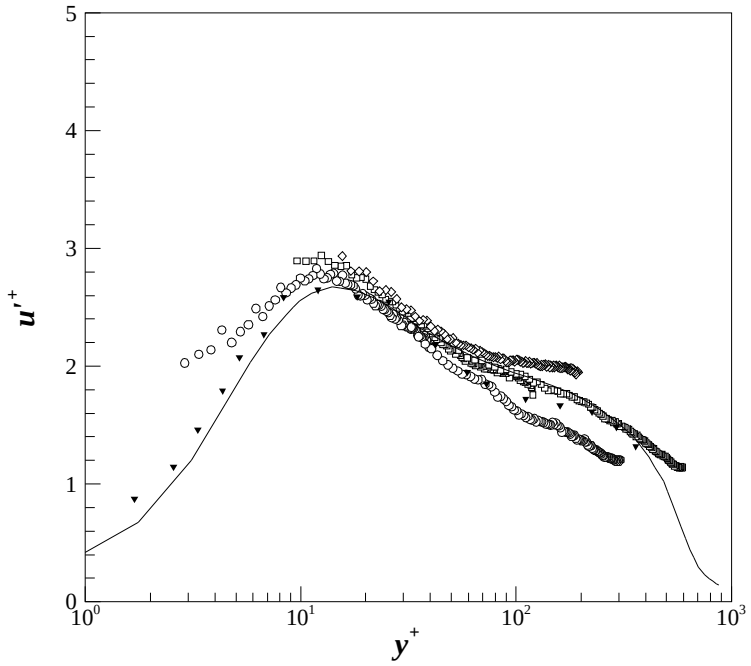

Figure 3.12 Normalized profiles of RMS of the streamwise velocity, u'^+, for Re = 5000 (○), 10,000 (□), 20,000 (◊). Compare data with Tachie et al. (2003) (▼) for $Re_\theta = 1450$ and DNS data by Spalart (1988) (——) for $Re_\theta = 1410$.

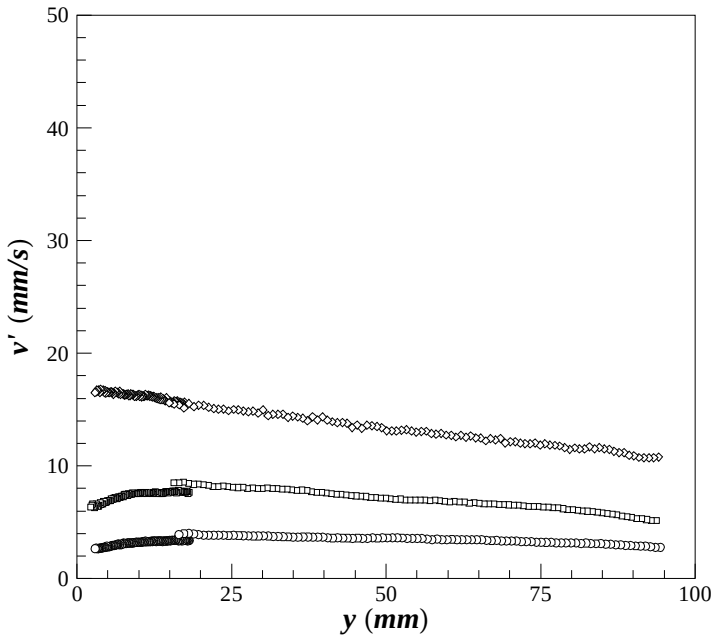

Figure 3.13 Profiles of RMS of the vertical velocity, v', for Re = 5000 (○), 10,000 (□), 20,000 (◊).

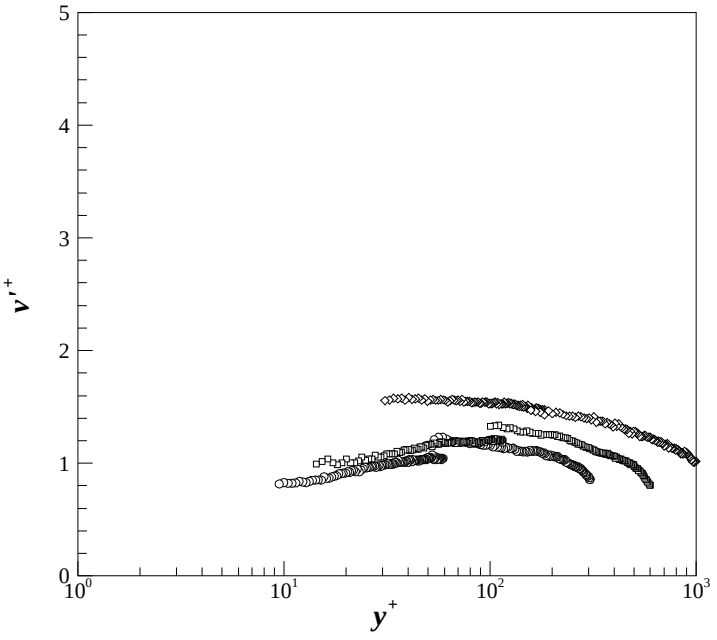

Figure 3.14 Normalized profiles of RMS of the vertical velocity, v'^{+}, for Re = 5000 (○), 10,000 (□), 20,000 (◊).

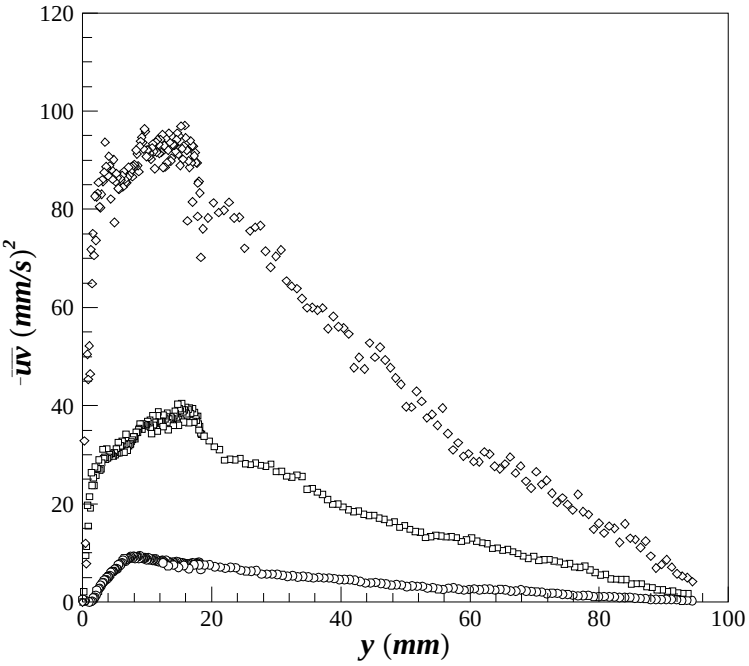

Figure 3.15 Reynolds shear stress profiles for *Re* **= 5000 (○), 10,000 (□), 20,000 (◊).**

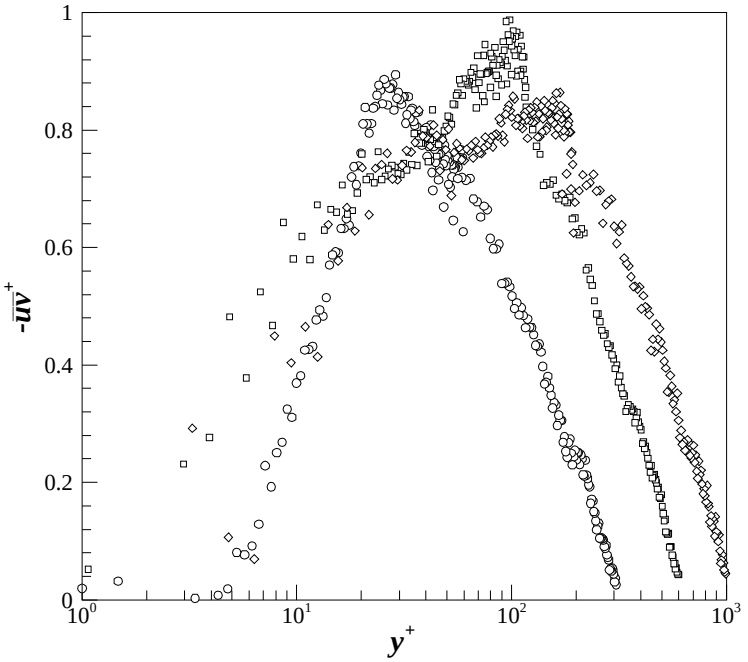

Figure 3.16 Normalized Reynolds shear stress profiles for *Re* **= 5000 (○), 10,000 (□), 20,000 (◊).**

Chapter 4

Small-Scale Structure of the Passive Scalar Field

The passive scalar field is formed by iso-kinetic release of the high Schmidt number scalar at mid-depth in the turbulent boundary layer of an open channel flow. As described in the previous Chapter, the passive scalar field was measured using PLIF for several combinations of downstream distance, Reynolds number, and passive scalar injection length scale (i.e. the nozzle diameter). Figure 4.1 and 4.2 show color dye visualizations of the plume mixing in the turbulent boundary layer at various Reynolds numbers and injection length scales. For each of the cases, it is clear that the local structure is a function of downstream distance from the source, Reynolds number and injection length scale. With increasing Reynolds number, the filament structure appears more fine and the plume overall is more homogeneous. With increasing nozzle diameter, the plume appears less intermittent and more homogenous.

Figure 4.3 shows samples of the high resolution concentration fields measured at six downstream distances for the case of Reynolds number equal to 10,000 and nozzle diameter equal to 4.7 mm. In general, the passive scalar field evolves due to the stretching and folding action of the fluctuating velocity field. The filament of scalar is advected downstream by the mean flow, while also being dispersed in all directions due to the fluctuating components of the velocity field. The scalar field thus generated is well connected and only appears as disconnected sheets in the measured two-dimensional transects of the field. The effect of molecular diffusion plays a minimal role in the

development of the large-scale plume structure. However, molecular diffusion is critically important to the mixing process because it limits the development of structure below the Batchelor length scale and acts to locally dilute the filament concentration. The sparse filament structure shown in Figure 4.3 is qualitatively different than that obtained from scalar injection through turbulent jets (e.g. Catrakis 2000 or Villermaux & Innocenti 1999). For the case of turbulent jets, clear fluid is entrained into the initially homogenous jet core, which leads to a less sparse (and less intermittent) concentration field.

The objective of this Chapter is to present a "traditional" analysis of the small-scale structure of the passive scalar field as it develops from structure at a single scale to the familiar cascade structure described in literature. As evident in the visualizations shown in Figures 4.1 and 4.2, the small-scale structure may be described in terms of the local anisotropic characteristics and intermittency of the plume. Here anisotropy is attributed to the magnitude of mean gradients while intermittency is the fraction of time the plume is present at a given point in space. High-resolution measurements for this flow configuration have not been reported previously. In addition, we discuss the effects of the experimental parameters, namely distance from the source, Reynolds number, and the nozzle diameter.

4.1 Large-scale description of the passive scalar field

Table 4.1 presents the characteristics of the turbulent velocity field for three Reynolds numbers. The velocity gradient, $d\langle U\rangle/dy$, and velocity fluctuation magnitude, u', data

correspond to the nozzle elevation. The mean turbulent kinetic energy dissipation rate is estimated based on the turbulence intensity, u', and the size of large scale eddies, approximately $H/2$, (i.e. $\varepsilon = \frac{u'^3}{H/2}$). The Taylor micro-scale Reynolds number is in the range 63 – 120, where the Taylor micro-scale is estimated from the isotropy approximation of $\left(15\upsilon u'^2/\varepsilon\right)^{1/2}$. The Batchelor length scale ($\eta_B = \eta Sc^{-1/2}$) of the passive scalar field varies in the range 9 – 24 μm.

Table 4.1 Flow characteristics.

Re	Re_λ	η (μm)	η_B (μm)	$v_\eta = (\nu\varepsilon)^{1/}$ (mm/s)	$t_\eta = (\nu/\varepsilon)^{1/2}$ (s)	ε (m^2/s^3)	$\frac{d\langle U\rangle}{dy}$ (s^{-1})	u' (mm/s)
5,000	63	758	24	1.3	0.6	3.0×10^{-6}	0.18	5.3
10,000	94	417	13	2.4	0.2	3.3×10^{-5}	0.38	11.8
20,000	120	291	9	3.4	0.08	1.4×10^{-4}	0.70	19.1

4.1.1 Mean scalar concentration

The mean (or average) scalar concentration is estimated from the 12,000 PLIF images captured for each case. The mean scalar concentration is defined as:

$$\langle\Theta\rangle = \frac{1}{T}\int_0^T \Theta\, dt \qquad (4.1)$$

where T is the total sampling time of the concentration measurement. Figure 4.4 shows the centerline variation of average scalar concentration for three Reynolds numbers with a constant injection length scale of 4.7 mm. For each Reynolds number, the mean concentration is orders of magnitude lower than the filament concentration in the instantaneous fields (Figure 4.3). The dashed line represents the estimated mean concentration as $x \to \infty$. The mean concentration decreases rapidly with downstream distance from the source, and the rate of change appears to decrease with x. The mean concentration decreases at a rate slower than a power law decrease due to the bounded width of the flow in the vertical direction. In particular, the flume bed and flow surface restrict the mixing in the vertical direction.

Near the source the lowest Reynolds number yields the maximum mean concentration, while the highest Reynolds number yields the lowest mean concentration. At $x/H = 40$, the trend is reverse. The cross over of the profiles is due to the fact that the concentration filament for the highest Reynolds number encounters less stirring before reaching $x/H = 40$ due to larger mean longitudinal velocity. Figure 4.5 shows the mean concentration versus the number of mean eddy turnovers. The number of mean eddy turnovers, N_{eddy}, is estimated from the following relation:

$$N_{eddy} = \frac{x/\langle U \rangle}{\frac{u'/\left(d\langle U \rangle/dy\right)}{u'}} = \left(x/\langle U \rangle\right) d\langle U \rangle/dy \qquad (4.2)$$

where $x/\langle U \rangle$ is the mean travel time of the filament from the source to location x, $u'/\left(d\langle U \rangle / dy\right)$ is the characteristic large-scale eddy size, and $\frac{u'/\left(d\langle U \rangle / dy\right)}{u'}$ is the characteristics "turnover" time of the large-scale eddies. The mean velocity and shear values are interpolated from the profiles in Figure 3.9 at the elevation of the nozzle centerline. The figure shows a near collapse of the profiles for $N_{eddy} > 1$, while there is significant Reynolds number dependence for $N_{eddy} < 1$. However, other interpretations cannot be ruled out. In the region between $N_{eddy} = 1$ and where the free surface and bed begins to affect the centerline concentration (i.e. $2 < x/H < 20$), the decrease appears to follow a power law with a scaling of $x^{-1.25\pm0.1}$. The power law scaling suggests a period of anomalous diffusion.

Figure 4.6 shows the centerline variation of the average scalar concentration for the three injection length scales for the Reynolds number of 10,000. Comparison of Figure 4.6 with Figure 4.5 indicates that the profile is more sensitive to the injection length scale than to the Reynolds number. The average concentration increases with the injection length scale due to the increased spatial homogeneity near the plume centerline.

4.1.2 Standard deviation of scalar concentration fluctuation

The variance of the scalar fluctuations is defined by the following equation using the Reynolds decomposition notation, $\Theta = <\Theta> + \theta$:

$$\left\langle \theta^2 \right\rangle = \frac{1}{T}\int_0^T \left(\Theta - \left\langle \Theta \right\rangle\right)^2 dt \tag{4.3}$$

The standard deviation is the square root of the variance. Figure 4.7 shows the centerline decrease of standard deviation of the scalar concentration fluctuations for three Reynolds numbers. The figure shows rapid decrease of the standard deviation with distance from the source and also a decrease of the standard deviation with increasing Reynolds number. It can be argued that the standard deviation is zero at the source and rises to a maximum followed by a rapid decrease approaching zero for the fully-mixed condition far downstream. The maximum standard deviation appears to occur in the range $0 < x/H \leq 1$ for each Reynolds number. Figure 4.8 shows the variance decrease with respect to number of mean eddy turnovers for each Reynolds number. The overall curvature of the profiles indicates that the decrease is faster than a power law. However, an exponential decay cannot be confirmed from the data as power law can be fit through the data for $N_{eddy} > 1$.

Figure 4.9 shows the ratio of the standard deviation to the mean concentration for each Reynolds number. The profiles are clearly Reynolds number dependent, and the maximum of the ratio appears to occur for $x/H > 1$. The magnitude of the ratio decreases with increasing Reynolds number. Similar trend was observed for the measurement of the ratio on the centerline of a jet (Miller & Dimotakis 1991). The downstream distance of the peak in these profiles decreases with Reynolds number. The slope of the profiles near the source appears to be similar for each Reynolds number.

Figure 4.10 shows the centerline profile of the standard deviation of the scalar fluctuations for the three injection length scales at constant Reynolds number. The standard deviation increases with the injection length scale. Figure 4.11 shows the ratio of the standard deviation to the mean concentration. The ratio decreases with the injection length scale indicating that the mean concentration increases faster than the standard deviation with increasing injection length scale. Also, the downstream position of the maximum peak ratio appears to be independent of the injection length scale. The slope of the profiles near the source is also dependent on the injection length scale, apparently decreasing with increasing injection length scale.

4.1.3 Higher order moments of scalar concentration fluctuations

The skewness, $\langle\theta^3\rangle/\langle\theta^2\rangle^{3/2}$, and kurtosis, $\langle\theta^4\rangle/\langle\theta^2\rangle^2$, are the normalized 3rd- and 4th-order central moments of the scalar concentration fluctuations. Figure 4.12 shows the centerline variation of the skewness of the scalar fluctuations for three Reynolds numbers. The magnitude of skewness indicates that the probability density function (PDF) of the scalar fluctuations differs significantly from a symmetric distribution. For each case, the profile increases to a maximum, then slowly decreases. The value of the local maximum appears to decrease with Reynolds number. The location of the peak is closer to the source with increasing Reynolds number. The skewness appears to decrease downstream of the peak. If the trend continues towards zero, then the PDF may be approaching a Guassian distribution far downstream of the source. Figure 4.13 reveals the effect of injection length scale on the skewness profile. The peak value of the

skewness decreases with increasing Reynolds number. The magnitude of the skewness decreases with Reynolds number suggesting that the distributions become more symmetric.

Figures 4.14 and 4.15 show the effect of Reynolds number and injection length scale on the kurtosis of the scalar fluctuations along the centerline. These figures suggest that the dependence of the kurtosis on Reynolds number and is injection length scale similar to that for the skewness.

4.1.4 Large-scale or external intermittency of scalar concentration fluctuation

Chatwin and Sullivan (1989) define the intermittency factor as the fraction of time the scalar concentration is greater than a threshold value. In the current work, the threshold value is equal to the mean concentration. It may be theoretically argued that the intermittency factor takes the value of 1.0 and 0.5 at $x = 0$ and $x \to \infty$, respectively, along the plume centerline. Figures 4.16 and 4.17 show the intermittency factor profiles for the three Reynolds numbers and three injection length scales, respectively. The figures show an initial decrease of intermittency factor from the value of 1.0 reaching a minimum value followed by a gradual increase toward the value of 0.5. The intermittency factor increases with both Reynolds number and injection length scale. Therefore, the concentration dye filaments are encountered more frequently at a point with increasing Reynolds number or injection length scale.

4.2 Concentration variation across the local measurement region

In order to analyze the effects of mean concentration gradient on the small-scale structure of the scalar field, the measurement region below the nozzle centerline (shown in Figure 3.8) is chosen due to the presence of a near constant mean gradient. Figure 4.18 shows vertical profiles of the mean scalar field in this region normalized by the local spatial average of the scalar concentration, $\langle \Theta^* \rangle$, for the three Reynolds number cases. It is clear that the vertical mean gradient decreases with distance from the source. Figure 4.19 shows that the longitudinal profiles of the normalized mean concentration vary minimally for each case. Thus, the vertical gradient plays a dominant role in the turbulent production of scalar fluctuations. The lateral scalar gradient along the width of the flume is assumed to be negligible due to the symmetry about the plume centerline.

Figure 4.20 and 4.21 show the effects of nozzle diameter on the vertical and longitudinal mean scalar gradients, respectively. The nozzle diameters as a fraction of the water depth are $0.02H$, $0.05H$, and $0.1H$. The vertical gradients are clearly influenced by the injection length scale. The vertical gradient for the largest nozzle diameter is close to zero, whereas the smaller injection length scales produce a significant vertical gradient that decreases with distance from the source. The longitudinal gradients are mild, similar to those shown in Figure 4.19.

4.3 Probability density function of the scalar fluctuations

The probability density function (PDF) completely describes the statistical behavior of the fluctuating scalar concentration. The PDF evaluated at $x \in \mathbb{R}$, for a continuous random variable *X*, that has values in the range $-\infty < X < \infty$, is defined as the function whose integral over the interval $(-\infty, x)$ is equal to the cumulative density function (CDF) evaluated at x. The CDF evaluated at x, is the probability that $X \leq x$. For "well-behaved" random variables the PDF is simply the derivative of the cumulative density function. PDFs of the scalar field in the uniform gradient region are estimated by averaging the PDF calculated for each measurement point in the region.

Figure 4.22 shows the scalar PDF calculated at six downstream distances for the three Reynolds numbers. The normalized scalar concentration has values only between zero and unity corresponding to the limiting concentrations of the ambient fluid and the injected tracer reflecting the bounded nature of scalar concentration. It must be noted that the bounded nature of the scalar also bounds the scalar variance between zero and $\langle\Theta\rangle(1-\langle\Theta\rangle)$ (Dimotakis & Miller 1990). It can be argued that the PDF of the concentration immediately downstream of the source has a bi-modal shape with a dirac-delta spike at zero and unity. As the plume mixes in the downstream direction the spike at zero appears to evolve a tail, while the spike at one appears to flatten as its center drifts toward lower concentration values. Further downstream the peak near one decreases in magnitude and eventually is dominated by the exponential-like tail. The Reynolds number significantly influences the evolution of the PDF. Close to the source, the spike

near one appears to reduce in size with increasing Reynolds number. The spike is almost absent for the highest Reynolds number case for x = 0.1 mm ($x/H = 1.0$). This indicates that the intermittent bursts of near-source-concentration reduce with increasing Reynolds number. The presence of the spike indicates a strong influence of the source. It implies that scalar fluctuations are more likely to have concentrations closer to that of the source than the local average concentration. It is important to realize that the signal to noise ratio is worse for samples outside of dye filaments. Thus, the spike at zero concentration appears more smoothed out than reality and therefore the PDF underestimates the higher order moments. However, the shape of the PDFs shown agree well with the PDFs measured for similar high Schmidt number experiments by Villermaux et al. (1998) and Rehab et al. (2001).

Figure 4.23 shows the PDFs of the scalar fluctuations normalized by the standard deviation for the three Reynolds numbers. The figure depicts the evolution of the PDFs from bi-modal to that with an elongated tail. Notice that the probability density of negative fluctuations is greater than that of positive fluctuations. This is explained with the intermittency factor discussed in Section 4.1.4 which is essentially the ratio of the area under the PDF over positive fluctuations to that over negative fluctuations. The figure shows that the tail of the PDF appears to grow with increasing distance from the source and Reynolds number. Fluctuations as large as 50 standard deviations have been observed for the highest Reynolds number. Also, the PDF distributions appear to collapse better with increasing distance from the source and Reynolds number. The slope of the elongated tails appears unaffected by Reynolds number.

Figure 4.24 shows the scalar PDF calculated at different downstream distances for the three injection length scales. The shape of the PDF is shown to significantly depend on the injection length scale. The spike near one appears to increase in size with the injection length scale. Also, the probability density of higher concentration (i.e. $\Theta > 0.1\Theta_O$) increases with the injection length scale. This observation is consistent with the intermittency factor data (Figure 4.17). Figure 4.25 shows the normalized scalar fluctuation PDF for the same cases. The PDFs show better collapse with increasing injection length scale. Most importantly, the slope of the elongated tail is also observed to depend on the injection length scale. The PDFs have steeper tails with increasing injection length scale indicating that the tails are sensitive to initial conditions.

It may be concluded from these data that the PDF of scalar fluctuations cannot be assumed to follow either exponential or Gaussian distributions, or in general any standard distribution. This conclusion agrees with the previous observations of Yee et al. (1993) for an atmospheric plume and to observations of Villermaux et al. (1998) and Rehab et al. (2001). The PDF distribution is clearly dependent on the presence of the mean scalar gradient and the nature of the initial conditions. As described in Section 2.2.4.1 there is a continuing debate over the Gaussianity of the PDF of scalar fluctuations and the existence of exponential tails. Our data clearly demonstrates that the overall shape of the scalar PDF is strongly dependent on the nature of how the scalar is introduced into the flow, initial conditions, and the boundedness of the scalar concentration. Most importantly the nature of the positive tail of the PDF agrees with the exponential nature

suggested by Pumir (1991). However, our unique contribution to the ongoing debate is the evidence supporting the dependence of the tail of the PDF on the nature of the source of scalar field such as the injection length scale. Note that the limitations of the experiment with respect to a poor signal to noise ratio does not apply to the tail of the PDFs because of high signal to noise ratio at the upper end of the sensor dynamic range.

4.4 Probability density function of scalar gradients

The PDF of scalar gradient is related closely to the local structure of the scalar field. Previous studies have repeatedly shown that the mean scalar gradient affects the smallest scales by skewing the PDF of the scalar gradient (Sreenivasan 1991, Warhaft 2000). Figure 4.26 shows the PDF of the fluctuating longitudinal scalar gradient at six distances downstream from the source for three Reynolds numbers. All PDFs are normalized by the standard deviation to demonstrate the changes in the dynamics of the scalar gradient fluctuations. The range of scalar gradient fluctuations increases with downstream distance from roughly ±10 standard deviations for the nearest case to greater than ±40 standard deviations for the farthest case. The PDFs are also slightly skewed with the negative tail more flared than the positive tail. This clearly reveals that the presence of scalar gradient contributes to the local anisotropy of the passive scalar structure with a greater frequency of negative fluctuations than positive ones. Increasing Reynolds number appears to spread the PDFs of the near source cases due to the presence of finer scales and steeper instantaneous scalar gradients. The PDFs farther downstream are relatively unaffected by the increase in Reynolds number. Although the distributions are far from Gaussian, an exponential tail cannot be confirmed from the figures.

Figure 4.27 shows the PDF for the vertical scalar gradient. These PDFs appear to be more spread out for the near source cases than those in Figure 4.26, which indicates that the instantaneous vertical gradients cover a broader range than the longitudinal gradients. The range of fluctuations increases from about ±20 standard deviations for the nearest case to over ±40 standard deviations for the farthest case. Also, the positive tail is more flared than the negative tail, which indicates the effect of the mean scalar gradient.

Figure 4.28 shows the skewness and kurtosis of the PDFs shown in Figures 4.26 and 4.27. Departure of the skewness of the scalar gradient from zero is a convenient indicator of local anisotropy of the scalar field. The skewness of both the longitudinal gradients and vertical gradients are of $O(1)$ magnitude and appear fairly constant with downstream distance. The skewness has a magnitude around 1.0 for each Reynolds number. Therefore, an increase in Reynolds number does not appear to reduce anisotropy of the scalar structure. The skewness values reported herein are higher than the values reported by Yeung et al. (2002, 2004) for the case of high Schmidt number passive scalar mixing driven by a mean gradient in DNS simulations of locally isotropic velocity field. This may indicate that the mean velocity gradient and other anisotropic characteristics of the velocity field also contribute to the anisotropy of the passive scalar structure.

The kurtosis of the scalar gradients shown in Figure 4.28 is one to two orders of magnitude higher than those reported in Yeung et al. (2002). The figure shows that the kurtosis increases from $O(10^2)$ to $O(10^4)$ with increasing downstream distance. A high

value of the kurtosis indicates a distribution with a high peak and long tails. For comparison, a Gaussian distribution has a kurtosis value of 3. The large value of Kurtosis is mainly due to the intermittent and bounded nature of the scalar field thus leading to large number of samples of near zero gradient, which correspond to measurements in spatially homogeneous regions of free stream fluid. The steep gradients at the boundary of the dye filaments are much larger that the gradients within the dye filaments thus appearing are extreme fluctuations. The kurtosis increases with distance as due to the spreading of the PDFs with distance. The steepness of the kurtosis curve reduces with increasing Reynolds number and the gradient direction appears to affect the kurtosis mildly.

Figure 4.29 shows the calculated PDFs of the longitudinal scalar gradient at six distances downstream from the source for the three injection length scales. As with Figure 4.26 the PDFs show the negative tail more flared than the positive tail. The PDF for the largest injection length scale is much narrower than the smaller injection length scales. The PDFs calculated far downstream were relatively unaffected by Reynolds number. In contrast, the PDFs for the far downstream cases shown in Figure 4.29 show significant effect of injection length scale (initial conditions). The range of fluctuations clearly decreases with increasing injection length scale depicted by the narrowing of the PDFs. The PDFs of the vertical scalar gradient (Figure 4.30) are similar to those of the longitudinal gradient. Figure 4.30 also shows the positive tails to be more flared than the negative tails due to the positive vertical mean gradient. Figure 4.31 shows that the skewness is of $O(1)$ magnitude and appear to decrease in magnitude mildly with

increasing injection length scale. In contrast, the skewness remains around 1.0 in Figure 4.28 for varying Reynolds number. The increase in injection length scale appears to reduce the kurtosis of the PDF of scalar gradient.

4.5 Passive scalar power spectrum

The passive scalar power spectrum has been the primary focus of classical theory for characterizing the structure of passive scalars in turbulent flows. The most important results for the case of high Schmidt number passive scalars include the power spectrum characterization via scaling laws in the inertial-convective, viscous-convective, and viscous-diffusive regime. With the assumption of local isotropy of the velocity field and the passive scalar field, the scaling laws were predicted to be proportional to $k^{-5/3}$, k^{-1}, and an exponential roll off in the respective regimes. Here, we examine the one-dimensional spectral characteristics of the local structure of the passive scalar within the constant mean gradient areas for the different Reynolds numbers and injection length scales at different distances from the source.

The one-dimensional power spectrum is calculated by averaging the power spectra estimated for parallel one-dimensional spatial transects of the scalar field. The power spectrum of each transect is estimated via standard algorithms that employ features such as data windowing using the Bartlett window provided in Press et al. (2002). A noise floor is identified in the averaged one-dimensional power spectrum and subtracted to generate the optimal (Weiner) filtered power spectrum estimate. The averaged power

spectrum of the scalar field is calculated for the longitudinal wave-numbers and vertical wave-numbers in order to study any directional dependence.

Figure 4.32 shows the one dimensional longitudinal power spectra of the passive scalar field at six distances for the three Reynolds numbers with the horizontal axes normalized by the Batchelor length scale. The normalized wave-number corresponding to the Kolmogorov length scale, η_B / η, is of the order of $Sc^{-1/2} \approx 3\times10^{-2}$ and is indicated in each figure. The wave-number corresponding to the source injection size, D, is also shown on each of the plots. Each power spectrum shows evidence of scaling behavior in the inertial-convective range. There is a clear transition around the wave-number corresponding to the Kolmogorov length scale with the magnitude of the spectral slope increasing into and within the viscous-convective regime. The spectra have been cut-off before the highest resolved wave-number ($k\eta_B = 0.5$) as the energy from random noise dominates the signal. This transition near the wave-number corresponding to the Kolmogorov length scale is observed for all spectrum calculated in the present study.

The slope of the spectrum in the inertial-convective range appears to decrease (in magnitude) mildly with increasing distance for each Reynolds numbers (see Figure 4.32). Also, the width of the inertial-convective range clearly increases with increasing Reynolds number. The spectral variation in the viscous-convective regime for the spectra for any Reynolds number appears to remain parallel to each other without significant variation for each distance. However, note that the spectra for the two fields near the source for the highest Reynolds number appear to be relatively flatter in the viscous-

convective regime. Variation with respect to Reynolds number in the viscous-convective regime is hard to determine from the figure.

Figure 4.33 shows the one-dimensional vertical power spectra for the passive scalar field at different distances for the three Reynolds numbers. Similar to the longitudinal spectra, the inertial-convective range slopes reduce mildly with increasing downstream distance while the inertial-convective range expands with increasing Reynolds number. Also, the spectra in the viscous-convective regime appear to be parallel to each other for a given Reynolds number. It must be noted that the finite size of the source is larger than the corresponding inertial-convective range.

More quantitative comparisons are established by examining the logarithmic derivative (i.e. the slope on a log-log plot) of each spectra. Figure 4.34 shows the logarithmic derivative of the one-dimensional longitudinal spectra plotted in Figure 4.32. The dashed line in the plot represents the -5/3 slope corresponding to the slope of inertial-convective range predicted by the KOC argument. The decrease in the magnitude of the inertial-convective range slope with downstream distance and the increase in the width of the inertial-convective range with Reynolds number can be seen in Figure 4.34. For the lowest Reynolds number, the inertial-convective range scaling of the spectra for the case nearest to the source is $\propto k^{-3}$. The scaling exponent decreases in magnitude with increasing Reynolds number and the scaling is $\propto k^{-2}$ for the highest Reynolds number. With increased distance from the source, the magnitude of the exponent quickly decrease

to a value near $k^{-5/3}$ for each of the Reynolds numbers. Moreover, slopes less than 5/3 in magnitude are evident in the plot.

These variations may be attributed to a combination of factors. To explain these variations recall that Sreenivasan (1996) showed that the inertial-convective range spectral slopes were less than 5/3 in magnitude and approached this value only with increasing Reynolds number. Also, Dowling & Dimotakis (1990) showed that strong intermittency and mean scalar gradient increased the spectral slope in the inertial-convective range of the passive scalar spectra. For the data shown in Figure 4.34, the mean scalar gradient and intermittency appear to explain the increase of magnitude of the spectral slope for the near source cases. Slopes with magnitude less than 5/3 are observed far downstream due to the fact that the Reynolds number is much lower than the required Reynolds number (i.e. $Re_\lambda > 2000$ for shear flows, Sreenivasan 1996) to be reasonably close to 5/3. In fact, the absence of intermittency and mean gradient should produce a slope even lower than those observed far downstream for the given Reynolds number. It may be concluded that the spectral slope in the inertial-convective range is more sensitive to intermittency and mean scalar gradient than Reynolds number in shear flows.

Figure 4.35 shows the logarithmic derivative of the one-dimensional vertical spectra plotted in Figure 4.33. Here, the inertial-convective range slope variation due to intermittency and mean-scalar gradient is more dramatic compared to the variation in the longitudinal spectra. This is due to the stronger and more variable vertical mean scalar

gradient as evident in Figure 4.18. Also, the range of slopes is smaller than the ranges observed in Figure 4.35. This is attributed to the presence of a mean vertical velocity gradient as it is the only factor that may influence the spectral behavior in the vertical direction. Thus, it may be concluded that presence of mean velocity gradient decreases the range of the slope of the one-dimensional passive scalar spectrum.

The magnitude of the logarithmic derivatives (in Figures 4.34 and 4.35) show no indication of a k^{-1} scaling behavior in the viscous-convective regime. It must be noted that although the spectral data is dominated by noise for about half of the viscous-convective regime, the data on the lower wave-number portion of the viscous-convective regime is still sufficient to speculate on the existence of Batchelor's scaling. Also the amount of time the scalar blobs are exposed to turbulence is greater that the Batchelor's diffusion time (time required to reach viscous-convective equilibrium), $t_B = t_\eta \ln Sc$. For the three Reynolds numbers the Batchelor's diffusion time is 2.0, 0.6, and 0.3 s while the travel time for the scalar to reach the first measurement location is 1.7, 0.8, and 0.4 s respectively. The observations in Figure 4.34 and 4.35 are therefore in conflict with Batchelor's k^{-1} prediction. The variation of the logarithmic derivatives (in Figure 4.34 and 4.35) in the viscous-convective regime appears to be a straight line in agreement with Miller & Dimotakis (1996). A straight line in this plot corresponds to a log-normal spectral decrease. The mean scalar gradient does not appear to affect the logarithmic derivatives as there is a good collapse in the viscous-convective regime for each of the Reynolds numbers. The increase in Reynolds number appears to increase the linearity of the logarithmic derivative profiles indicating the widening of the range of linear behavior

of these plots in the viscous-convective regime. In Figure 4.34, there is no significant change in the slope of the linear fit with Reynolds number. However, the slope of the logarithmic derivative in the viscous-convective regime shown in Figure 4.35 for the vertical spectra is less in magnitude than that in Figure 4.34 for the longitudinal spectra. This reduction can only be attributed to the mean vertical velocity gradient as all other factors have shown to have no effect in this regime. It may therefore be concluded that the spectral characteristics in the viscous-convective regime are influenced by presence of mean gradients in the velocity field and unaffected by the presence of strong mean scalar gradients. The two cases near the source for the highest Reynolds number case shown in Figure 4.35 appear to disagree significantly with the other profiles. The reason behind the deviation is unclear and may be due to noise as can be seen in Figure 4.33.

Figures 4.36 and 4.37 shows the one dimensional power spectra of the passive scalar field in the longitudinal and vertical directions, respectively, at different distances for the three injection length scales. The wave-number corresponding to the smallest injection length scale falls within the inertial-convective range while the higher injection length scales fall outside the inertial-convective range. The only noticeable change in the spectra with respect to injection length scale is the increase in the overall energy with increasing injection length scale. This is due to the increase in scalar variance (see Figure 4.10) with increasing injection length scale. Other features of the spectra with respect to the inertial-convective and viscous-convective regimes show similar characteristics as discussed for the spectra with different Reynolds numbers, but mild differences are hard to detect in the figure.

Figures 4.38 and 4.39 shows the logarithmic derivatives of the spectra shown in Figure 4.36 and 4.37, respectively. The injection length scale can be seen to influence the spectra both directly and indirectly. The direct influence is evident for the smallest injection length scale which falls within the inertial-convective range. Recall that Villermaux et al. (2001) introduced the "cascade-bypass" situation that arises when the scalar is released at a length scale within the inertial-convective range. It was shown that the scalar spectrum bypasses the $k^{-5/3}$ scaling for wave-numbers higher than the injection wave-number and assumed a k^{-1} scaling due to the presence of a dominant stretching rate associated with the initial size of the scalar blob. The slope of the inertial-convective range for the scalar field far downstream from the source of the smallest injection length scale (Figure 4.38(a)) appear to show close to k^{-1} scaling in agreement with the cascade-bypass situation. Moreover, the slope of the inertial-convective range for the vertical spectra shown in Figure 4.38(a) appear to match the k^{-1} scaling better than the longitudinal spectra. Hence, the cascade-bypass situation explains the k^{-1} scaling for both longitudinal and vertical spectra observed far downstream. The bypass is more prominent in the vertical spectra perhaps due to the fact that the dimension D of the nozzle is aligned with the vertical direction.

The injection length scale also influences the spectra in an indirect manner as a consequence of its role as the initial condition for the scalar field. The spectrum is influenced by changes in intermittency and mean scalar gradient, which depend on the injection length scale. This is evident as the slopes observed near the source are greater

in magnitude and vary with injection length scale. The longitudinal mean scalar gradient decreases with increasing injection length scale (see Figure 4.6), and the scalar field is less intermittent with increasing injection length scale (see Figure 4.17). The combined effect is evident in Figure 4.38 and 4.39 with the maximum inertial-convective slope magnitude observed closest to the source and decreasing (mildly) for increasing injection length scale. The effects of injection length scale on the viscous-convective regime appear to be minimal as seen in Figure 4.38 and 4.39.

Our data mainly depicts variation of inertial-convective range scaling exponent as a function of intermittency and mean gradients; absence of Batchelor's k^{-1} scaling; and applicability of cascade-bypass as suggested by Villermaux et al. (2001). Regarding the Batchelor's scaling, it must be realized that a consequence of Batchelor's k^{-1} scaling is the logarithmic divergence of the scalar variance as $Sc \to \infty$, which is inconsistent with the upper bound on the scalar variance of $\langle\Theta\rangle\left(1-\langle\Theta\rangle\right)$. We therefore suggest that the spectra deviates from Batchelor's scaling in order to satisfy the additional condition of an upper bound on the area under the spectrum.

4.6 Structure functions of the scalar field

According to KOC theory, the structure functions of the passive scalar field assume scaling behavior in the inertial-convective regime given by: $<\Delta\theta_r^n> \propto r^{\zeta^n}$. The theory predicts ζ^n to be equal to $n/3$. As described in the literature review the phenomenological model failed to fully capture the characteristics of the passive scalar

field. The scaling exponents were found to be less than $n/3$ in many experiments and appeared to approach a constant value (a phenomenon now referred as saturation of the scaling exponents). The failure was attributed to the fact that KOC theory did not account for the intermittency of the dissipation of the scalar variance (Obukhov 1962). The refined similarity hypotheses for passive scalars (RSHP) incorporated the intermittency to yield better agreement between theory and experimental observation for the scaling exponents (Monin and Yaglom 1975). Although the scaling exponents predicted by RSHP were not universal, the predictions yielded some universal characteristics of the dissipation field, such as a joint log-normal distribution between the fluctuating dissipation rates of kinetic energy and scalar variance. Nevertheless, the validity of RSHP (with its assumption of local isotropy) is questionable due to the fundamentally anisotropic nature of the scalar field (Shraiman and Siggia 2000).

Accepting the fact that the scalar field is anisotropic, the following question is addressed in this study: *How does the scaling behavior of the structure functions relate to global anisotropic characteristics* (*i.e. mean scalar field, initial conditions, and low Reynolds number*)? This section examines the scaling behavior in the inertial-convective regime of the structure functions of the scalar field in the constant mean scalar gradient regions for the different distances, Reynolds numbers, and injection length scales and tests the applicability of the local-isotropy assumption for the scalar field studied.

Spatially-averaged structure functions were calculated by combining the structure function calculated for parallel one-dimensional spatial transects of the scalar field. The

structure functions thus generated are spatially-averaged within the constant mean scalar gradient region of the measurement window. Structure functions are calculated in the longitudinal and vertical directions. In order to ensure that a sufficient number of samples were measured for reliable estimates of the higher order structure functions (maximum of $n = 12$), error analysis on the data obtained was conducted. Note that calibration errors do not affect the measurements of concentration fluctuations as much as the error in the measurement of concentration itself due to the inherent filtering by the subtraction of the mean concentration. Random measurement noise, therefore, plays a more dominant role in the errors of the higher order scalar moments.

Figure 4.40 shows a typical ensemble of scalar increments measured near the source with a separation distance in the inertial-convective regime. The total number of samples (12,000×number of spatial ensembles per image) is about 5 to 6 million, of which only 2 million are shown in the figure. Figure 4.41 shows the PDF of the scalar increment in the inertial-convective range for the nearest and the farthest downstream measurement locations. The PDF corresponds to the fluctuation of the scalar increment normalized by the standard deviation. The distribution of the scalar increment is bounded by $-1 \le \Delta\theta_r / \Theta_o \le 1$ due to the bounded nature of the fluctuations. However, the normalization in Figure 4.41 reveals fluctuations up to 30 standard deviations.

In order to explore the variability of the estimate of the moments of $\Delta\theta_r$ with respect to sample size, we calculated the moments of $\Delta\theta_r$ for sub-samples of the total sample size. Figure 4.42 shows the scatter in the estimate of the second-order moment of $\Delta\theta_r$ with

respect to the number of samples considered for ensemble averaging. As seen in the figure the scatter covers more than 5 decades for samples sizes as low as the order of 10^3. The scatter significantly reduces with increasing sample size. A measure of the scatter is given by the standard error and we are interested in estimating this for the sample size corresponding to the total number of samples obtained. The standard error of the n^{th}-order structure function, $\delta\left(<\Delta\theta_r^n>\right)$, can be estimated from the following equation.

$$\delta\left(<\Delta\theta_r^n>\right)=\frac{\left\langle\left(\Delta\theta_r^n-<\Delta\theta_r^n>\right)^2\right\rangle^{1/2}}{\sqrt{N_{samples}}} \tag{4.4}$$

where $N_{samples}$ is the number of independent realizations of $\Delta\theta_r$. Figure 4.43 shows the scatter in the percentage standard error estimates of the second-order structure function for a given sample size of measurements of the scalar increment (with a separation within the inertial-convective range). The line represents the average of the scatter. From the figure it is clear that the average standard error of the second-order structure function decreases with increasing number of samples. Also, the scatter around the average standard error decreases with increasing number of samples. For sufficiently large number of samples the average standard error varies as: $\delta\left(<\Delta\theta_r^n>\right)\propto N_{samples}^{-1/2}$ indicating that the variance of $<\Delta\theta_r^n>$ has sufficiently converged. Also, the standard error reduces to $\approx 0.25\%$ for the largest sample size (approximately 6 million).

Figure 4.44 shows the average standard error variation with respect to sample size for even-order structure functions for the measurement location closest to and farthest from the source. The error increases with the order of the function and the distance from the source. Also the $N_{samples}^{-1/2}$ scaling is achieved sluggishly in Figure 4.44(b), which indicates a slow statistical convergence. The maximum standard error corresponds to $\approx 3.0\%$ for the 12^{th}-order structure function measured at 4 m downstream of the source. The error estimates for each Reynolds number and nozzle diameter have been confirmed to be of the same order. The standard error estimates for odd-order structure functions resulted in a significant percent error due to the close proximity of the odd-order moments to zero. Therefore, meaningful interpretations of the odd-order structure functions were not achieved.

4.6.1 PDF of scalar differences

The anomalous scaling observed in the passive scalar structure functions are attributed to the internal intermittency of the scalar field. The PDF of scalar differences depicts the influence of intermittency on structure functions. Figure 4.45 shows the PDF of longitudinal scalar increments as a function of increments for different distances from the source for the Reynolds number of 10,000 and injection length scale of 4.7 mm. The PDF spreads out and changes shape with increasing separation distance. Note that scaling behavior of the structure functions in the inertial-convective range implies that the PDF evolves (with increasing r) in a manner such that its moments increase as a power law. The figure shows no evidence of a Gaussian distribution for any case. The PDFs far

from the source appear to have elongated tails corresponding to the elongated tails observed in the PDFs of scalar fluctuations. The PDFs also appear to be mildly skewed due to the presence of the mean scalar gradient.

Figure 4.46 shows the PDFs of vertical scalar increments for the same cases. The effect of the vertical mean gradient on these PDFs is clearly evident. The negative tails are more flared than the positive tails causing non-zero skewness. This demonstrates that a mean scalar gradient imposes anisotropy even at the smallest scales.

4.6.2 Structure functions

Figure 4.47 shows the longitudinal second-order structure functions calculated at six downstream distances for three Reynolds numbers. The horizontal axes are normalized with the Batchelor length scale and the inertial-convective regime is within the range $30 \ll r/\eta_B \ll 100$. The structure functions appear to follow a scaling behavior within the inertial-convective regime, which is consistent with the scaling observed in the scalar power spectra. The slope of the structure function distribution in the inertial-convective regime appears to vary with distance from the source, while variations with respect to Reynolds number are hard to distinguish from the figure.

Figure 4.48 shows the vertical second-order structure functions calculated at six downstream distances for three Reynolds numbers. The structure functions again appear to posses scaling behavior in the inertial-convective regime with mild dependence on downstream distance and Reynolds number. Close inspection reveals that the slope in the

inertial-convective range appears to be flatter than that for the longitudinal structure functions.

Figures 4.49 and 4.50 show the longitudinal and vertical structure functions with varying source nozzle length scale. As with the structure functions shown in Figures 4.47 and 4.48 a mild dependence with downstream distance and nozzle diameter is noticeable. However, it is difficult to comment on the effect of nozzle diameter based on the figure and the structure function scaling exponents reveal more information.

4.6.3 Structure function scaling exponents

Higher even-order structure functions were calculated and the respective slope in the inertial-convective range (i.e. the scaling exponents) were determined from the logarithmic derivatives of the structure functions. Figure 4.51 shows the estimated inertial-convective range scaling exponents for the even-order longitudinal structure functions as a function of downstream distance from the source for the three Reynolds numbers. The scaling exponents initially decrease then gradually increase with downstream distance from the source. The curves corresponding to different orders appear to be nearly parallel to each other. The trend appears to correlate with the evolution of the skewness and kurtosis of the scalar fluctuations (see Figures 4.12 and 4.14), which indicates that the structure function scaling exponents are highly sensitive to the higher order moments of the scalar fluctuation PDFs. The magnitude of the exponents measured close to the source is, in general, larger than the KOC prediction.

The magnitude decreases below the KOC prediction before beginning to increase with downstream distance and appears to asymptote to $n/3$ far downstream.

Figure 4.52 shows the inertial-convective range scaling exponents for the even-order vertical structure functions as a function of downstream distance from the source for the three Reynolds numbers. The magnitude of these exponents is remarkably different than their longitudinal counterparts. Here, the exponents near the source are less than the KOC prediction and decrease further before increasing and apparently asymptoting to $n/3$. The exponents appear to be saturated due to the presence of a stronger vertical mean scalar gradient and vertical mean velocity gradient. The difference is also due to higher skewness of the scalar increments in the vertical direction compared to that of the longitudinal scalar increments (see Figures 4.45 and 4.46).

Figure 4.53 shows the Reynolds number effects on the scalar exponents in the inertial-convective regime for the longitudinal and vertical second-order structure functions shown in Figure 4.51 and 4.52, respectively. Again, the exponents in Figure 4.53 initially decrease before reaching a local minimum followed by an asymptotic increase to $n/3$. In Figure 4.53(a), the local minimum for the longitudinal exponent occurs downstream of the source at a distance dependent on the Reynolds number. The location is farther downstream for the lower Reynolds number cases. The magnitude of the exponent close to the source also appears to decrease with Reynolds number. For the vertical exponents, the magnitude of the exponent close to the source also appears to decrease with Reynolds

number (Figure 4.53(b)). The downstream distance of the minimum does not noticeably depend on Reynolds number.

Figure 4.54 shows the longitudinal exponents as a function of the order of the structure function. The dashed line represents the KOC prediction of $\zeta^n = n/3$. The scaling exponents close to the source are clearly above the KOC prediction. The function $\zeta_x^n(n)$ appears to be parallel to the KOC prediction close to the source and evolves into a non-linear relationship away from the source. $\zeta_x^n(n)$ is also observed to saturate (i.e. approach a constant value) with increasing n due to the intermittency phenomena of the scalar variance dissipation. Figure 4.55 shows the vertical scaling exponents as a function of the order of the structure function. The magnitude of the vertical scaling exponents is less than the magnitude of the longitudinal scaling exponents and also saturates for smaller values of n.

Figure 4.56 shows the estimated inertial-convective range scaling exponents for the longitudinal even-order structure functions for the three injection length scales. The general trend of the exponents with downstream distance from the source is the same as discussed above. The initial decrease in magnitude of the scaling exponents appears to be steeper for the smallest injection length scale, while the larger nozzle diameters caused an almost identical initial decrease. The local minima of the scaling exponents appears to occur close to the source ($5 < x/H < 10$) for $D = 2.2$ mm, whereas that for the larger diameters occur at about $x/H = 20$. Figure 4.57 shows the inertial-convective scaling exponents for the vertical structure functions for the three injection length scales. The

variation with distance downstream is qualitatively similar to that discussed for Figure 4.52.

Figure 4.58 depicts the effect of nozzle diameter on the second-order exponents of the longitudinal and vertical structure functions. The small injection length scale case yields the smallest magnitude for the local minima. This effect is an indirect influence of the source diameter as the initial condition and are related to the variations in the higher-order moments of the scalar fluctuations (shown in Figs. 4.13 and 4.15). It can be concluded that the scalar field is far from satisfying the conditions of local isotropy even at 4 m downstream from the source. However, scaling behavior for the structure functions exists and depends on the local higher order moment of the scalar fluctuations.

Figures 4.59 and 4.60 show the longitudinal and vertical scaling exponents as a function of the order, n. Both the longitudinal and vertical scaling exponents saturate with increasing n, but the vertical scaling exponents saturate rapidly due to the presence of a strong mean gradient in both the scalar field and the transporting velocity field.

4.7 Correlation functions of the scalar field

In addition to structure functions, we also examine the behavior of two-point correlation functions and an equilateral triangular three-point correlation function of the scalar field in the uniform mean scalar gradient region. Of particular interest is the behavior of these functions in the inertial-convective regime and the effects of distance from the source, Reynolds number, and nozzle diameter.

4.7.1 Two-point correlation function

Figures 4.61 and 4.62 show the longitudinal correlation function, $\langle \theta(x)\theta(x+r_x) \rangle$, and the vertical correlation function, $\langle \theta(y)\theta(y+r_y) \rangle$, calculated at the six downstream distances for the three Reynolds numbers. The correlation functions shown are not normalized by the variance, $\langle \theta^2 \rangle$, averaged over the uniform mean-gradient region. Therefore, the correlation function magnitude is observed to decrease with increasing distance from the source. In the inertial-convective regime, $30 \ll r/\eta_B \ll 100$, there appears to be a hint of scaling behavior. The presence of a scaling law was further supported by the logarithmic derivative of the shown structure functions. It was observed that the logarithmic derivative assumed an inflection point within the inertial-convective range. We therefore define the inertial-convective range exponent for the correlation function as the value of the logarithmic derivative at the inflection point. From the figures, the steepness of the correlation functions in the inertial-convective range appears to be mildly dependent on the distance from the source and Reynolds number. Figures 4.63 and 4.64 show the correlation functions for the three nozzle diameters. Mild dependence of the steepness of the correlation functions in the inertial-convective range on the nozzle diameter is observed.

Figure 4.65 shows the inertial-convective scaling exponents of the two-point correlation functions for the three Reynolds numbers. The magnitude of the exponents is dependent on both distance from the source and the Reynolds numbers. In general, the magnitude

of the exponent initially decreases with increasing downstream distance followed by a slow increase . The magnitude of the exponents is also sensitive to Reynolds number as they decrease in magnitude with increasing Reynolds number. In particular, the exponents for the vertical correlation function are more sensitive to Reynolds number. The decrease in the exponents may signify better correlation between the scalar fluctuations due to the higher the intermittency factor. The intermittency factor is defined as the fraction of time that the concentration is above the mean, and it also indicates the fraction of space that is occupied by the concentration filaments. As a final note, the exponents calculated for the longitudinal and vertical correlation functions are different presumably do the different mean scalar gradient differences.

Figure 4.66 shows the inertial-convective scaling exponents of the two-point correlation functions for the three nozzle diameters. The magnitude of the exponents decrease with increasing nozzle diameter, although the exponent for the vertical correlation function for the smallest nozzle deviates from the trend. The trends again can be explained from the intermittency factor, which increases with increasing nozzle diameter resulting in higher spatial correlations.

4.7.1 A three-point correlation function

It is apparent that the implications of the similarity hypothesis are more general than the scaling behavior of the structure functions. In particular, due to the multi-fractal picture of the phenomenology, the joint probability density function of the fluctuations, $\theta(\vec{x}_i)$, at

a set of measurement locations $\vec{x}_i$ varies in a peculiar manner with the overall size of the collection of points $\vec{x}_i$, whenever this set of points is separated in such a way that $\eta \ll \left|\vec{x}_j - \vec{x}_k\right| \ll L$ for any $\vec{x}_j, \vec{x}_k \in \{\vec{x}_i\}$ and $j \neq k$. The variation of the scalar increment PDF in the inertial-convective range is one way of approaching the "universal" properties of the joint PDF of the two points. We hypothesize that if scaling behavior exists in the two-point correlation functions in the inertial-convective range, then there may be a corresponding scaling behavior in the three-point correlation function.

In Figure 4.67, we define two three-point correlators to examine possible scaling behavior. The three points form an equilateral triangle with each side of size r. The correlator in Figure 4.67(a) has two points aligned in the longitudinal direction with the third point offset in the vertical direction and is termed the "longitudinal three-point correlation function", $\langle \theta_1 \theta_2 \theta_3 \rangle_\Delta$. The correlator in Figure 4.67(b) has two points aligned in the vertical direction with the remaining point offset in the longitudinal direction and is termed the "vertical three-point correlation function", $\langle \theta_1 \theta_2 \theta_3 \rangle_\triangleright$.

Figures 4.68 and 4.69 show the longitudinal and vertical three-point correlation functions calculated at the six downstream distances for the three Reynolds numbers. Figures 4.70 and 4.71 show the variation of the correlation functions with nozzle diameter. The overall trends of these correlation functions are similar to the respective two-point correlation functions with a hint of inertial-convective scaling behavior.

Figures 4.72 and 4.73 show the respective inertial-convective scaling exponents defined as the magnitude of the logarithmic derivative at the inflection point in the inertial-convective range. The trends for the scaling exponents of the three-point correlation functions are similar to those of the two-point correlation functions. The magnitude of the three-point scaling exponents first decrease followed by an increase with increasing downstream distance. The magnitude of the scaling exponents of the three-point correlation functions decrease with nozzle diameter. However, the exponents appear to be insensitive to the Reynolds number.

(a)

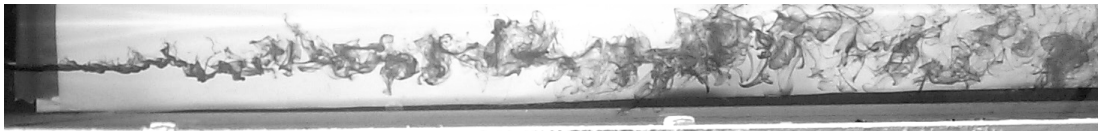

(b)

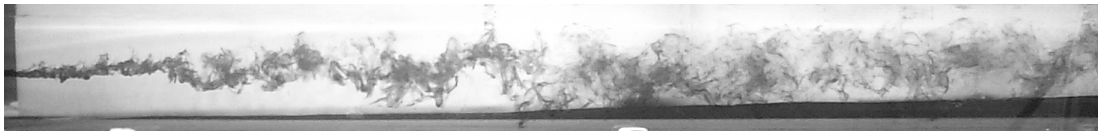

(c)

Figure 4.1 Color dye visualization of the plume mixing at (a) $Re = 5000$, (b) 10,000, and (c) 20,000 with a nozzle diameter of $D = 4.7$ mm.

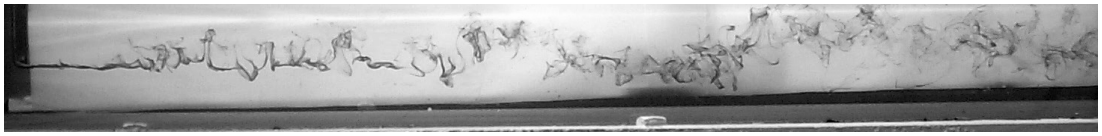

(a)

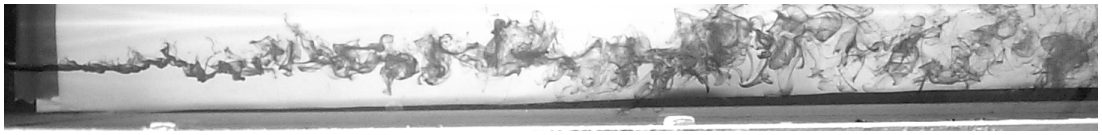

(b)

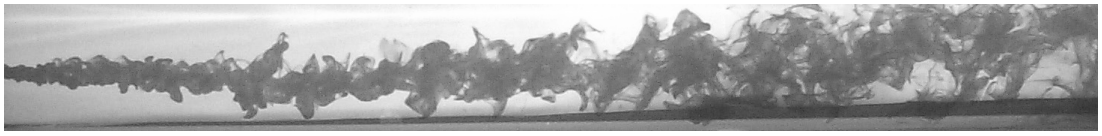

(c)

Figure 4.2 Color dye visualization of the plume mixing for (a) $D = 2.2$ mm, (b) 4.7 mm, and (c) 9.4 mm at a constant Reynolds number of 10,000.

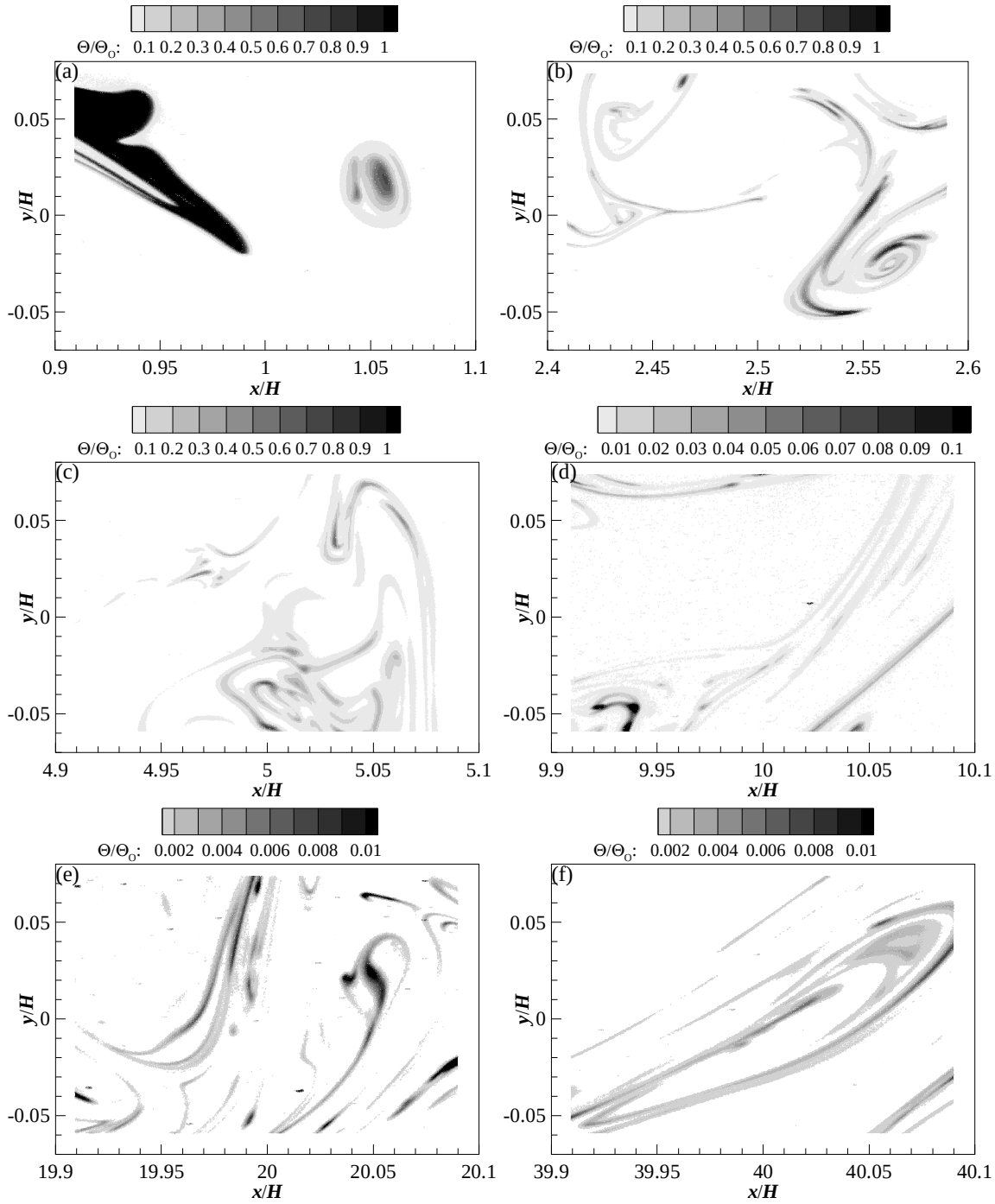

Figure 4.3 Sample concentration fields at (a) x = 0.1 m, (b) 0.25 m, (c) 0.5 m, (d) 1 m, (e) 2 m, and (f) 4 m. Data shown for Re = 10,000 and D = 4.7 mm.

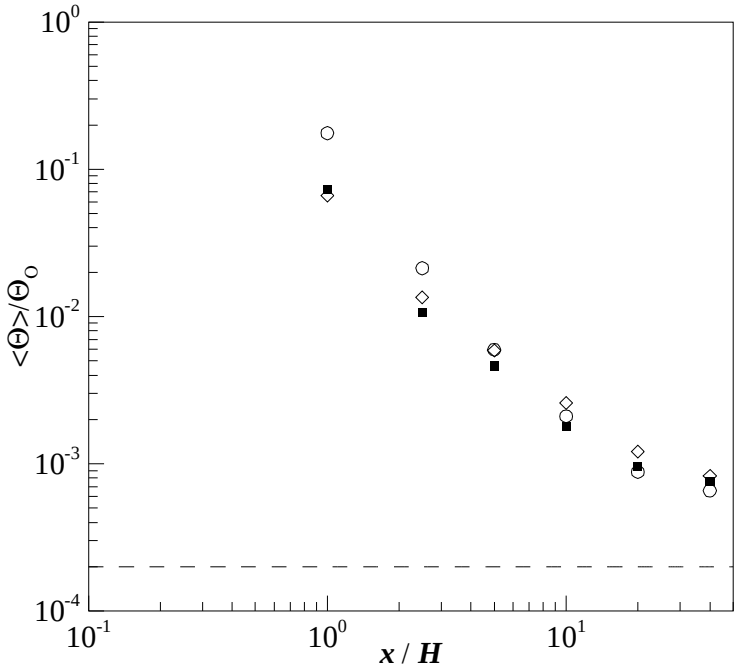

Figure 4.4 Centerline variation of average scalar concentration as a function of Reynolds numbers. Data shown for D = 4.7 mm and Re = 5000 (○), 10,000 (■), and 20,000 (◊).

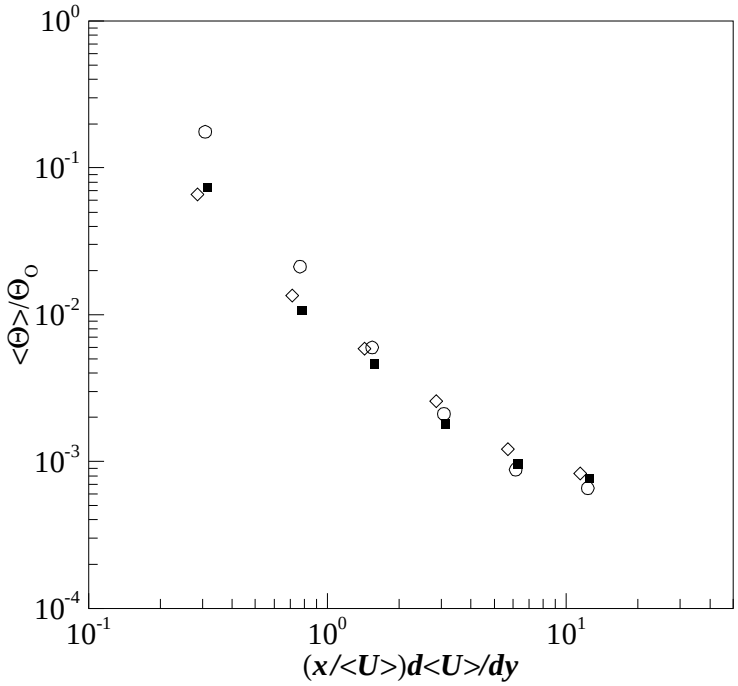

Figure 4.5 Average scalar concentration along the centerline as a function of mean eddy turnover for three Reynolds numbers. Data shown for D = 4.7 mm and Re = 5000 (○), 10,000 (■), and 20,000 (◊).

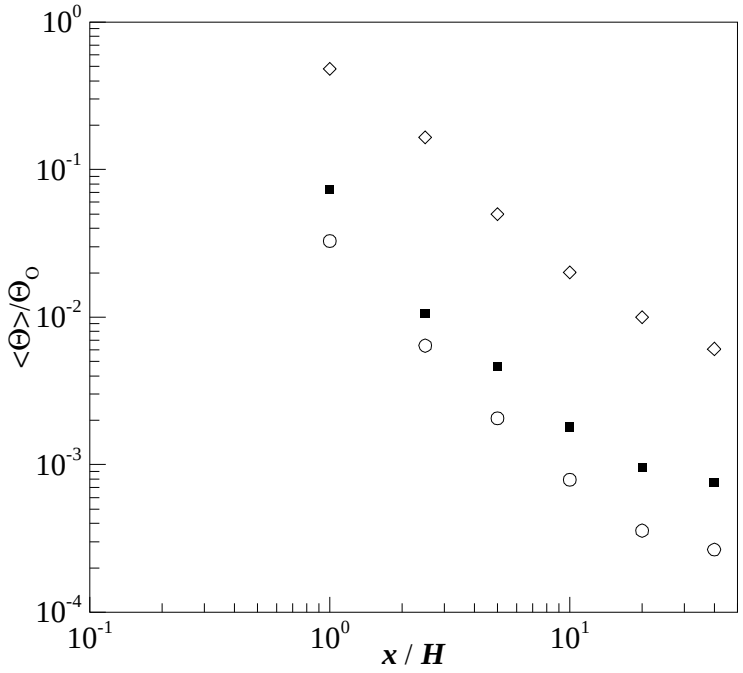

Figure 4.6 Centerline variation of average scalar concentration as a function of source nozzle diameter. Data shown for Re = 10,000 and D = 2.2 mm (○), 4.7 mm (■), and 9.4 mm (◊).

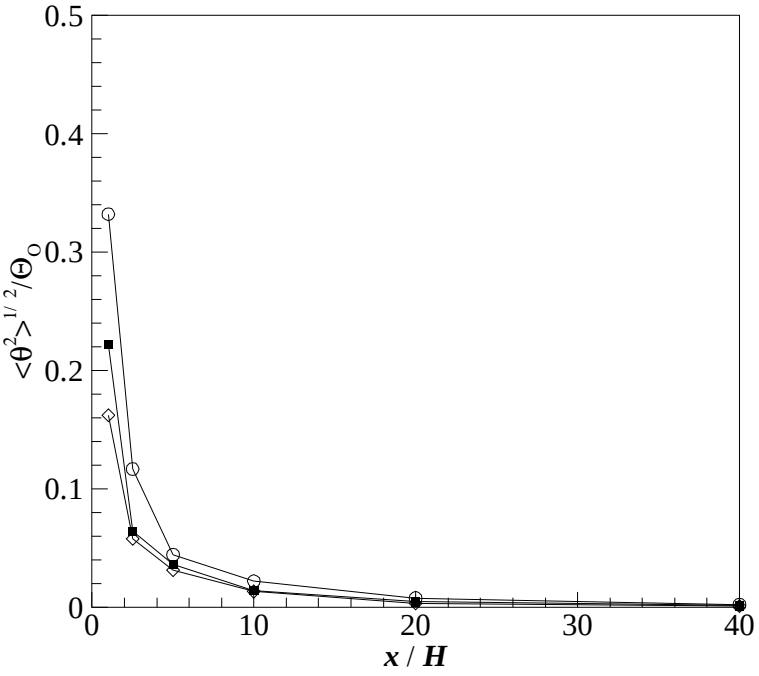

Figure 4.7 Centerline profile of standard deviation of scalar fluctuations as a function of Reynolds number. Data shown for D = 4.7 mm and Re = 5000 (○), 10,000 (■), and 20,000 (◊).

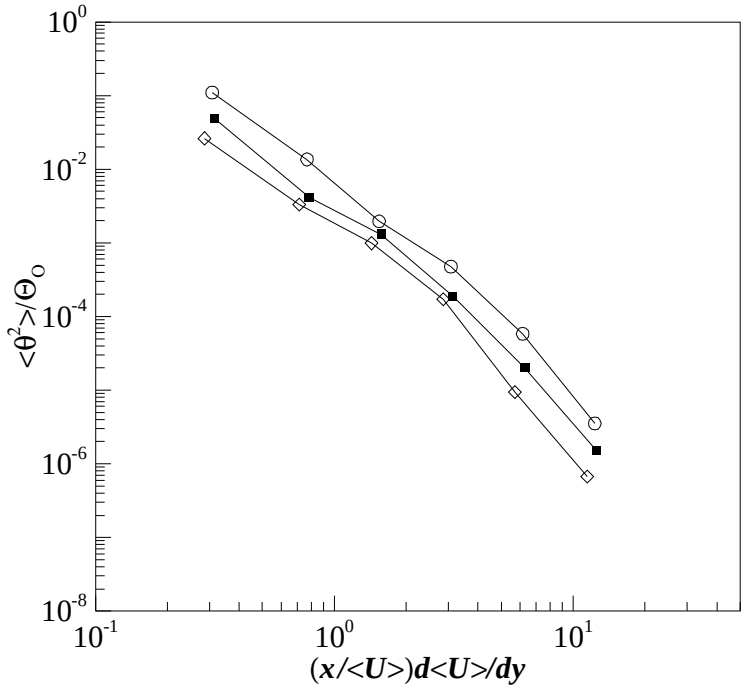

Figure 4.8 Variance of scalar fluctuations along the centerline as a function mean eddy turnover for three Reynolds numbers. Data shown for D = 4.7 mm and Re = 5000 (○), 10,000 (■), and 20,000 (◊).

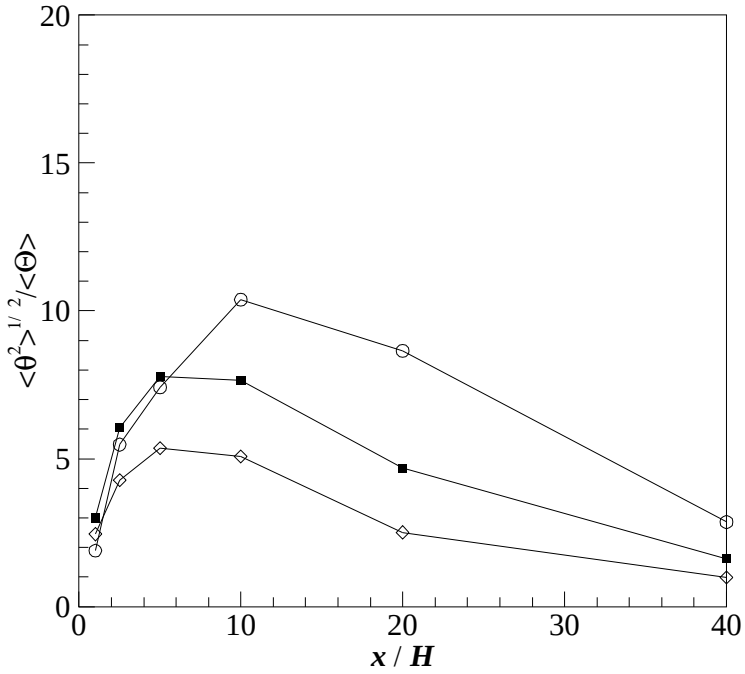

Figure 4.9 Ratio of standard deviation to average scalar concentration as a function of Reynolds number. Data shown for D = 4.7 mm and Re = 5000 (○), 10,000 (■), and 20,000 (◊).

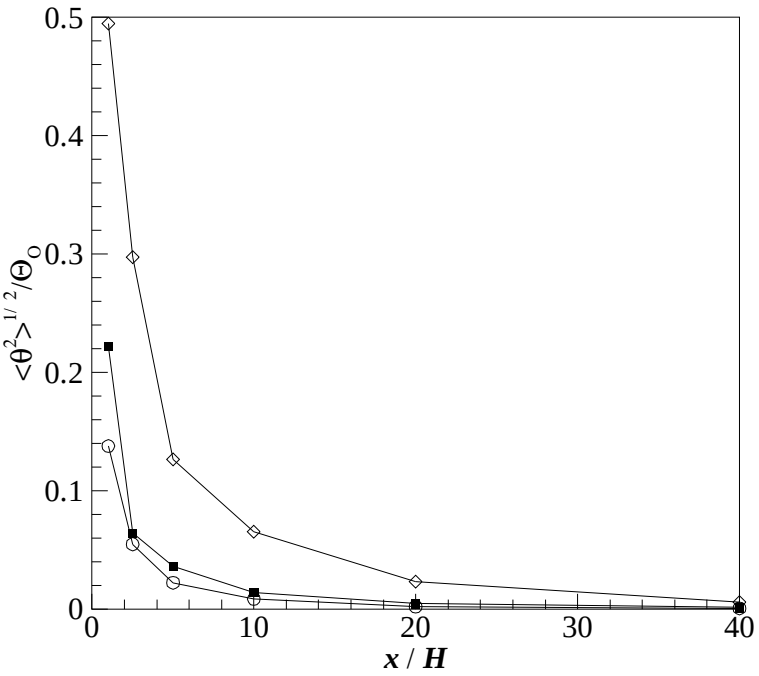

Figure 4.10 Centerline profile of standard deviation of scalar fluctuations as a function of source nozzle diameter. Data shown for Re = 10,000 and D = 2.2 mm (○), 4.7 mm (■), and 9.4 mm (◊).

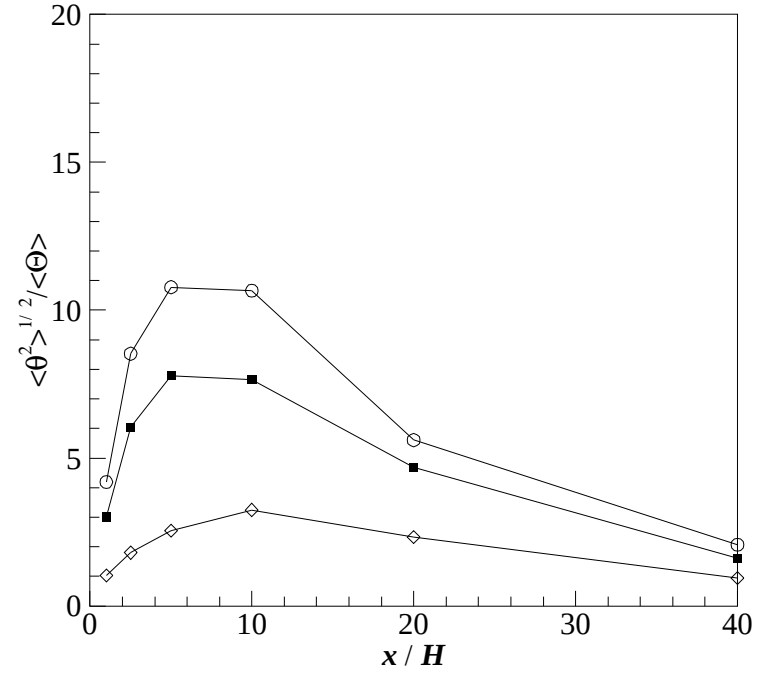

Figure 4.11 Ratio of standard deviation to average scalar concentration as a function of source nozzle diameter. Data shown for Re = 10,000 and D = 2.2 mm (○), 4.7 mm (■), and 9.4 mm (◊).

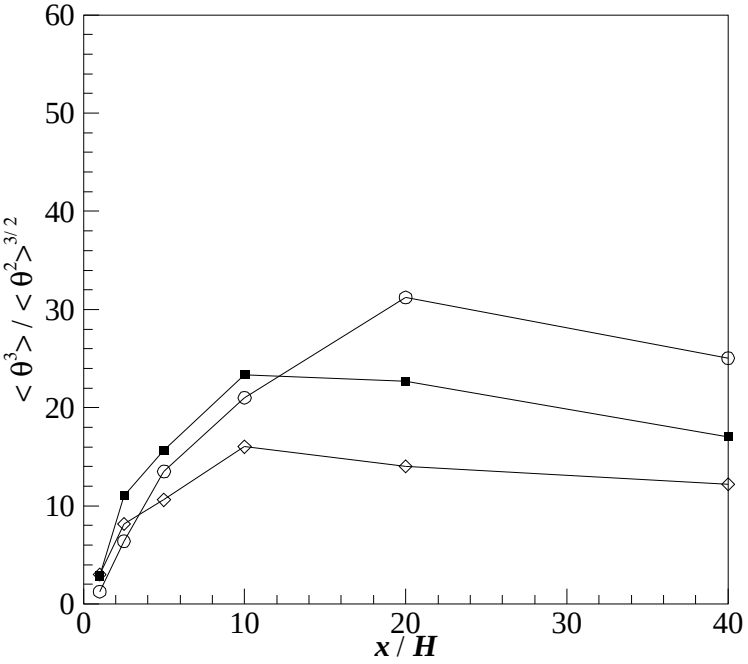

Figure 4.12 Centerline profile of skewness of the scalar fluctuations as a function of Reynolds number. Data shown for D = 4.7 mm and Re = 5000 (○), 10,000 (■), and 20,000 (◊).

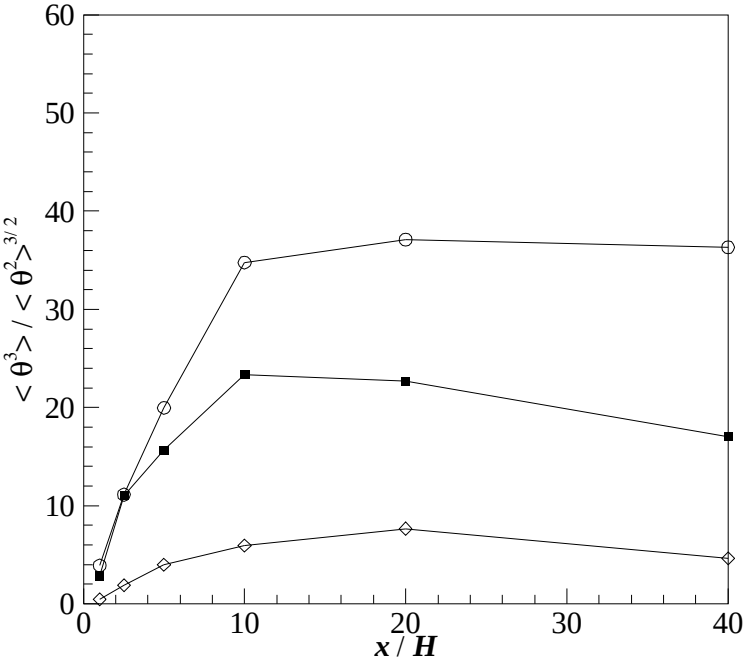

Figure 4.13 Centerline profile of skewness of the scalar fluctuations as a function of source nozzle diameter. Data shown for Re = 10,000 and D = 2.2 mm (○), 4.7 mm (■), and 9.4 mm (◊).

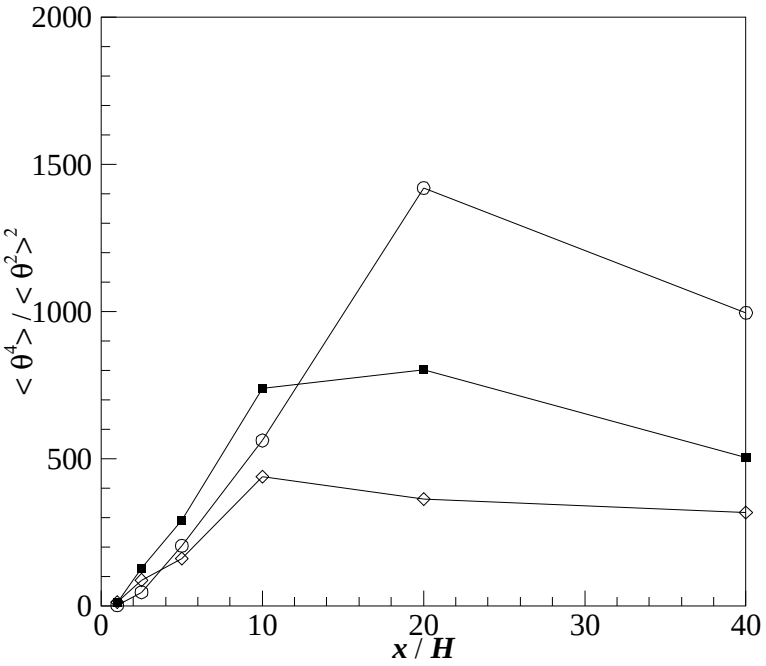

Figure 4.14 Centerline profile of kurtosis of the scalar fluctuations as a function of Reynolds number. Data shown for D = 4.7 mm and Re = 5000 (○), 10,000 (■), and 20,000 (◊).

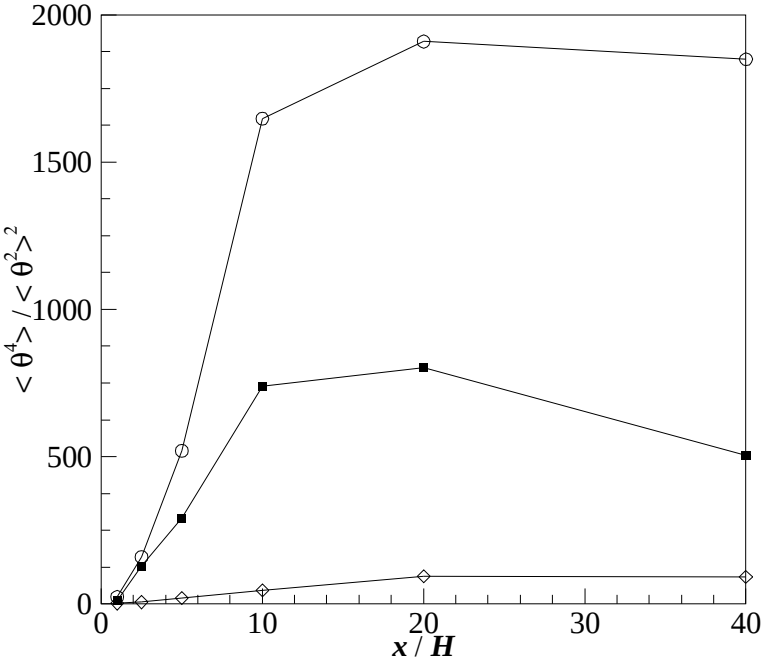

Figure 4.15 Centerline profile of kurtosis of the scalar fluctuations as a function of source nozzle diameter. Data shown for Re = 10,000 and D = 2.2 mm (○), 4.7 mm (■), and 9.4 mm (◊).

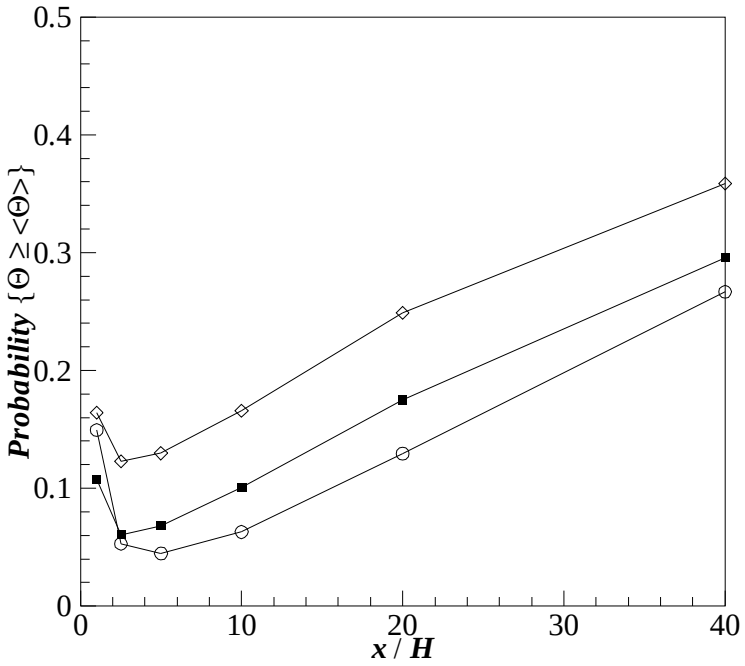

Figure 4.16 Centerline profile of the probability of the concentration exceeding the local average value as a function of Reynolds number. Data shown for D = 4.7 mm and Re = 5000 (○), 10,000 (■), and 20,000 (◊).

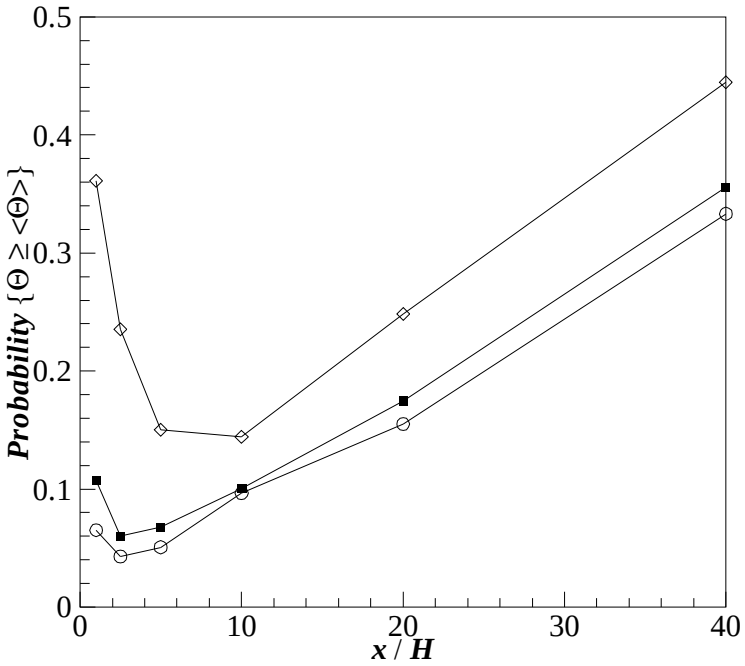

Figure 4.17 Centerline profile of the probability of the concentration exceeding the local average value as a function of source nozzle diameter. Data shown for Re = 10,000 and D = 2.2 mm (○), 4.7 mm (■), and 9.4 mm (◊).

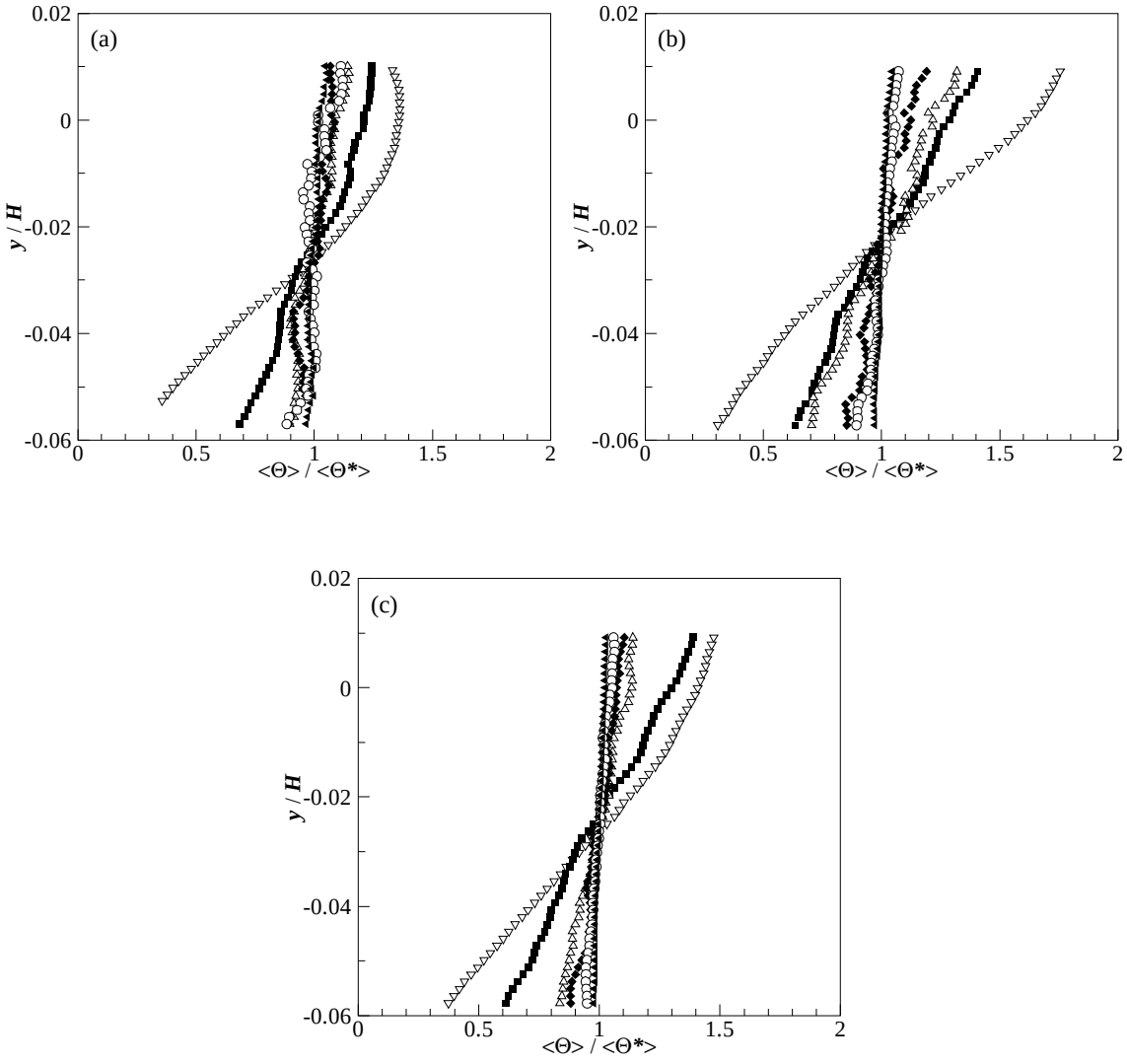

Figure 4.18 Locally normalized vertical concentration profiles for (a) Re **= 5000, (b) 10,000, and (c) 20,000. Data shown for** D **= 4.7 mm at** x **= 0.1 m (▽), 0.25 m (■), 0.5 m (△), 1 m (♦), 2 m (○), and 4 m (◄).**

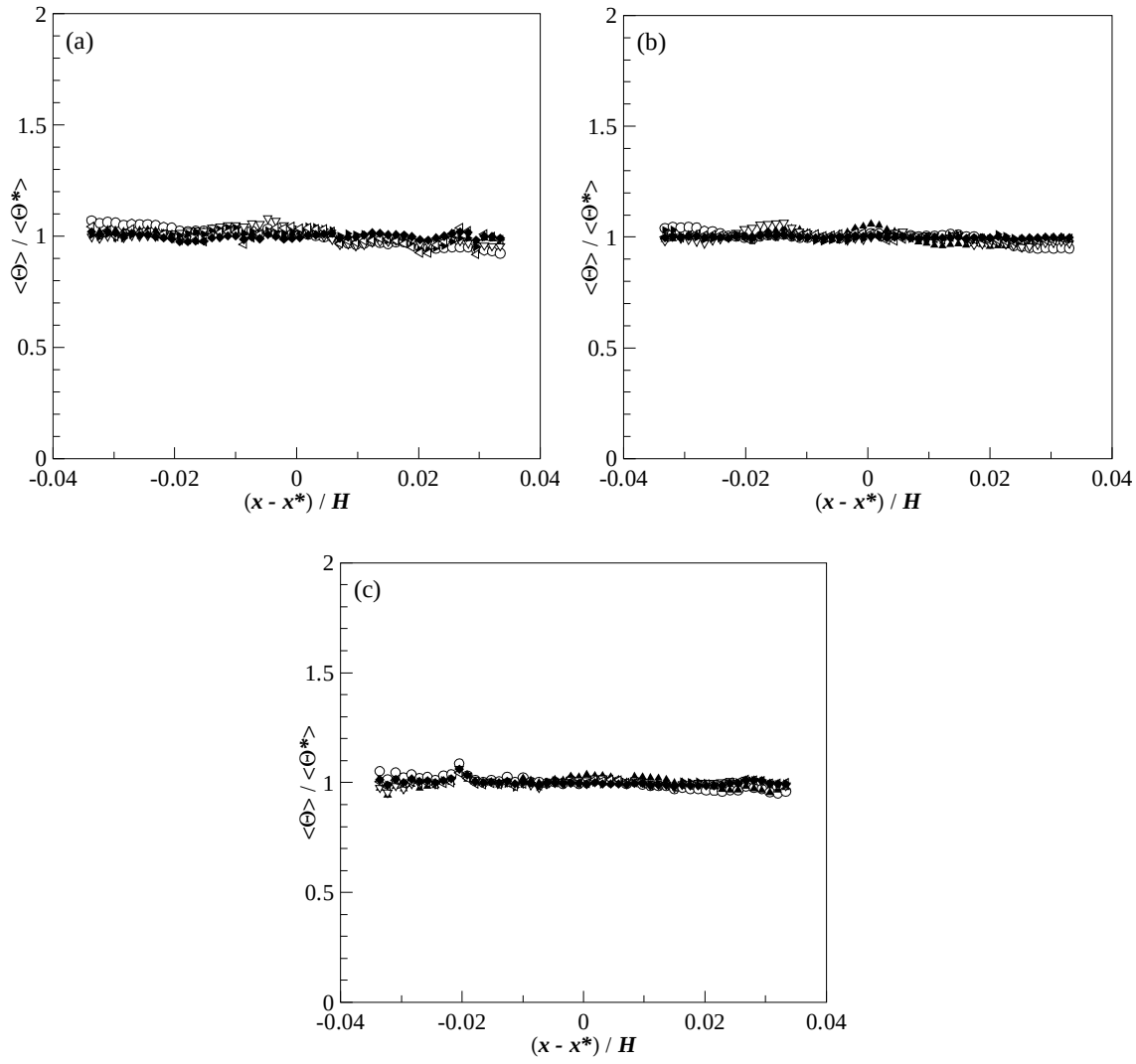

Figure 4.19 Locally normalized longitudinal concentration profiles for (a) *Re* **= 5000, (b) 10,000, and (c) 20,000. Data shown for** *D* **= 4.7 mm at** *x* **= 0.1 m (▽), 0.25 m (■), 0.5 m (△), 1 m (♦), 2 m (○), and 4 m (◀).**

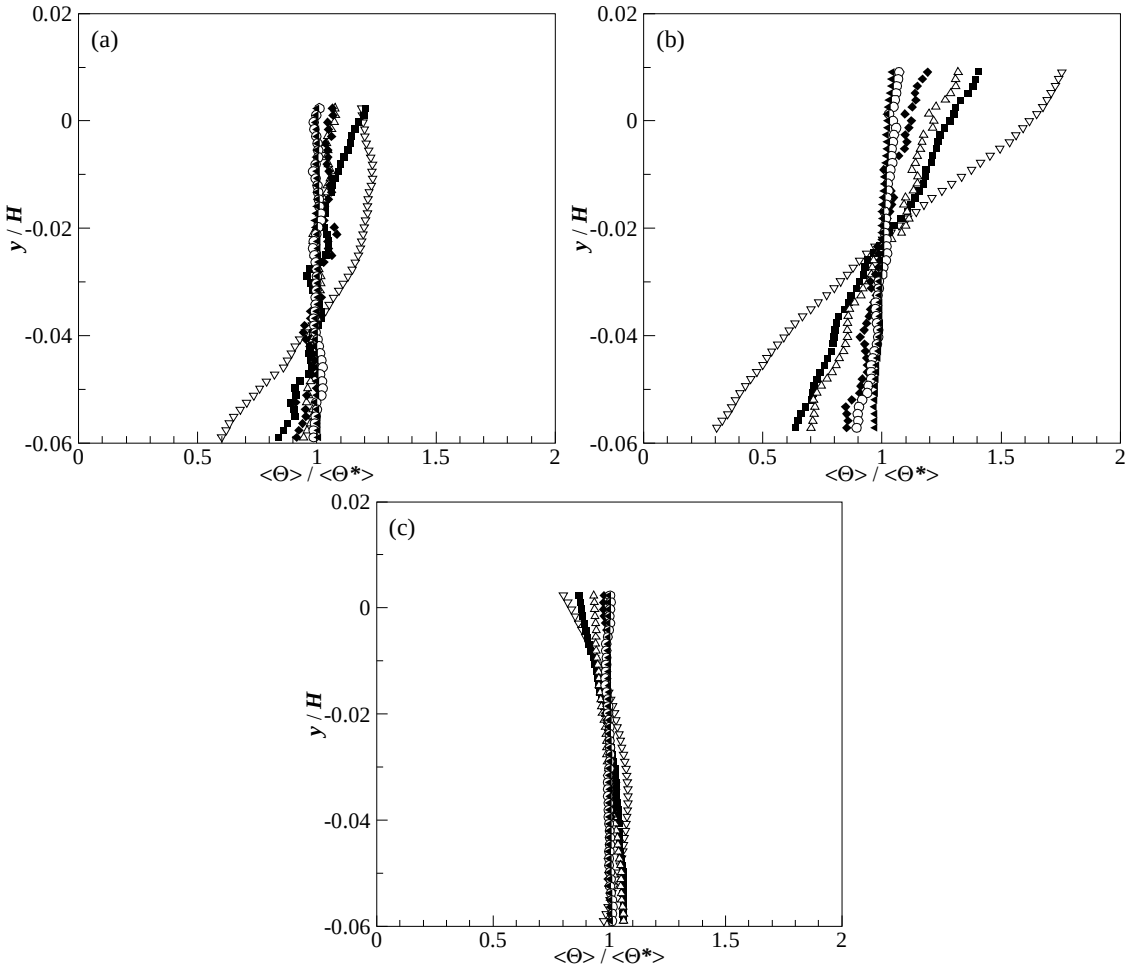

Figure 4.20 Locally normalized vertical concentration profiles for (a) D = 2.2 mm, (b) 4.7 mm, and (c) 9.4 mm. Data shown for Re = 10,000 at x = 0.1 m (▽), 0.25 m (■), 0.5 m (△), 1 m (♦), 2 m (○), and 4 m (◄).

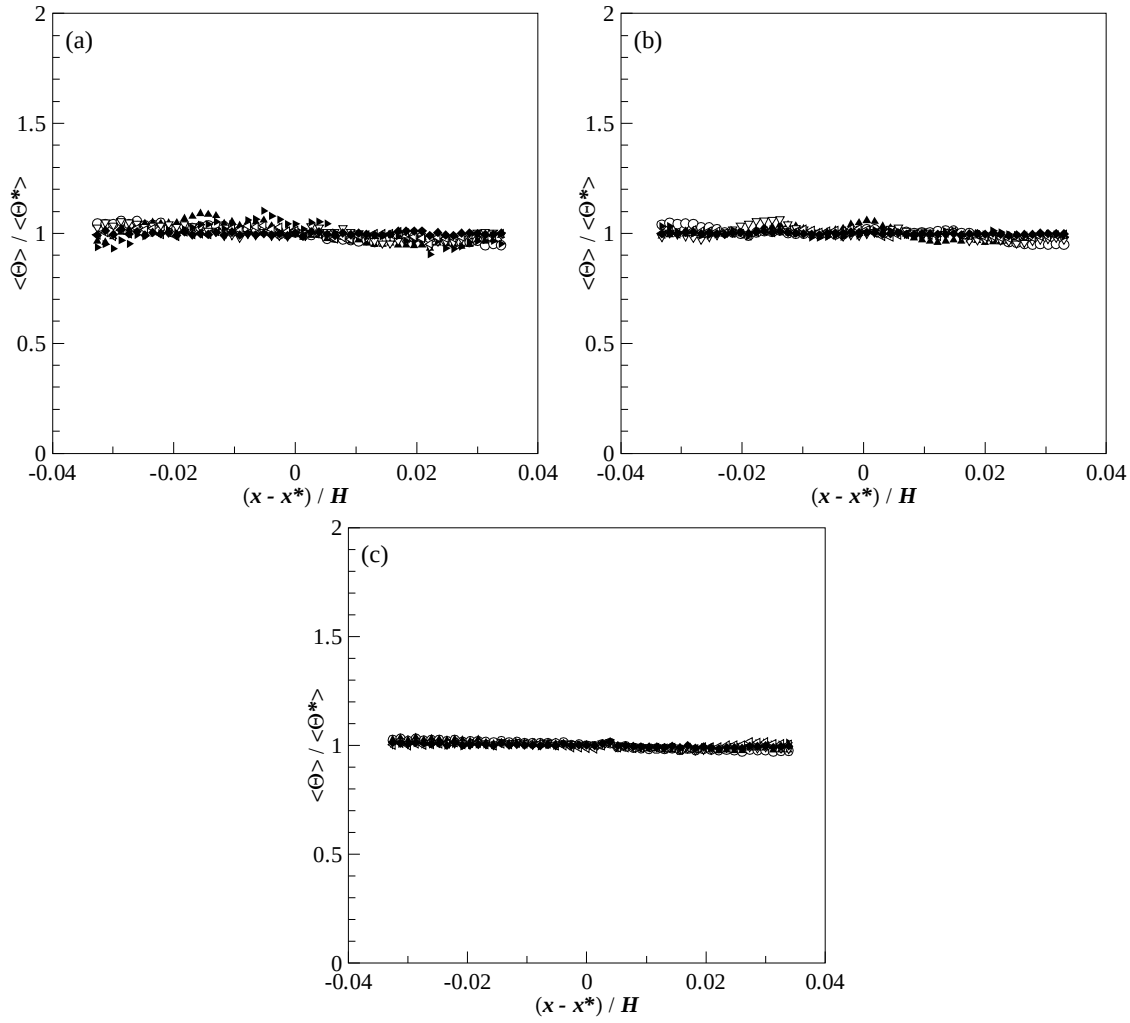

Figure 4.21 Locally normalized longitudinal concentration profiles for (a) D **= 2.2 mm, (b) 4.7 mm, and (c) 9.4 mm. Data shown for** Re **= 10,000 at** x **= 0.1 m (▽), 0.25 m (■), 0.5 m (△), 1 m (♦), 2 m (○), and 4 m (◀).**

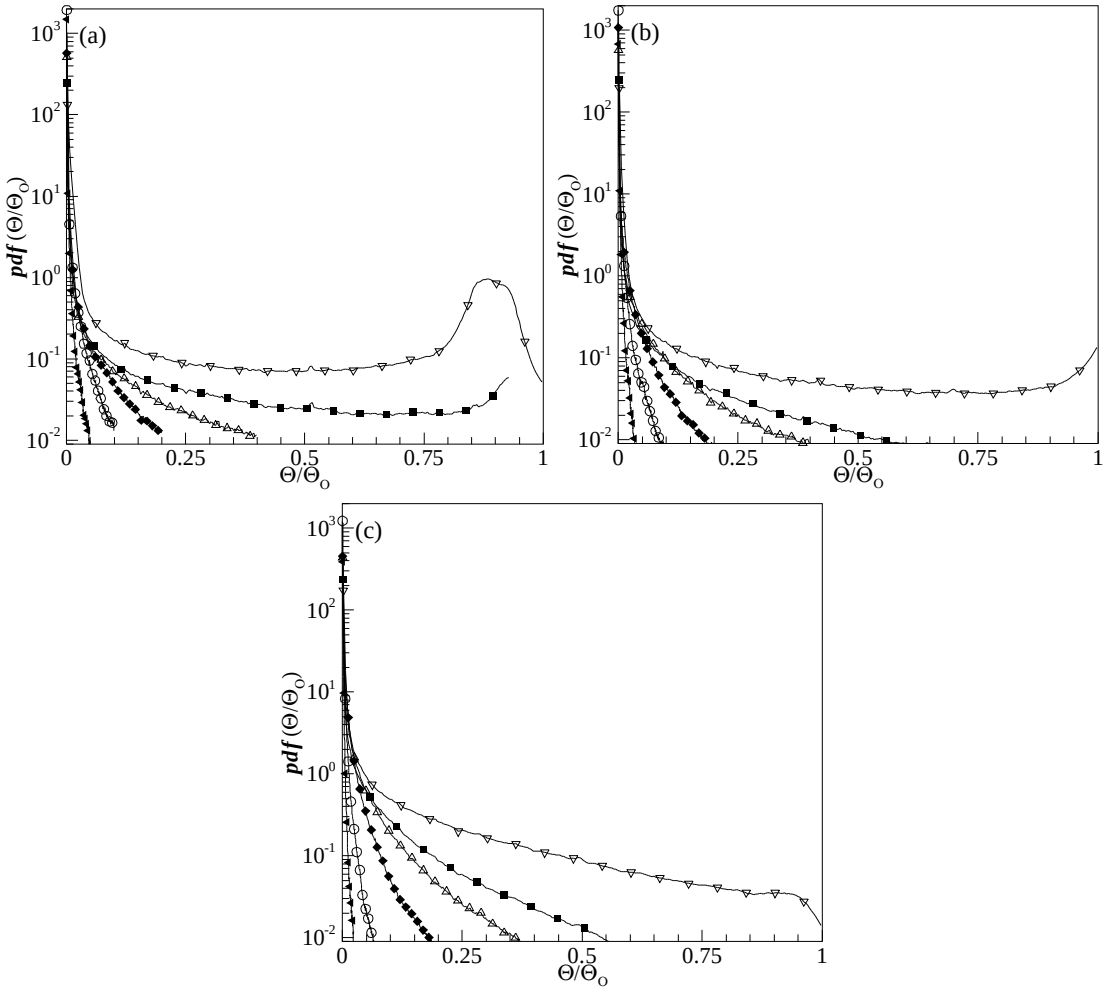

Figure 4.22 Probability density function of scalar concentration for (a) Re **= 5000, (b) 10,000, and (c) 20,000. Data shown for** D **= 4.7 mm at** x **= 0.1 m (▽), 0.25 m (■), 0.5 m (△), 1 m (♦), 2 m (○), and 4 m (◀).**

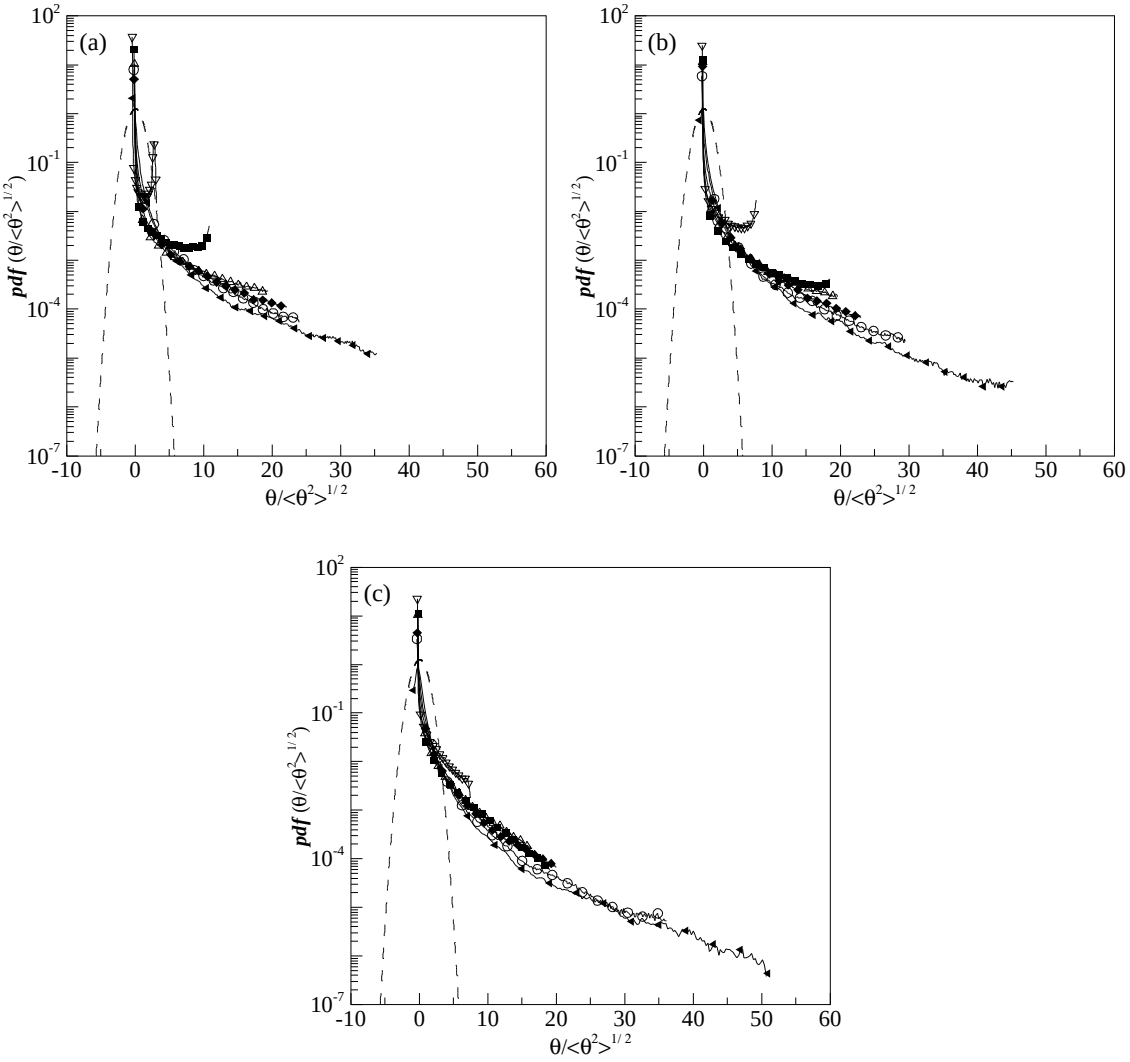

Figure 4.23 Probability density function of scalar fluctuation normalized by the standard deviation for (a) Re = 5000, (b) 10,000, and (c) 20,000. Data shown for D = 4.7 mm at x = 0.1 m (▽), 0.25 m (■), 0.5 m (△), 1 m (♦), 2 m (○), and 4 m (◀). Dashed line represents the standard normal distribution.

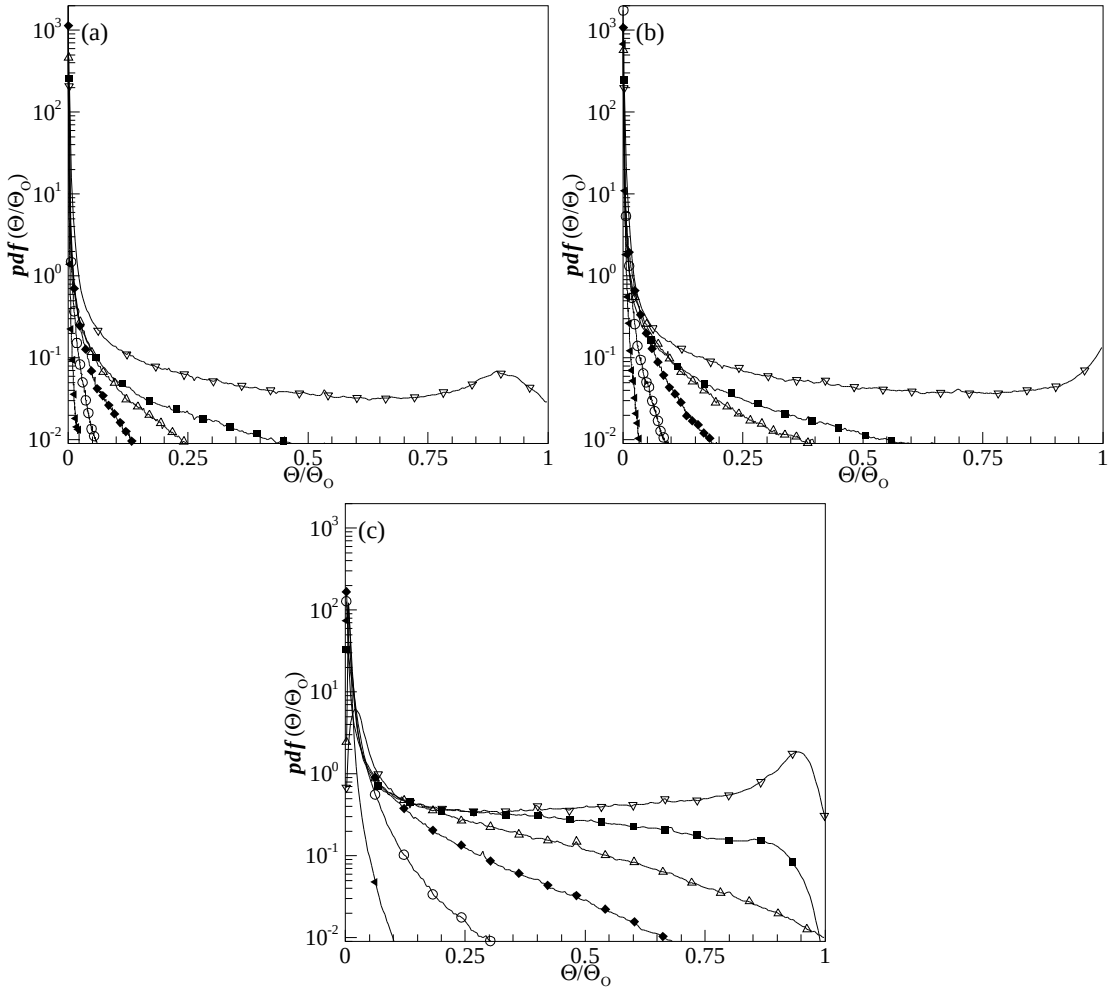

Figure 4.24 Probability density function of scalar concentration for (a) D **= 2.2 mm, (b) 4.7 mm, and (c) 9.4 mm. Data shown for** Re **= 10,000 at** x **= 0.1 m (▽), 0.25 m (■), 0.5 m (△), 1 m (♦), 2 m (○), and 4 m (◀).**

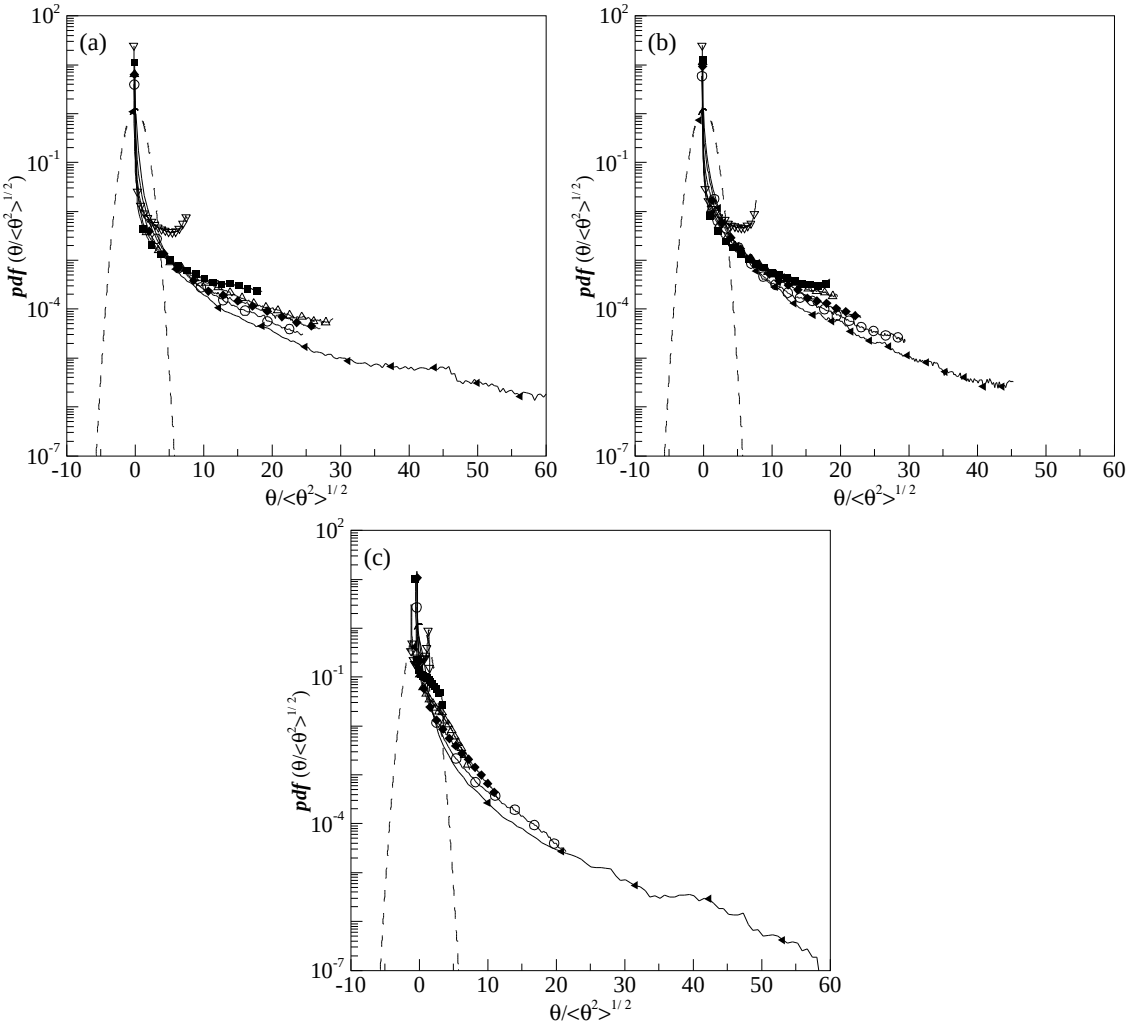

Figure 4.25 Probability density function of the scalar fluctuations normalized by the standard deviation for (a) D = 2.2 mm, (b) 4.7 mm, and (c) 9.4 mm. Data shown for Re = 10,000 at x = 0.1 m (▽), 0.25 m (■), 0.5 m (△), 1 m (♦), 2 m (○), and 4 m (◄). Dashed line represents the standard normal distribution.

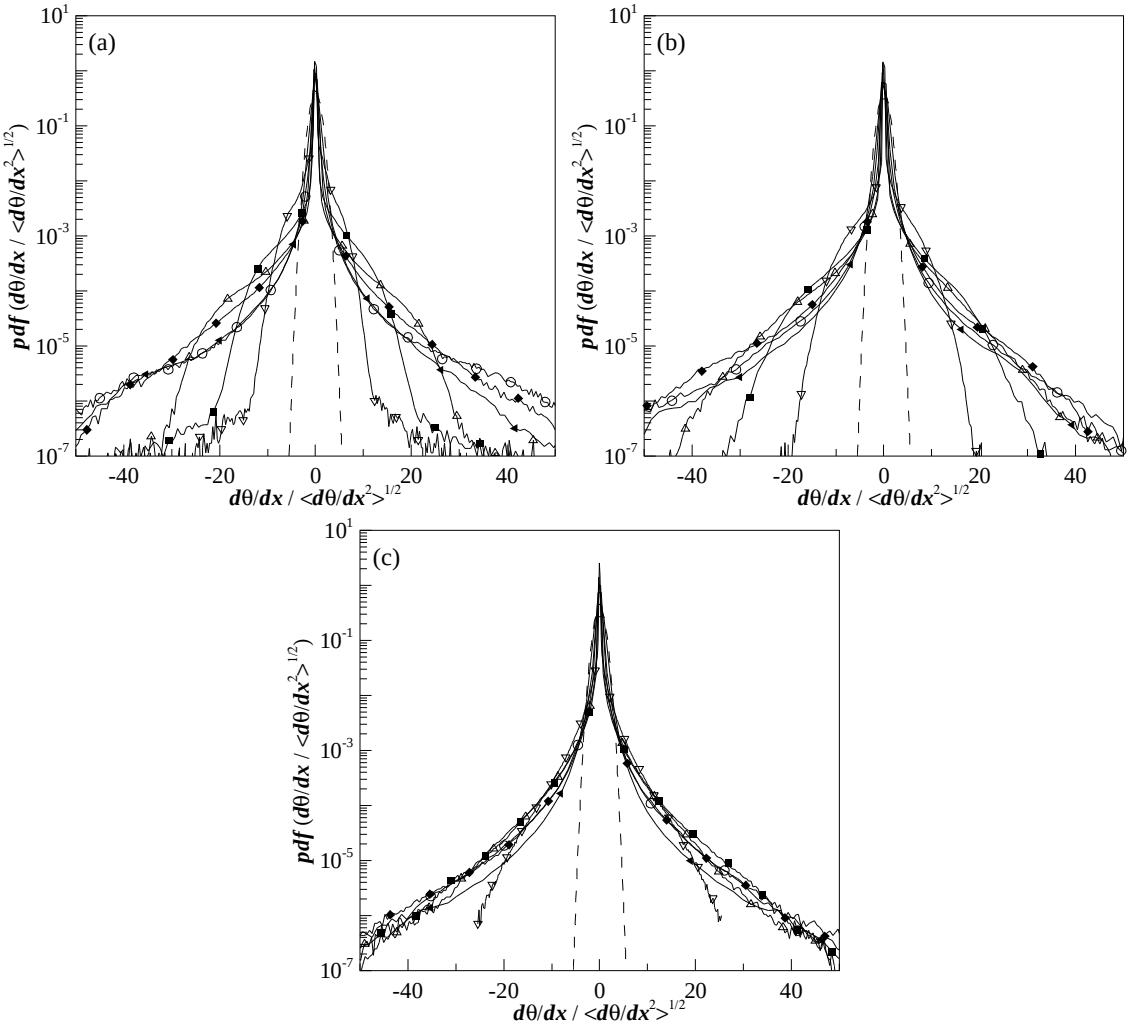

Figure 4.26 Probability density function of the longitudinal scalar gradient fluctuations normalized by the standard deviation for (a) Re **= 5000, (b) 10,000, and (c) 20,000. Data shown for** D **= 4.7 mm at** x **= 0.1 m (▽), 0.25 m (■), 0.5 m (△), 1 m (♦), 2 m (○), and 4 m (◀). The dashed line corresponds to a Gaussian distribution.**

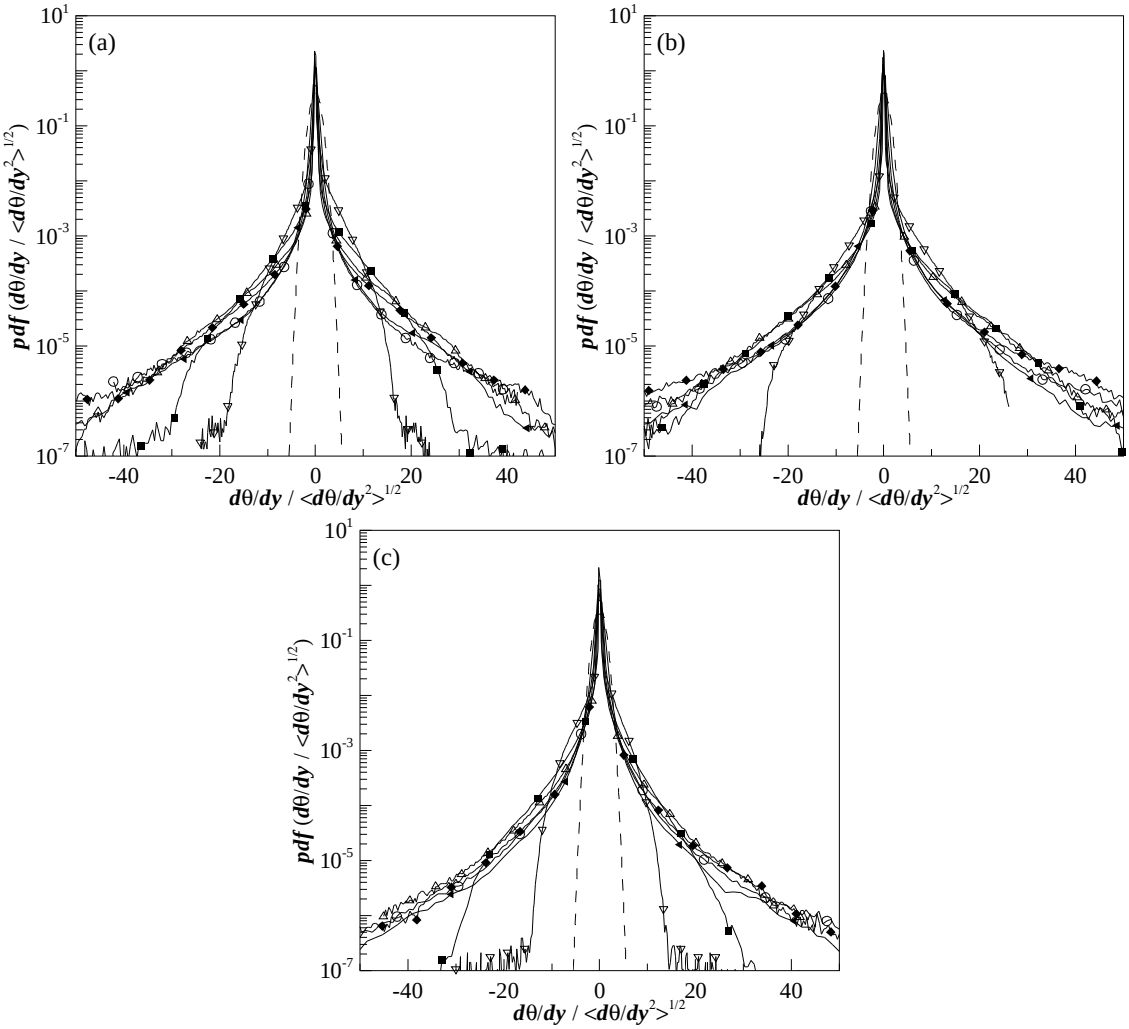

Figure 4.27 Probability density function of the vertical scalar gradient fluctuations normalized by the standard deviation for (a) Re **= 5000, (b) 10,000, and (c) 20,000. Data shown for** D **= 4.7 mm at** x **= 0.1 m (▽), 0.25 m (■), 0.5 m (△), 1 m (♦), 2 m (○), and 4 m (◄). The dashed line corresponds to a Gaussian distribution.**

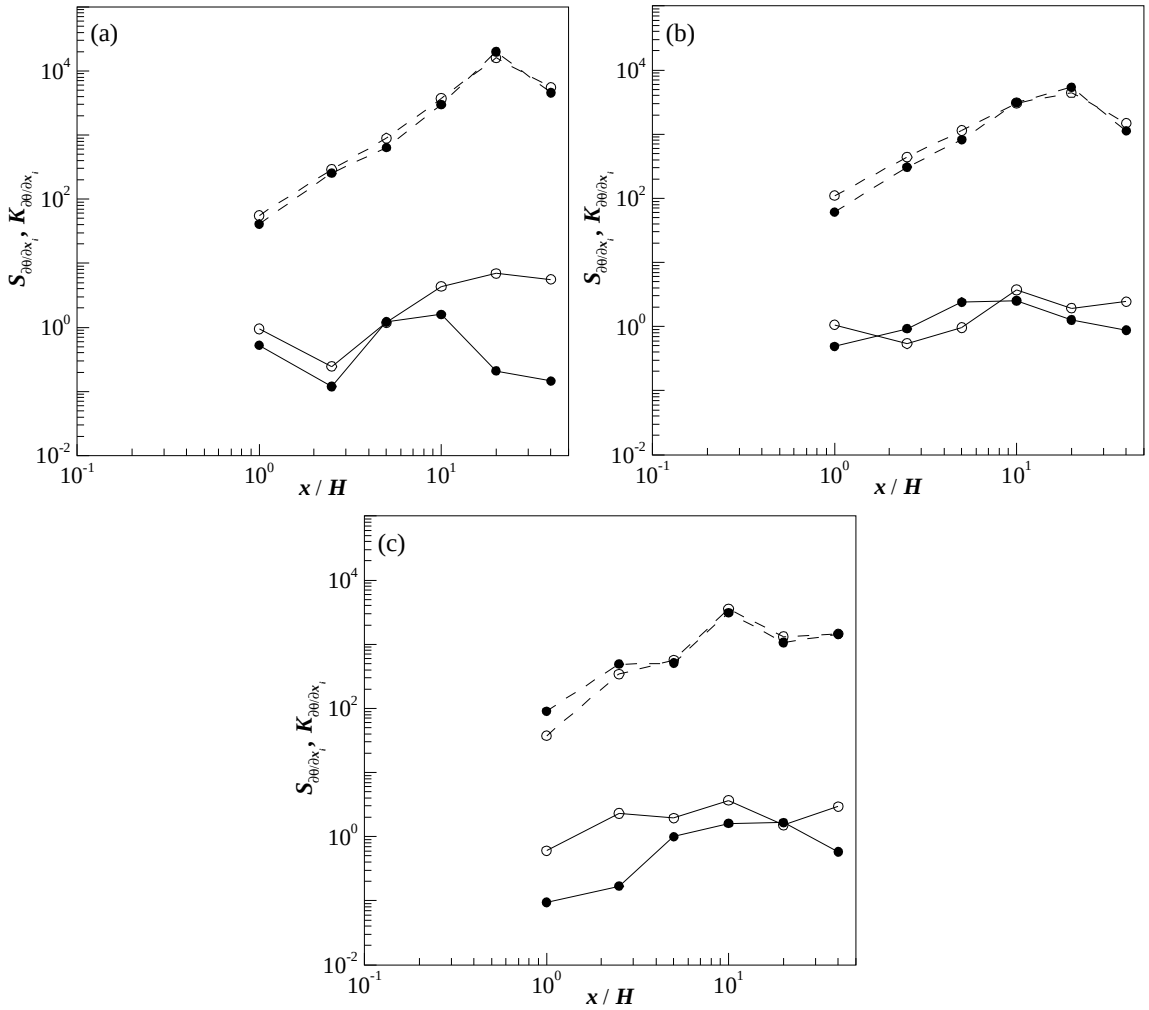

Figure 4.28 Skewness and kurtosis of the scalar gradient components as a function of downstream distance for (a) Re **= 5000, (b) 10,000, and (c) 20,000. Data shown for** D **= 4.7 mm. The filled circles indicate the longitudinal component and the open circles indicate the vertical component. The dashed line indicates the kurtosis and the continuous line indicates the skewness.**

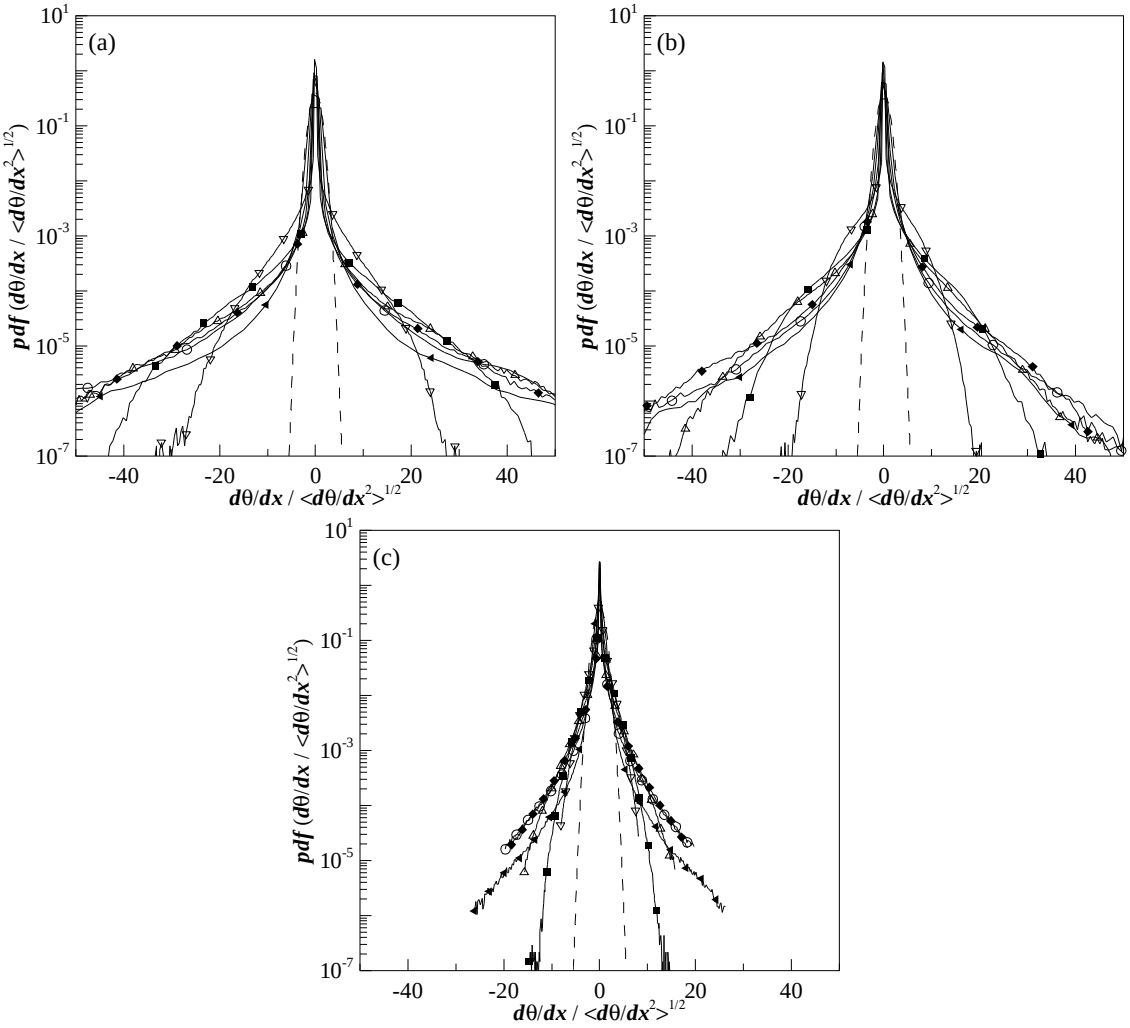

Figure 4.29 Probability density function of the longitudinal scalar gradient fluctuations normalized by the standard deviation for (a) D **= 2.2 mm, (b) 4.7 mm, and (c) 9.4 mm. Data shown for** Re **= 10,000 at** x **= 0.1 m (▽), 0.25 m (■), 0.5 m (△), 1 m (♦), 2 m (○), and 4 m (◀). The dashed line corresponds to a Gaussian distribution.**

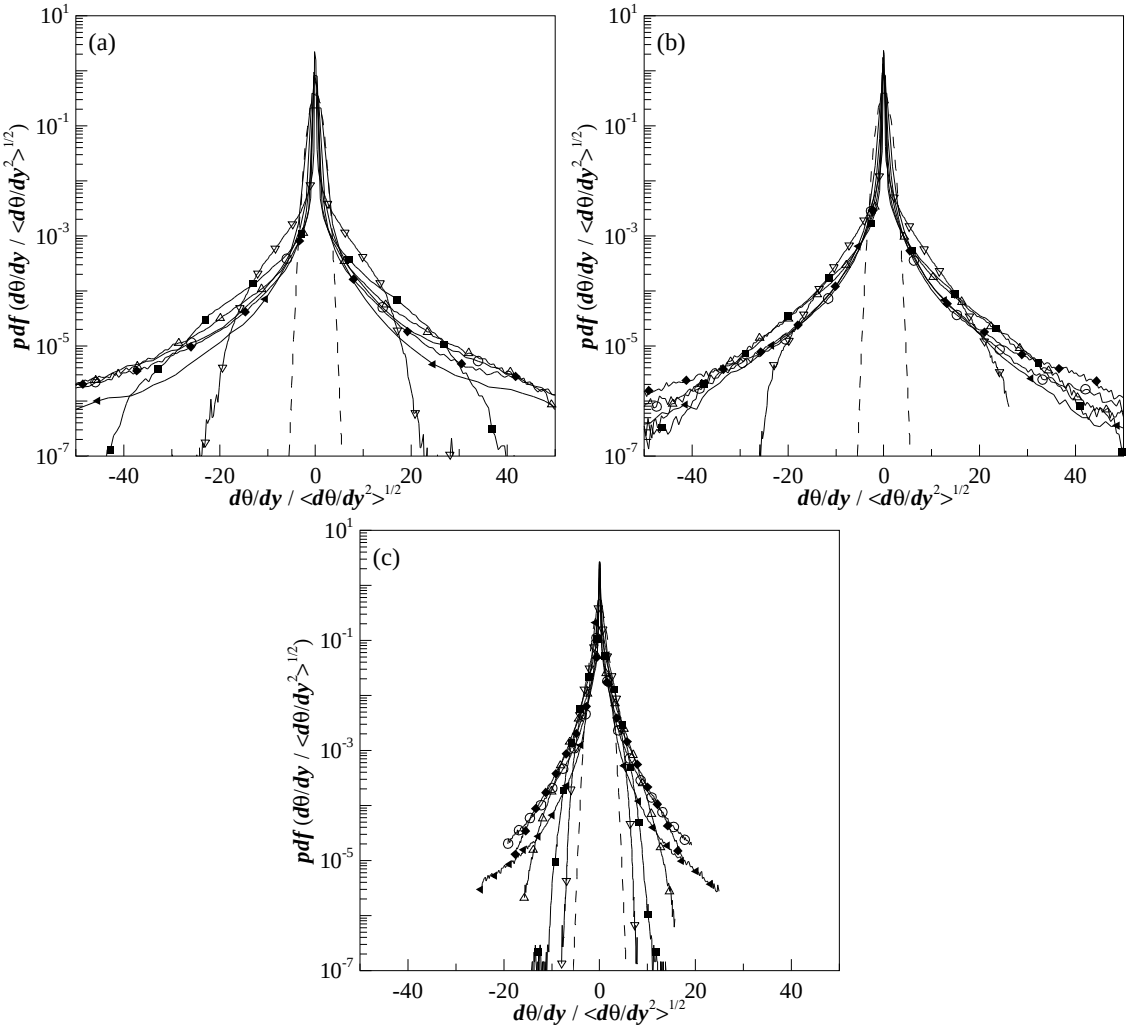

Figure 4.30 Probability density function of the vertical scalar gradient fluctuations normalized by the standard deviation for (a) D = 2.2 mm, (b) 4.7 mm, and (c) 9.4 mm. Data shown for Re = 10,000 at x = 0.1 m (▽), 0.25 m (■), 0.5 m (△), 1 m (♦), 2 m (○), and 4 m (◄). The dashed line corresponds to a Gaussian distribution.

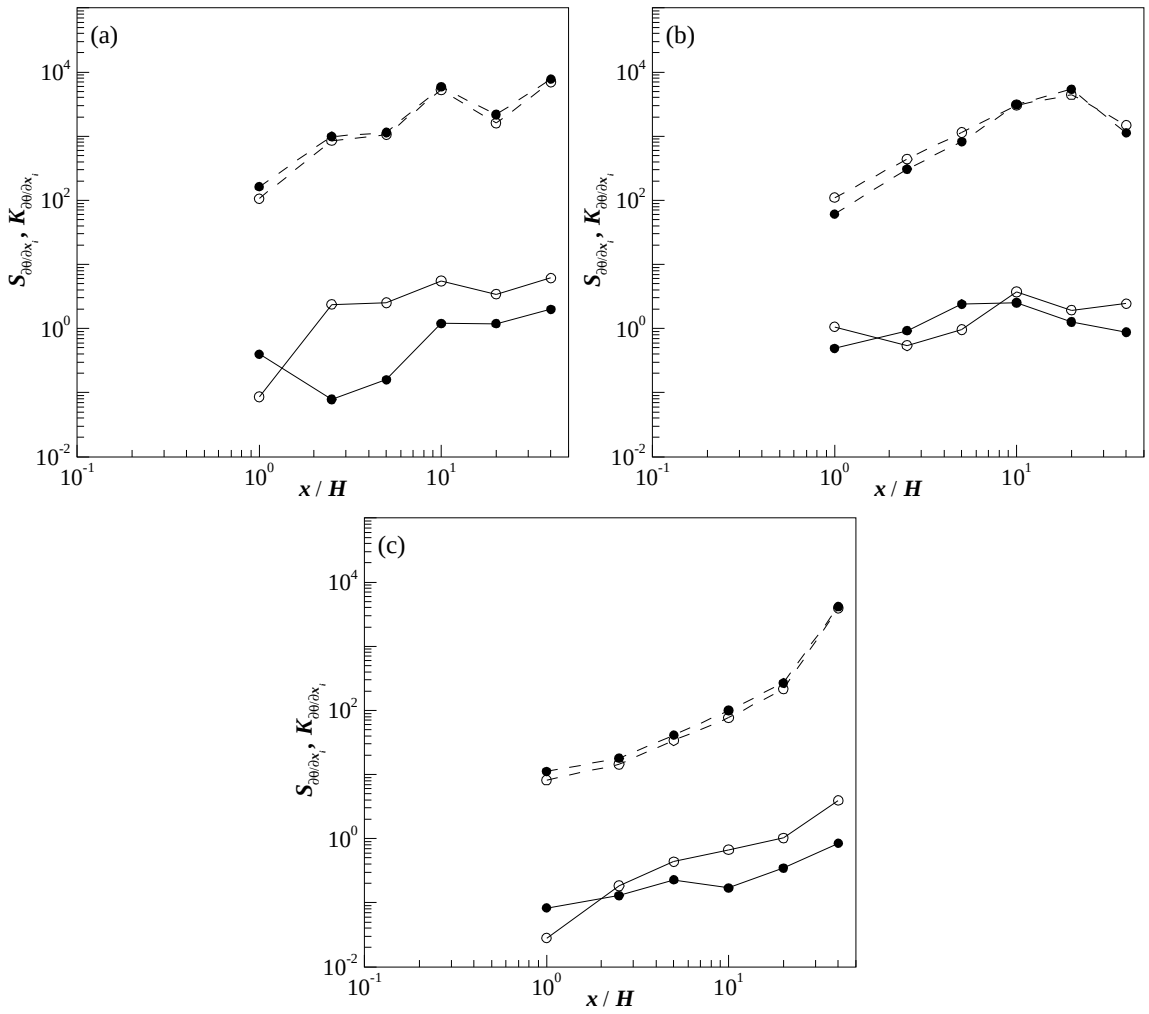

Figure 4.31 Skewness and kurtosis of the scalar gradient components as a function of downstream distance for (a) D = 2.2 mm, (b) 4.7 mm, and (c) 9.4 mm. Data shown for Re = 10,000. The filled circles indicate the longitudinal component and the open circles indicate the vertical component. The dashed line indicates the kurtosis and the continuous line indicates the skewness.

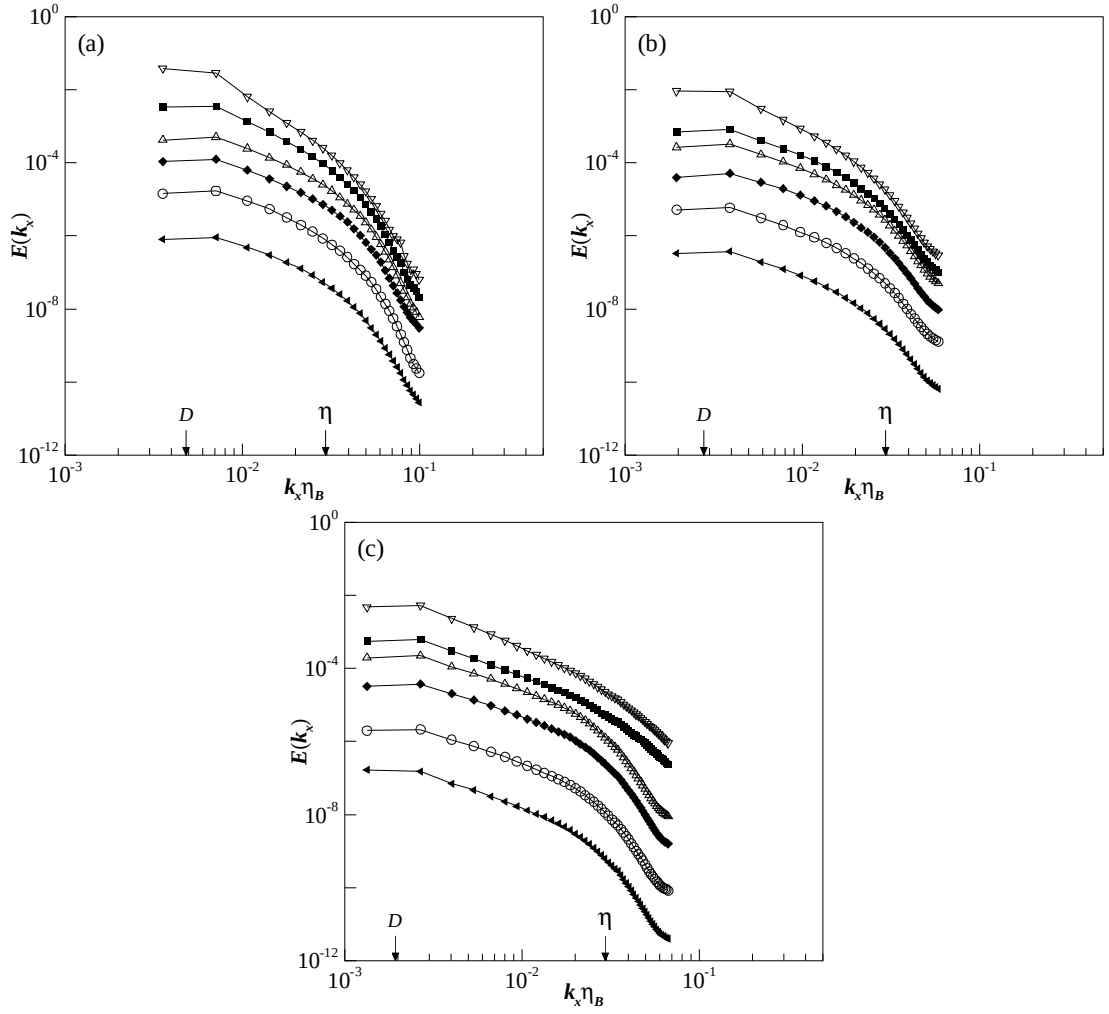

Figure 4.32 Longitudinal spectra of the fluctuating scalar field for (a) Re **= 5000, (b) 10,000, and (c) 20,000. Data shown for** D **= 4.7 mm at** x **= 0.1 m (▽), 0.25 m (■), 0.5 m (△), 1 m (♦), 2 m (○), and 4 m (◀).**

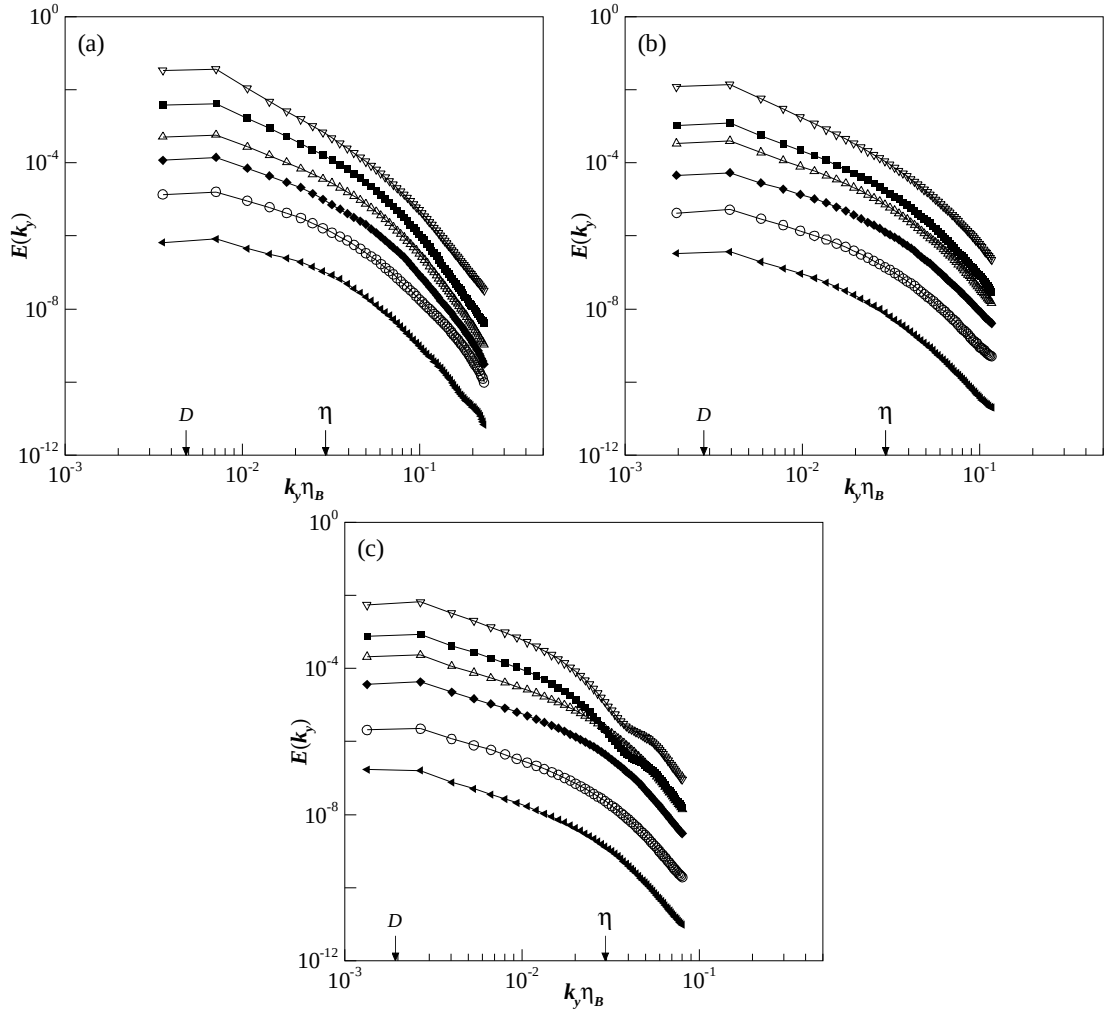

Figure 4.33 Vertical spectra of the fluctuating scalar field for (a) Re **= 5000, (b) 10,000, and (c) 20,000. Data shown for** D **= 4.7 mm at** x **= 0.1 m (▽), 0.25 m (■), 0.5 m (△), 1 m (♦), 2 m (○), and 4 m (◀).**

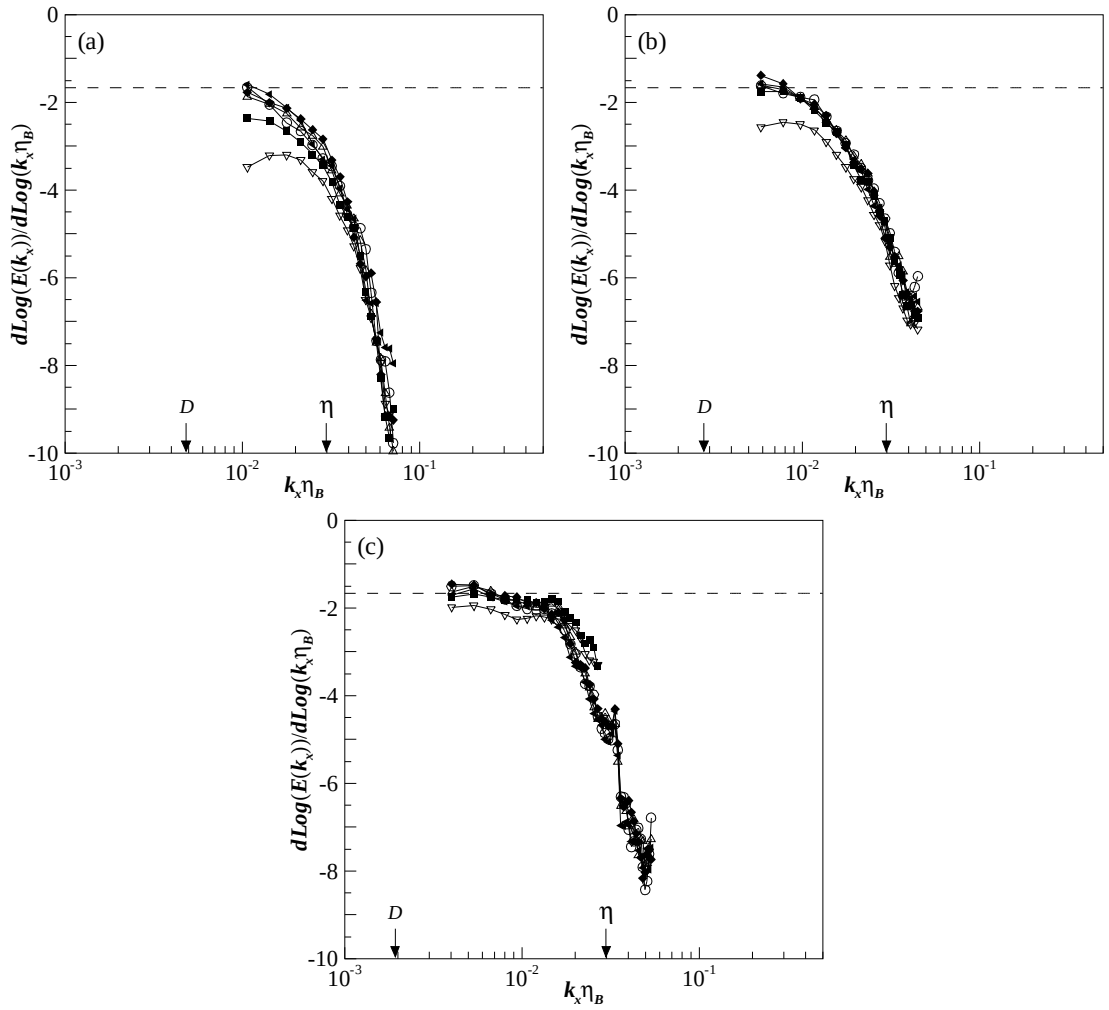

Figure 4.34 Logarithmic derivative of the longitudinal spectra of the fluctuating scalar field for (a) Re **= 5000, (b) 10,000, and (c) 20,000. Data shown for** D **= 4.7 mm at** x **= 0.1 m (▽), 0.25 m (■), 0.5 m (△), 1 m (♦), 2 m (○), and 4 m (◀).**

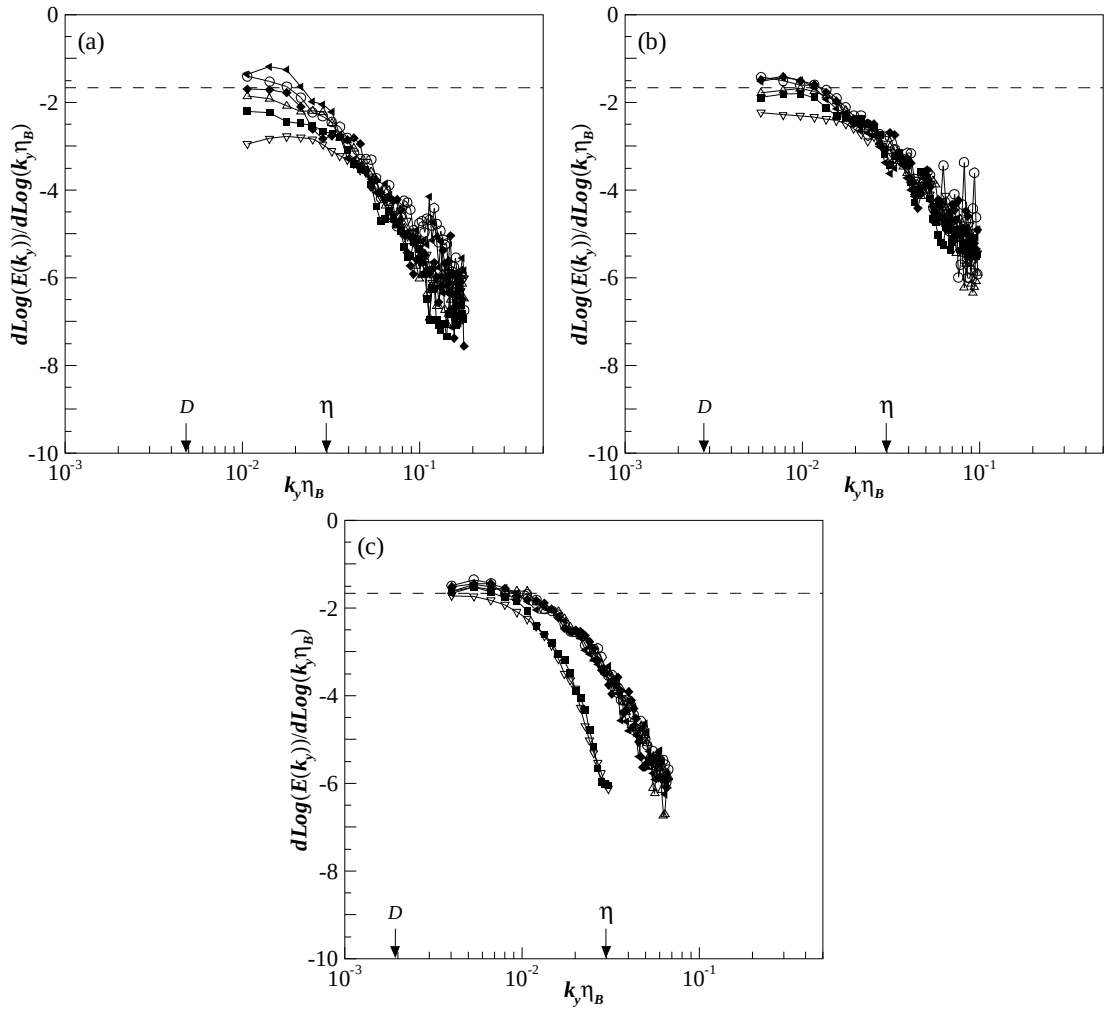

Figure 4.35 Logarithmic derivative of the vertical spectra of the fluctuating scalar field for (a) Re **= 5000, (b) 10,000, and (c) 20,000. Data shown for** D **= 4.7 mm at** x **= 0.1 m (▽), 0.25 m (■), 0.5 m (△), 1 m (♦), 2 m (○), and 4 m (◀).**

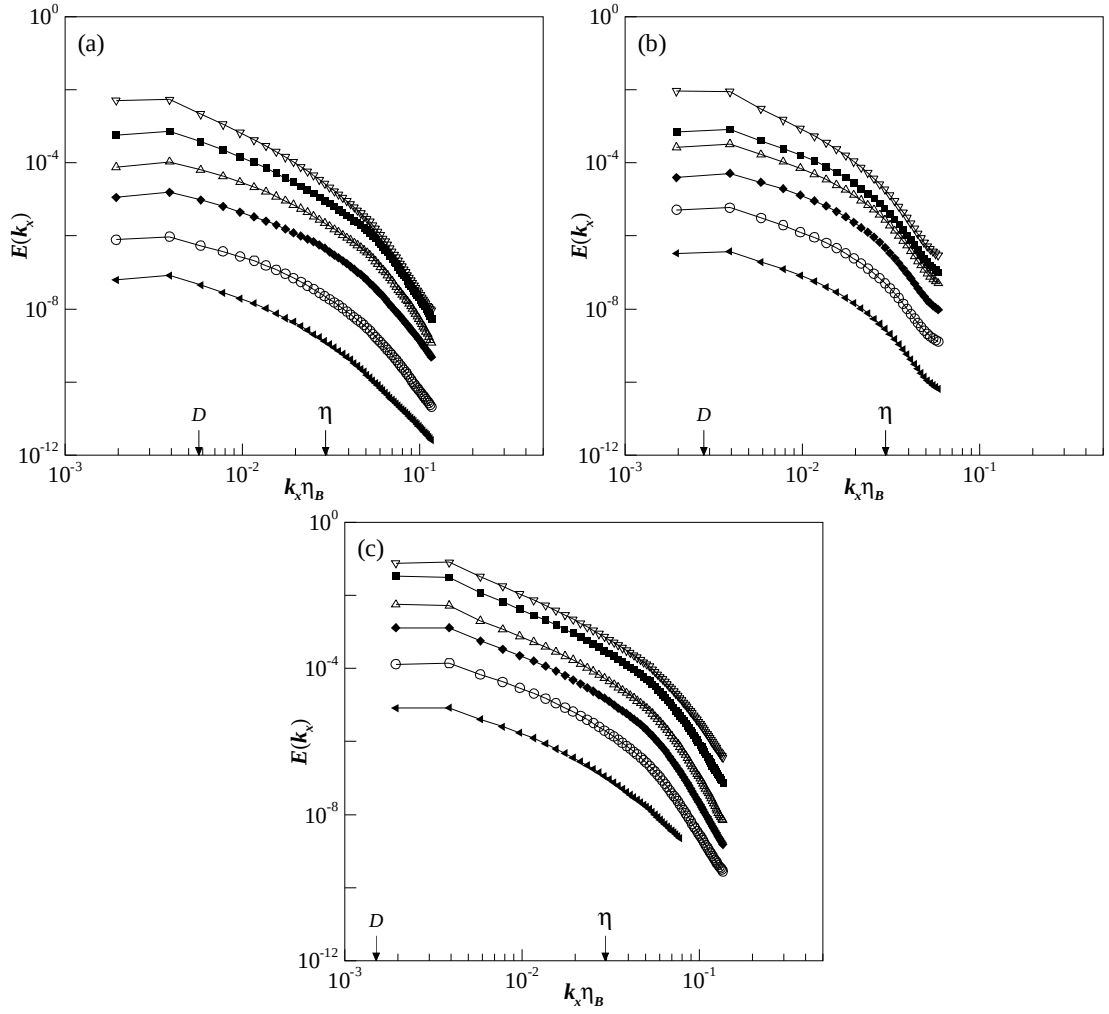

Figure 4.36 Longitudinal spectra of the fluctuating scalar field for (a) D **= 2.2 mm, (b) 4.7 mm, and (c) 9.4 mm. Data shown for** Re **= 10,000 at** x **= 0.1 m (▽), 0.25 m (■), 0.5 m (△), 1 m (♦), 2 m (○), and 4 m (◀).**

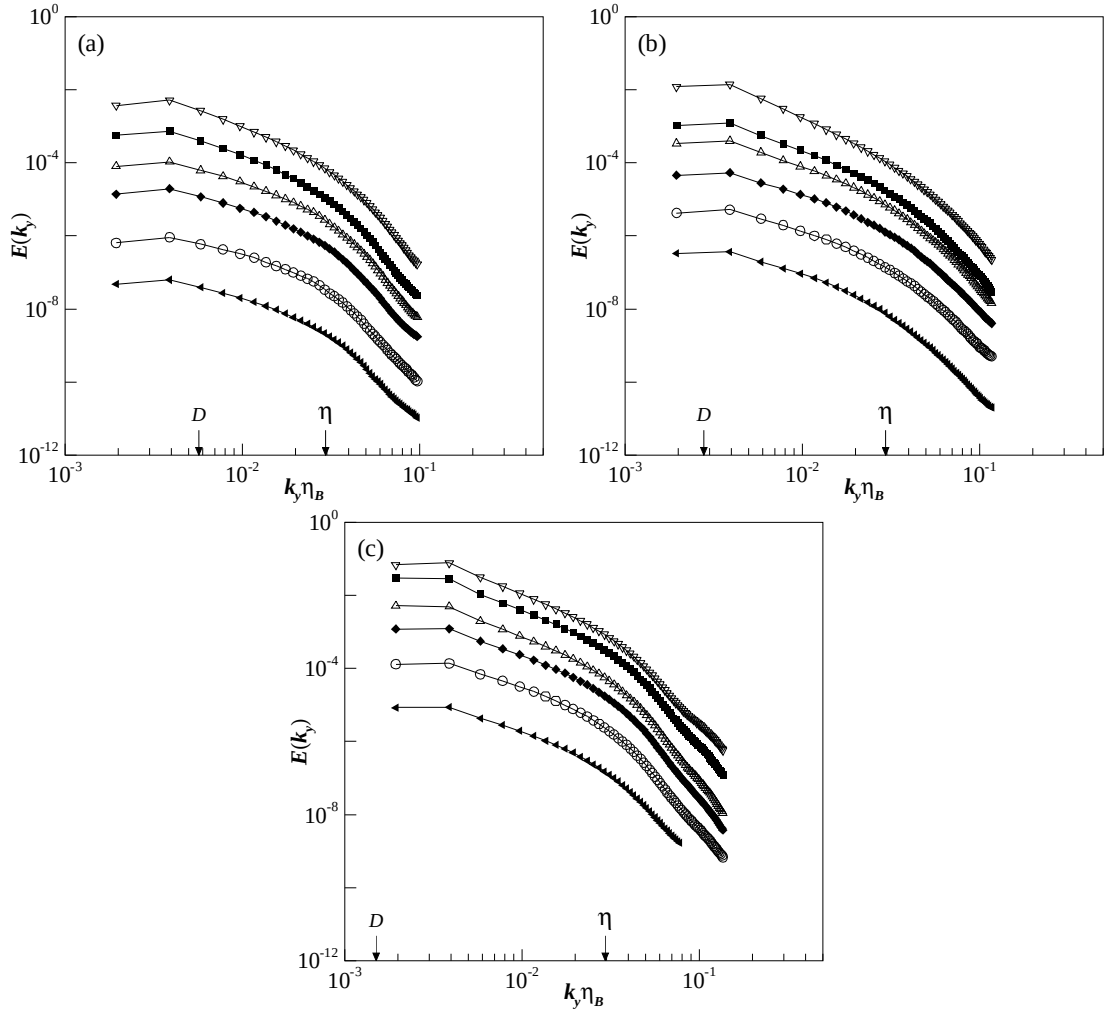

Figure 4.37 Vertical spectra of the fluctuating scalar field for (a) D = 2.2 mm, (b) 4.7 mm, and (c) 9.4 mm. Data shown for Re = 10,000 at x = 0.1 m (▽), 0.25 m (■), 0.5 m (△), 1 m (♦), 2 m (○), and 4 m (◀).

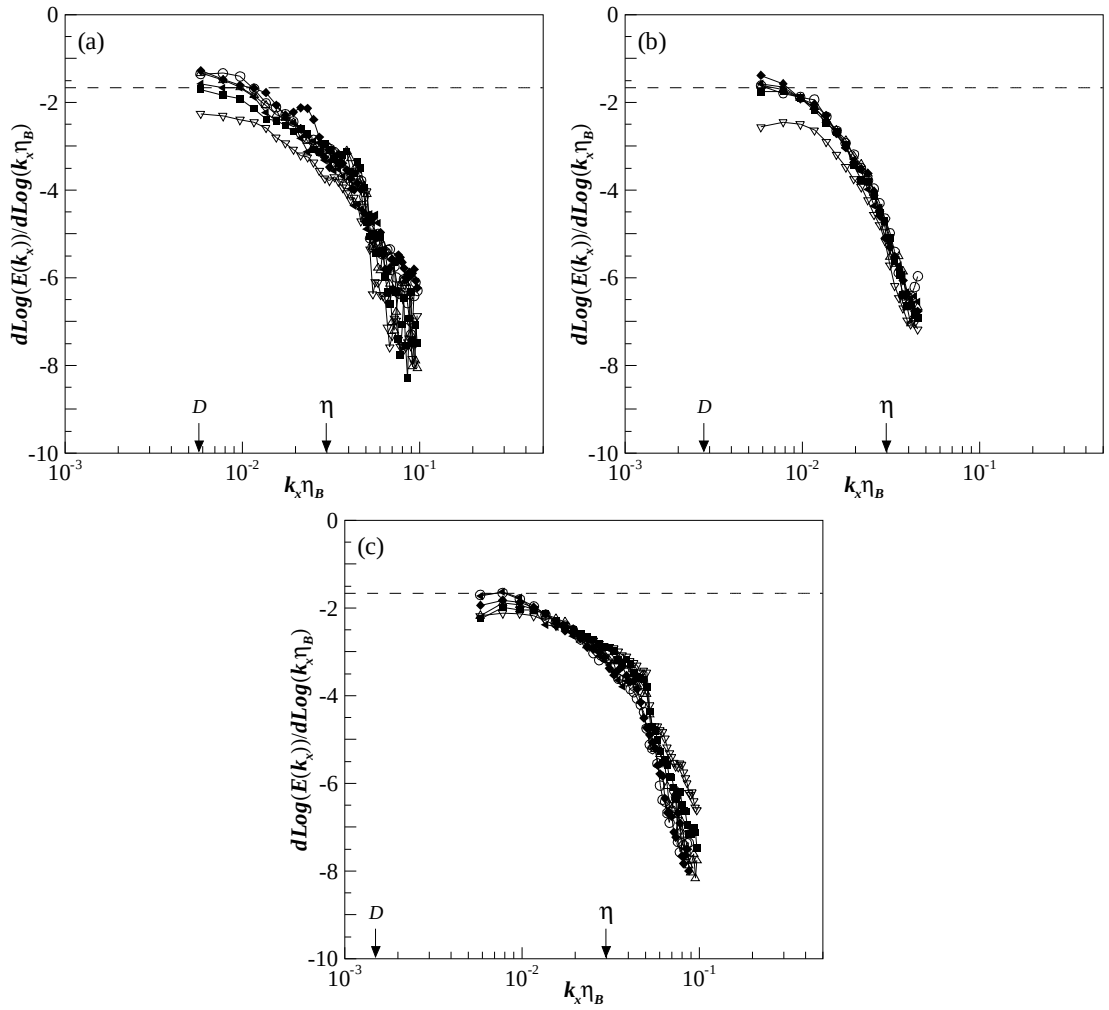

Figure 4.38 Logarithmic derivative of the longitudinal spectra of the fluctuating scalar field for (a) D **= 2.2 mm, (b) 4.7 mm, and (c) 9.4 mm. Data shown for** Re **= 10,000 at** x **= 0.1 m (▽), 0.25 m (■), 0.5 m (△), 1 m (♦), 2 m (○), and 4 m (◀).**

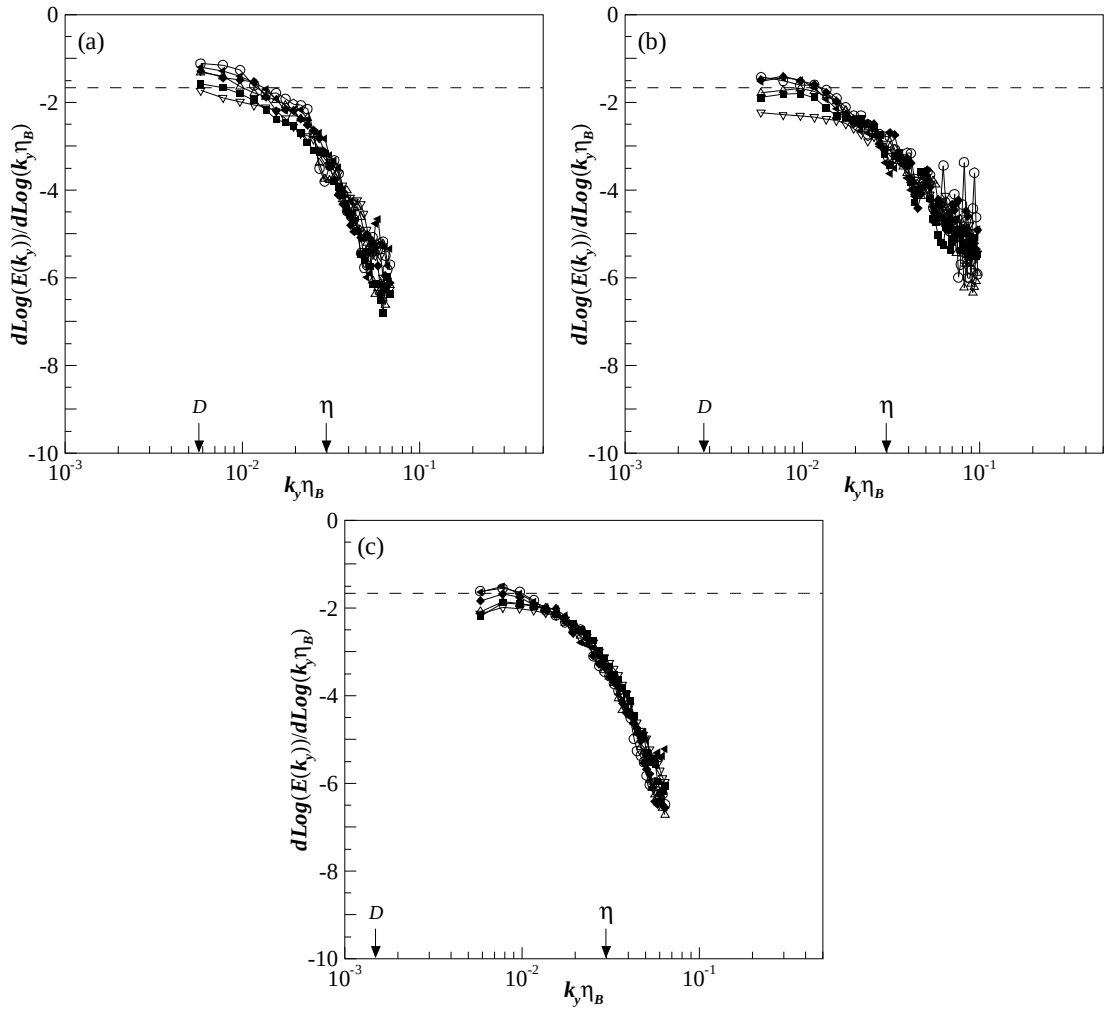

Figure 4.39 Logarithmic derivative of the vertical spectra of the fluctuating scalar field for (a) D = 2.2 mm, (b) 4.7 mm, and (c) 9.4 mm. Data shown for Re = 10,000 at x = 0.1 m (▽), 0.25 m (■), 0.5 m (△), 1 m (♦), 2 m (○), and 4 m (◀).

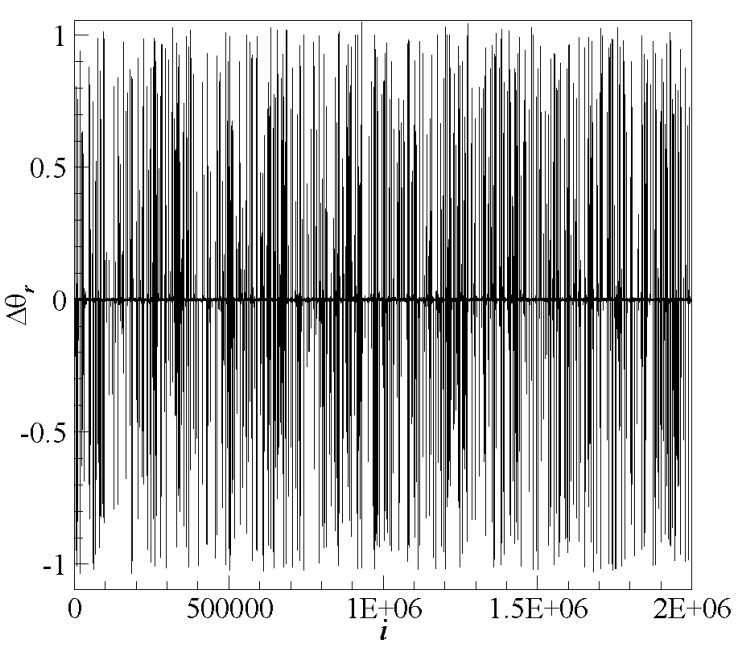

Figure 4.40 Sample sequence of the scalar increment $\Delta\theta_r$ for a separation distance in the inertial-convective range. Data shown for Re = 10,000 and D = 4.7 mm at x = 0.1 m.

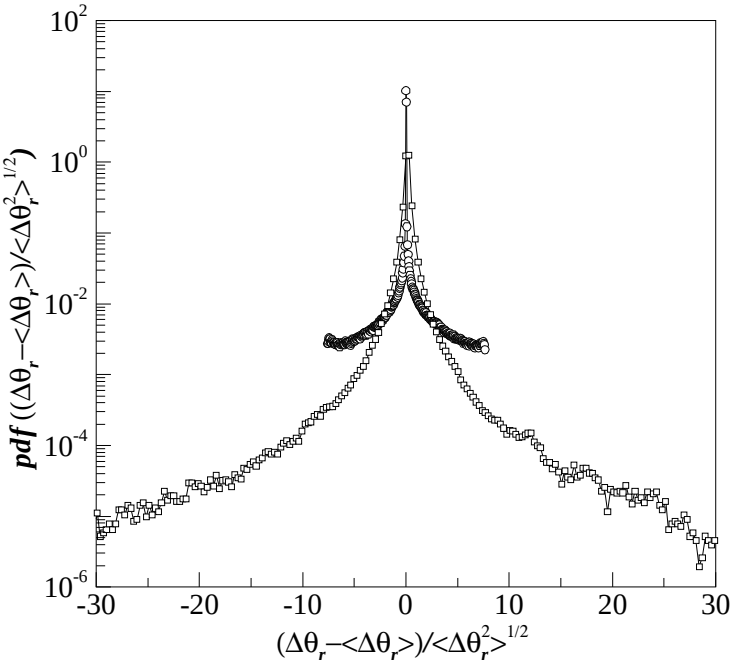

Figure 4.41 Probability density function of the normalized scalar increment $\left(\Delta\theta_r - \left\langle \Delta\theta_r \right\rangle\right) / \left\langle \Delta\theta_r^2 \right\rangle^{1/2}$. Data shown for Re = 10,000 and D = 4.7 mm at x = 0.1 m (○) and 4.0 m (□).

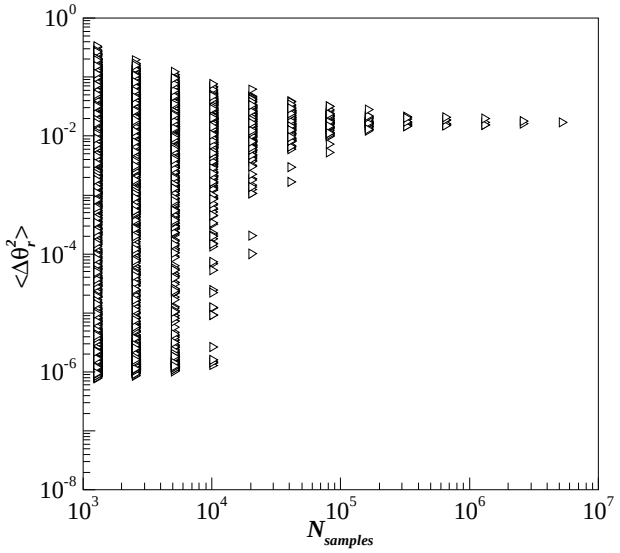

Figure 4.42 Second-order structure function as a function of the number of samples for a separation distance in the inertial-convective range. Data shown for Re = 10,000 and D = 4.7 mm at x = 0.1 m.

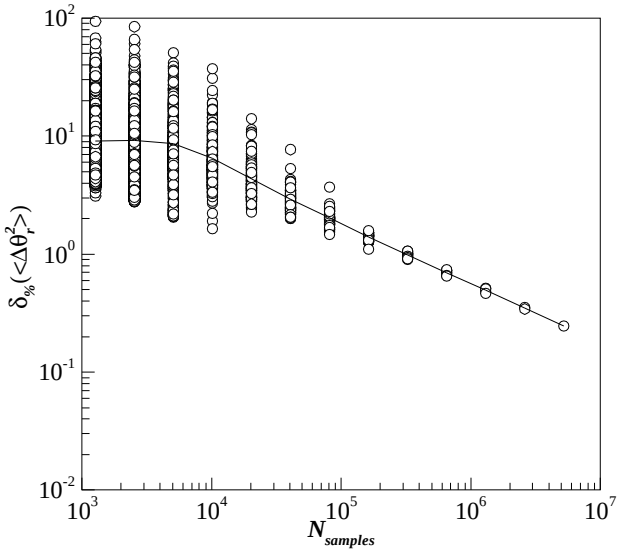

Figure 4.43 The standard error as a function of number of samples used to calculate the second-order structure function for a separation distance in the inertial-convective range. Data shown for Re = 10,000 and D = 4.7 mm at x = 0.1 m. The vertical axis represents percent error as: $\delta_{\%}\left(<\Delta\theta_r^2>\right)=\frac{\delta\left(<\Delta\theta_r^2>\right)}{<\Delta\theta_r^2>}\times 100$ where $\delta\left(<\Delta\theta_r^2>\right)=\frac{\left\langle\left(\Delta\theta_r^2-<\Delta\theta_r^2>\right)^2\right\rangle^{1/2}}{\sqrt{N_{samples}}}$ is the standard error estimate of $<\Delta\theta_r^2>$. The line indicates the average of the data points.

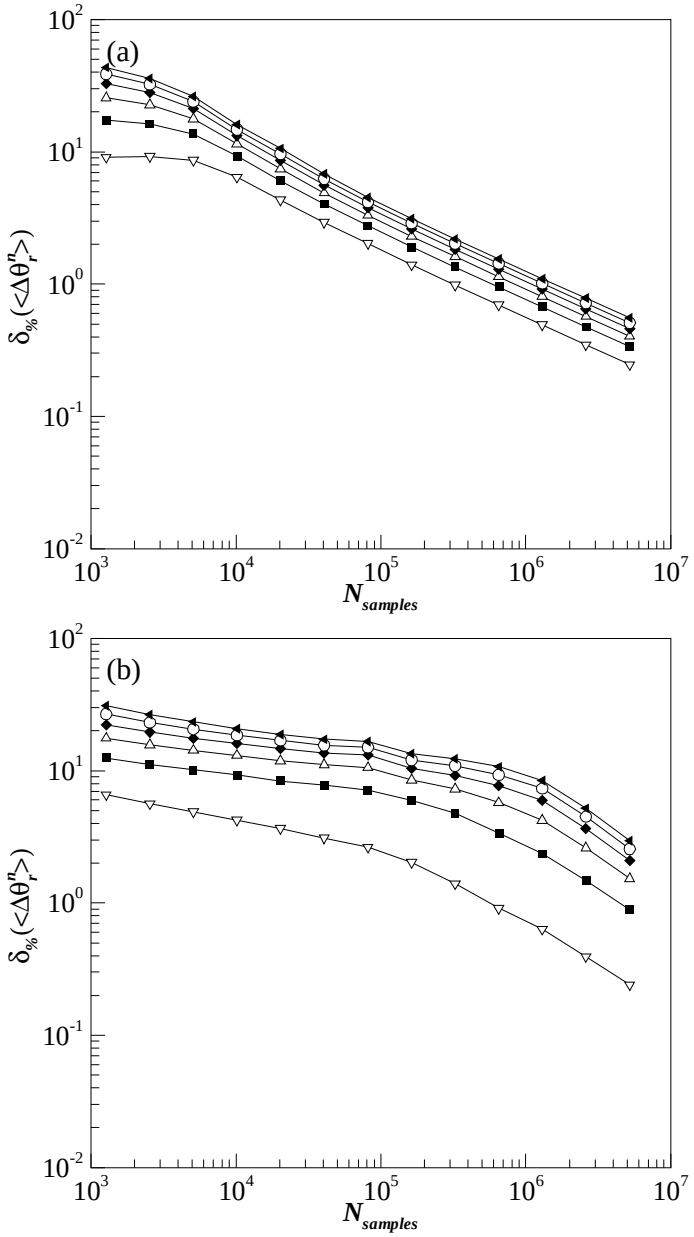

Figure 4.44 The standard error as a function of the number of samples used to calculate the n^{th} -order structure function for a separation distance in the inertial-convective range for n = 2 (▽), 4 (■), 6 (△), 8 (♦), 10 (○), and 12 (◀). Data shown for D = 4.7 mm, Re = 10,000 and (a) x = 0.1 m, and (b) 4 m.

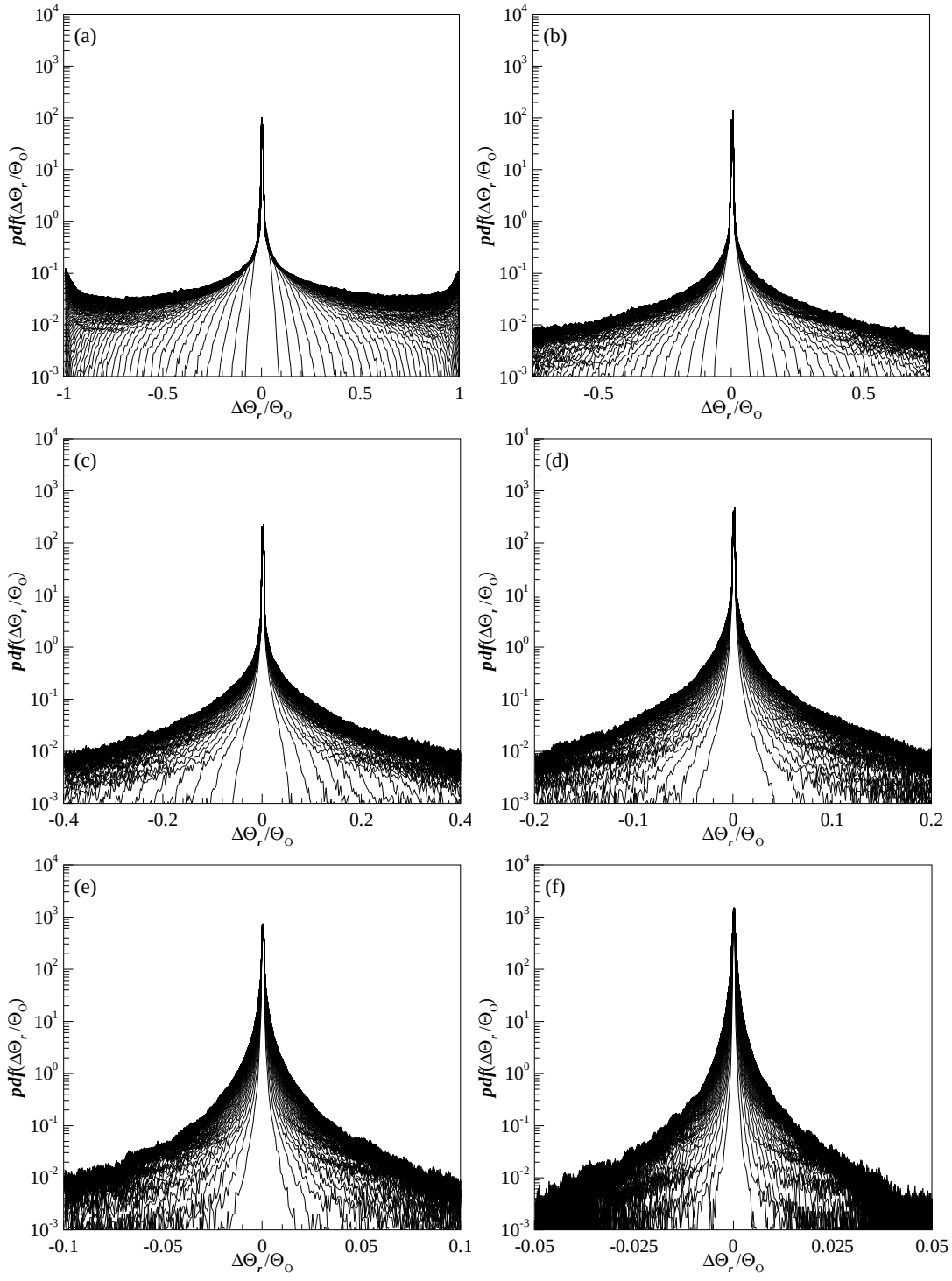

Figure 4.45 Probability density function of longitudinal scalar increments. Data shown for Re = 10,000 and D = 4.7 mm at (a) x = 0.1 m, (b) 0.25 m, (c) 0.5 m, (d) 1 m, (e) 2 m, and (f) 4 m for separation distance, r, between 0 and $100\eta_B$.

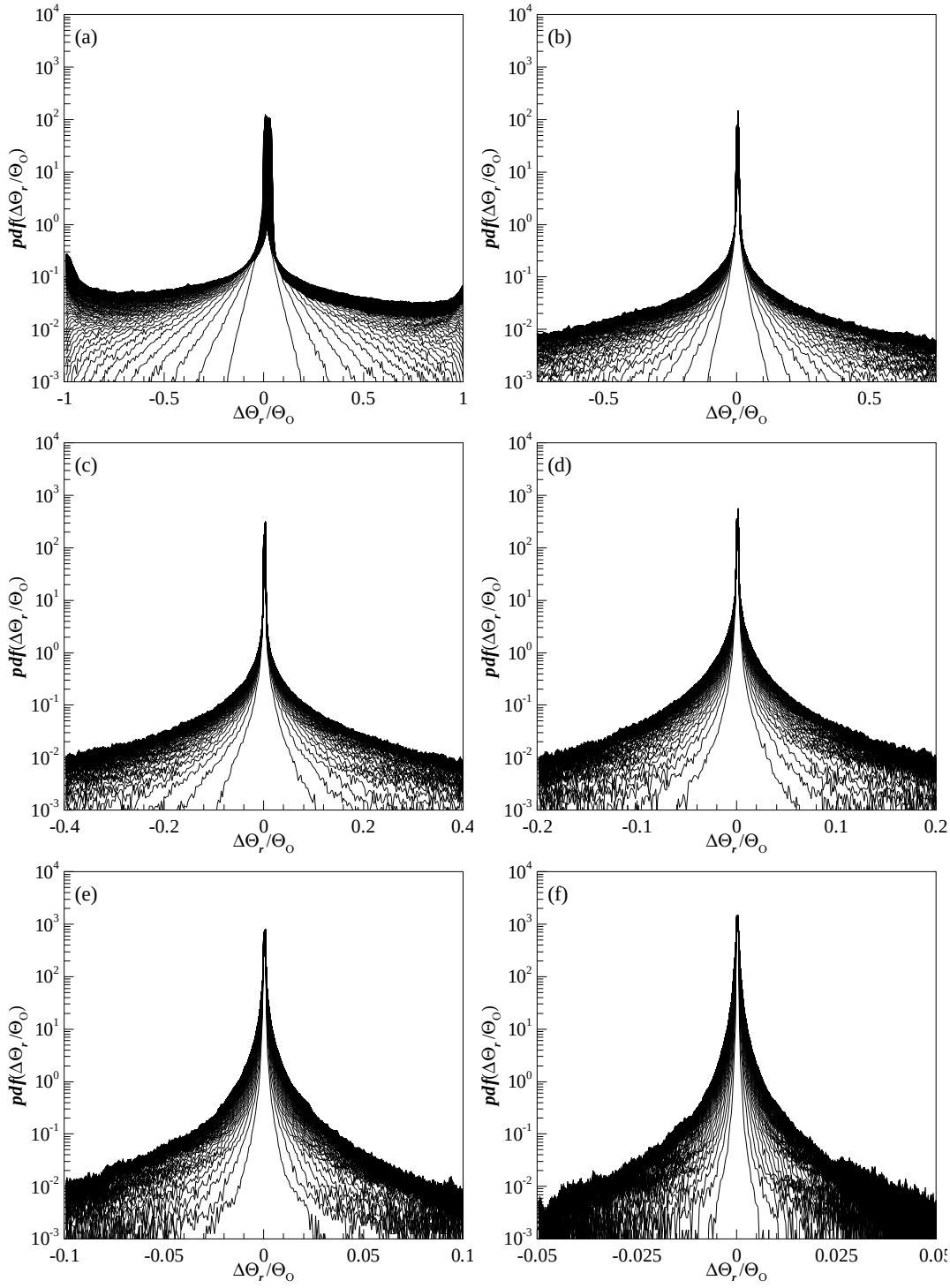

Figure 4.46 Probability density function of vertical scalar increments. Data shown for Re **= 10,000 and** D **= 4.7 mm at (a)** x **= 0.1 m, (b) 0.25 m, (c) 0.5 m, (d) 1 m, (e) 2 m, and (f) 4 m for separation distance,** r **, between 0 and** $100\eta_B$ **.**

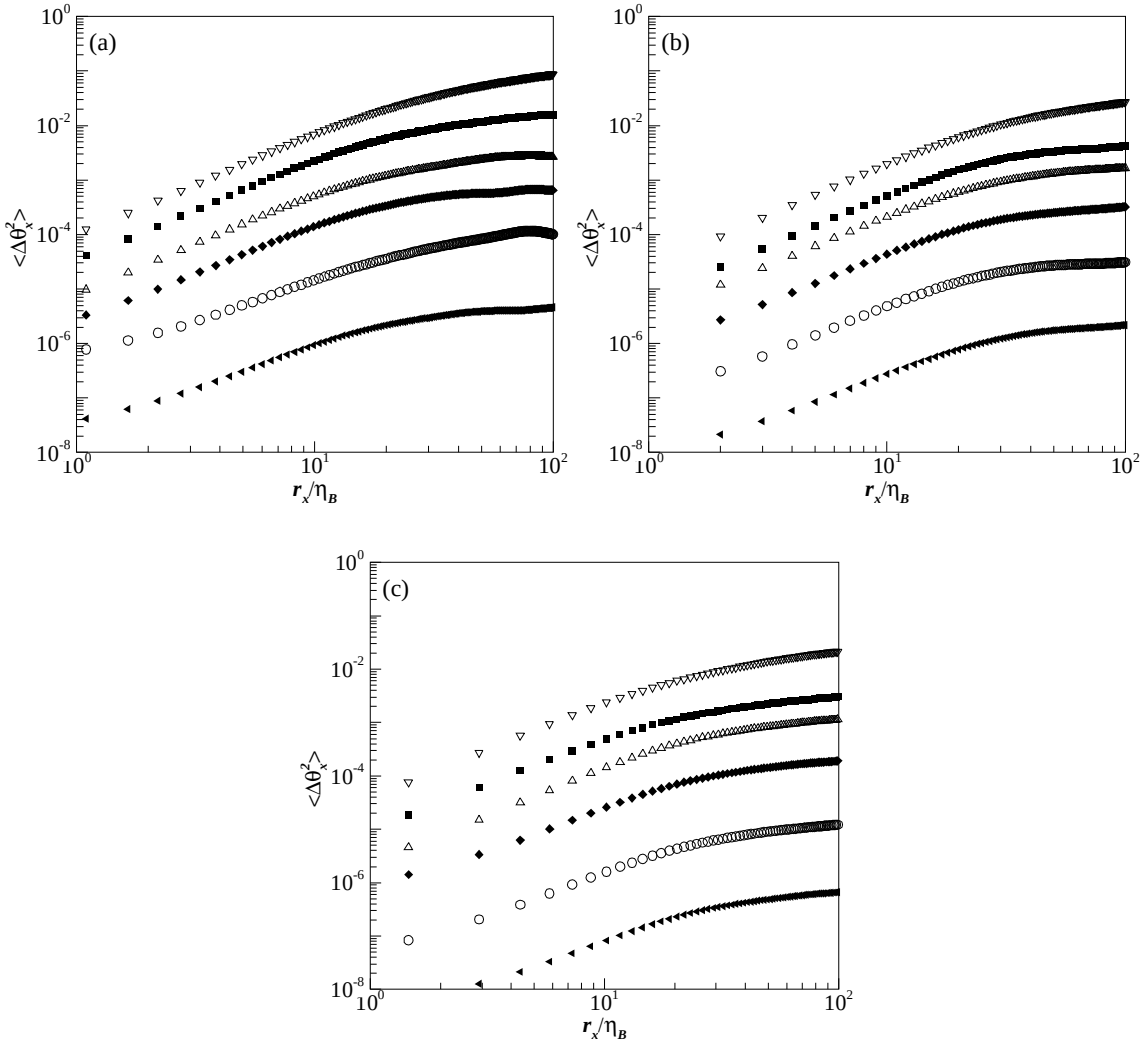

Figure 4.47 Longitudinal second-order structure function of the fluctuating scalar field for (a) *Re* = 5000, (b) 10,000, and (c) 20,000. Data shown for *D* = 4.7 mm at *x* = 0.1 m (▽), 0.25 m (■), 0.5 m (△), 1 m (♦), 2 m (○), and 4 m (◀).

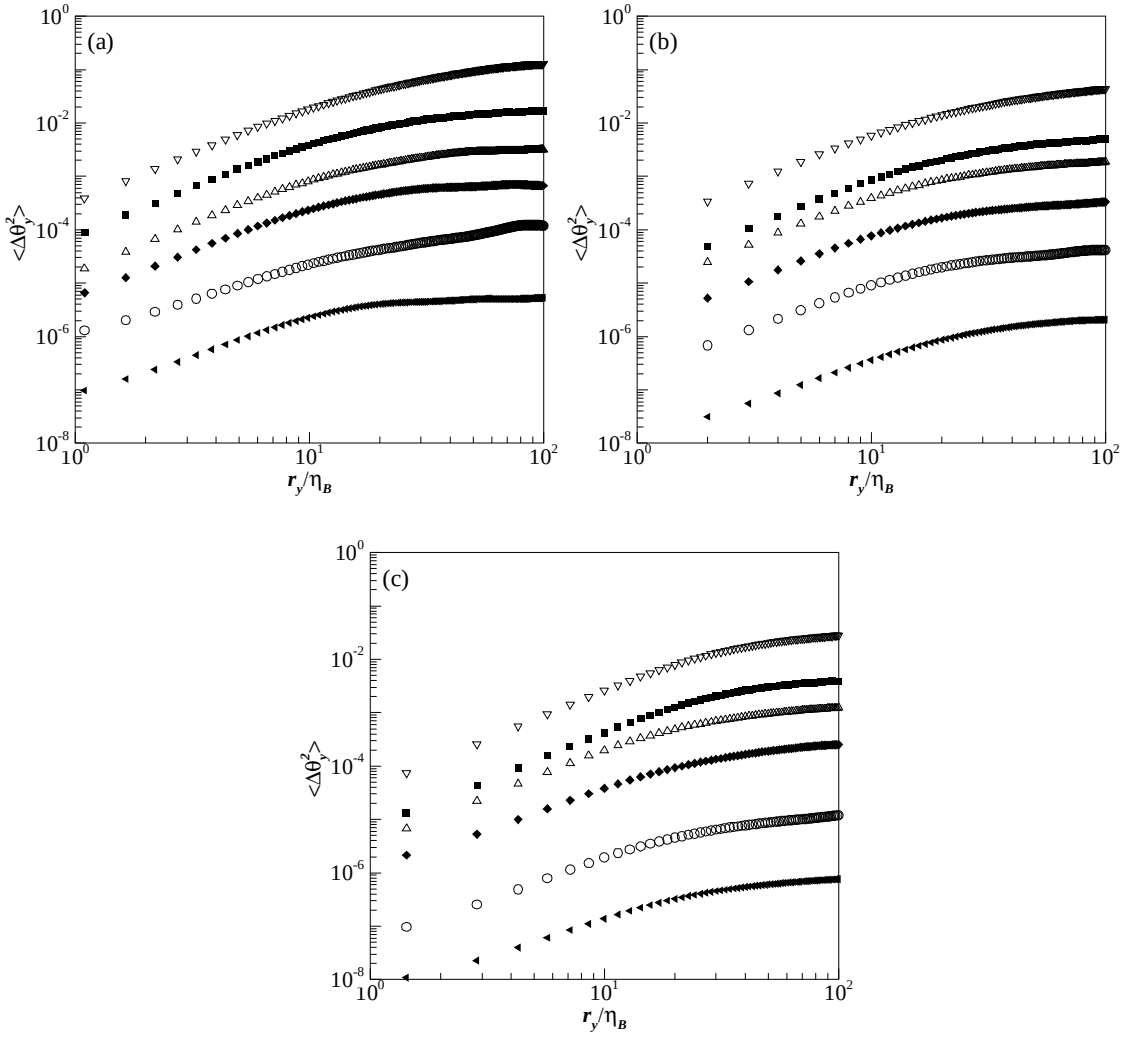

Figure 4.48 Vertical second-order structure function of the fluctuating scalar field for (a) Re = 5000, (b) 10,000, and (c) 20,000. Data shown for D = 4.7 mm at x = 0.1 m (▽), 0.25 m (■), 0.5 m (△), 1 m (♦), 2 m (○), and 4 m (◀).

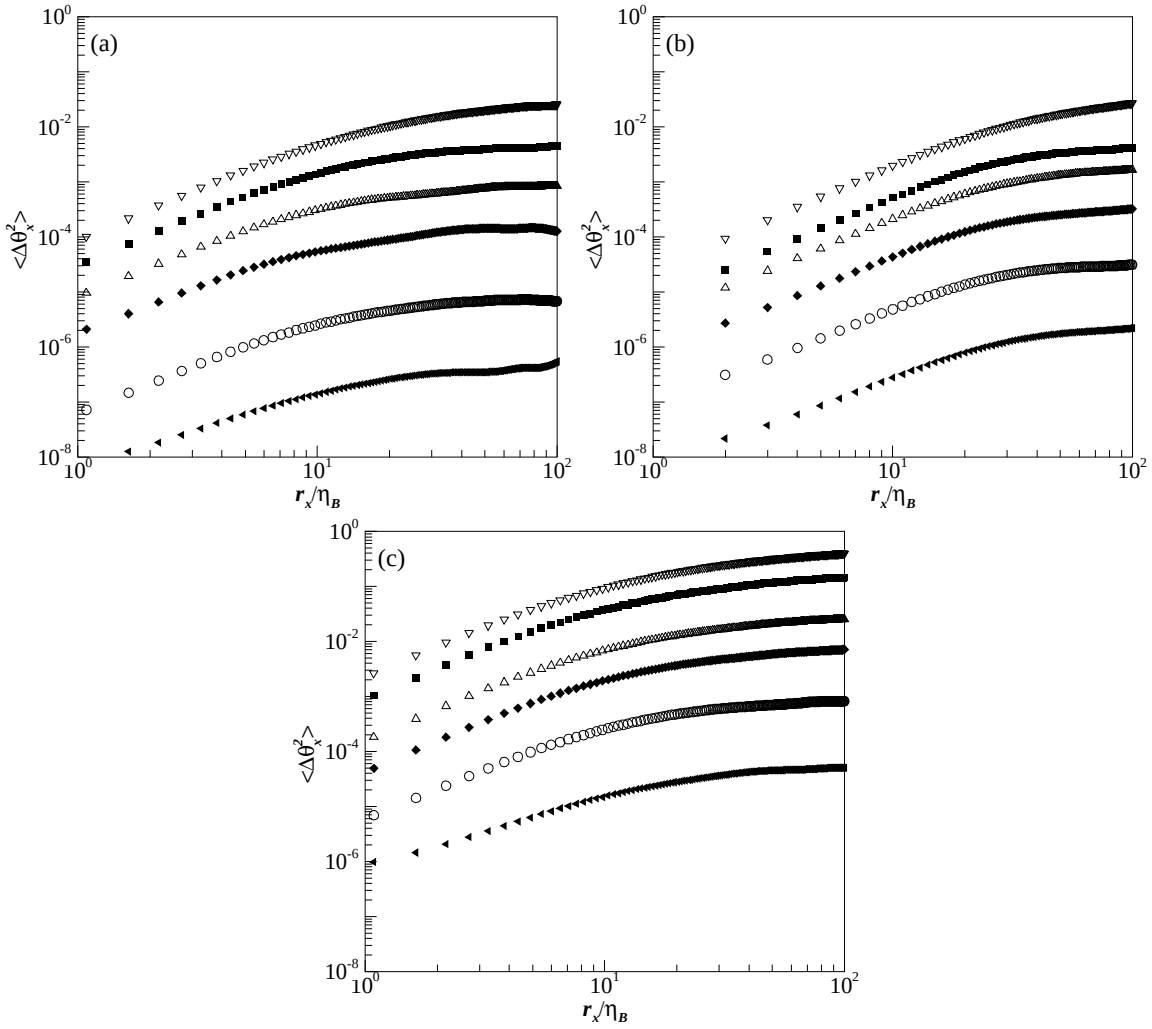

Figure 4.49 Longitudinal second-order structure function of the fluctuating scalar field for (a) D **= 2.2 mm, (b) 4.7 mm, and (c) 9.4 mm. Data shown for** Re **= 10,000 at** x **= 0.1 m (▽), 0.25 m (■), 0.5 m (△), 1 m (♦), 2 m (○), and 4 m (◀).**

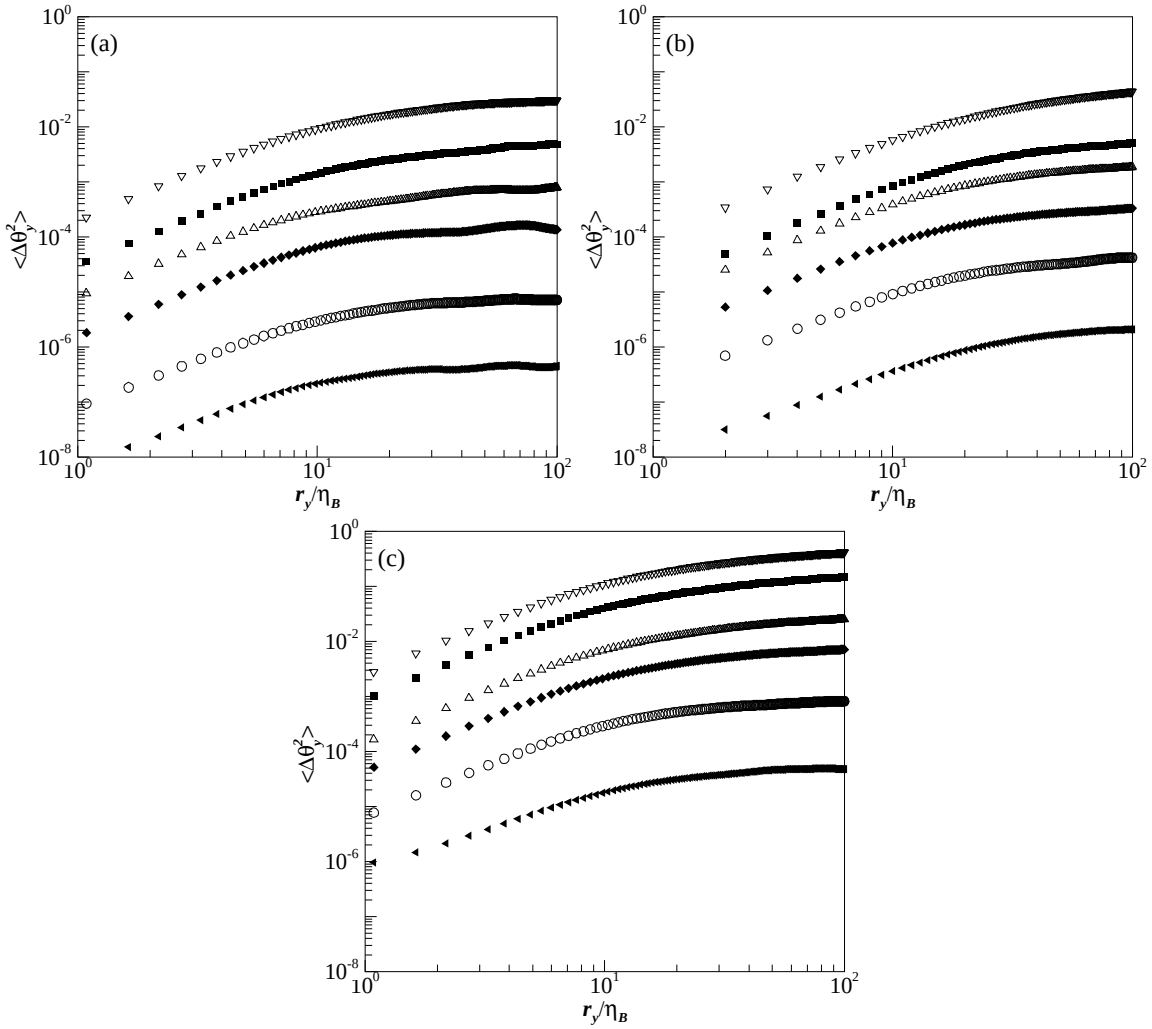

Figure 4.50 Vertical second-order structure function of the fluctuating scalar field for (a) D = 2.2 mm, (b) 4.7 mm, and (c) 9.4 mm. Data shown for Re = 10,000 at x = 0.1 m (▽), 0.25 m (■), 0.5 m (△), 1 m (♦), 2 m (○), and 4 m (◀).

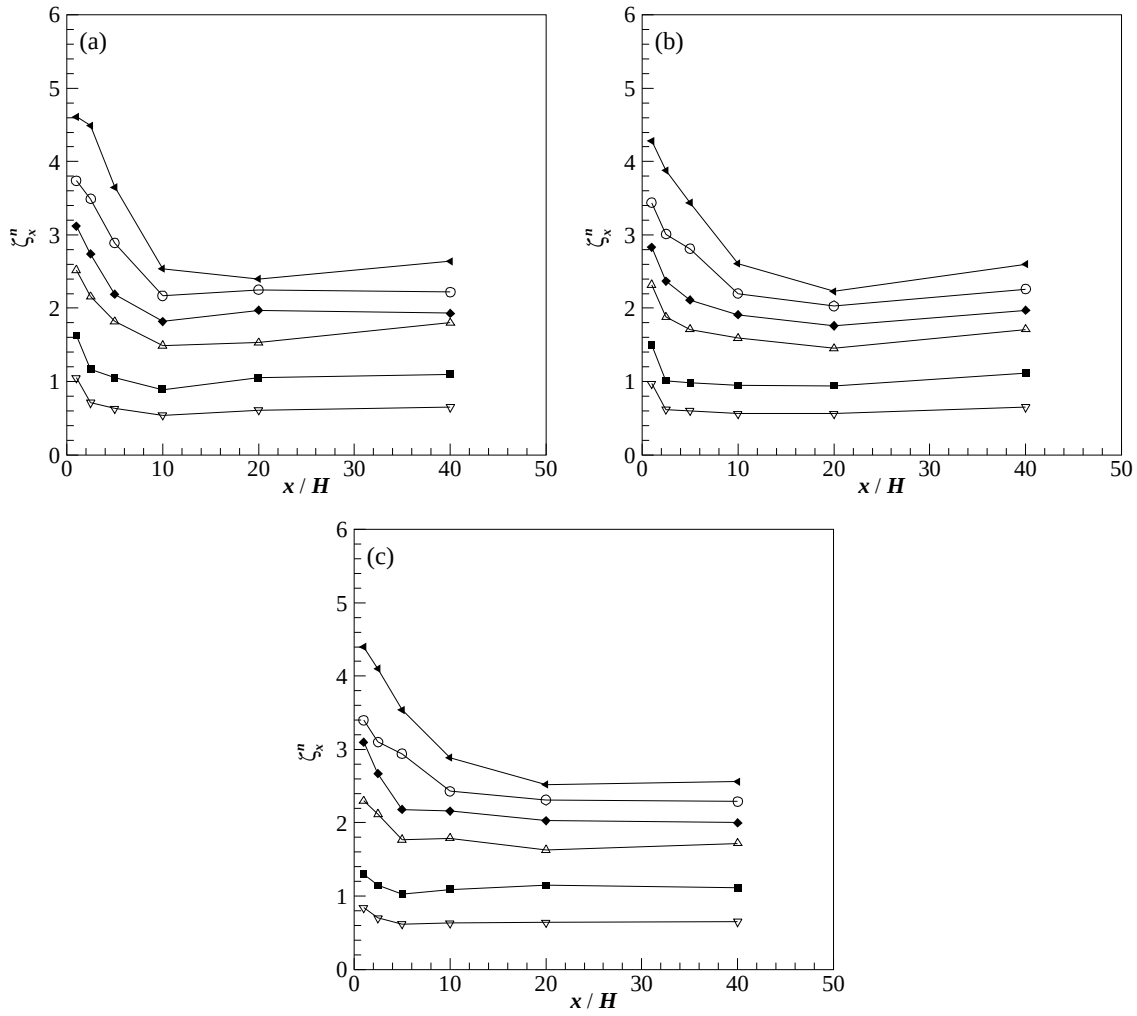

Figure 4.51 Inertial-convective scaling exponent of the longitudinal n^{th}-order structure function of the fluctuating scalar field for three Reynolds numbers for n = 2 (▽), 4 (■), 6 (△), 8 (♦), 10 (○), and 12 (◀). Data shown for D = 4.7 mm and (a) Re = 5,000, (b) 10,000 and (c) 20,000.

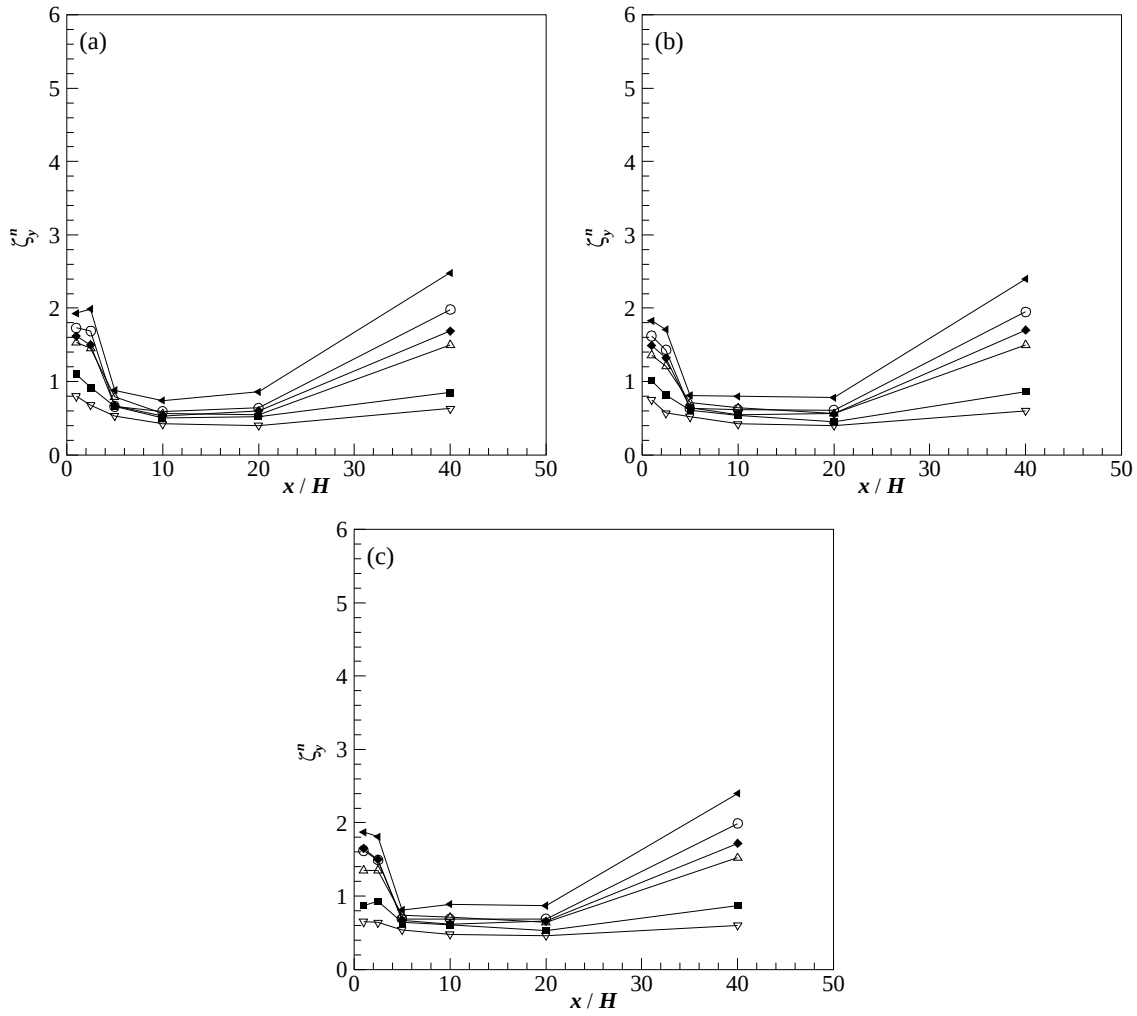

Figure 4.52 Inertial-convective scaling exponent of the vertical n^{th} -order structure function of the fluctuating scalar field for three Reynolds numbers for n = 2 (▽), 4 (■), 6 (△), 8 (♦), 10 (○), and 12 (◀). Data shown for D = 4.7 mm and (a) Re = 5,000, (b) 10,000, and (c) 20,000.

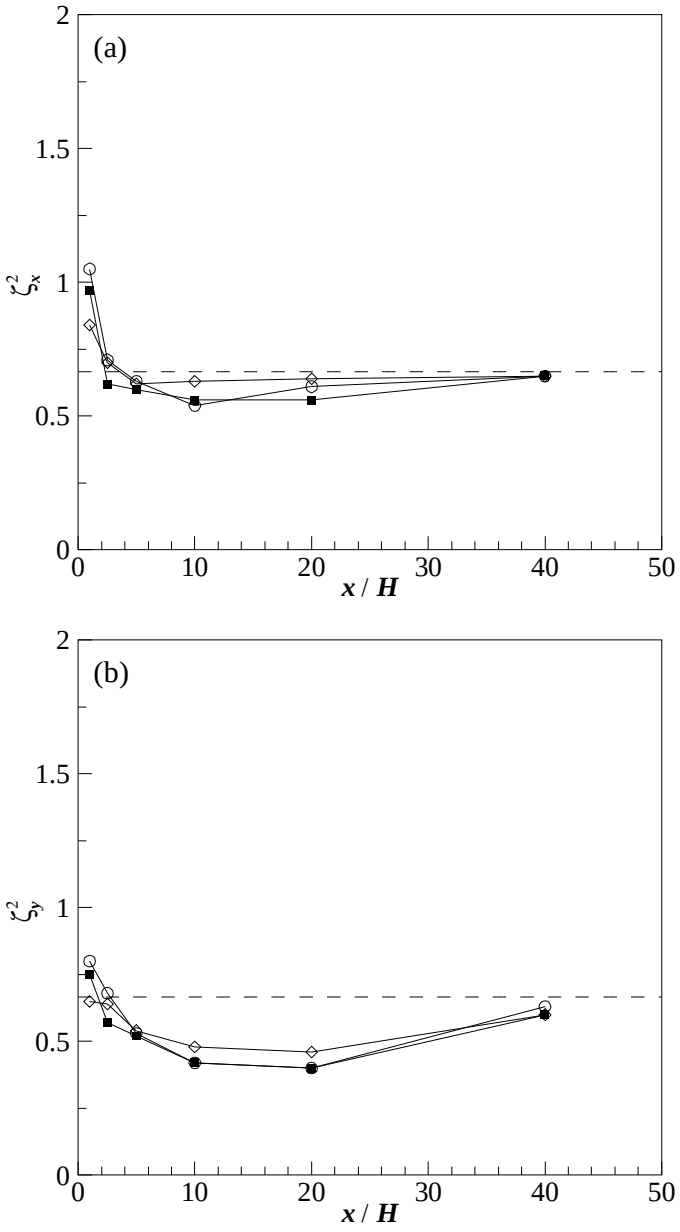

Figure 4.53 Inertial-convective scaling exponent of the (a) longitudinal and (b) vertical second-order structure function for three Reynolds numbers. Data shown for D = 4.7 mm and Re = 5000 (○), 10,000 (■), and 20,000 (◊).

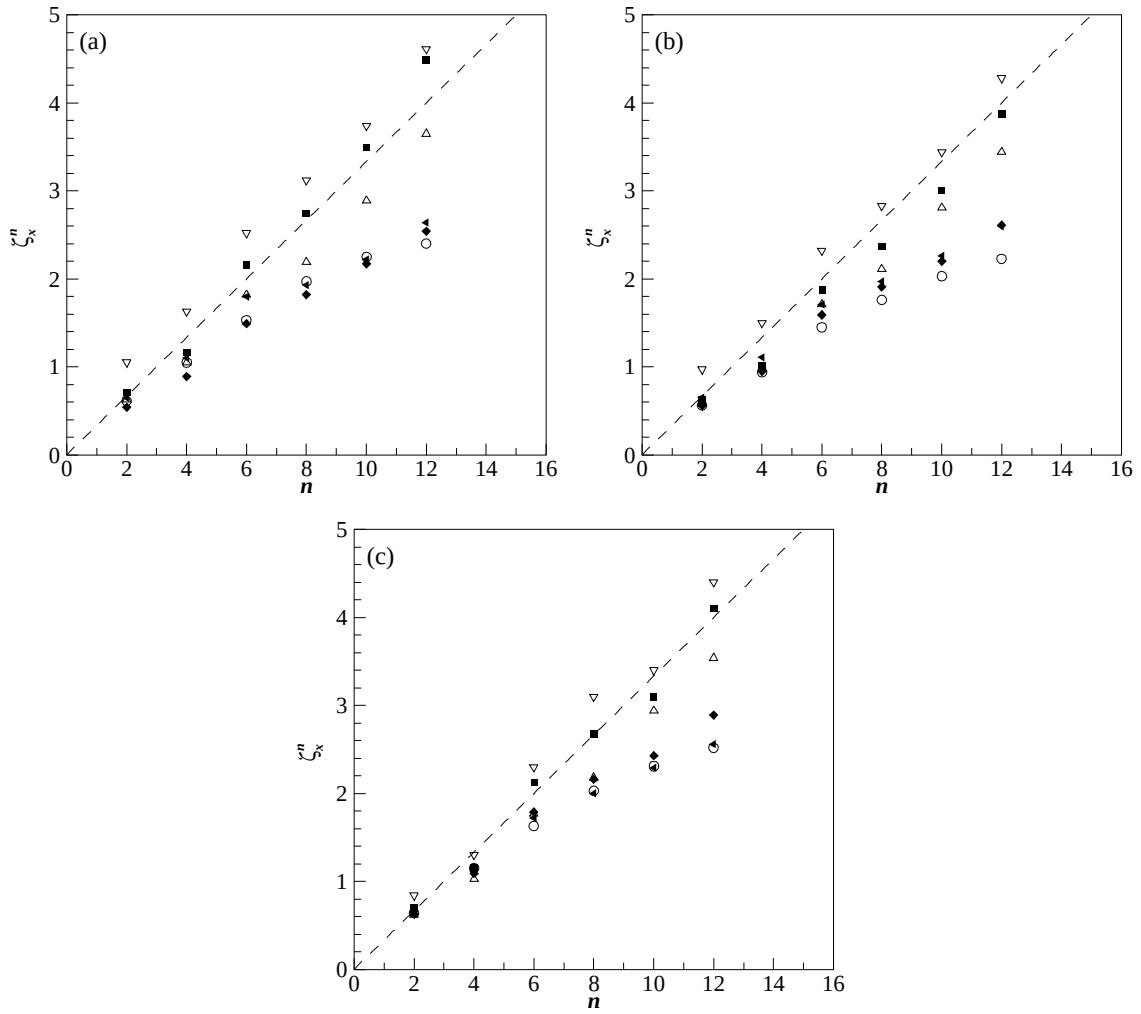

Figure 4.54 Inertial-convective scaling exponent of the longitudinal n^{th}-order structure function of the fluctuating scalar field as a function of n at x = 0.1 m (▽), 0.25 m (■), 0.5 m (△), 1 m (♦), 2 m (○), and 4 m (◀). Data shown for D = 4.7 mm and (a) Re = 5000, (b) 10,000, and (c) 20,000.

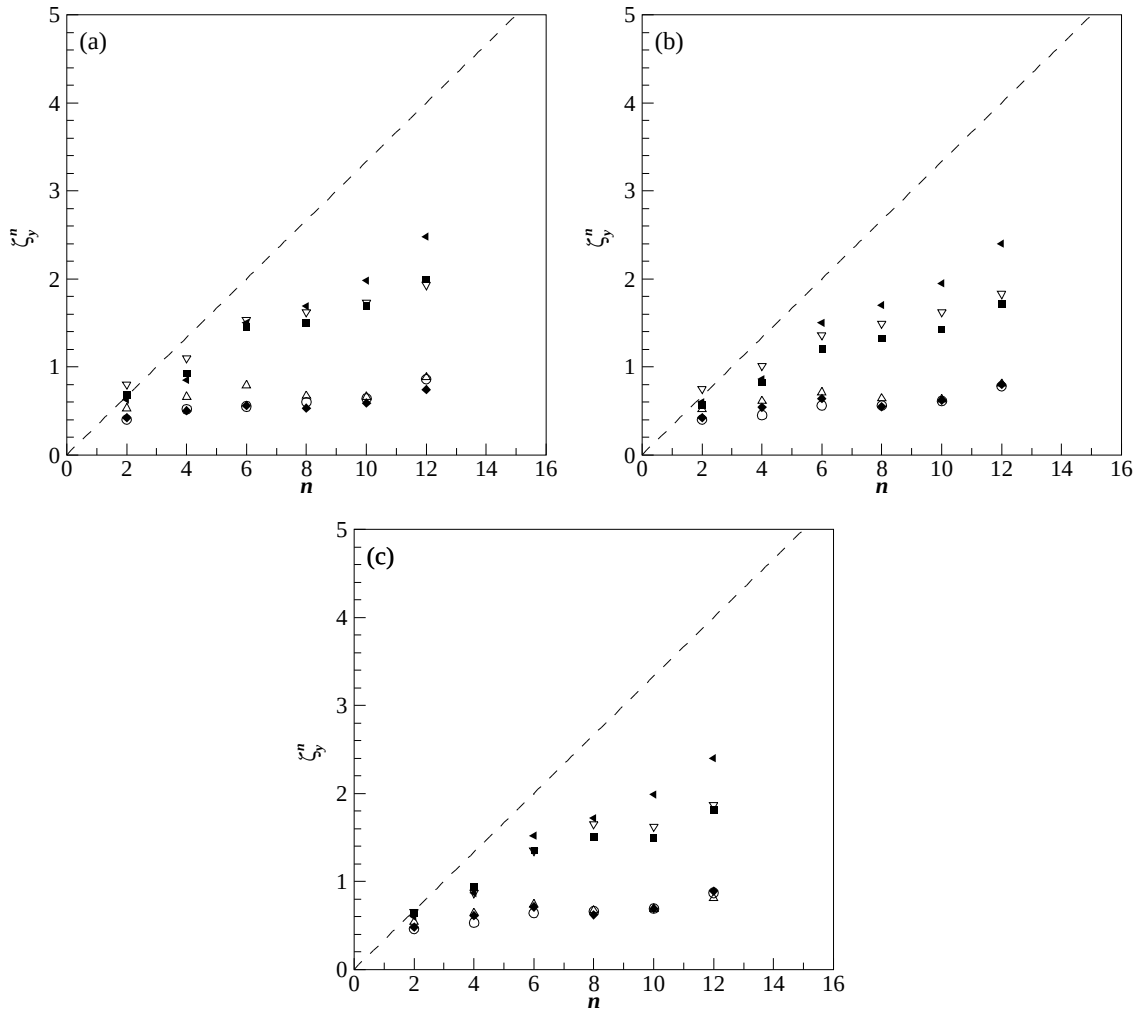

Figure 4.55 Inertial-convective scaling exponent of the vertical n^{th} -order structure function of the fluctuating scalar field as a function of n at x = 0.1 m (▽), 0.25 m (■), 0.5 m (△), 1 m (♦), 2 m (○), and 4 m (◀). Data shown for D = 4.7 mm and (a) Re = 5000, (b) 10,000, and (c) 20,000.

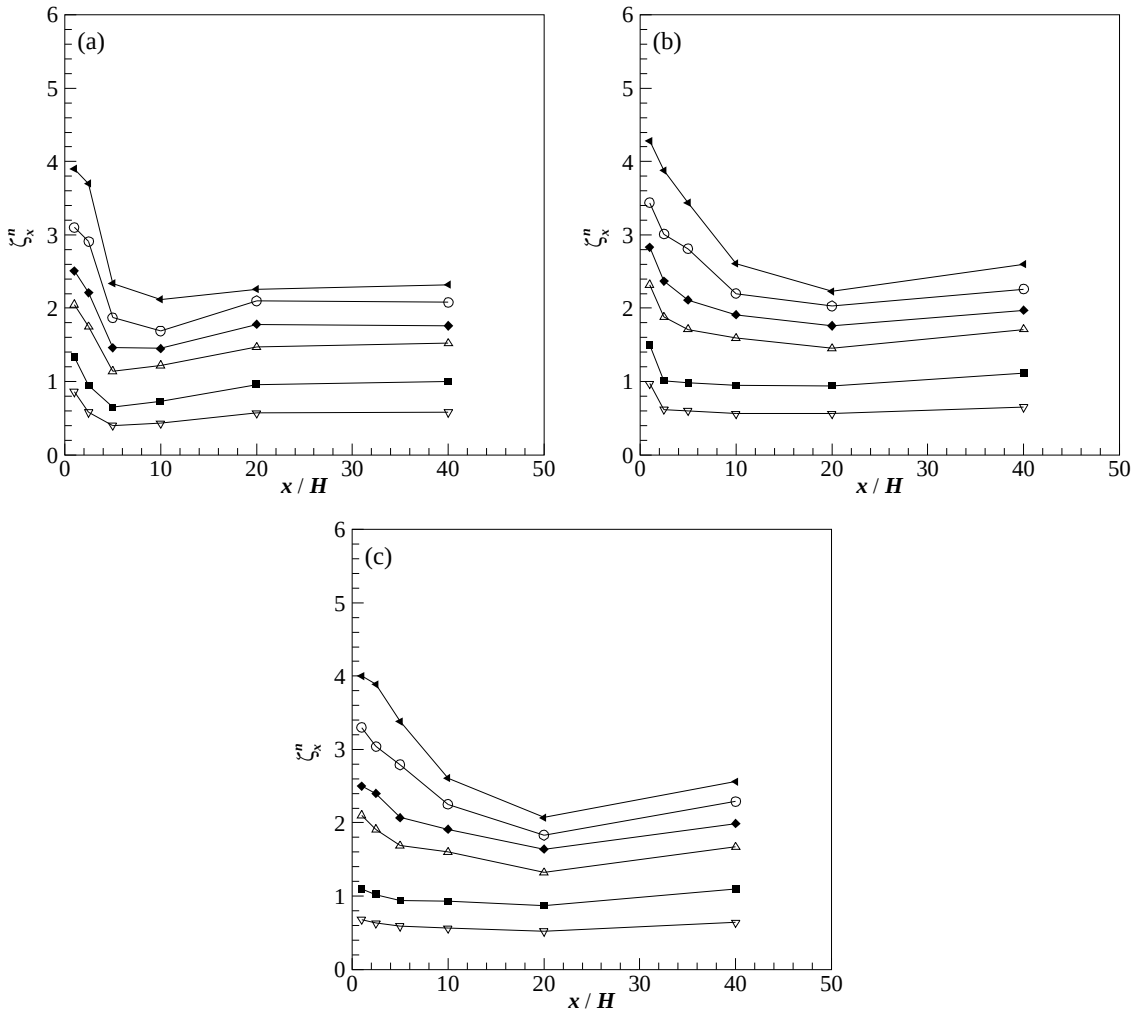

Figure 4.56 Inertial-convective scaling exponent of the longitudinal n^{th}-order structure function of the fluctuating scalar field for three source nozzle diameters for n = 2 (▽), 4 (■), 6 (△), 8 (♦), 10 (○), and 12 (◀). Data shown for Re = 10,000 and (a) D = 2.2 mm, (b) 4.7 mm, and (c) 9.4 mm.

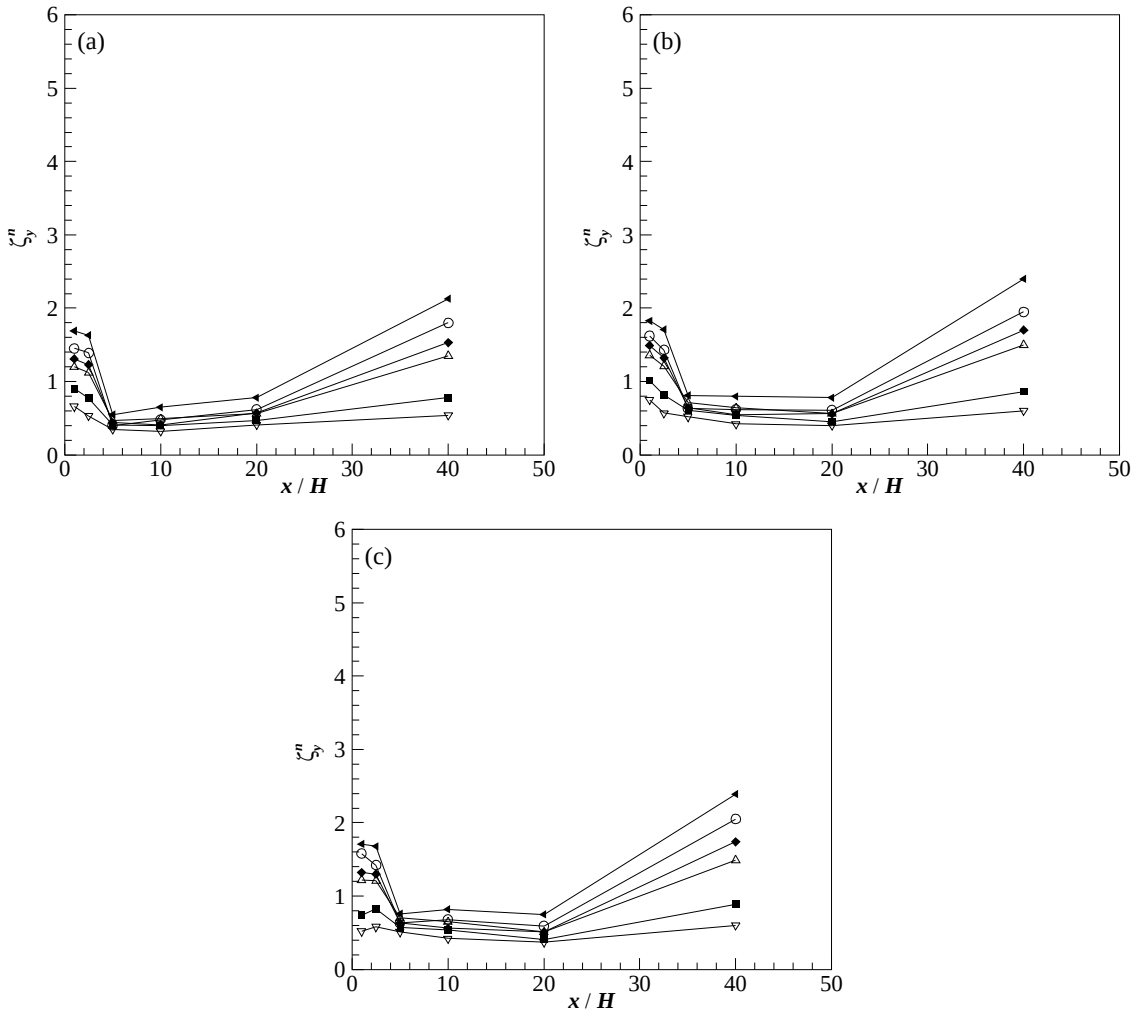

Figure 4.57 Inertial-convective scaling exponent of the vertical n^{th}-order structure function of the fluctuating scalar field for three source nozzle diameters for n = 2 (▽), 4 (■), 6 (△), 8 (♦), 10 (○), and 12 (◀). Data shown for Re = 10,000 and (a) D = 2.2 mm, (b) 4.7 mm, and (c) 9.4 mm.

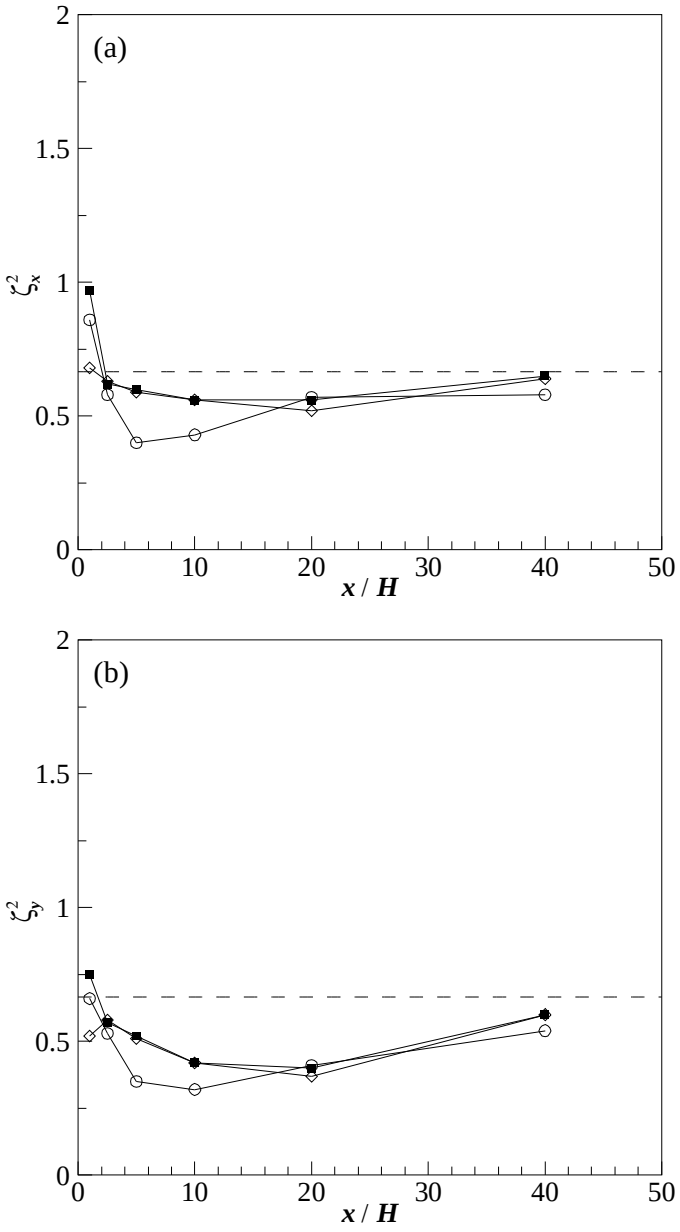

Figure 4.58 Inertial-convective scaling exponent of the (a) longitudinal and (b) vertical second-order structure functions for three source nozzle diameters. Data shown for Re = 10,000 and D = 2.2 mm (○), 4.7 mm (■), and 9.4 mm (◊).

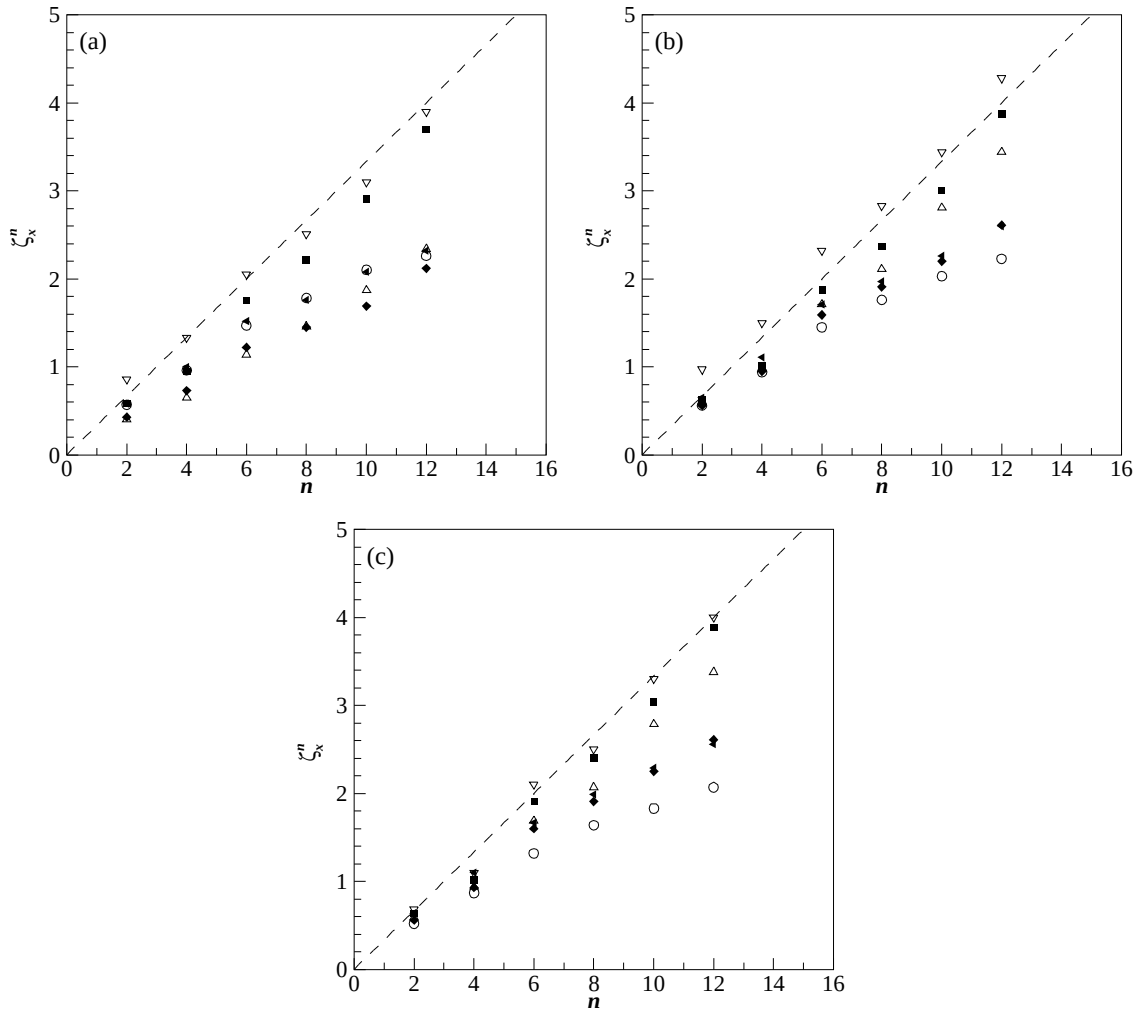

Figure 4.59 Inertial-convective scaling exponent of the longitudinal n^{th}-order structure function of the fluctuating scalar field as a function of n at x = 0.1 m (▽), 0.25 m (■), 0.5 m (△), 1 m (♦), 2 m (○), and 4 m (◀). Data shown for Re = 10,000 and (a) D = 2.2 mm, (b) 4.7 mm, and (c) 9.4 mm.

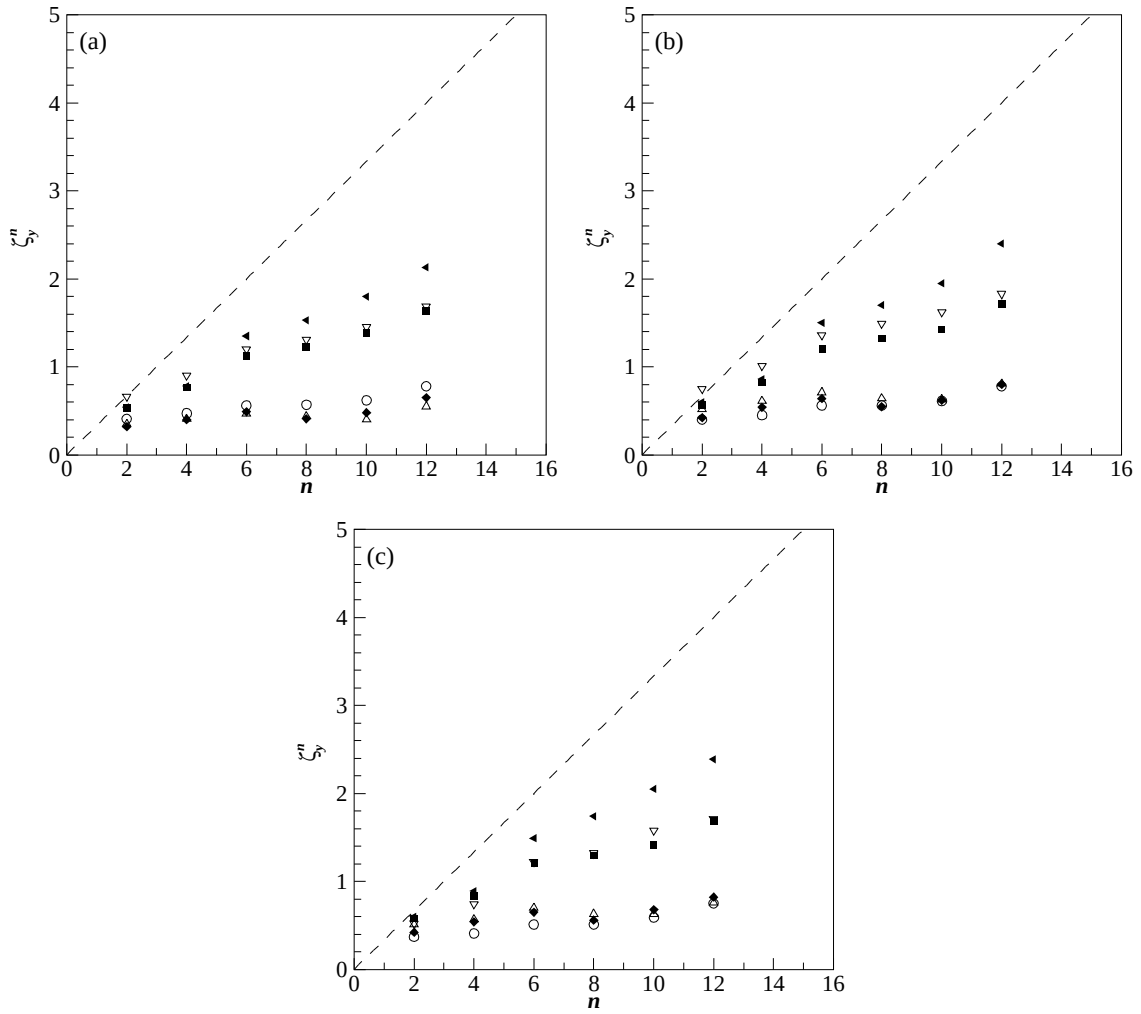

Figure 4.60 Inertial-convective scaling exponent of the vertical n^{th} -order structure function of the fluctuating scalar field as a function of n at x = 0.1 m (▽), 0.25 m (■), 0.5 m (△), 1 m (♦), 2 m (○), and 4 m (◀). Data shown for Re = 10,000 and (a) D = 2.2 mm, (b) 4.7 mm, and (c) 9.4 mm.

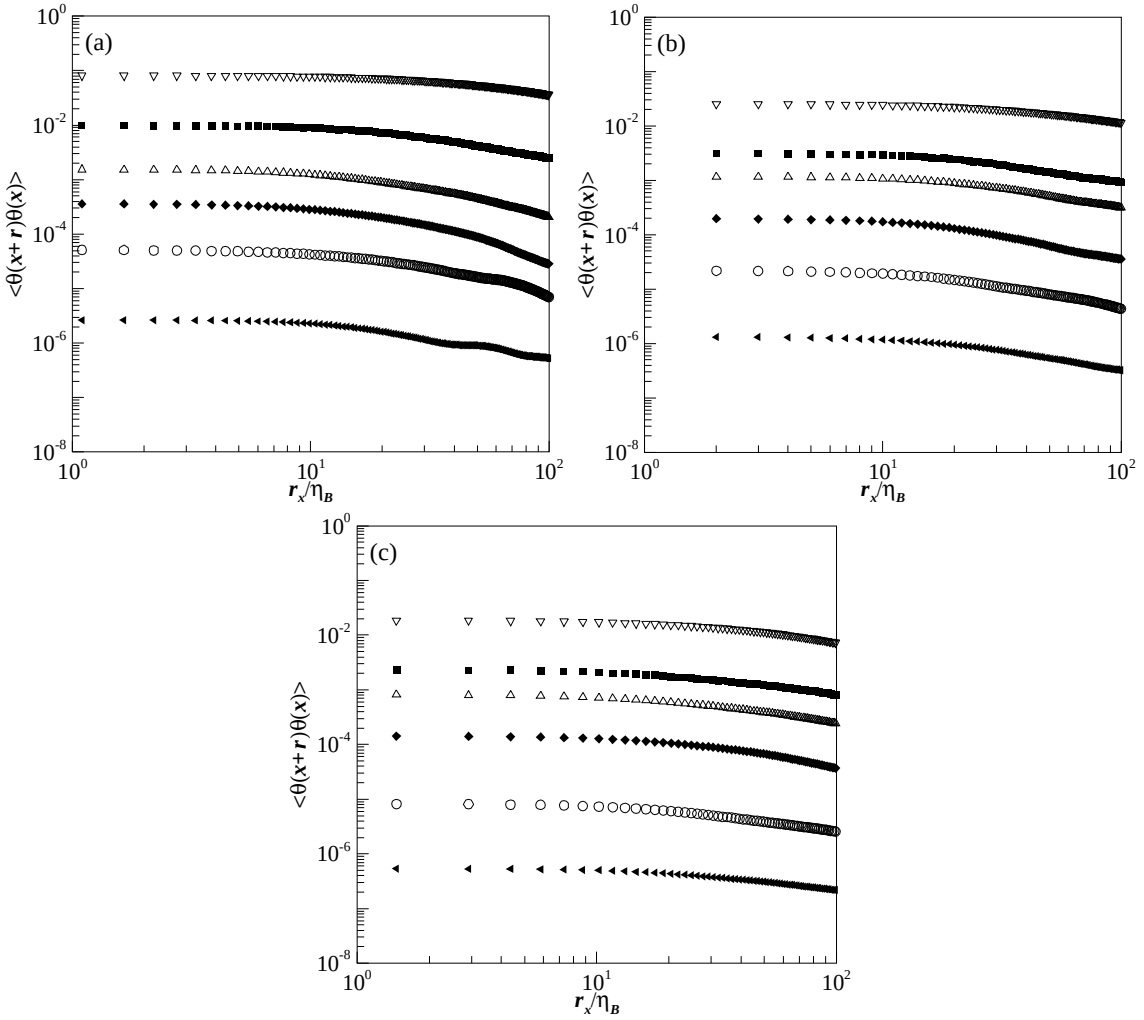

Figure 4.61 Longitudinal two-point correlation function of the fluctuating scalar field for (a) *Re* **= 5000, (b) 10,000, and (c) 20,000. Data shown for** *D* **= 4.7 mm at** *x* **= 0.1 m (▽), 0.25 m (■), 0.5 m (△), 1 m (♦), 2 m (○), and 4 m (◀).**

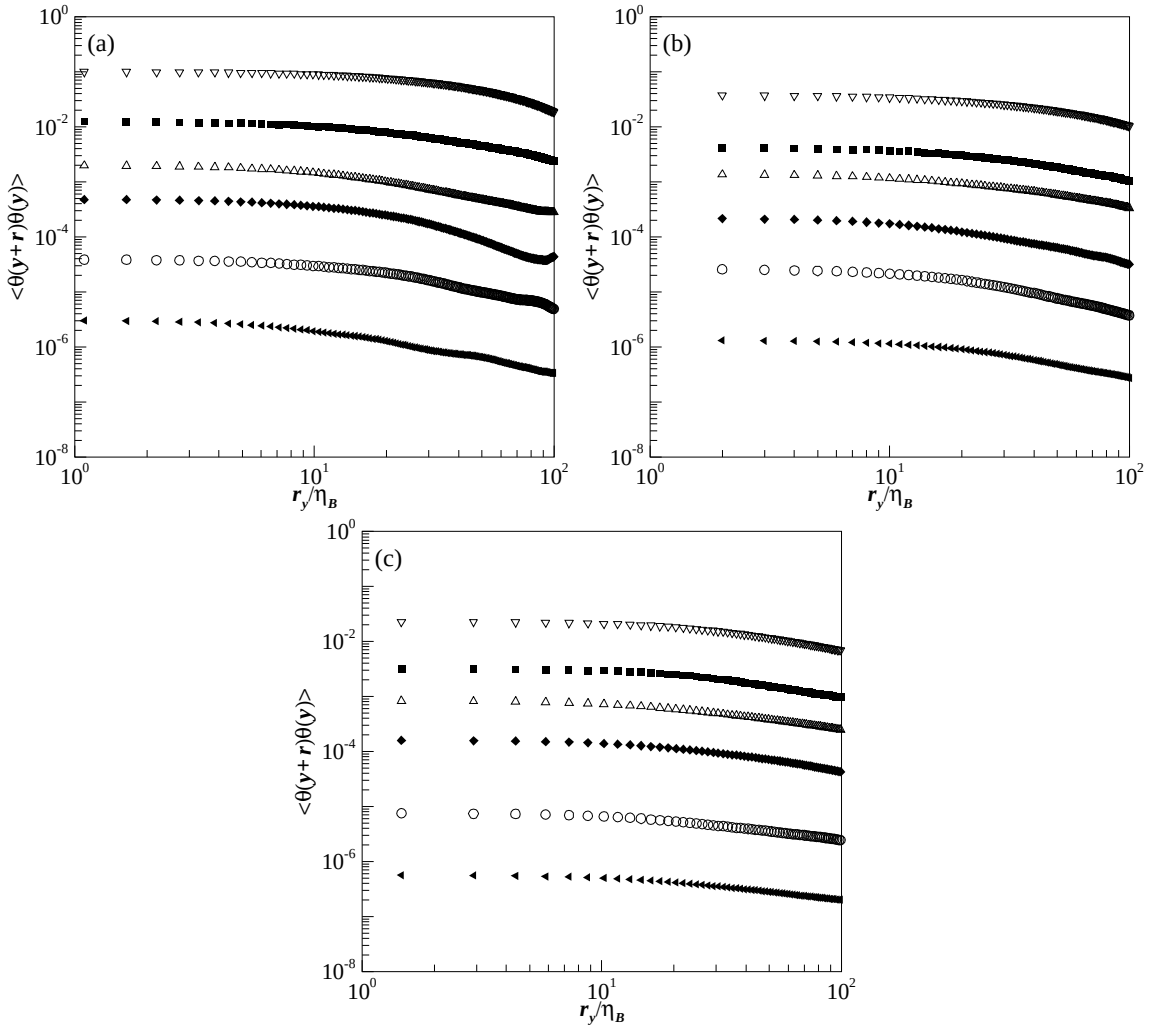

Figure 4.62 Vertical two-point correlation function of the fluctuating scalar field for (a) Re **= 5000, (b) 10,000, and (c) 20,000. Data shown for** D **= 4.7 mm at** x **= 0.1 m (▽), 0.25 m (■), 0.5 m (△), 1 m (♦), 2 m (○), and 4 m (◀).**

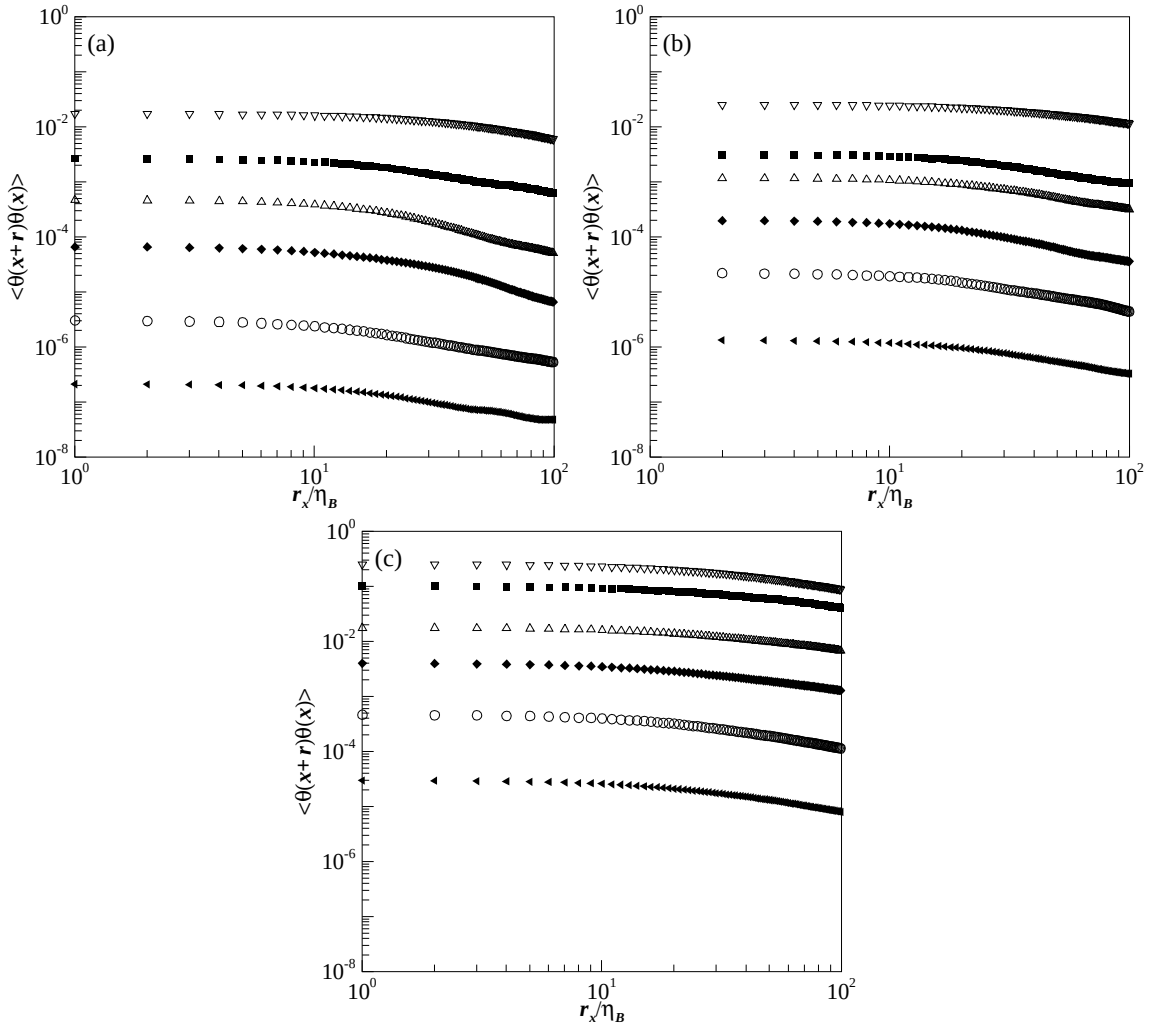

Figure 4.63 Longitudinal two-point correlation function of the fluctuating scalar field for (a) D = 2.2 mm, (b) 4.7 mm, and (c) 9.4 mm. Data shown for Re = 10,000 at x = 0.1 m (▽), 0.25 m (■), 0.5 m (△), 1 m (♦), 2 m (○), and 4 m (◀).

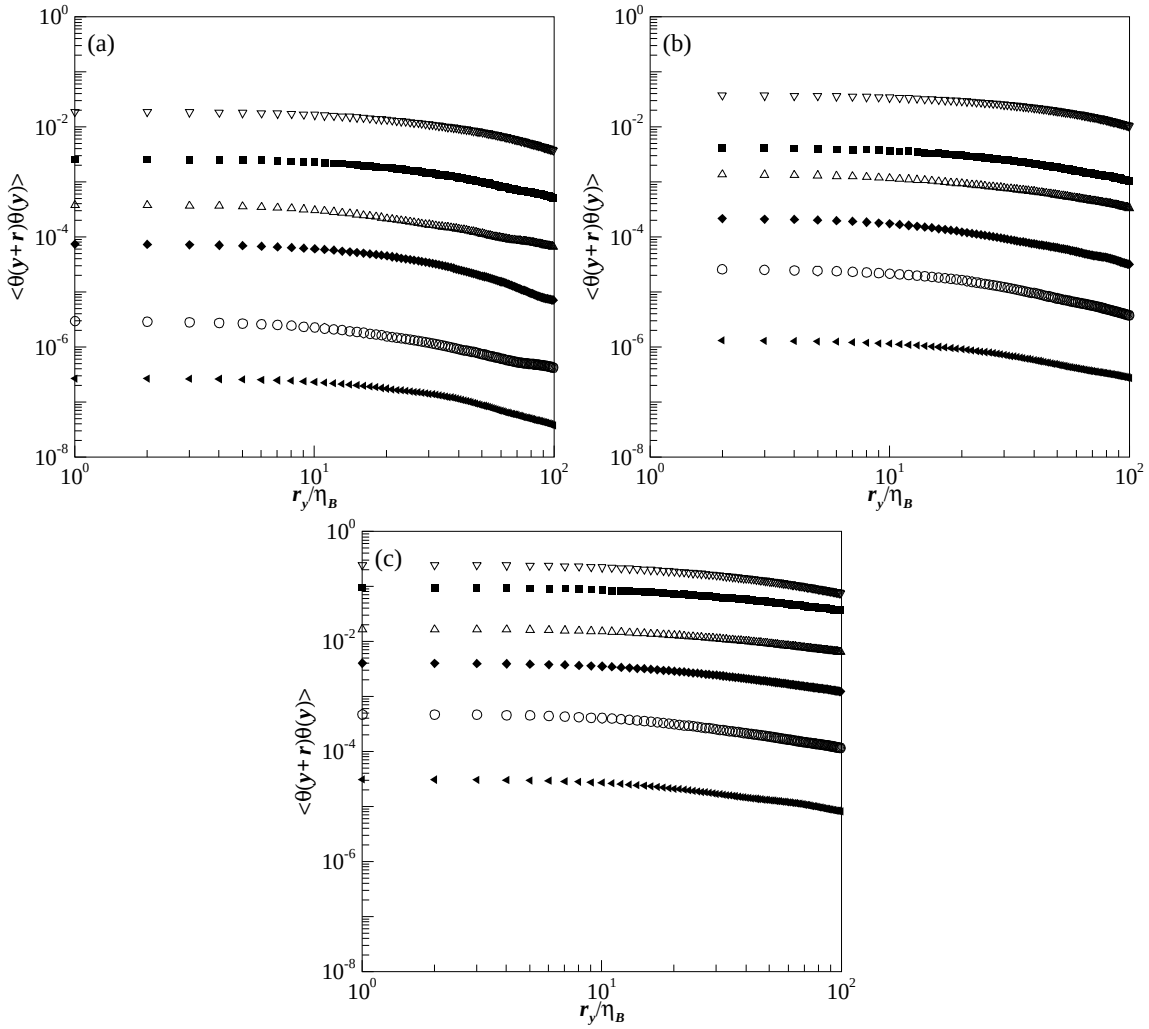

Figure 4.64 Vertical two-point correlation function of the fluctuating scalar field for (a) D **= 2.2 mm, (b) 4.7 mm, and (c) 9.4 mm. Data shown for** Re **= 10,000 at** x **= 0.1 m (▽), 0.25 m (■), 0.5 m (△), 1 m (♦), 2 m (○), and 4 m (◄).**

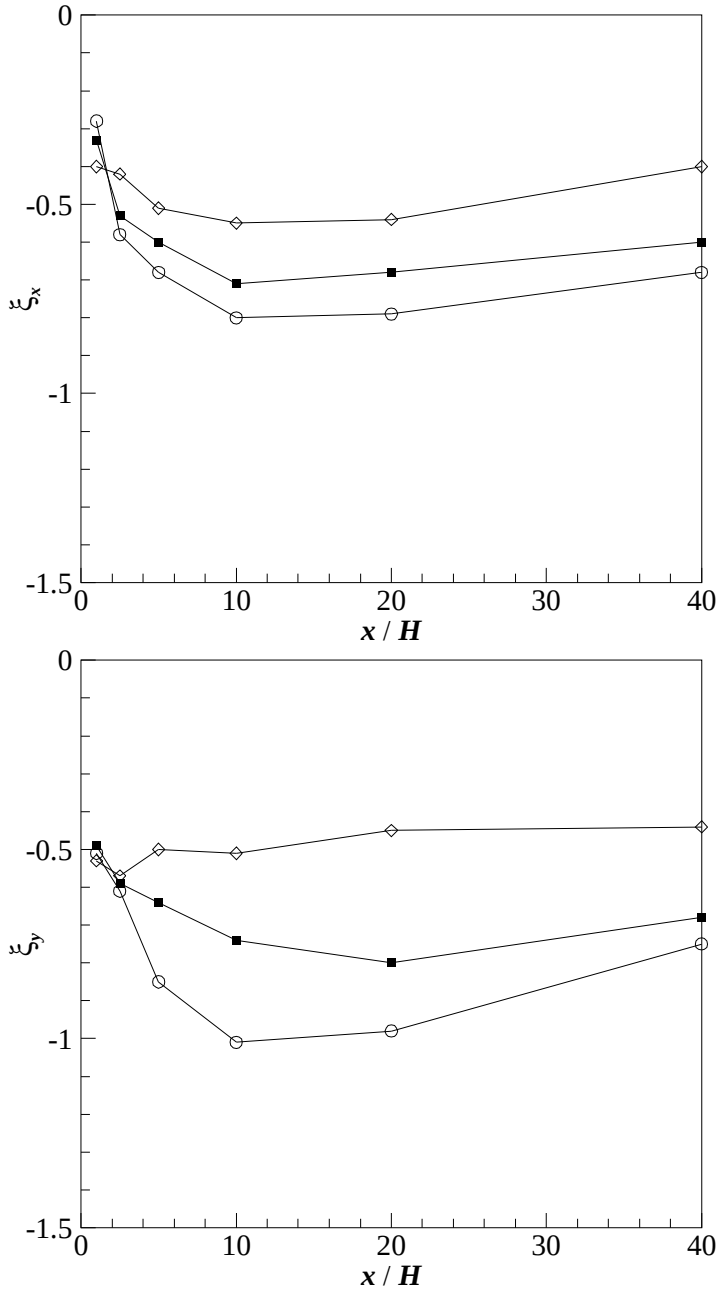

Figure 4.65 Scaling exponent in the inertial-convective regime of the (a) longitudinal and (b) vertical two-point correlation functions for three Reynolds numbers. Data shown for D = 4.7 mm and Re = 5000 (○), 10,000 (■), and 20,000 (◊).

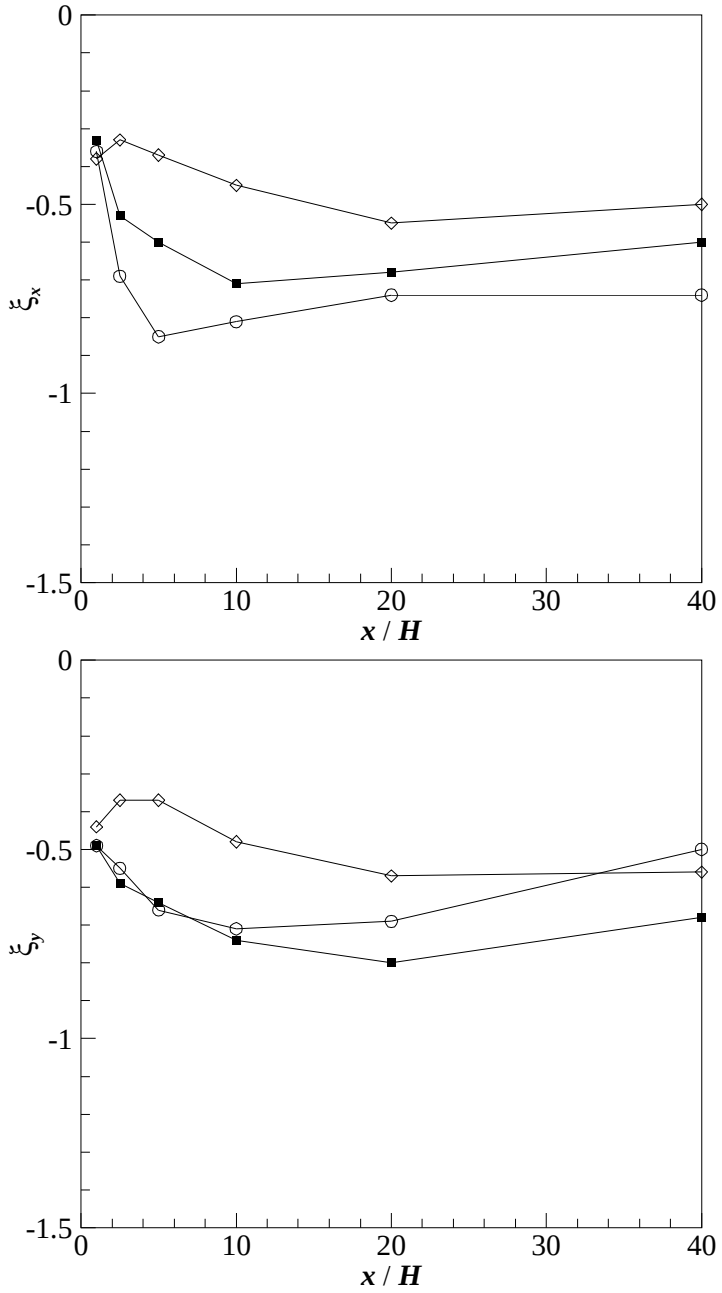

Figure 4.66 Scaling exponent in the inertial-convective regime of the (a) longitudinal and (b) vertical two-point correlation functions for three source nozzle diameters. Data shown for Re = 10,000 and D = 2.2 mm (○), 4.7 mm (■), and 9.4 mm (◊).

Figure 4.67 Definition of the geometry of the (a) longitudinal, and (b) vertical three-point correlation functions. The arrow shows the direction of the streamwise direction.

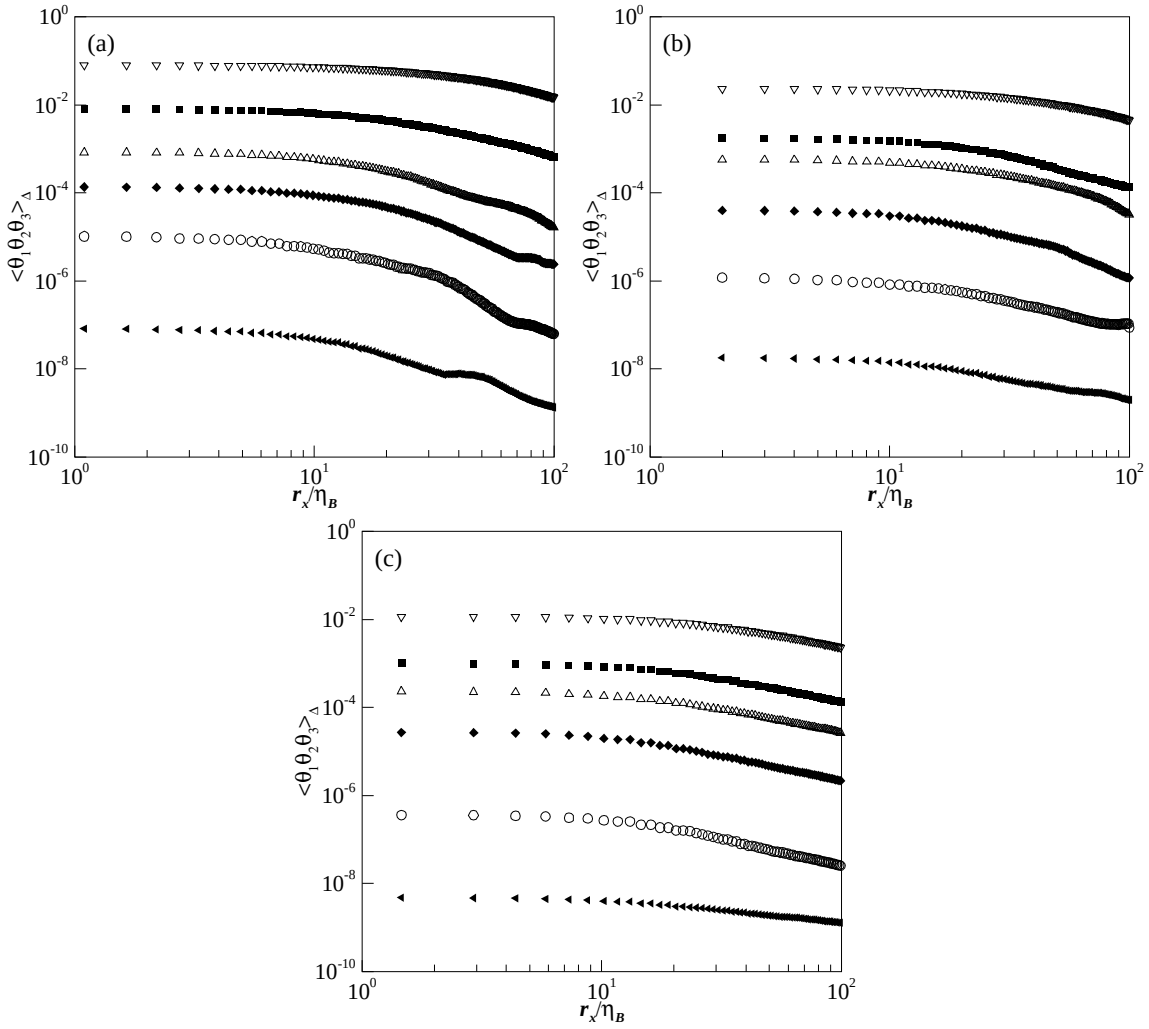

Figure 4.68 Longitudinal three-point correlation function of the fluctuating scalar field for (a) Re = 5000, (b) 10,000, and (c) 20,000. Data shown for D = 4.7 mm at x = 0.1 m (▽), 0.25 m (■), 0.5 m (△), 1 m (♦), 2 m (○), and 4 m (◀).

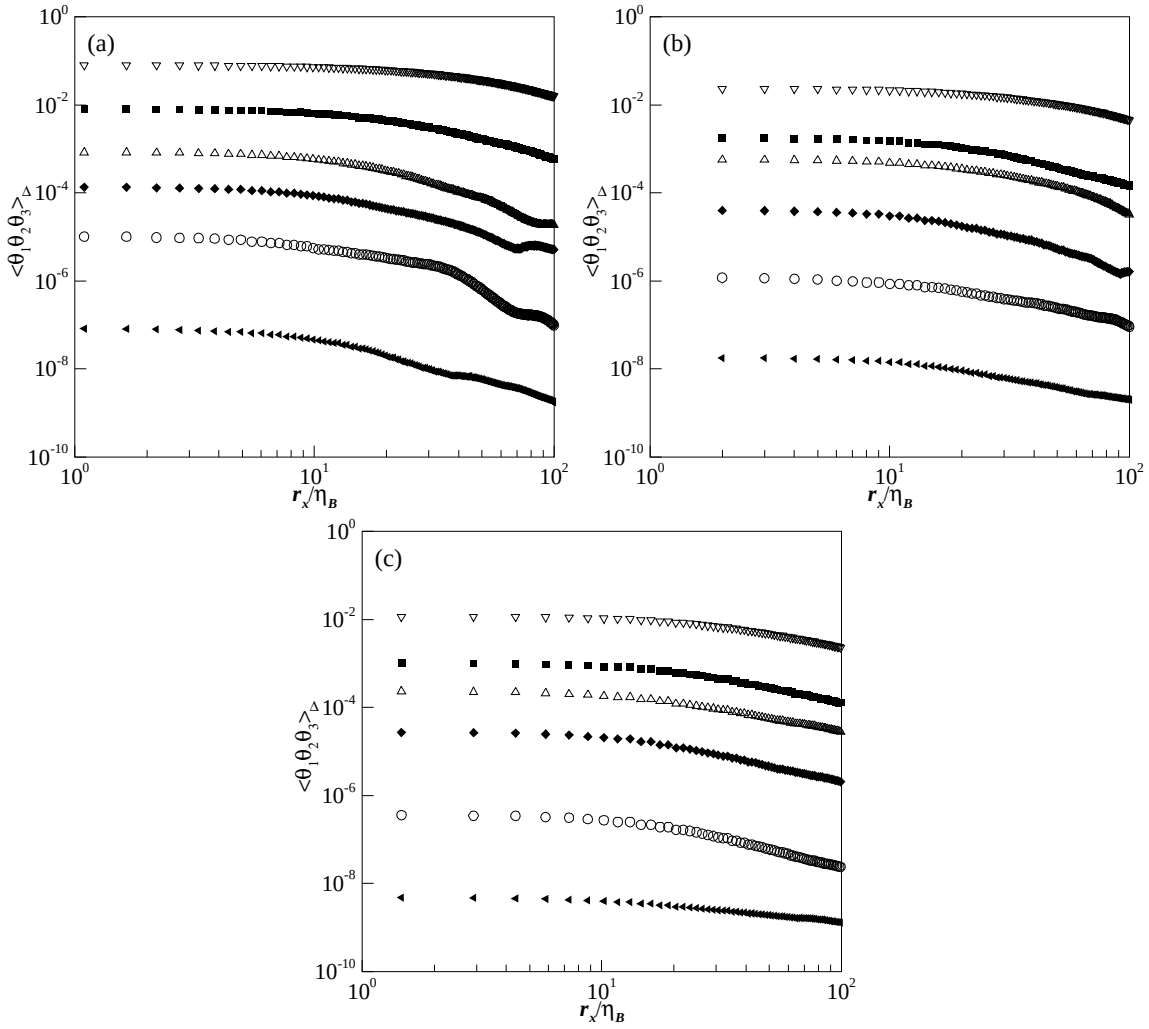

Figure 4.69 Vertical three-point correlation function of the fluctuating scalar field for (a) Re = 5000, (b) 10,000, and (c) 20,000. Data shown for D = 4.7 mm at x = 0.1 m (▽), 0.25 m (■), 0.5 m (△), 1 m (♦), 2 m (○), and 4 m (◀).

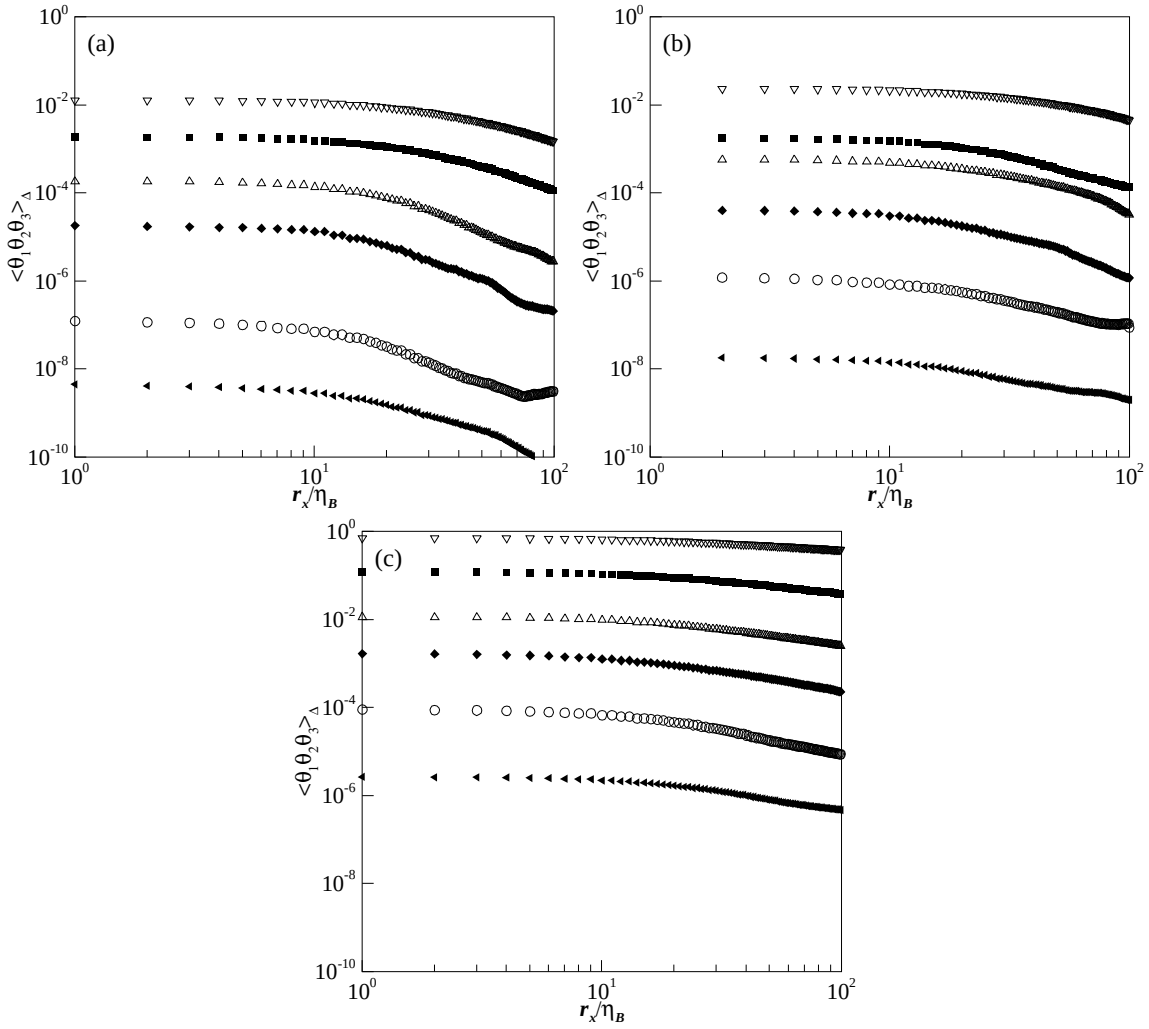

Figure 4.70 Longitudinal three-point correlation function of the fluctuating scalar field for (a) D = 2.2 mm, (b) 4.7 mm, and (c) 9.4 mm. Data shown for Re = 10,000 at x = 0.1 m (▽), 0.25 m (■), 0.5 m (△), 1 m (♦), 2 m (○), and 4 m (◀).

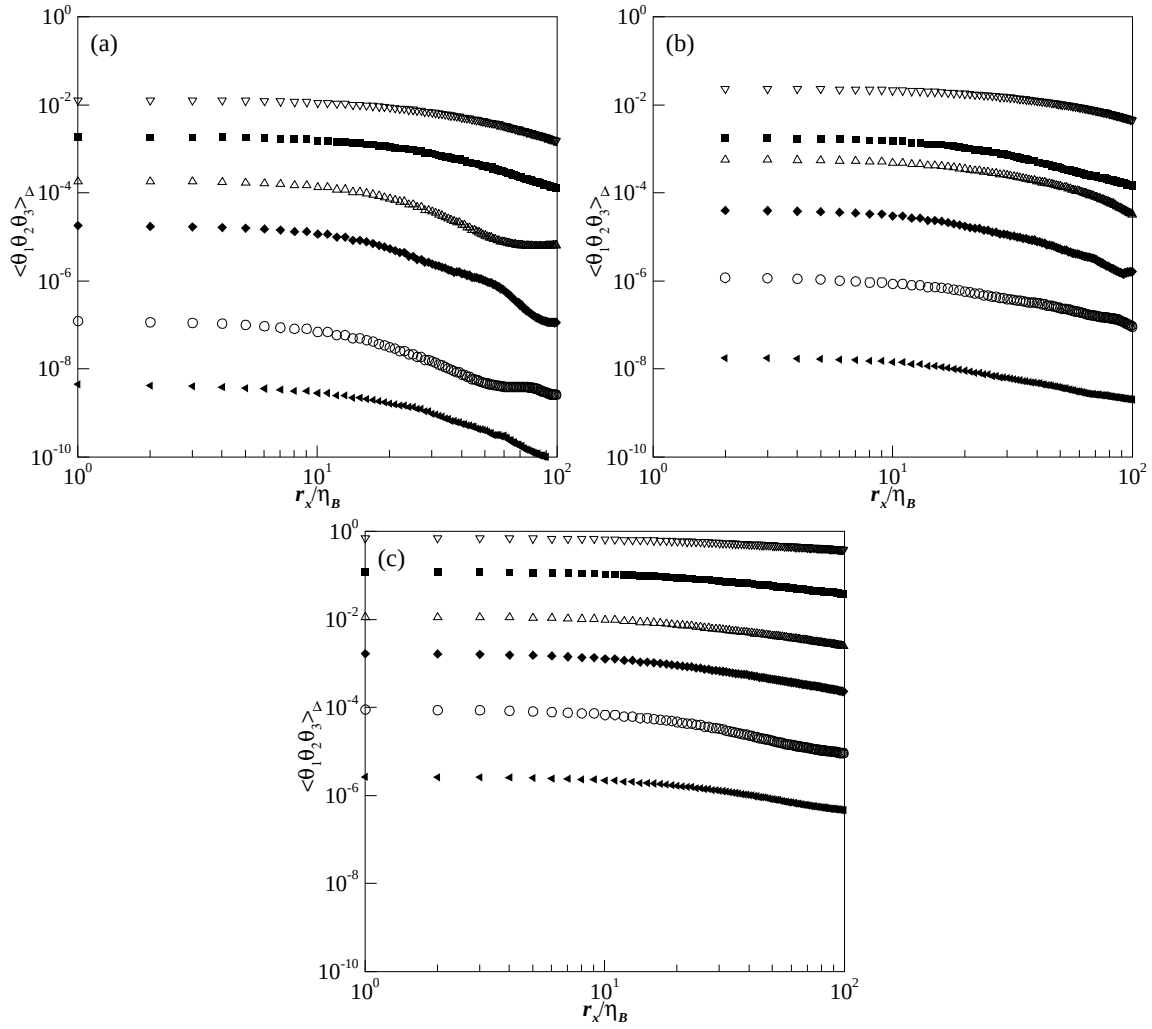

Figure 4.71 Vertical three-point correlation function of the fluctuating scalar field for (a) D = 2.2 mm, (b) 4.7 mm, and (c) 9.4 mm. Data shown for Re = 10,000 at x = 0.1 m (▽), 0.25 m (■), 0.5 m (△), 1 m (♦), 2 m (○), and 4 m (◀).

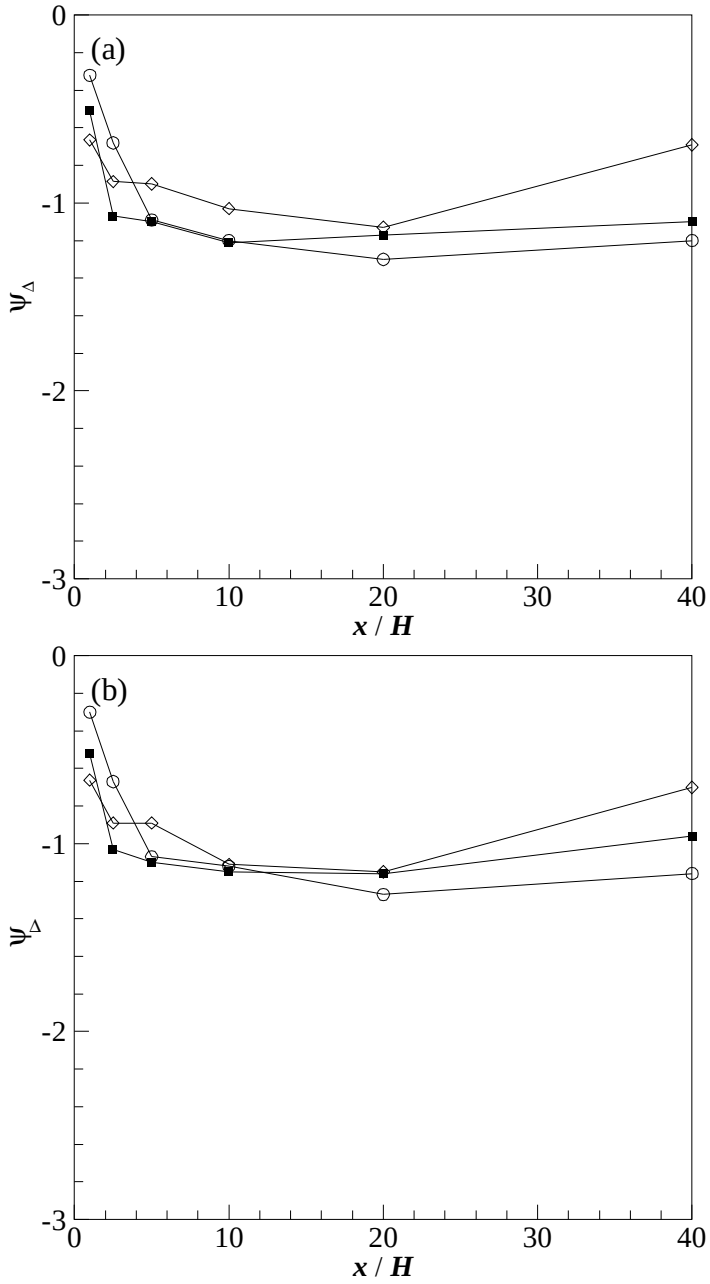

Figure 4.72 Inertial-convective scaling exponent of the (a) longitudinal and (b) vertical three-point correlation function for three Reynolds numbers. Data shown for D = 4.7 mm and Re = 5000 (○), 10,000 (■), and 20,000 (◊).

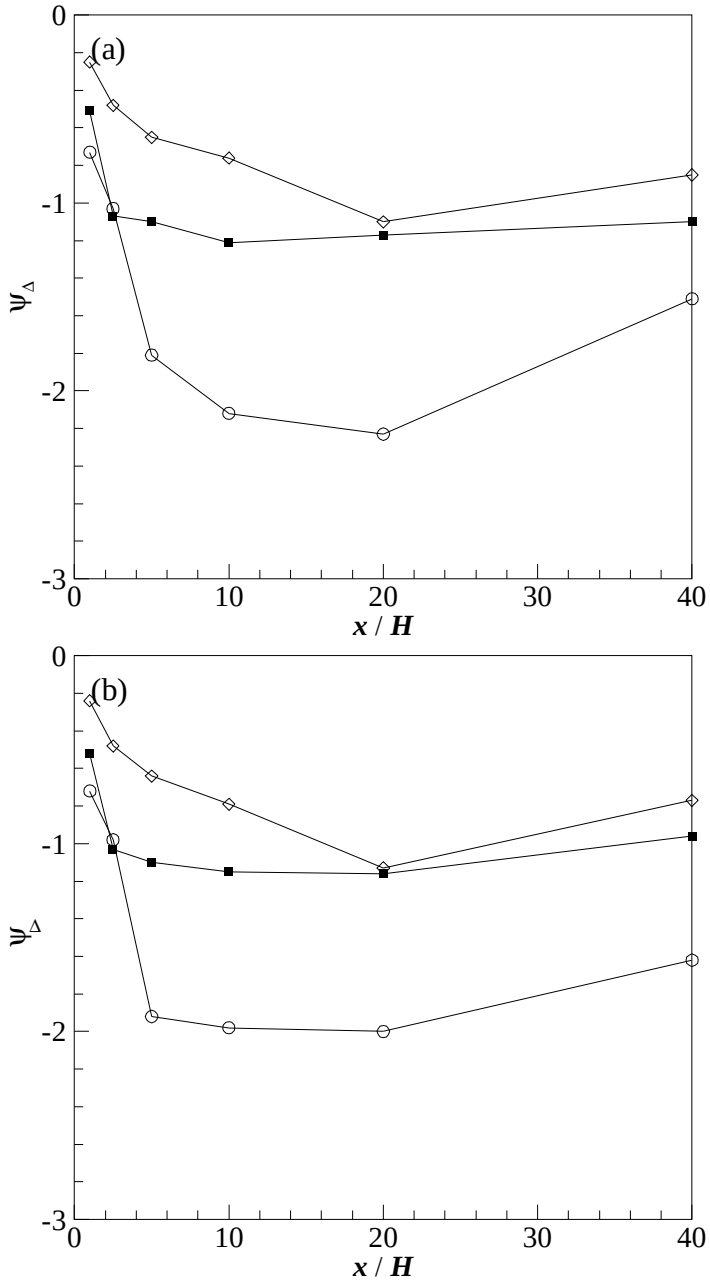

Figure 4.73 Inertial-convective scaling exponent of the (a) longitudinal and (b) vertical three-point correlation function for three source nozzle diameters. Data shown for Re = 10,000 and D = 2.2 mm (○), 4.7 mm (■), and 9.4 mm (◊).

Chapter 5

Fractal Geometry of the Passive Scalar Iso-surfaces

5.1 Introduction

The previous Chapter described the passive scalar field from a classical turbulence theory point of view. It is clear that the scaling behavior deviates from the local isotropic predictions at modest Reynolds numbers due to a number of global anisotropic characteristics such as mean scalar and velocity gradients, large-scale intermittency of the scalar field, and the injection size of the scalar. Addressing the dynamics of clearly anisotropic fields from a classical isotropic turbulence theory perspective obviously does not characterize the mixing dynamics completely. For instance, the passive scalar field in this study is essentially the union of partially mixed scalar filaments with the surrounding unmixed fluid. The mixed and unmixed regions of the flow are separated by sharp interfaces with steep gradients. These interfaces are typically wrinkled and convoluted surfaces that are constantly evolving and advecting with the turbulent flow. The description of the geometry of scalar interfaces is of immense practical importance for many natural and engineered reactive and non-reactive mixing problems.

The motivation for an alternative analysis approach, which describes the geometry of the scalar interfaces, arises from the fact that mixing of mixed and unmixed fluids occurs at the interface through molecular diffusion across the steep gradient. The rate of mixing is therefore primarily dependent on the total area of the interface and the strength of the gradient at the interface. Fluid turbulence increases the interface area via stretching and

folding actions and continually develops steep scalar gradients across the interface. The characterization of passive scalar interfaces is therefore critical to develop models for prediction of pollutant levels in natural situations such as volcanic eruptions or discharge of waste-water into a stream. Such a characterization is also important in reactive mixing where the interfacial area governs the rate of the chemical reaction between two chemical species (e.g. gasoline and air) which is often desired to be most efficient.

As described in the Chapter 2, fractal geometry provides a number of measures to describe complex geometrical shapes and can be applied to scalar interfaces. This chapter aims to complement the classical analysis in the previous chapter by employing the tools of fractal geometry. The passive scalar iso-surfaces are first characterized through fractal measures followed by a study of the evolution of these measures with the mixing of the plume. The primary focus is the effect of flow parameters such as Reynolds number and injection length scale on the evolution of these measures. The set of fractal measures used to study the geometry of scalar iso-surfaces include the coverage count, coverage fraction, coverage dimension, coverage length, largest empty box (LEB)-scale PDF, scale cumulative length-area ratio, scale local length area density, and lacunarity. The numerical methods used and a description of these measures follows.

5.2 Numerical method

Concentration iso-surfaces for defined concentration threshold levels were extracted for the scalar field captured in the 512×512 pixel array corresponding to the "uniform mean gradient" region (see Figure 3.8) using the boundary outline pixel methodology. The

box-counting algorithm (Schuerg 2003) is used to generate the coverage count for the iso-surface generated for every image. The coverage count is used to calculate all fractal measures of interest, except lacunarity for which a gliding-box algorithm is implemented.

5.2.1 Concentration thresholds

Concentration iso-surfaces corresponding to four thresholds were extracted for each image. The threshold concentration, $\Theta_{th}(m)$, corresponds to m times the local concentration standard deviation above the local mean concentration (i.e. $\Theta_{th}(m) = \langle \Theta \rangle + m \langle \theta^2 \rangle^{1/2}$), where m is chosen to be 1, 3, 5 and 7. These thresholds are chosen to examine the effects of varying concentration threshold on the fractal measures. The range of concentration thresholds is bounded due to noise and limited sample size of the data sets. Due to the intermittent nature of the plume, the local mean concentration is orders of magnitude lower than the instantaneous concentration. The signal to noise ratio of intensities corresponding to concentrations lower than the local mean are poor and therefore limits the range of thresholds to be greater than the mean concentration. Also, for $m > 7$ only a small number of images contain an iso-surface, which prevents statistically-converged measures. Therefore, noise and total sample size determine the range of concentration thresholds that may be chosen.

5.2.2 Scalar iso-surface extraction

Schuerg (2003) discusses several iso-surface extraction methods and concludes that the boundary outline pixel approach is the superior method. A primary advantage of the boundary outline pixel method is that it eliminates the asymmetry between identifying

"island" and "lakes" in the field. The boundary outline pixel methodology identifies a pixel to be either a boundary pixel or otherwise. The methodology considers the concentration of every pixel and compares it with the concentration of the eight neighboring pixels to identify boundary pixels. A pixel under consideration is examined as the "center pixel". If the concentration of the center pixel is greater than or equal to the threshold concentration, then the surrounding eight pixels are examined for threshold crossings. A neighboring pixel with a concentration below the threshold indicates a crossing in between that pixel and the center pixel. A linear interpolation of the concentration between the two pixels is used to calculate the location of the crossing. The pixel closest to the crossing is then flagged as a boundary outline pixel. If the location is exactly in the middle of the two pixels then both pixels are flagged as the boundary outline pixel.

The above methodology is used for every image to generate the iso-surface for the defined concentration thresholds. The outcome is a binary image consisting of the iso-surface.

5.3 Fractal measures and calculations

The fractal dimension described in the literature review is a phenomenological definition. A more rigorous and general definition is the Hausdorff dimension, $\dim_H$, which is defined based on the *s*-dimensional Hausdorff measure, $H^s(A)$, of a set $A \subset \mathbb{R}^n$. Where the *s*-dimensional Hausdorff measure is defined as:

$$H^s(A) = \lim_{\delta \to 0} \left(\inf \left\{ \sum_{1}^{\infty} |Z_i|^s : \{Z_i\} \textit{is a } \delta\textit{-cover of } A \right\} \right) \tag{5.1}$$

where the δ-cover $\{Z_i\}$ is defined as the countable or finite union of non-empty open sets $Z_i \subset \mathbb{R}^n$ with diameter $|Z_i| = \sup\{|x-y| : x, y \in Z_i\}$ less than δ that cover the set A (i.e. $A \subseteq \bigcup_{i=1}^{\infty} Z_i$). The Hausdorff measure defined above satisfies all the properties of a measure and most importantly is equal to zero if $s > \dim_H$ and infinite for $s < \dim_H$ for a unique real number, $0 \le \dim_H < \infty$. The Hausdorff dimension, $\dim_H$, is thus defined as the infimum of all $s > 0$ such that $H^s(A) = 0$. Other variations of the above definition exist, for instance the Hausdorff-Besicovitch dimension is defined similar to the Hausdorff dimension with the constraint that $\{Z_i\}$ be open balls of diameter less than δ.

5.3.1 Coverage count and coverage dimension

The above definition of fractal dimension is difficult to implement practically due to the challenge of obtaining the most economical coverage. To avoid these complications another fractal dimension, called the coverage dimension, is widely used as an alternative. The coverage dimension is defined as the logarithmic derivative of the coverage count of the fractal. The coverage count of the fractal is obtained by the box-counting algorithm, which subdivides the domain into a grid of box size λ, and counts the number of boxes, $N_d(\lambda)$, that contain any part of the object. The box counting algorithm counts $N_d(\lambda)$ for consecutively smaller box sizes to generate the coverage

count of the object. The function $N_d(\lambda)$ is called the coverage count. The coverage dimension or box-counting dimension, $D_d(\lambda)$, is then defined as:

$$D_d(\lambda) = -\frac{d \log N_d(\lambda)}{d \log \lambda} \tag{5.2}$$

The term fractal dimension is used synonymously with coverage dimension for the rest of the Chapter. In general, the coverage dimension is not equal to the Hausdorff dimension even for simple deterministic self-similar fractals, but it successfully captures most characteristics of fractals. These advantages motivated most previous work on fractal objects in turbulence to use the coverage dimension as the tool of choice.

The choice of the starting location for the box-counting subdivision is arbitrary and affects the coverage count calculation. Following the algorithm described in Schuerg (2003) the starting location for the subdivision is shifted to eight locations in both the horizontal and vertical coordinate directions. The coverage count is ensemble averaged over the estimates from each of the shifted starting locations. The shifting algorithm is constrained at the largest and finest scales due to the finite image size and image resolution, respectively. Subdivision boxes that extend past the boundary of the image are filled with image data from the opposite side of the image (i.e. a wrap around approach).

5.3.2 Coverage statistics

There are a number of other measures based on the coverage count that yield a comprehensive description of the fractal geometry of the iso-surfaces. These measures are collectively called the coverage statistics. The coverage statistics of a set focus on the

space filling properties and scale distributions of the set. Catrakis and Bond (2000) provided a valuable overview of the coverage statistics.

All of the measures in the coverage statistics are based on the coverage count generated by the box-counting algorithm. In the box-counting algorithm, the maximum image area is termed as the bounding box of size δ_b ($=512$ pixels for the present study). The bounding box is subdivided into $N_{2,tot}(\lambda)$ squares of area λ^2, and the number of squares that contain any part of the iso-surface is counted as $N_2(\lambda)$. The subscript 2 stands for the embedding dimension, $d=2$ for our measurements. The coverage count is generated for the range $0<\lambda<\delta_b$ at logarithmically equally-spaced discrete values of λ. The coverage count and the coverage dimension can be related by integrating Equation 5.2 to yield:

$$N_d(\lambda) = \exp\left(\int_{\lambda}^{\delta_b} D_d\left(\tilde{\lambda}\right) d\ln\tilde{\lambda} \right) \tag{5.3}$$

The above equation demonstrates the fact that the coverage count at a given scale λ is dependent on the complexity at all scales above λ. The coverage fraction, $F_d(\lambda)$, is defined as the fraction of space occupied by the object at a scale λ. It is estimated as the ratio between the coverage count and the maximum boxes for the scale size λ, given by the following equation:

$$F_d(\lambda) = \frac{N_d(\lambda)}{N_{d,tot}(\lambda)} = \frac{N_d(\lambda)}{(\delta_b/\lambda)^d} \tag{5.4}$$

where the subscript d refers to the embedding dimension which is equal to 2 for the present measurements.

The coverage length, $L_d(\lambda)$, measures the total length of the fractal in the bounding box using the ruler of size λ. For the present case with $d = 2$, this measure corresponds to the length of the interface boundary for the scalar field measured. For higher dimension, it corresponds to interface area, volume, and so on per bounding box. This measure is estimated as:

$$L_d(\lambda) = \lambda^{d_t} N_d(\lambda) \tag{5.5}$$

where d_t is the topological dimension of the set and is equal to 1 for our measurements. Note that $L_d(\lambda)$ increases with decreasing λ and tends to the total coverage length, $L_{d,tot}$, as $\lambda \to \eta_B$, which is the smallest length scale of structure present in the scalar field. For $\lambda < \eta_B$, no additional fine structure exists in the iso-surface, which results in no change in $L_d(\lambda)$. We represent this measure as the coverage length per unit bounding box area.

Another measure is the largest empty box scale PDF (LEB-scale PDF), $f_d(\lambda)$, which is defined as the probability density of finding a λ-size largest empty box that contains no part of the object. For a unit embedding dimension the LEB-scale PDF is the PDF of spacing between consecutive points of the set. The significance of the LEB-scale PDF can be understood by interpreting the coverage fraction in a different manner. Recall that

the coverage fraction at a scale λ is the fraction of λ-sized boxes that contains any part of the object. This fraction is also the probability that a λ-sized box placed randomly in the bounding box covers some part of the object. This probability is also the probability that boxes of size λ and smaller do not contain any part of the fractal. This, in fact, corresponds to the cumulative density function of the largest empty box, i.e. the LEB-scale CDF. Therefore the LEB-scale PDF is the derivative of the coverage fraction, and by definition of coverage fraction, the area under the LEB-scale PDF is 1. Formally, $f_d(\lambda)$ and $F_d(\lambda)$ are related as:

$$f_d(\lambda) = \frac{dF_d(\lambda)}{d\lambda} \tag{5.6}$$

The LEB-scale PDF is also a measure of the distance from a randomly placed point in the bounding box to the nearest part of the object.

Catrakis et al. (2002) proposed an area-volume ratio, $\Omega_3(\lambda)$, as the ratio of the total interfacial area normalized by the volume of the bounding box. The total interfacial area is estimated as $L_3(\lambda) = \lambda^2 N_3(\lambda)$ and the volume of the bounding box equals δ_b^3. This dimension is generalized to other embedding dimensions, for $d \geq 2$, by the following relationship:

$$\Omega_d(\lambda) = \frac{\lambda^{d_t} N_d(\lambda)}{\left(\delta_b^d\right)^{d_t/d}} = \left(\frac{\lambda}{\delta_b}\right)^{d_t} N_d(\lambda) \tag{5.7}$$

For our data the embedding dimension is $d = 2$, thus this measure is interpreted as the length-area ratio and is qualitatively the same as the coverage length per bounding box area. Catrakis et al. (2002) also defined the logarithmic derivative of $\Omega_d(\lambda)$ and related it to the fractal dimension as:

$$\alpha_\Omega(\lambda) = \frac{d \log \Omega_d(\lambda)}{d \log \lambda} = D_d(\lambda) - d_t \tag{5.8}$$

In general, $\Omega_d(\lambda)$ increases with decreasing scale λ, and tends towards the total area-volume ratio of the iso-surface, $\Omega_{d,tot}$, as $\lambda \to \eta_B$.

Catrakis et al. (2002) also introduced the area-volume density parameter, $g_3(\lambda)$, as the local contribution at scale λ to the cumulative area-volume ratio $\Omega_3(\lambda)$. $g_d(\lambda)$ is therefore defined as the negative of the derivative of $\Omega_d(\lambda)$ given by:

$$g_d(\lambda) = -\frac{d\Omega_d(\lambda)}{d\lambda} \tag{5.9}$$

The logarithmic derivative of $g_d(\lambda)$ is also has significance. If it is a constant value, then that indicates a power law scaling behavior (i.e. $g_d(\lambda) \propto \lambda^{-\alpha_g}$, where $\alpha_g(\lambda)$ is the logarithmic derivative defined in the following equation). Also, $\alpha_g(\lambda) \geq 0$ can be considered as a scale-local dimension.

$$\alpha_g(\lambda) = -\frac{d \log g_d(\lambda)}{d \log \lambda} \tag{5.10}$$

The above mentioned fractal measures are estimated from the discrete coverage count $N_2(\lambda)$ generated at 10 levels of λ, using the box-counting algorithm of the boundary outline of the passive scalar at the defined thresholds levels. The 10 levels of λ, denoted by λ_s, correspond to 512, 256, 128, 64, 32, 16, 8, 4, 2 and 1 pixels for $s = 1, 2, ..., 10$ (where the size of the bounding box is $\delta_b = 512$). Therefore, $\lambda_s / \delta_b = 2^{-s}$.

Because some of the fractal measures introduced above are non-linearly related to coverage count, there is an ambiguity with respect to ensemble averaging the results for the 12,000 images recorded at any location. For example, the coverage dimension may be calculated as the logarithmic derivative of the average coverage count of all the image samples, or the average of the logarithmic derivatives of the individual coverage counts for each image. The two results will obviously defer and we argue that the later is not justified from the following discussion. Suppose A is an unbounded multi-fractal set in $\mathbb{R}^n$ and the coverage dimension of A is defined as above. It is desired that the coverage dimension (or any other coverage statistic) of A be estimated experimentally from a collection of disjoint boxes $Z_i \subset \mathbb{R}^n$ with $|Z_i| = \delta_b^n$ and $\lim_{k \to \infty} \bigcup_{i=1}^{k} Z_i \to A$. It is clear that the coverage count of A, $N_A(\lambda)$, for the range of scales given by $0 \le \lambda \le \delta_b$ is the sum of the coverage counts of the individual Z_i, $N_{Z_i}(\lambda)$ (i.e. $N_A(\lambda) = \sum_i N_{Z_i}(\lambda)$) by definition. The coverage dimension, $D_A(\lambda)$, therefore by definition is the logarithmic derivative of $N_A(\lambda)$, with the approximation better for a bigger collection of Z_i. Because A is an arbitrary multi-fractal there may be a non-empty subset $\Pi \subset \{Z_i\}$ such

that $Z_i \cap A = \varnothing$ for all $Z_i \in \Pi$. Since the coverage dimension and coverage count are defined only for non-empty bounding boxes, defining the coverage dimension as the average of individual coverage dimensions, $D_{Z_i \cap A}(\lambda)$, is undefined. Some authors have previously chosen to ignore $Z_i \in \Pi$ to obtain the average coverage dimension over the individual coverage dimensions (e.g. Frederiksen et al. 1996). However, we argue that such an approach is inconsistent with the definition of coverage count as the result depends on the size of the bounding box, δ_b. For instance, reducing the size of the bounding box would result in ignoring of a larger number of empty boxes which biases the measures to be more space filling than the object really is.

From the above argument it is clear that all fractal measures must be derived from the averaged coverage count. The following equations are used to calculate the fractal measures from the average of the discrete coverage count obtained for every case, $\langle N_2(\lambda_s) \rangle$. The discretized equations for coverage fraction, F_2; coverage length, L_2; length-area ratio, Ω_2; coverage dimension, D_2; LEB-scale PDF, f_2; length-area ratio exponent, α_Ω; length-area density, g_2; and length-area density exponent, α_g; are respectively:

$$\langle F_2(\lambda_s / \delta_b) \rangle = \left(\frac{\lambda_s}{\delta_b} \right)^2 \langle N_2(\lambda_s / \delta_b) \rangle \tag{5.11}$$

$$\langle L_2(\lambda_s / \delta_b) \rangle = \lambda_s \langle N_2(\lambda_s / \delta_b) \rangle \tag{5.12}$$

$$\langle \Omega_2(\lambda_s / \delta_b) \rangle = \frac{\lambda_s}{\delta_b} \langle N_2(\lambda_s / \delta_b) \rangle \tag{5.13}$$

$$\left\langle D_2\left(\lambda_{s+1/2}/\delta_b\right)\right\rangle = -\frac{\log_{10}\left\langle N_2\left(\lambda_s/\delta_b\right)\right\rangle - \log_{10}\left\langle N_2\left(\lambda_{s+1}/\delta_b\right)\right\rangle}{\log_{10}\left(\lambda_s/\delta_b\right) - \log_{10}\left(\lambda_{s+1}/\delta_b\right)} \tag{5.14}$$

$$\left\langle f_2\left(\left(\lambda_s+\lambda_{s+1}\right)/2\delta_b\right)\right\rangle = \frac{\left\langle F_2\left(\lambda_s/\delta_b\right)\right\rangle - \left\langle F_2\left(\lambda_{s+1}/\delta_b\right)\right\rangle}{\left(\lambda_s/\delta_b\right) - \left(\lambda_{s+1}/\delta_b\right)} \tag{5.15}$$

$$\left\langle \alpha_\Omega\left(\lambda_{s+1/2}/\delta_b\right)\right\rangle = -\frac{\log_{10}\left\langle \Omega_2\left(\lambda_s/\delta_b\right)\right\rangle - \log_{10}\left\langle \Omega_2\left(\lambda_{s+1}/\delta_b\right)\right\rangle}{\log_{10}\left(\lambda_s/\delta_b\right) - \log_{10}\left(\lambda_{s+1}/\delta_b\right)} \tag{5.16}$$

$$\left\langle g_\Omega\left(\left(\lambda_s+\lambda_{s+1}\right)/2\delta_b\right)\right\rangle = -\frac{\left\langle \Omega_2\left(\lambda_s/\delta_b\right)\right\rangle - \left\langle \Omega_2\left(\lambda_{s+1}/\delta_b\right)\right\rangle}{\left(\lambda_s/\delta_b\right) - \left(\lambda_{s+1}/\delta_b\right)} \tag{5.17}$$

$$\left\langle \alpha_g\left(\left[\left(\left(\lambda_s+\lambda_{s+1}\right)\right)\left(\left(\lambda_{s-1}+\lambda_s\right)\right)\right]^{0.5}/2\delta_b\right)\right\rangle = -\frac{\log_{10}\left\langle g_\Omega\left(\left(\lambda_s+\lambda_{s+1}\right)/2\delta_b\right)\right\rangle - \log_{10}\left\langle g_\Omega\left(\left(\lambda_{s-1}+\lambda_s\right)/2\delta_b\right)\right\rangle}{\log_{10}\left(\left(\lambda_s+\lambda_{s+1}\right)/2\delta_b\right) - \log_{10}\left(\left(\lambda_{s-1}+\lambda_s\right)/2\delta_b\right)} \tag{5.18}$$

In addition to the above coverage statistics, the lacunarity measure is also calculated from the boundary pixel images of the measured scalar fields. The lacunarity is not related to the coverage count and is a measure of the homogeneity of the iso-surfaces. The lacunarity is defined as the ratio of second moment to the square of the average of the spatial mass-distribution function of any set. The gliding-box algorithm is used to generate the mass distribution function for a given scale size λ. In this algorithm, a box of size λ glides across the set, sequentially residing in all possible positions. The number of pixels in the gliding box that contain any part of the fractal is defined as the mass of the gliding box. As the gliding box takes all possible positions in the bounding box, the mass fluctuates according to the spatial distribution of the set. The PDF of these

fluctuations of the mass is the mass-distribution at scale size λ, $pdf_\lambda(m)$. The Lacunarity at scale size λ, $\Lambda(\lambda)$, is defined as:

$$\Lambda(\lambda) = \frac{\int_{m=0}^{\infty} m^2 \, pdf_\lambda(m)\, dm}{\left(\int_{m=0}^{\infty} m \, pdf_\lambda(m)\, dm \right)^2} = 1 + \frac{\sigma_m^2}{\mu_m^2} \tag{5.19}$$

where σ_m^2 is the variance and μ_m is the mean of the mass-distribution function. A lacunarity of 1 indicates homogeneity, whereas larger values indicate spatial in-homogeneity.

5.4 Fractal geometry of iso-surfaces

5.4.1 Qualitative description

A sequence of boundary outline images for the concentration threshold $\Theta_{th}(m) = \langle \Theta \rangle + \langle \theta^2 \rangle^{1/2}$ (i.e. $m = 1$) is shown in Figures 5.1 – 5.6. Each figure corresponds to 16 consecutive images captured at each of the downstream distances for the case of $Re = 10,000$ and $D = 4.7$ mm. To get an idea of the physical dimension, compare the first iso-surface image in Figure 5.1 with Figure 4.1(a). Figures 5.1 – 5.6 provide a qualitative picture of the temporal and spatial evolution of the passive scalar iso-surfaces. The iso-surfaces appear randomly located in space and time with a shape that is impossible to define with Euclidian geometry. Also, the iso-surfaces occupy a very small portion of the bounding box leaving a large portion of the bounding box without structure. The convoluted nature of the iso-surfaces represents structure over a large range of scales from the Batchelor scale to the scale of the bounding box. The

scalar iso-surfaces possesses structure at larger scales (up to the integral length scale), but since the data corresponds to a zoomed-in view of the scalar field, we only examine the geometry within the dissipative scales (i.e. from the Batchelor scale to the upper end of the inertial-convective range). Schuerg (2003) showed that the coverage statistics calculated from the zoomed-in view are valid in this range. Another important observation is that the iso-surface structure is visually unlike the passive scalar iso-surfaces generated by a high-momentum jet (e.g. Catrakis & Dimotakis 1996). The iso-surface structure in the present study is sparse without whorls or saddle structures. In addition, a single realization of the iso-surface cannot represent the true nature of the iso-surfaces, thus necessitating an ensemble averaging approach for the fractal characteristics.

By comparing the iso-surface sequences for the six downstream distances, it is clear that there is a qualitative change in the passive scalar structure. Farther from the source, the scalar structure appears to be more stretched and thinner. Also the fraction of images containing iso-surfaces is minimal for the $x/H = 2.5$ case and appears to increase with the downstream distance. This trend is similar to the previously discussed large-scale intermittency of the scalar field (see Figure 4.14).

The following subsections, 5.4.2 – 5.4.9, describes the scalar iso-surfaces quantitatively with respect to the coverage statistics. The primary focus is on the effects of concentration threshold, velocity characteristics (governed by Reynolds number of the

boundary layer flow), mean scalar characteristics (governed by distance from the source), and injection length scale (nozzle diameter) on these measures.

5.4.2 Coverage Count

The coverage count, $\langle N_2(\lambda)\rangle$, is essentially the average number of squares of size λ necessary to cover the iso-surface extracted from any realization of the scalar field. Obviously, this number increases with decreasing λ. Figure 5.7 shows the variation of the coverage count with respect to the four levels of threshold (m = 1, 3, 5, and 7). For reference, Table 5.1 tabulates the value of the Kolmogorov, Batchelor, and nozzle length scales in terms of the boundary box size.

Figure 5.7 shows a linear variation of the logarithm of $\langle N_2(\lambda)\rangle$ versus the logarithm of λ/δ_b over a significant range of λ/δ_b. The coverage count decreases with λ and threshold level. The variation with respect to threshold level is consistent with Miller and Dimotakis (1991) for passive scalar mixing in a jet. Also, the coverage count at $\lambda = \delta_b$ is not necessarily unity and decreases with increasing threshold due to the presence of empty bounding boxes. As the scale size increases and crosses over the Kolmogorov scale (at $\log_{10}(\lambda/\delta_b)$ = -1.2), the slope of the coverage count appears to reduce and the curve becomes flatter.

Table 5.1 Values of various length scales with respect to the bounding box size.

Re	*D* **(mm)**	$\log_{10}(D/\delta_b)$	η_B **(μm)**	$\log_{10}(\eta_B/\delta_b)$	η **(μm)**	$\log_{10}(\eta/\delta_b)$
5,000	4.7	-0.2	24	-2.5	758	-1.0
10,000	2.2	-0.5	13	-2.7	417	-1.2
10,000	4.7	-0.2	13	-2.7	417	-1.2
10,000	9.4	0.2	13	-2.7	417	-1.2
20,000	4.7	-0.2	9	-2.9	291	-1.4

Figure 5.8 shows the variation of coverage count with increasing distance from the source for the four threshold levels. Although there appears to be mild changes in the slope of the coverage count curves, it is difficult to determine a trend in the coverage count with respect to distance from the source. However, the variation in the magnitude of coverage count due to varying distance from the source appears to decrease with increasing threshold. In particular, the separation of the profiles decreases with increasing threshold.

Figure 5.9 shows the variation of the coverage count as a function of Reynolds number. It is clear that the coverage count monotonically increases with Reynolds number at scale sizes smaller than the Kolmogorov scales. However, for larger scale sizes there appears to be crossover among the curves for the different Reynolds numbers. This may indicate that at scales larger than the chosen bounding box, the coverage count decreases with increase in Reynolds number.

Figure 5.10 shows the variation of the coverage count as a function of the injection length scale. The coverage count is observed to increase with the nozzle diameter with the amount of increase smaller at larger scales. The curves appear to collapse for scale sizes larger than the Kolmogorov length scale.

5.4.3 Coverage Fraction

The coverage fraction, $\langle F_2(\lambda) \rangle$, is the expected fraction of the bounding box that is occupied by the iso-surface at a scale size of λ. The coverage fraction is also interpreted as the probability that a box of size λ placed randomly in the bounding box will contain any part of the iso-surface. Yet another interpretation is that it is the probability that the size of the largest-empty box, which does not contain any part of the fractal, is of size λ or less. Figure 5.11 shows the variation of the coverage fraction curve for the four concentration thresholds. The coverage fraction increases with scale size irrespective of the threshold level. Also, for higher thresholds the slope of the curve clearly increases as the scale size crosses over the Kolmogorov length scale and the curves appear to coverge at a scale larger than the size of the bounding box. The curves are nearly parallel in the viscous-convective regime ($-2.7 < \log_{10}(\lambda/\delta_b) < -1.2$). The magnitude of the coverage fraction shows that the iso-surfaces occupy over 10% area of the bounding box at the scale size δ_b, whereas at the scale size of the Batchelor length scale, the iso-surfaces occupy less than one hundredth of the area. The coverage fraction is less than unity (< 0 in logarithmic scale) at scale size δ_b due to the empty realizations of the bounding box.

Figure 5.12 shows the variation of coverage fraction with increasing distance from the source for the four different thresholds. For the lowest threshold it is clear that the coverage fraction reflects the behavior of the large-scale intermittency. Recall that the intermittency decreases with distance reaching a minimum at $x/H = 2.5$ and later increases. The coverage fraction in the viscous-convective regime of Figure 5.12(a) shows the same trend, where the coverage fraction decreases with a minimum for $x/H = 2.5$ and increases steadily further downstream. From Figure 5.11 it was shown that the coverage fraction decreases with increasing threshold. Figure 5.12 indicates that the effect of increasing threshold is more severe at larger distances from the source. The trend in the viscous-convective regime of Figure 5.12(d) is the opposite of the trend in Figure 5.12(a). The coverage fraction curves appear to collapse in the inertial-convective range ($-1.2 < \log_{10}(\lambda/\delta_b) < 0$) as seen in Figure 5.12(d).

Figure 5.13 shows the variation of the coverage fraction as a function of the Reynolds number of the flow. The coverage fraction clearly increases with Reynolds number in the viscous-convective regime. However, in the inertial-convective regime the lowest Reynolds number yields the highest coverage fraction at scale sizes of the order of δ_b.

Figure 5.14 shows the variation of the coverage fraction as a function of the nozzle diameter. The coverage fraction increases with the injection length scale in the viscous-convective range, but the rate of increase appears to decreases for larger injection length scales. The coverage fraction curves for the higher injection length scales are closer to each other in the viscous-convective range than the coverage fraction curve for the lowest

injection length scale. The curves converge and in some cases cross in the inertial-convective regime.

5.4.4 Coverage Dimension

The coverage dimension $\langle D_2(\lambda)\rangle$, is perhaps the most studied fractal measure for passive scalar iso-surfaces. As reported in the literature review, contradicting observations exist regarding the coverage dimension of the passive scalar iso-surfaces. Sreenivasan and Meneveau (1986) observed a constant fractal dimension with respect to scale size, while Catrakis & Dimotakis (1996) observed a scale-dependent fractal dimension implying a level 3 complexity of the iso-surfaces. Figure 5.15 shows the variation of the coverage dimension with respect to concentration threshold. The coverage dimension approaches the topological dimension, $d_t = 1$, as $\lambda \to \eta_B$ reflecting the fact that iso-surfaces are ultimately smooth curves. From the figure the coverage dimension is clearly scale dependent, irrespective of threshold, in agreement with observations of Catrakis & Dimotakis (1996) for high momentum jets. The coverage dimension for all thresholds increases with scale in the viscous-convective range $-2.7 < \log_{10}(\lambda/\delta_b) < -1.2$, indicating that the convolution of the iso-surfaces appears to be more space filling. Also, the coverage dimension is less sensitive to variations in the concentration threshold. The coverage dimension appears to be the same for the three higher concentration thresholds, while that of the lowest threshold shows a mildly elevated coverage dimension. The elevated curve for the lowest threshold iso-surface was also observed by Schuerg (2003) and was attributed to noise.

The curves beyond the Kolmogorov length scale are sensitive to variations in the concentration threshold where coverage dimension appears to decrease with scale size for the higher concentration thresholds. The decrease in coverage dimension is due to the fact that at scales larger that the Kolmogorov scale, the scalar blobs are completely inside the λ-sized box thereby appearing as a collection of spots. This explains why the coverage dimension falls below $d_t = 1$. As the size of the boxes increases, the iso-surfaces appear more and more "spotty". Note that for the lowest concentration threshold the coverage dimension continues to increase with scale sizes in the inertial-convective regime. This variation is not an artifact of noise but instead indicates that the size of the scalar iso-surfaces (interpreted as a closed loop of iso-surface of a blob) at low thresholds increases faster than the size of iso-surfaces of higher thresholds. This is true because these iso-surfaces correspond to the far edges of the scalar blobs where molecular diffusion is expanding the iso-surface.

Figure 5.16 shows the variation of the coverage dimension with increasing distance from the source for different concentration threshold levels. The coverage dimension corresponding to the lower thresholds for the farthest downstream distance cases are not shown due to the influence of noise. It is clear from the figure that the coverage dimension in the viscous-convective regime is nearly independent of downstream distance from the source. Therefore, the coverage dimension in the viscous-convective regime is dependent on neither concentration threshold nor any global characteristic of the scalar field such as intermittency or the mean scalar gradient.

For scale sizes larger than the Kolmogorov length scale the coverage dimension is clearly dependent on the global characteristics of the mean scalar field. The coverage dimension in the inertial-convective regime decreases with increasing distance from the source. This indicates that the iso-surfaces become more sparse with less clusters of structure that tend to increase the coverage dimension. Also, in Figures 5.16(c and d) the coverage dimension curves in the inertial-convective regime for the far downstream cases vary little with distance. Most of the variation occurs for $x/H < 10$, indicating that an equilibrium is reached for $x/H > 10$ such that the characteristics of the geometry of the iso-surfaces are fixed in the inertial-convective regime . This trend cannot be confirmed in Figures 5.16(a and b) because noise elevated the coverage dimension curves for the farthest three measurement locations.

Figure 5.17 shows the variation of coverage dimension with Reynolds number. In the viscous-convective regime the coverage dimension appears to be independent of Reynolds number except for the lowest Reynolds number where the curve is flatter than those for higher Reynolds numbers. It can be concluded that the coverage dimension in the viscous-convective range behaves in a universal manner for high Reynolds numbers. In the inertial-convective range, the coverage dimension increases with Reynolds number. This increase may be explained from Figure 4.15 which shows the intermittency factor increasing with Reynolds number. This implies that the scalar field does not appear as sparse as for lower Reynolds number, thereby increasing the coverage dimension. Note that the coverage dimension remains below 1 in the inertial-convective range for the range of Reynolds numbers. For higher Reynolds number, the coverage

dimension in this range may exceed 1, which would indicate that the iso-surfaces, although sparse, have smoother large scale structures.

Figure 5.18 shows the variation of coverage dimension with nozzle diameter. The universal behavior in the viscous-convective regime is evident. In the inertial-convective regime the coverage dimension is lowest for D = 2.2 mm and highest for D = 4.7 mm. Because of the non-monotonic trend with nozzle size, there appears to be factors, besides intermittency (i.e. Figure 4.15), influencing the coverage dimension.

5.4.5 Coverage Length and its underestimate

From an application point of view, the coverage area ($L_3(\lambda)$) is the most important measure of iso-surfaces because it measures the total interfacial area of iso-surfaces. Therefore, this measure is useful to predict mixing efficiency or the kinetics of reactive mixing. The coverage length, $\langle L_2(\lambda)\rangle$, estimated for the planar images measures the average total iso-surface length per bounding box size, δ_b. Therefore, $\langle L_2(\lambda)\rangle$ is the lower dimensional analog of the coverage area of concentration iso-surfaces. Figure 5.19 shows the total coverage length in millimeters per square millimeter of the measurement region for different concentration thresholds. In the viscous-convective range, the coverage length decreases with increasing scale and the curves corresponding to different thresholds appear nearly parallel. Above the Kolmogorov length scale, there is a change in the trend dependent on the threshold. For the lowest threshold the coverage length continues to decrease, whereas for the other thresholds the curve attains a local minima followed by an increase in coverage length. The increase with increasing scale size is

possible as the coverage dimension at these scales is less than unity. Overall, the coverage length decreases with increasing threshold. This decrease with increasing threshold can be explained in analogy to the contour lines of "tapered peaks or hills" of concentration. Increasing the threshold moves the contour up the hill while reducing the perimeter of the contour. Notice that as $\lambda \to \eta_B$, the coverage length of each curve appears to reach a constant value (i.e. the slope is flat). This is the true length of the iso-surfaces while the lengths measured at higher scales may be interpreted as artifacts of lower resolution.

Schuerg (2003) introduced the coverage length underestimate, $\left\langle L_{2,u}\left(\lambda/\delta_b\right)\right\rangle$, defined as:

$$\left\langle L_{2,u}\left(\lambda/\delta_b\right)\right\rangle = \frac{\left\langle L_{2,tot}\right\rangle}{\left\langle L_2\left(\lambda/\delta_b\right)\right\rangle} \tag{5.20}$$

The coverage length underestimate is essentially the ratio of the total iso-surface length to the length as it appears at a higher scale size. This measure is useful because the coverage length underestimate shows universal characteristics similar to the coverage dimension. Figure 5.20 shows the coverage length underestimate for four thresholds. The coverage length underestimate is independent of the threshold level in the viscous-convective range. Note that the curve corresponding to the lowest threshold shows elevated coverage length underestimates (similar to the elevated coverage dimension in Figure 5.15) in this regime due to the presence of noise as discussed in the context of coverage dimension.

Figure 5.21 shows the variation of coverage length (millimeter per unit square millimeter) with increasing downstream distance from the source. Again, the intermittency factor of the scalar field appears to explain the trend. The coverage length increases with intermittency factor due to more filaments per bounding box. This can be seen in Figure 5.21(a) which shows the variation with distance for the smallest threshold. However, the trend is reversed in Figure 5.21(d), which corresponds to the highest threshold. The trend reversal is due to the stronger influence of threshold which reduces the coverage length. Therefore, the reduction in coverage length due to increase in threshold dominates the increase in coverage length due to higher intermittency factors away from the source. Figure 5.22 shows the variation of coverage length underestimate corresponding to the coverage lengths shown in Figure 5.21. The curves corresponding to the lowest thresholds for the farthest three downstream distances have been ignored due to bias from noise. It is clear that the viscous-convective regime shows independence of the coverage length underestimate from concentration threshold and distance from the source. The variation of coverage length underestimate in the inertial-convective range with respect to distance from the source is similar to that of coverage dimension (see Figure 5.16). The underestimate decreases with increasing length scale and distance from the source. Also, the effect of increasing distance is prominent only for $x/H < 10$, whereas mild variation in the underestimate curves is present for data downstream.

Figure 5.23 shows the variation of coverage length as a function of Reynolds number. The coverage length increases with Reynolds number in the viscous-convective regime.

However, the coverage length at the lowest Reynolds number is observed to yield the higher coverage length at scale sizes of the order of δ_b. Figure 5.24 shows the coverage length underestimate at different Reynolds numbers. The figure indicates that the coverage length underestimate is independent of the Reynolds numbers in the viscous-convective regime. In the inertial-convective range, the coverage length underestimate increases with Reynolds number.

Figure 5.25 shows the variation of the coverage length as a function of the injection length scale. The coverage length increases with injection length scale in the viscous-convective range, but the magnitude of change appears to decrease with larger injection length scales. This trend is similar to that observed for the coverage fraction shown in Figure 5.14. In the inertial-convective regime, the coverage length curves cross with the smallest nozzles yielding the largest coverage length. Figure 5.26 shows the coverage length underestimate corresponding to the data in Figure 5.25. The independence of the coverage length underestimate in the viscous-convective regime is clear. In the inertial-convective range, the coverage length underestimate increases with nozzle diameter. However, the curves for the two larger nozzle diameters appear very similar.

5.4.6 LEB-scale PDF

The LEB-scale PDF, $\langle f_2(\lambda) \rangle$, as introduced in Section 5.3.2, defines the probability density of finding a λ-sized largest empty box that contains no part of the object. Figure 5.27 shows a typical LEB-scale PDF of the scalar field for the four threshold concentrations. The PDF has distinct trends in the viscous-convective and the inertial-

convective ranges and the curves are qualitatively similar to those of the coverage length shown in Figure 5.19. Most of the reasoning associated with the trends in Figure 5.19 are applicable here. However, it must be pointed out that the area under the PDFs shown obviously decreases with increasing threshold. From this fact and the observation that the coverage fraction is not unity at the scale of the bounding box, we may conclude that the PDF curves at various thresholds cross each other and reverse order to satisfy the normalization criteria of the PDF. Overall the main conclusion for higher thresholds is that it is least probable to find largest empty boxes of size around the Kolmogorov length scale.

Figure 5.28 shows the variation of the LEB-scale PDF with downstream distance from the source. The trend observed is qualitatively similar to that observed for coverage length (in Figure 5.21). As with coverage length the variation of intermittency factor with downstream distance explains the variation of LEB-scale PDF with downstream distance.

Figure 5.29 shows the variation of the LEB-scale PDF with Reynolds number. Again, as observed for coverage length, the PDF increases with Reynolds number in the viscous-convective range, while the lowest Reynolds number yields the highest magnitude in the inertial-convective range. The LEB-scale PDF increases with nozzle diameter in the viscous-convective range, and the curves cross in the inertial-convective range (see Figure 5.30).

5.4.7 Scale-cumulative length-area ratio and its exponent

The scale cumulative length–area ratio, $\langle \Omega_2(\lambda) \rangle$, is nearly equivalent to coverage length (see Equations 5.5 and 5.7) and defers only in normalization for the present study. The scale-cumulative length-area ratio exponent corresponds to $\langle D_2(\lambda) \rangle - 1$. Therefore, these measures bring no new information about the fractal structure of the scalar field. Figures 5.31 – 5.38 are presented for completeness.

5.4.8 Scale-local length-area density and its exponent

The scale-cumulative length-area density, $\langle g_2(\lambda) \rangle$, and its exponent, $\langle \alpha_g(\lambda) \rangle$, are defined in Equations 5.9 and 5.10. Essentially, they are the slope of the scale-cumulative length-area ratio curve and the logarithmic derivative of the scale-cumulative length-area density, respectively. $\langle g_2(\lambda) \rangle$ is interpreted as the contribution to $\langle \Omega_2(\lambda) \rangle$ from the local features of the object structure at scale λ. It is easy to show a more direct relation by combining Equations 5.9 and 5.7 to yield:

$$g_d(\lambda) = \frac{\Omega_d(\lambda)}{\lambda}\left(D_d(\lambda) - d_t\right) = \frac{\Omega_d(\lambda)\alpha_\Omega(\lambda)}{\lambda} \tag{5.21}$$

Notice that $\langle g_2(\lambda) \rangle$ is negative when the coverage dimension is less than the topological dimension, which occurs for the scalar field in the present study. The significance of $\langle \alpha_g(\lambda) \rangle$ is that it corresponds to the local fractal dimension of the structure at the scale λ and is a better measure (than coverage dimension) to detect self-similarity of turbulent

iso-surface structure in the inertial-convective regime (Catrakis et al. 2002). Coverage dimension is limited to demonstrate self-similarity because it depends on structure at larger scales. This is evident from the relation between coverage dimension and the area-volume density exponent as:

$$D_3(\lambda) = 2 + \frac{\lambda g_3(\lambda)}{1 + \int_{\lambda}^{\delta_b} g_3(\tilde{\lambda}) d\tilde{\lambda}} \tag{5.22}$$

The above relation clearly shows the dependence on iso-surface structure at scales larger than λ. Catrakis et al. (2002) argued that the scale-cumulative length-area density exponent, $\langle \alpha_g(\lambda) \rangle$, is decoupled from contributions from larger or smaller scales and is therefore constant in the inertial-convective regime if any self-similarity existed. Therefore, $\langle \alpha_g(\lambda) \rangle$ is the physical counterpart of the spectral scaling behavior in the inertial-convective range as predicted by the KOC arguments (see Chapter 4). Catrakis et al. (2002) reported that the "fractal dimension at the local scale" was constant at $\alpha_g = 1.3$ in a significantly wide range in the inertial-convective regime.

Figure 5.39 shows the typical scale-local length-area density for the four concentration thresholds. The scale-local contribution to the scale-cummulative length-area ratio is dominated by the complexity in the viscous-convective regime. The contribution decreases with increasing scale. Above the Kolmogorov length scale, the contributions for the higher thresholds are negative due to the coverage dimension falling below the topological dimension (see Figure 5.15). These negative data are not shown in Figure

5.39 because of the logarithmic axis. Overall, $\langle g_2(\lambda)\rangle$ decreases with increasing threshold.

Figure 5.40 shows the exponent $\langle \alpha_g(\lambda)\rangle$ for four threshold values. From the definition in Catrakis et al. (2002), $\langle \alpha_g(\lambda)\rangle$ is undefined when the coverage dimension falls below the topological dimension. For the data shown in Figure 5.40, the higher threshold levels yield undefined $\langle \alpha_g(\lambda)\rangle$ in the inertial-convective regime. For the lowest threshold level, $\langle \alpha_g(\lambda)\rangle$ fluctuates around a value of approximately 1.2 in the inertial-convective regime, but it is difficult to determine from this data if $\langle \alpha_g(\lambda)\rangle$ is constant over the inertial-convective regime. At other scales there is no indication of self-similarity.

Figure 5.41 shows the variation of scale-local length-area ratio with downstream distance. As with other coverage statistics, the intermittency factor appears to explain the trend in the viscous-convective regime in Figure 5.41(a). The effect of threshold dominates the effect of downstream distance as seen by the reversal of the trend in Figure 5.41(d). Figure 5.42 shows the variation of the exponent $\langle \alpha_g(\lambda)\rangle$ with respect to downstream distance. As seen in Figure 5.42(b, c and d) there is no indication of self-similarity in the iso-surfaces at higher threshold in the inertial-convective regime. However, there is a mild indication of self-similarity in the inertial-convective regime for the lowest threshold (see Figure 5.42(a)). The curves have an approximately constant ($\langle \alpha_g(\lambda)\rangle \sim 1.2$) in the inertial-convective ranges for the two farthest downstream cases.

Figure 5.43 shows the variation of scale-local length-area ratio with respect to Reynolds number. $\langle g_2(\lambda)\rangle$ increases in the viscous-convective regime with increasing Reynolds number. Figure 5.44 shows the exponent $\langle \alpha_g(\lambda)\rangle$ for the lowest threshold level for three Reynolds numbers. The two higher Reynolds number cases show a significant range in which $\langle \alpha_g(\lambda)\rangle \sim 1.2$. This is consistent with Catrakis et al. (2002) where a value of 1.3 was reported. The lowest Reynolds number case deviates significantly from the constant value and data other threshold levels do not show a constant value for $\langle \alpha_g(\lambda)\rangle$.

Figure 5.45 shows the variation of scale-local length-area density with respect to injection length scale. In the viscous-convective regime, increasing the nozzle length scale increases $\langle g_2(\lambda)\rangle$ This is a consequence of the increasing intermittency factor with nozzle diameter. Figure 5.46 shows the variation of the exponent with the injection length scale. The scatter in the constant value of $\langle \alpha_g(\lambda)\rangle$ in the inertial-convective range appears to reduce with increasing nozzle diameter.

5.4.9 Lacunarity

Lacunarity, $\langle \Lambda(\lambda)\rangle$, is defined in Equation 5.19 as the ratio of the second moment of the mass distribution to the square of the first moment of the mass distribution. Lacunarity measures the homogeneity of the structure with a value of 1.0 for homogeneous structure. A higher value indicates inhomogeneity in the structure. Figure 5.47 shows the lacunarity function for different concentration thresholds. The lacunarity initially

decreases at the lower end of the viscous-convective range. From the minimum value, the lacunarity increases with increasing scale through the viscous-convective regime. Beyond the Kolmogorov length scale, the lacunarity decreases at higher scales. Increasing lacunarity corresponds to increasing patchy structure, therefore it can be inferred that the iso-surfaces viewed at the viscous-convective scales are highly irregular and decrease in homogeneity with increasing scale up to the Kolmogorov length scale. The increase in lacunarity also shows a near power law increase in the viscous-convective range. The figure also shows that the structure is most inhomogenous around the Kolmogorov length scale, which represents the size of the smallest eddies. Overall, the inhomogeneity (and lacunarity) increases with increasing concentration threshold. The slope of the approximate power-law in the viscous-convective range appears to be constant with respect to threshold. The steepness of the decrease in lacunarity in the inertial-convective range increases with threshold.

Figure 5.48 shows the variation of lacunarity with downstream distance from the source. Figure 5.48(a) shows that the lacunarity decreases with increasing intermittency factor at the lowest threshold. However, the effect of threshold dominates the effect of intermittency, which explains the reversal of trend in Figure 4.49(d).

Figure 5.49 shows the variation of lacunarity with Reynolds number. The lacunarity appears to decrease with increasing Reynolds number indicating an increase in homogeneity with Reynolds number. In Figure 5.50, lacunarity is observed to decrease

with increasing nozzle diameter. These trends are a consequence of the variation in intermittency.

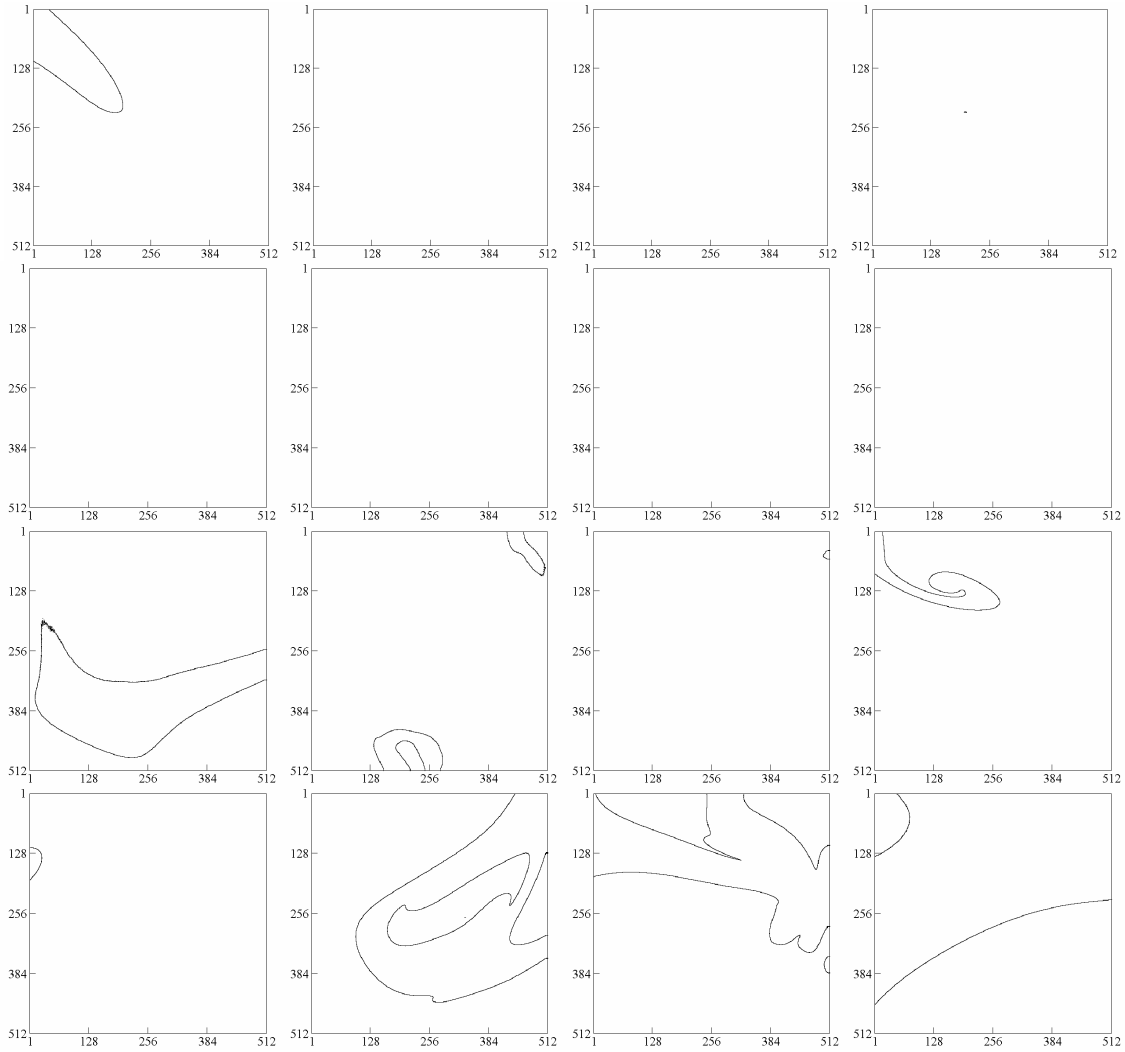

Figure 5.1 The first 16 consecutive samples from the set of 12,000 boundary-outline images at x = 0.1 m (x/H = 1.0) for a concentration threshold of $\Theta_{th}(m) = \langle\Theta\rangle + m\langle\theta^2\rangle^{1/2}$, where m = 1. For every image the streamwise direction is from left to right. The top left plot corresponds to the first captured image and the bottom right corresponds to image number 16.

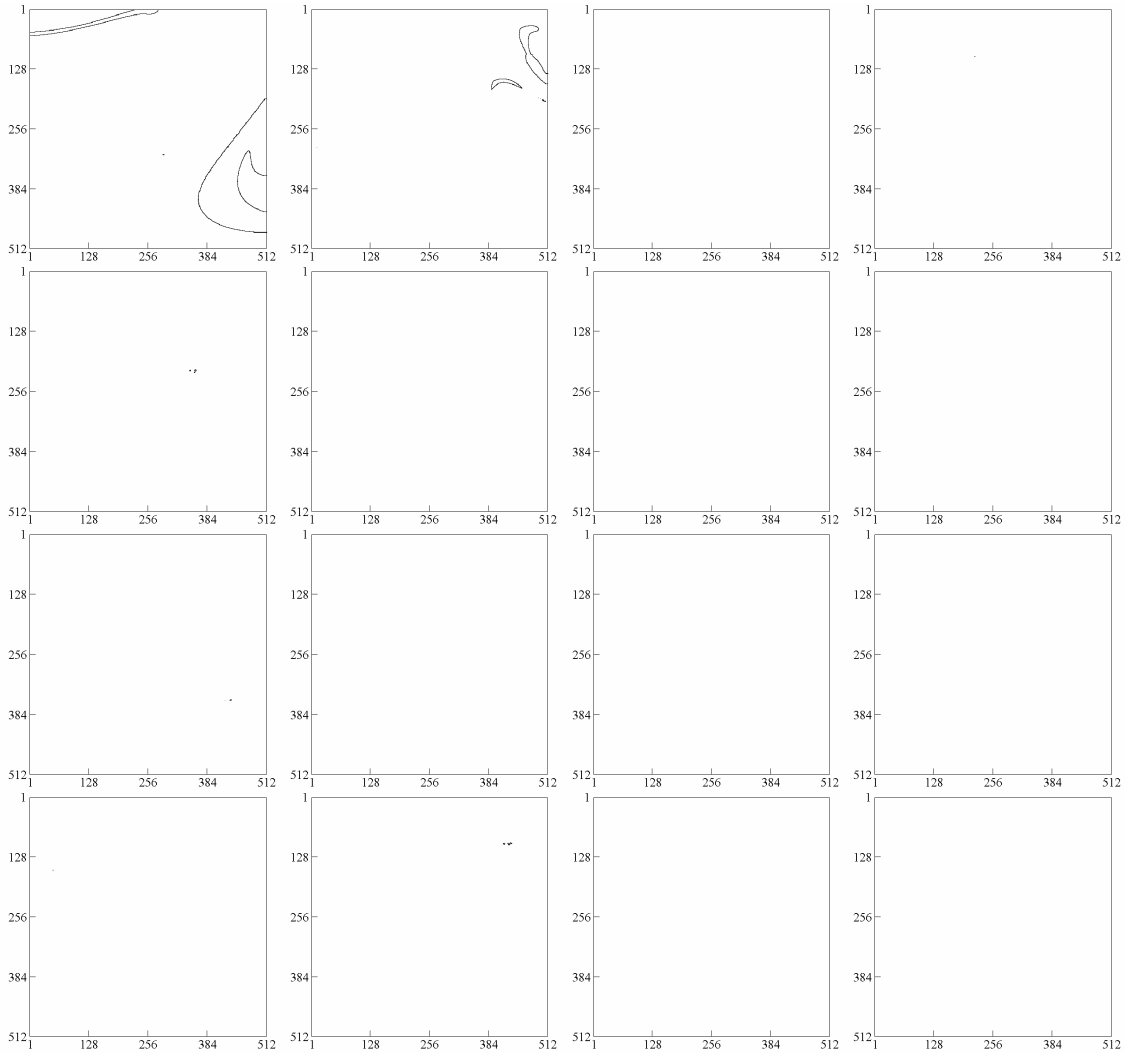

Figure 5.2 The first 16 consecutive samples from the set of 12,000 boundary-outline images at x = 0.25 m (x/H = 2.5) for a concentration threshold of $\Theta_{th}(m) = \langle\Theta\rangle + m\langle\theta^2\rangle^{1/2}$, where m = 1. For every image the streamwise direction is from left to right. The top left plot corresponds to the first captured image and the bottom right corresponds to image number 16.

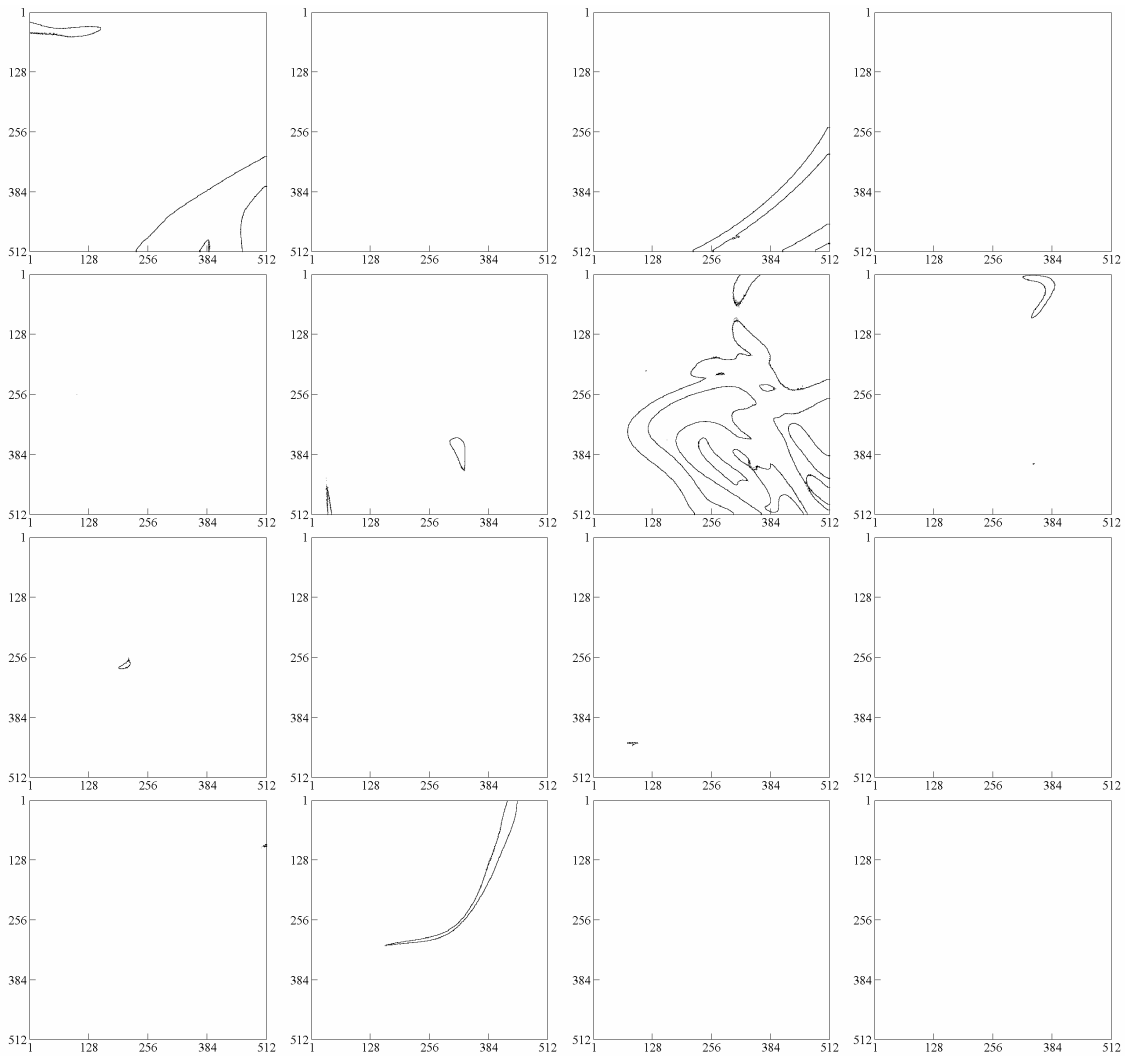

Figure 5.3 The first 16 consecutive samples from the set of 12,000 boundary-outline images at x = 0.5 m (x/H = 5.0) for a concentration threshold of $\Theta_{th}(m) = \langle\Theta\rangle + m\langle\theta^2\rangle^{1/2}$, where m = 1. For every image the streamwise direction is from left to right. The top left plot corresponds to the first captured image and the bottom right corresponds to image number 16.

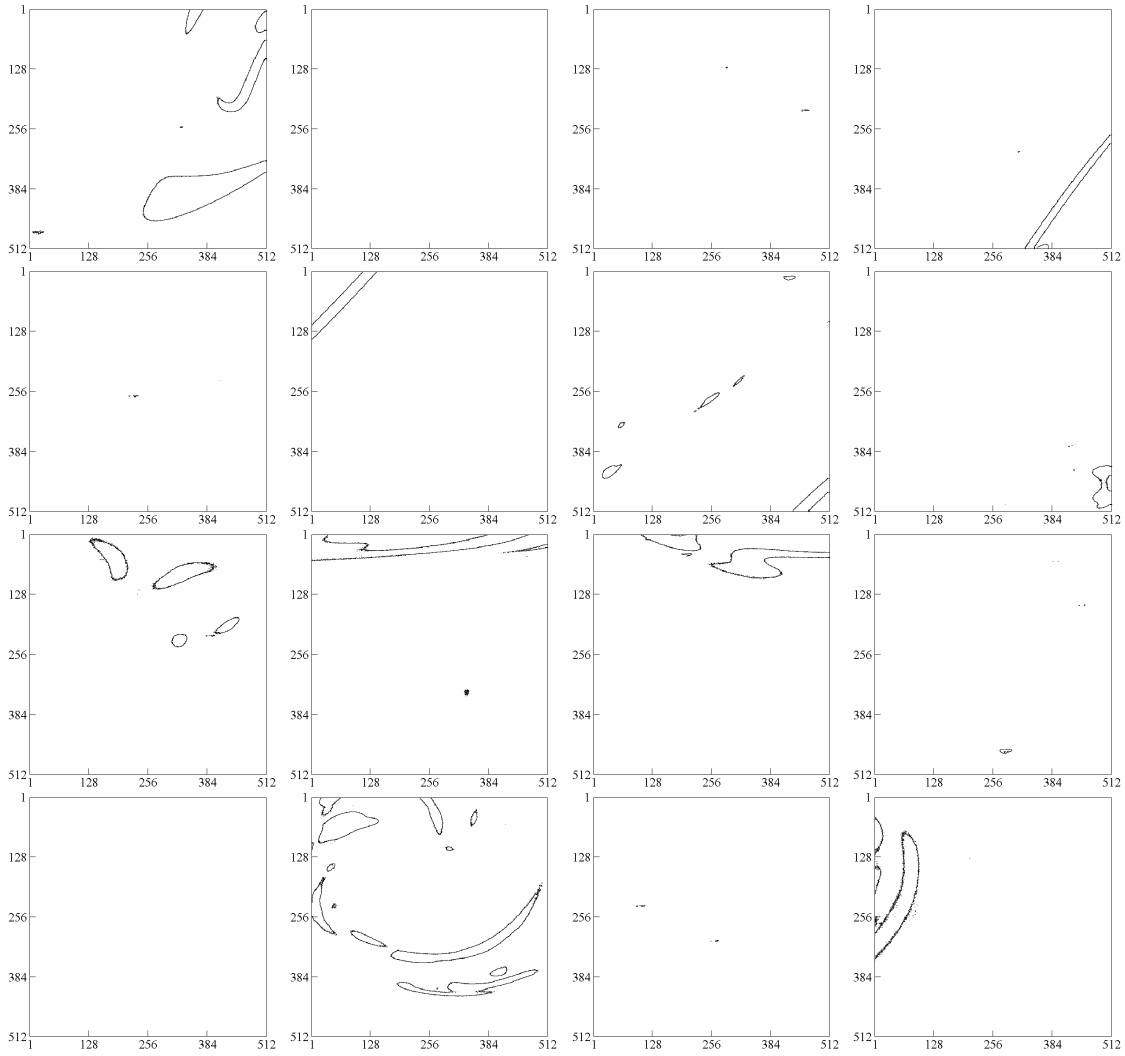

Figure 5.4 The first 16 consecutive samples from the set of 12,000 boundary-outline images at x = 1.0 m (x/H = 10.0) for a concentration threshold of $\Theta_{th}(m) = \langle\Theta\rangle + m\langle\theta^2\rangle^{1/2}$, where m = 1. For every image the streamwise direction is from left to right. The top left plot corresponds to the first captured image and the bottom right corresponds to image number 16.

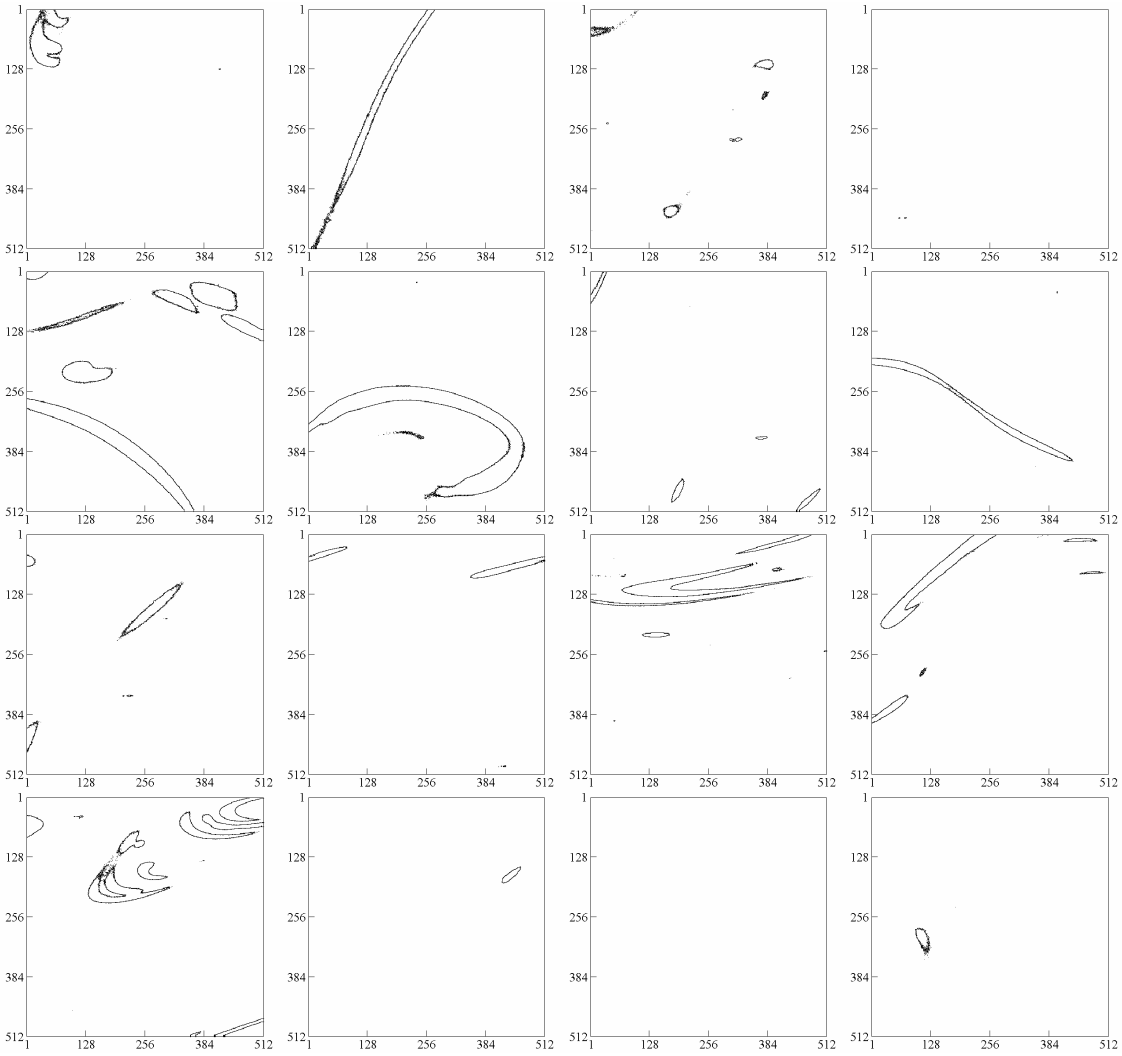

Figure 5.5 The first 16 consecutive samples from the set of 12,000 boundary-outline images at x = 2.0 m (x/H = 20.0) for a concentration threshold of $\Theta_{th}(m) = \langle\Theta\rangle + m\langle\theta^2\rangle^{1/2}$, where m = 1. For every image the streamwise direction is from left to right. The top left plot corresponds to the first captured image and the bottom right corresponds to image number 16.

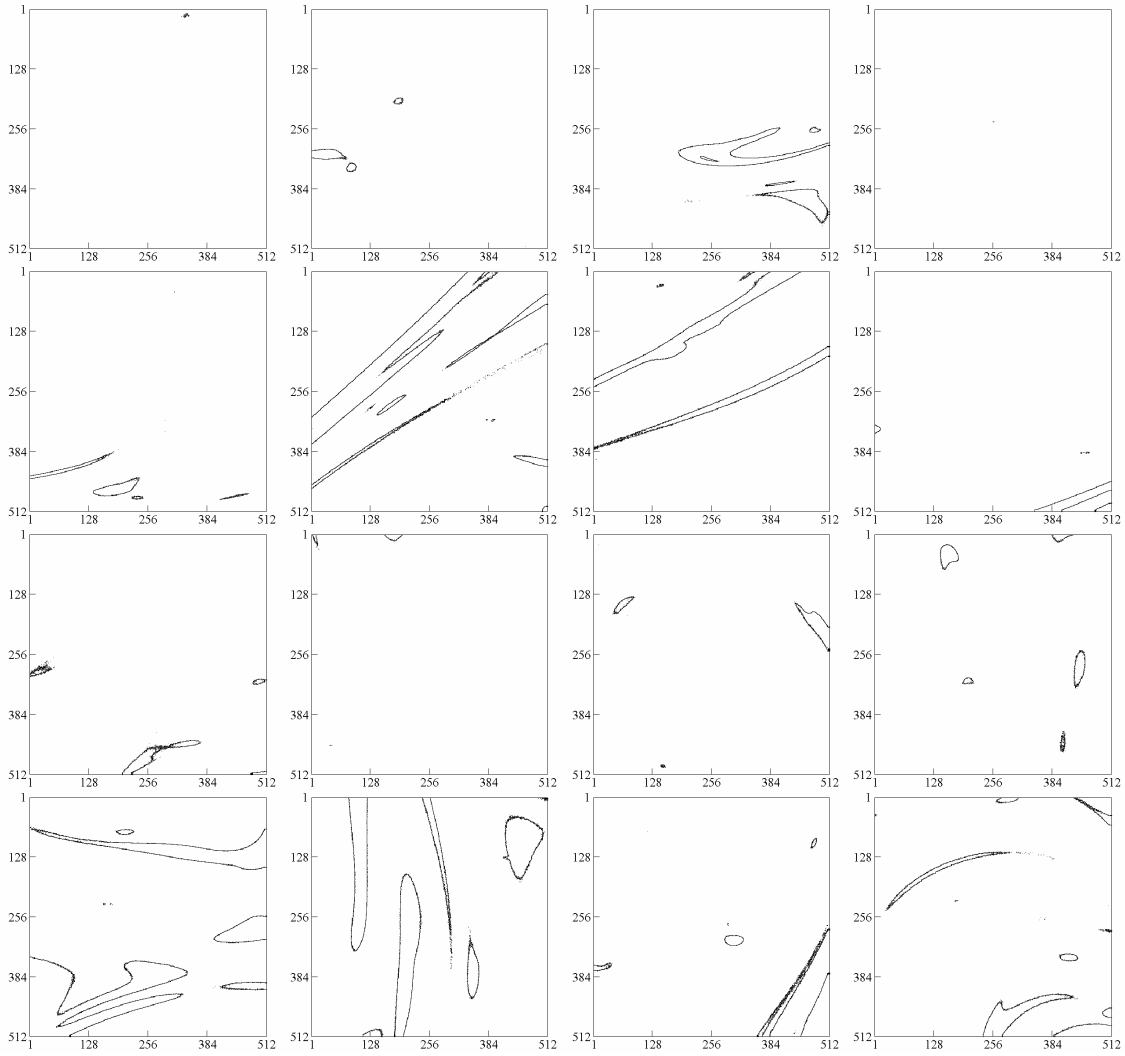

Figure 5.6 The first 16 consecutive samples from the set of 12,000 boundary-outline images at x = 4.0 m (x/H = 40.0) for a concentration threshold of $\Theta_{th}(m) = \langle\Theta\rangle + m\langle\theta^2\rangle^{1/2}$, where m = 1. For every image the streamwise direction is from left to right. The top left plot corresponds to the first captured image and the bottom right corresponds to image number 16.

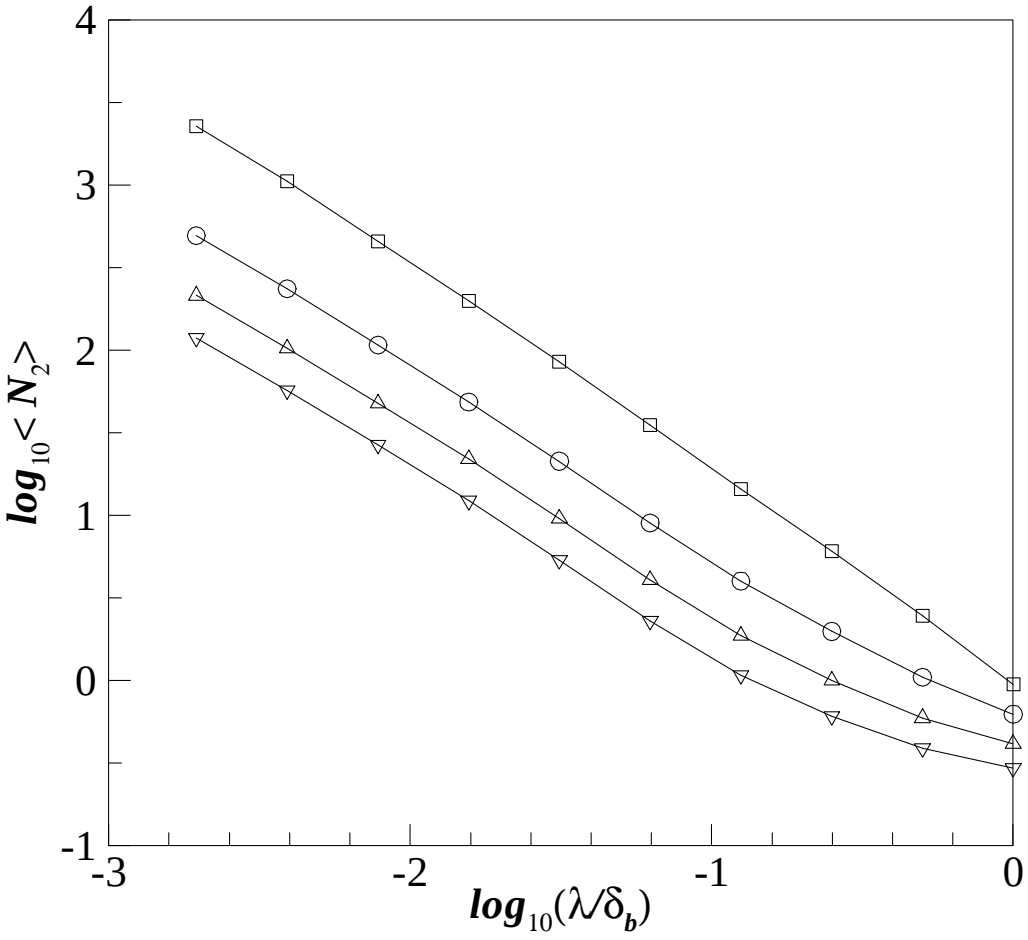

Figure 5.7 Coverage count as a function of concentration threshold. Data plotted versus normalized scale, λ/δ_b, for the passive scalar iso-surface at a concentration m times the local standard deviation above the local mean, for m = 1 (□), 3 (○), 5 (△), and 7 (▽), at x = 4 m; for D = 4.7 mm and Re = 10,000.

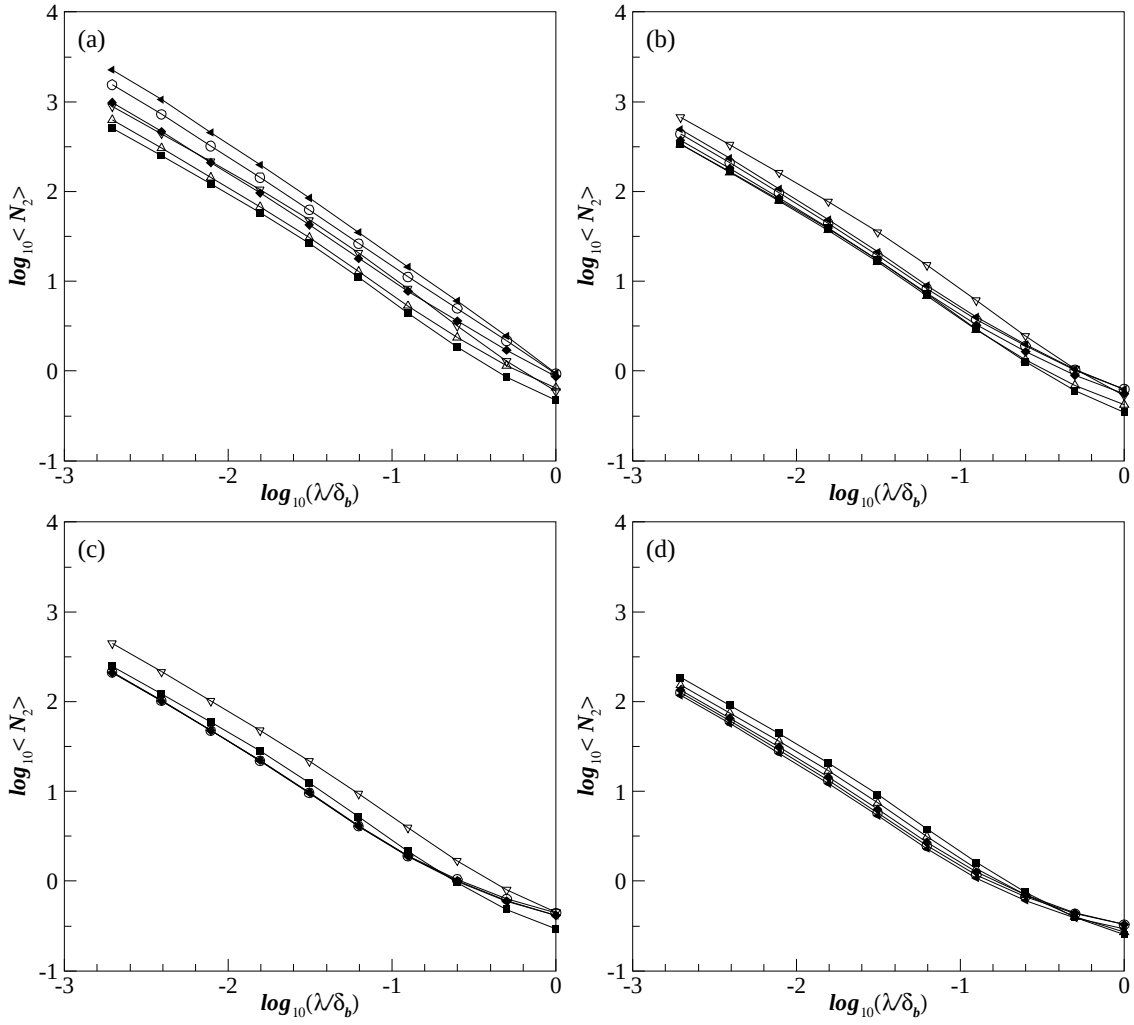

Figure 5.8 Coverage count as a function of distance from the source. Data plotted versus normalized scale, λ/δ_b, for the passive scalar iso-surface at a concentration m times the local standard deviation above the local mean, for (a) m = 1, (b) 3, (c) 5, and (d) 7, at x = 0.1 m (▽), 0.25 m (■), 0.5 m (△), 1 m (♦), 2 m (○), and 4 m (◀); for D = 4.7 mm and Re = 10,000.

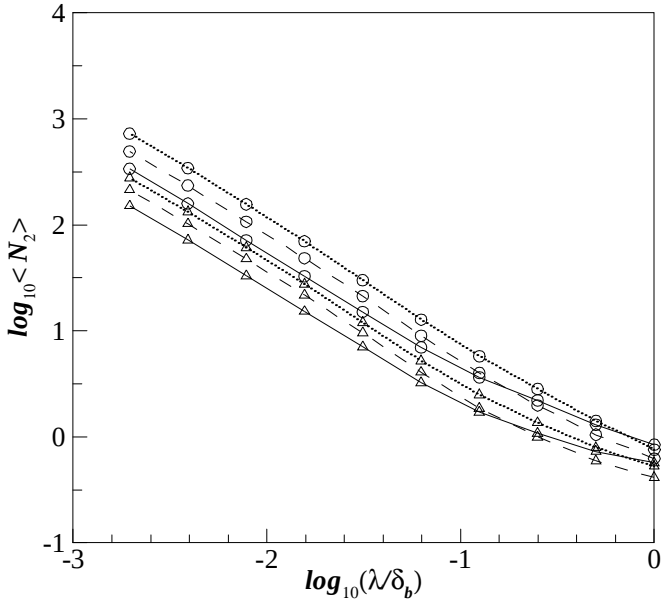

Figure 5.9 Coverage count as a function of Reynolds number. Data plotted versus normalized scale, λ/δ_b, for the passive scalar iso-surface at a concentration m times the local standard deviation above the local mean, for m = 3 (○) and 5 (△), at x = 4 m; for D = 4.7 mm and Re = 5000 (——), 10,000 (– – –), and 20,000 (••••••••).

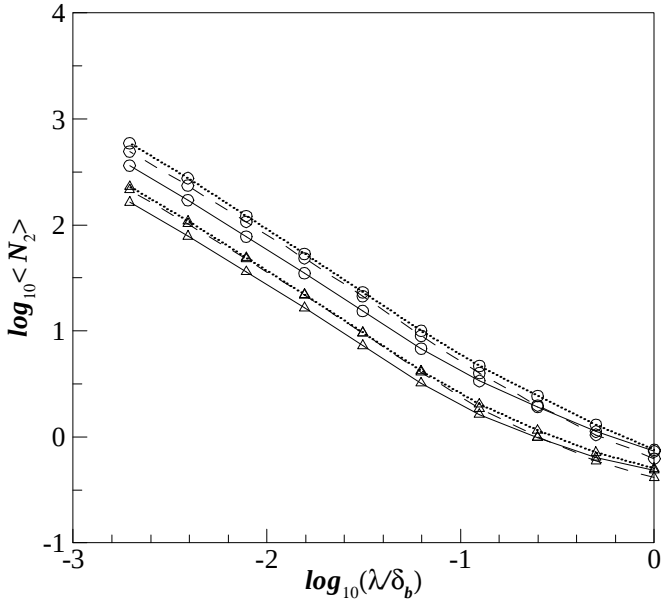

Figure 5.10 Coverage count as a function of source nozzle diameter. Data plotted versus normalized scale, λ/δ_b, for the passive scalar iso-surface at a concentration m times the local standard deviation above the local mean, for m = 3 (○) and 5 (△), at x = 4 m; for D = 2.2 mm (——), 4.7 mm (– – –), and 9.4 mm (••••••••) and Re = 10,000.

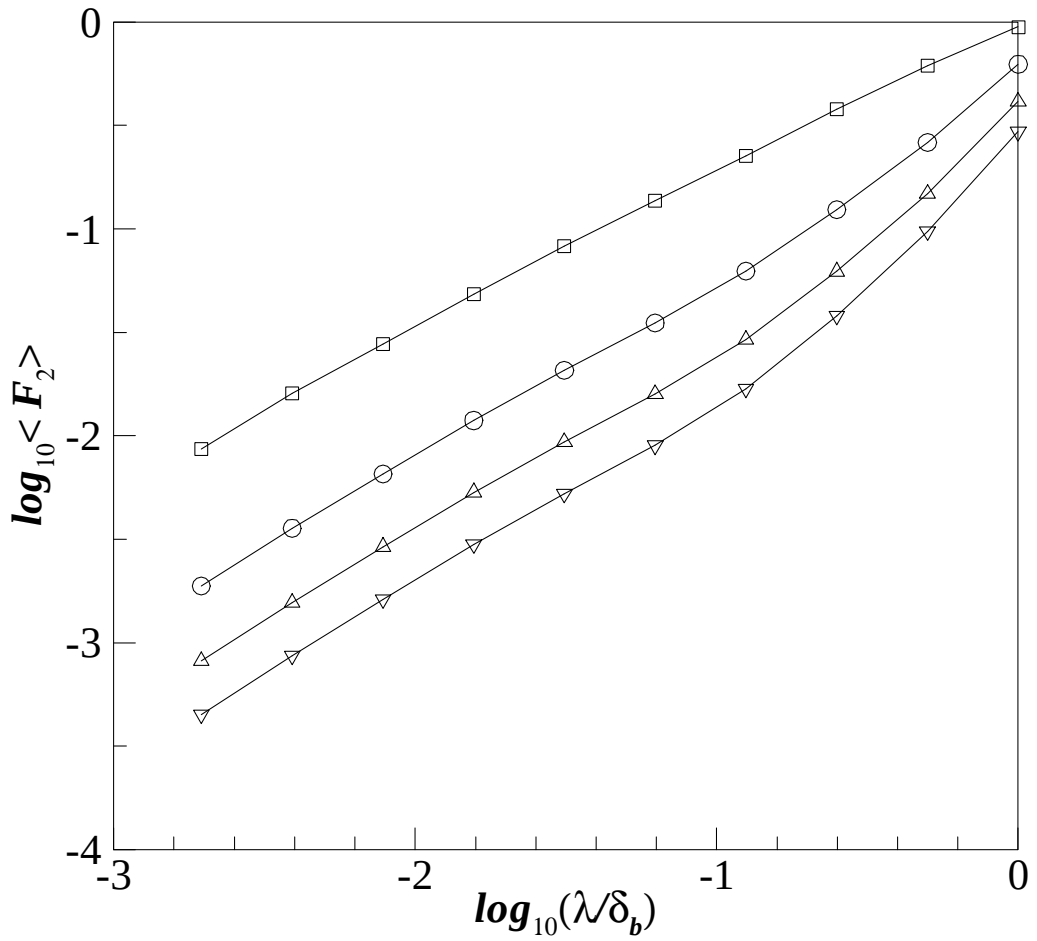

Figure 5.11 Coverage fraction as a function of concentration threshold. Data plotted versus normalized scale, λ/δ_b, for the passive scalar iso-surface at a concentration m times the local standard deviation above the local mean, for m = 1 (□), 3 (○), 5 (△), and 7 (▽), at x = 4 m; for D = 4.7 mm and Re = 10,000.

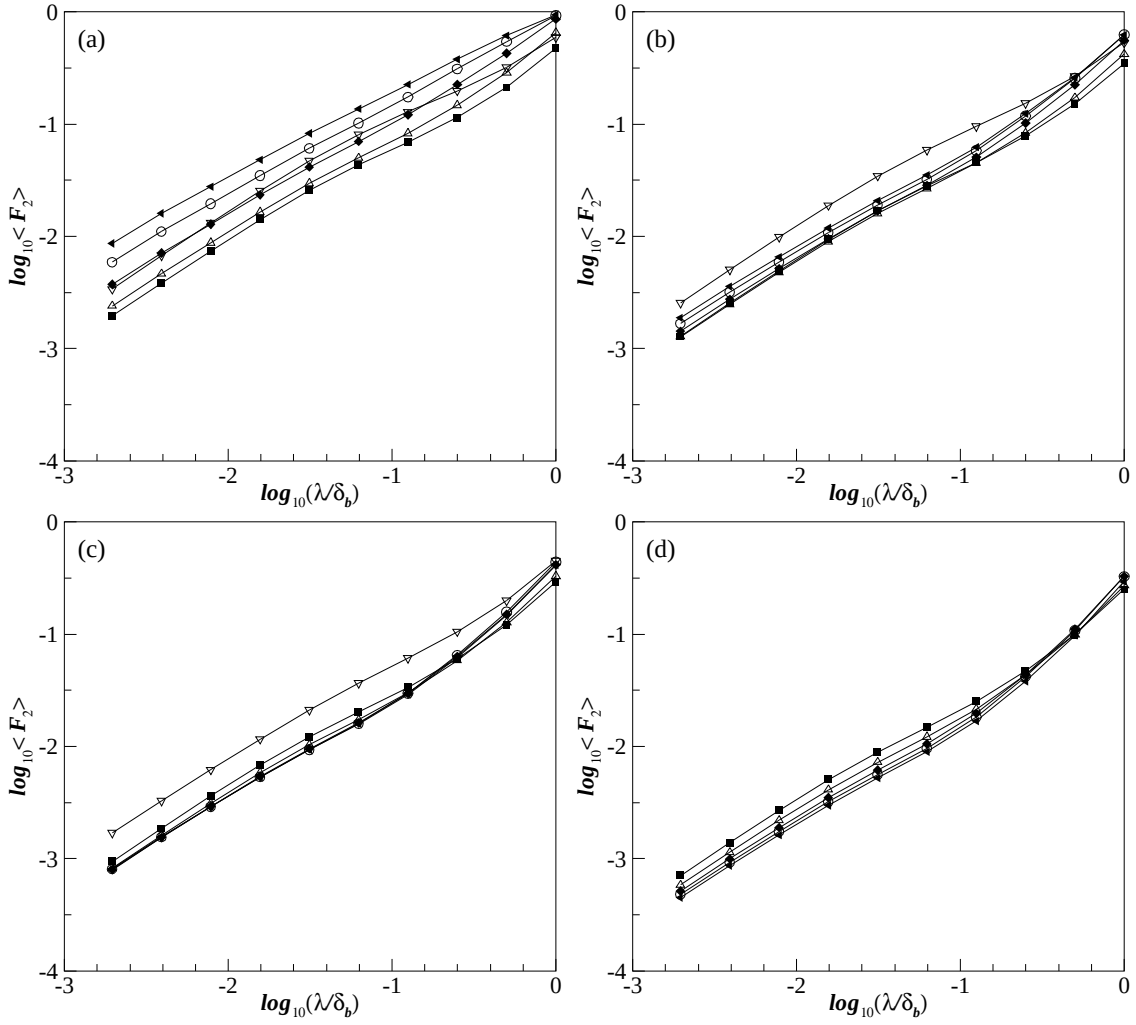

Figure 5.12 Coverage fraction as a function of distance from the source. Data plotted versus normalized scale, λ/δ_b, for the passive scalar iso-surface at a concentration m times the local standard deviation above the local mean, for (a) m = 1, (b) 3, (c) 5, and (d) 7, at x = 0.1 m (▽), 0.25 m (■), 0.5 m (△), 1 m (♦), 2 m (○), and 4 m (◀); for D = 4.7 mm and Re = 10,000.

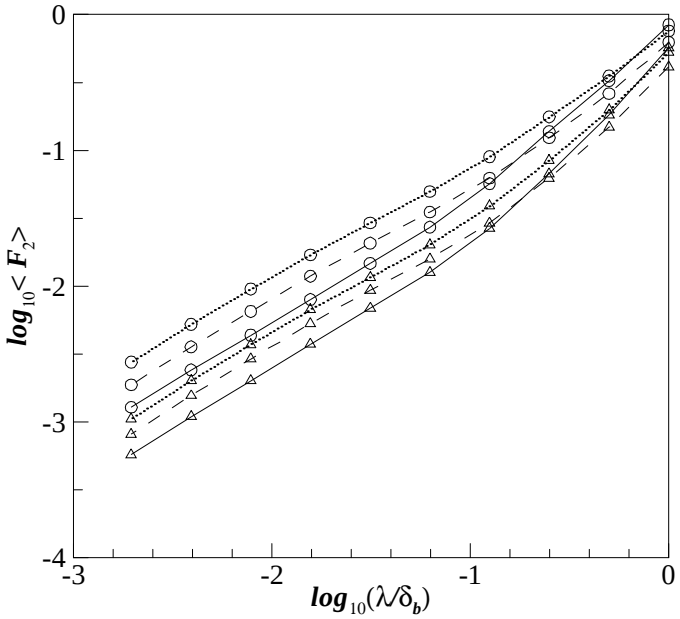

Figure 5.13 Coverage fraction as a function of Reynolds number. Data plotted versus normalized scale, λ/δ_b, for the passive scalar iso-surface at a concentration m times the local standard deviation above the local mean, for m = 3 (○) and 5 (△), at x = 4 m; for D = 4.7 mm and Re = 5000 (——), 10,000 (– – –), and 20,000 (••••••••).

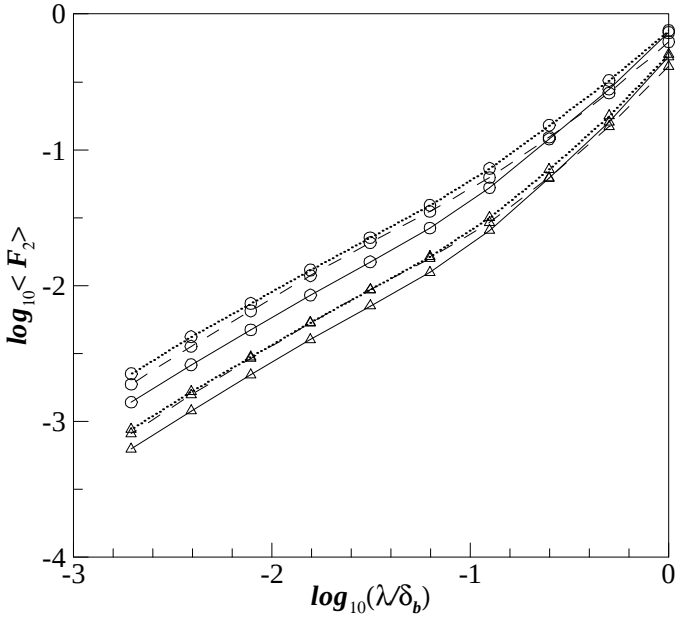

Figure 5.14 Coverage fraction as a function of source nozzle diameter. Data plotted versus normalized scale, λ/δ_b, for the passive scalar iso-surface at a concentration m times the local standard deviation above the local mean, for m = 3 (○) and 5 (△), at x = 4 m; for D = 2.2 mm (——), 4.7 mm (– – –), and 9.4 mm (••••••••) and Re = 10,000.

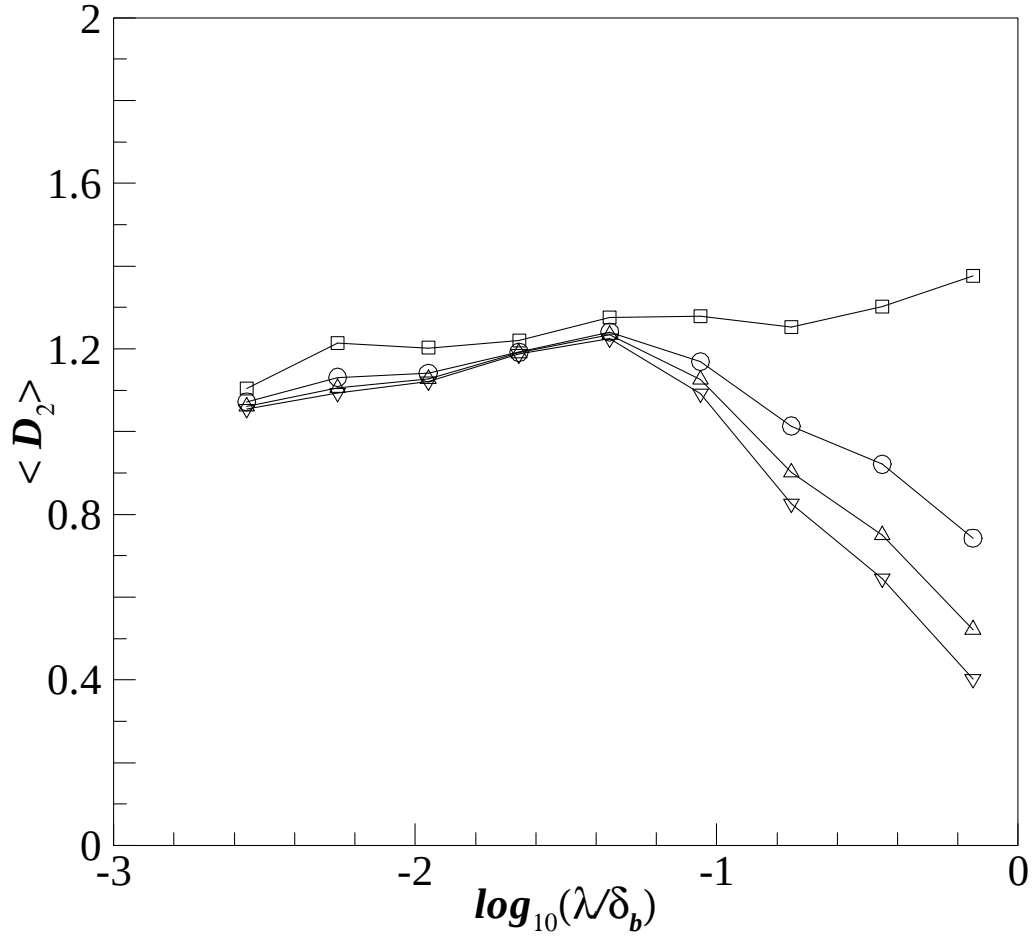

Figure 5.15 Coverage dimension as a function of concentration threshold. Data plotted versus normalized scale, λ/δ_b, for the passive scalar iso-surface at a concentration m times the local standard deviation above the local mean, for m = 1 (□), 3 (○), 5 (△), and 7 (▽), at x = 4 m; for D = 4.7 mm and Re = 10,000.

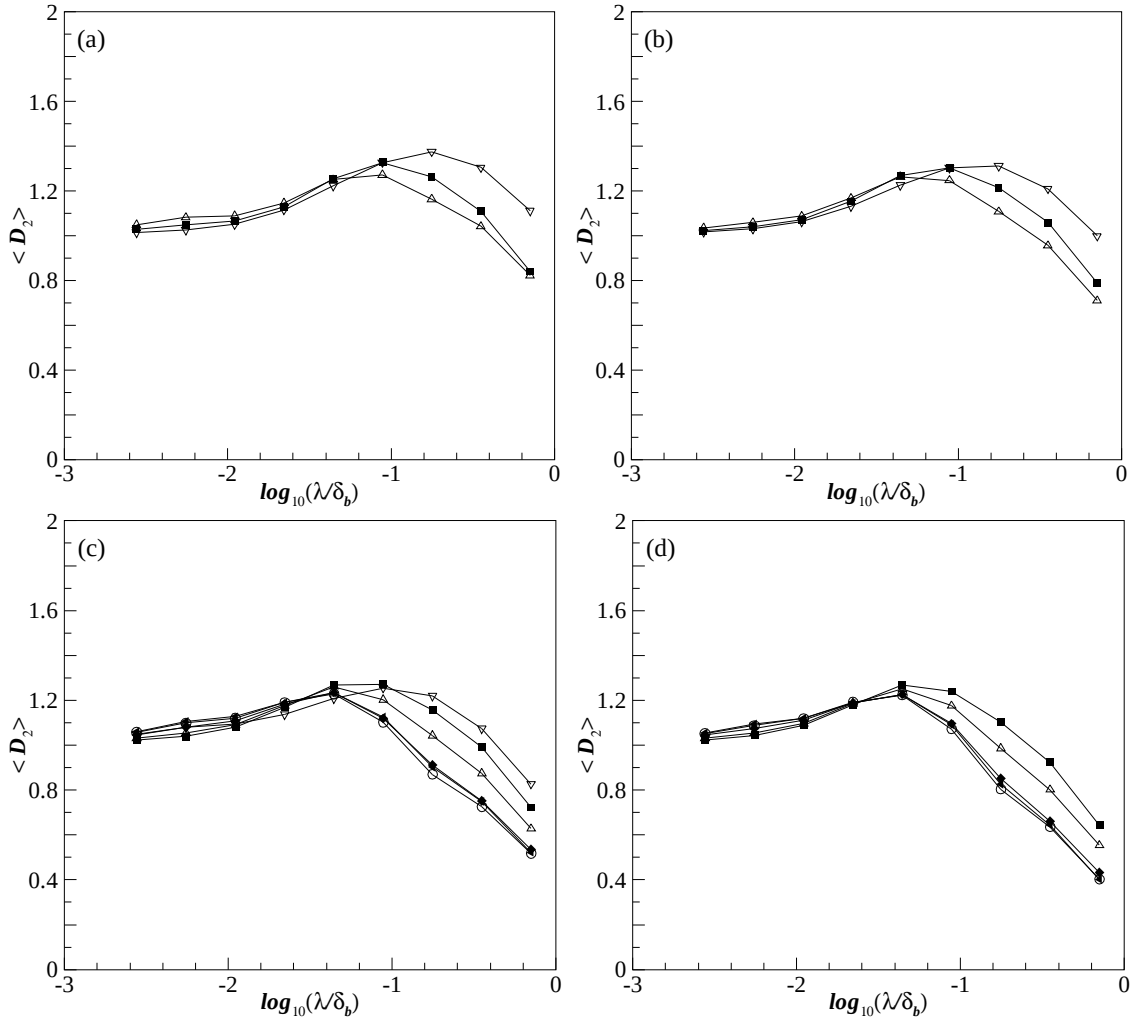

Figure 5.16 Coverage dimension as a function of distance from the source. Data plotted versus normalized scale, λ/δ_b, for the passive scalar iso-surface at a concentration m times the local standard deviation above the local mean, for (a) m = 1, (b) 3, (c) 5, and (d) 7, at x = 0.1 m (▽), 0.25 m (■), 0.5 m (△), 1 m (♦), 2 m (○), and 4 m (◀); for D = 4.7 mm and Re = 10,000.

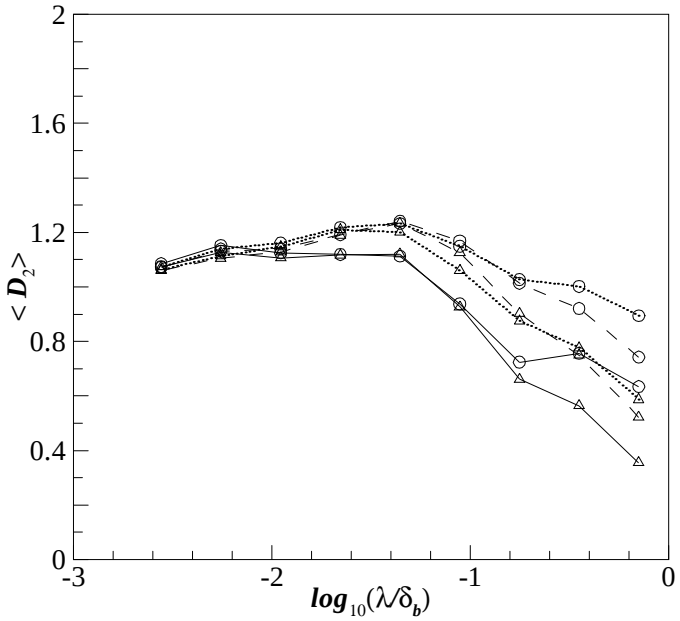

Figure 5.17 Coverage dimension as a function of Reynolds number. Data plotted versus normalized scale, λ / δ_b, for the passive scalar iso-surface at a concentration m times the local standard deviation above the local mean, for m = 3 (○) and 5 (△), at x = 4 m; for D = 4.7 mm and Re = 5000 (——), 10,000 (– – –), and 20,000 (••••••••).

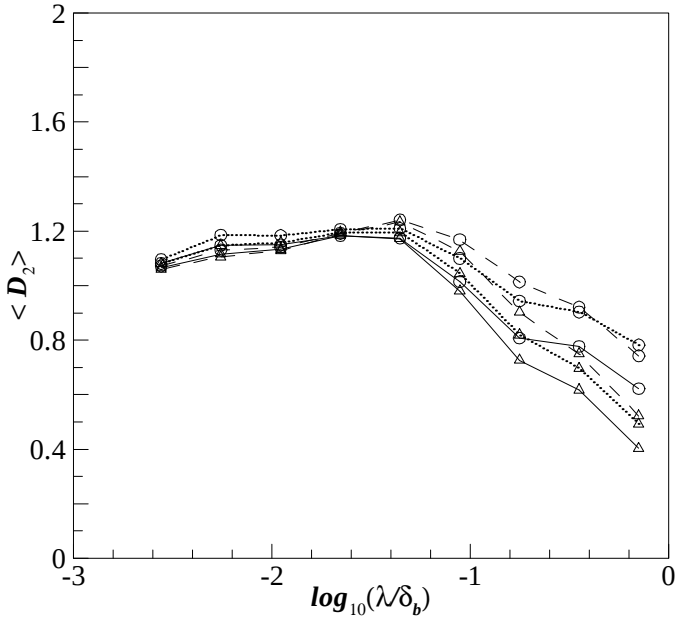

Figure 5.18 Coverage dimension as a function of source nozzle diameter. Data plotted versus normalized scale, λ / δ_b, for the passive scalar iso-surface at a concentration m times the local standard deviation above the local mean, for m = 3 (○) and 5 (△), at x = 4 m; for D = 2.2 mm (——), 4.7 mm (– – –), and 9.4 mm (••••••••) and Re = 10,000.

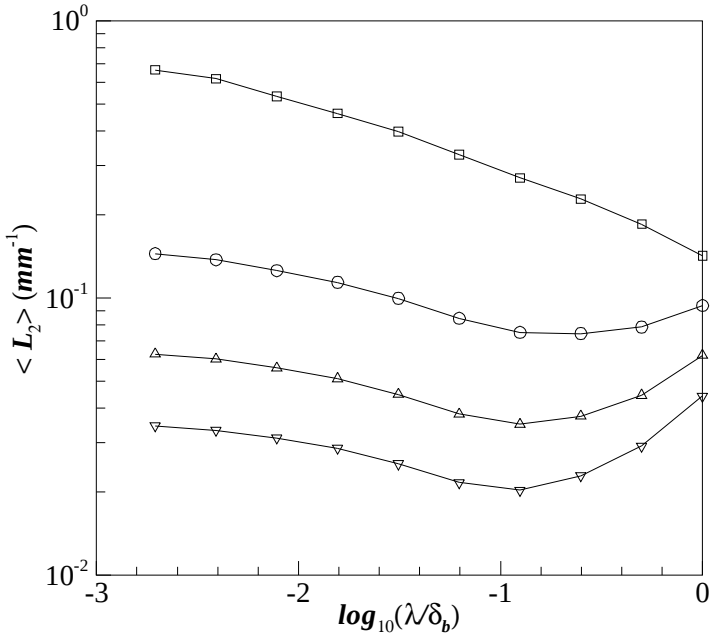

Figure 5.19 Coverage length as a function of concentration threshold. Data plotted versus normalized scale, λ/δ_b, for the passive scalar iso-surface at a concentration m times the local standard deviation above the local mean, for m = 1 (□), 3 (○), 5 (△), and 7 (▽), at x = 4 m; for D = 4.7 mm and Re = 10,000.

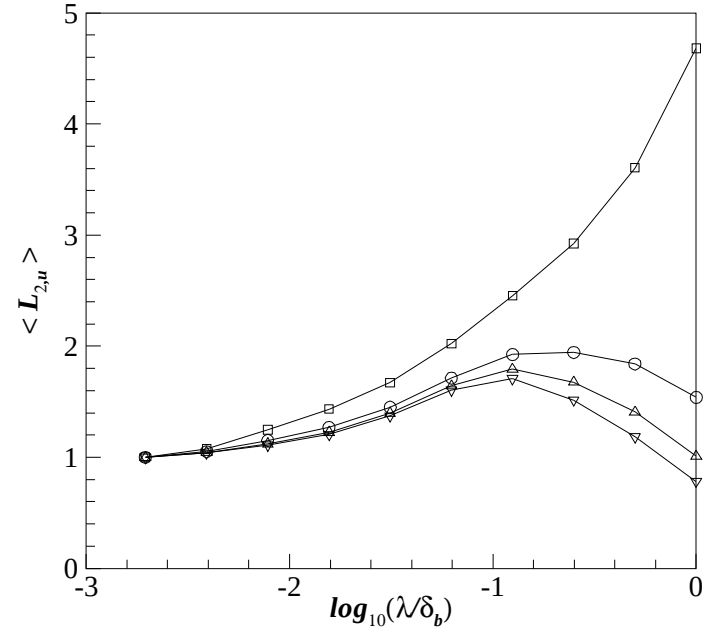

Figure 5.20 Underestimate of total coverage length as a function of concentration threshold. Data plotted versus normalized scale, λ/δ_b, for the passive scalar iso-surface at a concentration m times the local standard deviation above the local mean, for m = 1 (□), 3 (○), 5 (△), and 7 (▽), at x = 4 m; for D = 4.7 mm and Re = 10,000.

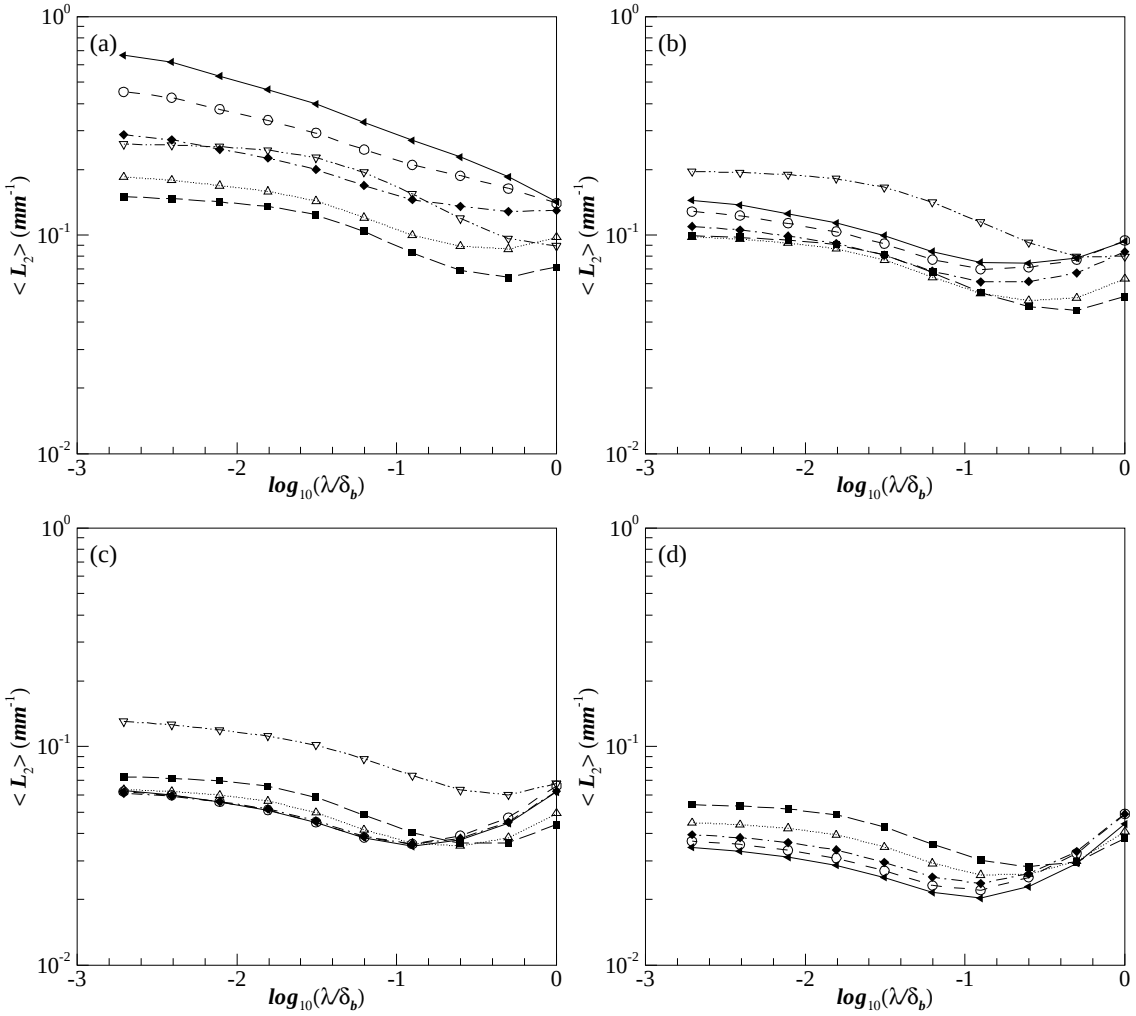

Figure 5.21 Coverage length as a function of distance from the source. Data plotted versus normalized scale, λ/δ_b, for the passive scalar iso-surface at a concentration m times the local standard deviation above the local mean, for (a) m = 1, (b) 3, (c) 5, and (d) 7, at x = 0.1 m (▽), 0.25 m (■), 0.5 m (△), 1 m (♦), 2 m (○), and 4 m (◀); for D = 4.7 mm and Re = 10,000.

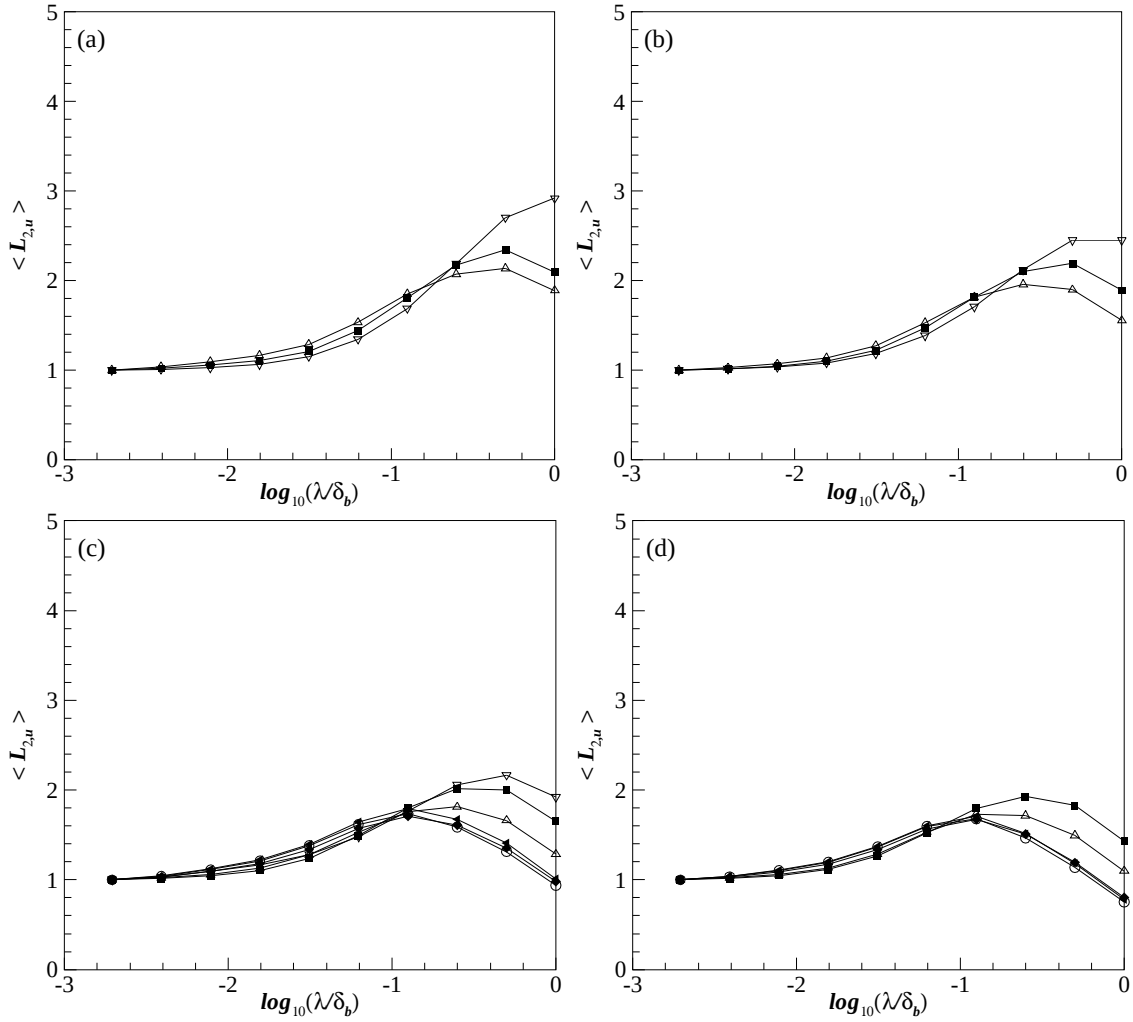

Figure 5.22 Coverage length underestimate as a function of distance from the source. Data plotted versus normalized scale, λ/δ_b, for the passive scalar iso-surface at a concentration m times the local standard deviation above the local mean, for (a) m = 1, (b) 3, (c) 5, and (d) 7, at x = 0.1 m (▽), 0.25 m (■), 0.5 m (△), 1 m (♦), 2 m (○), and 4 m (◀); for D = 4.7 mm and Re = 10,000.

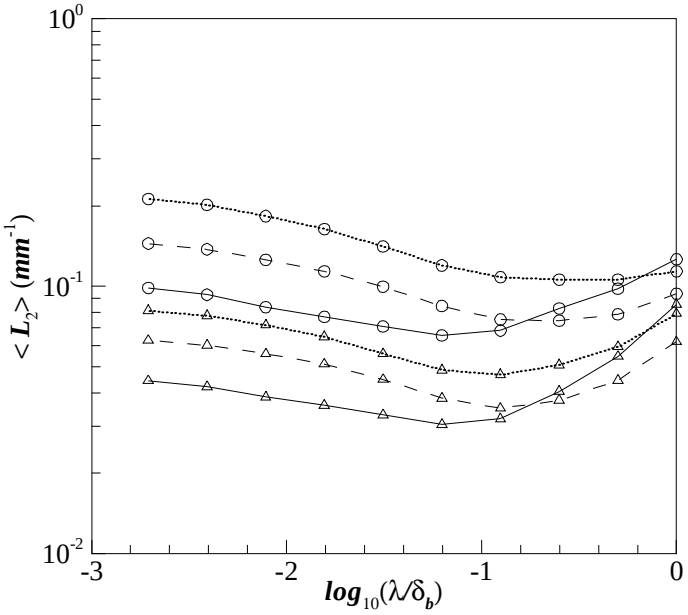

Figure 5.23 Coverage length as a function of Reynolds number. Data plotted versus normalized scale, λ/δ_b, for the passive scalar iso-surface at a concentration m times the local standard deviation above the local mean, for m = 3 (○) and 5 (△), at x = 4 m; for D = 4.7 mm and Re = 5000 (——), 10,000 (– – –), and 20,000 (••••••••).

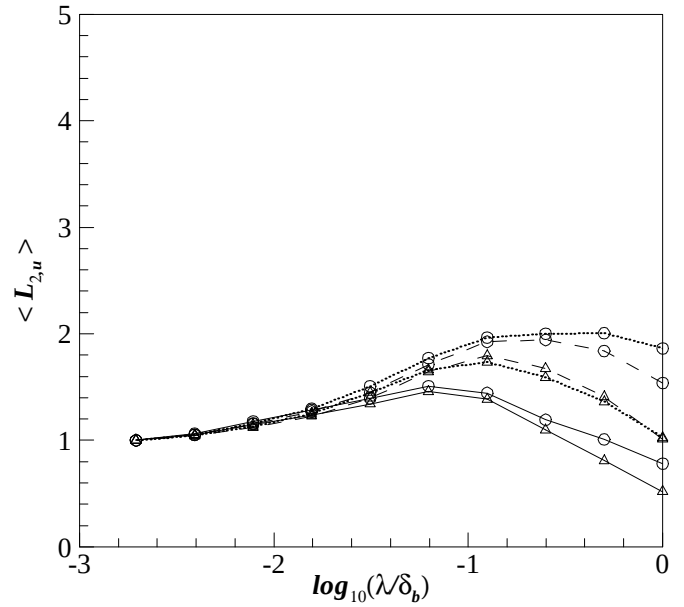

Figure 5.24 Coverage length underestimate as a function of Reynolds number. Data plotted versus normalized scale, λ/δ_b, for the passive scalar iso-surface at a concentration m times the local standard deviation above the local mean, for m = 3 (○) and 5 (△), at x = 4 m; for D = 4.7 mm and Re = 5000 (——), 10,000 (– – –), and 20,000 (••••••••).

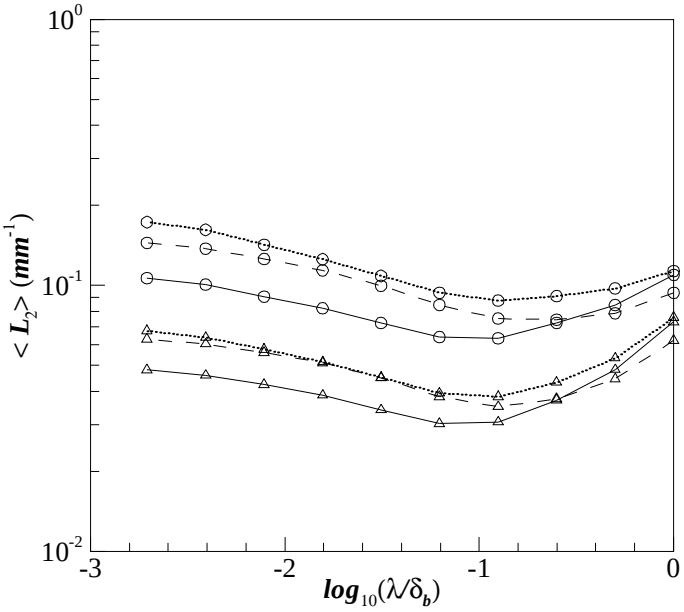

Figure 5.25 Coverage length as a function of source nozzle diameter. Data plotted versus normalized scale, λ/δ_b, for the passive scalar iso-surface at a concentration m times the local standard deviation above the local mean, for m = 3 (○) and 5 (△), at x = 4 m; for D = 2.2 mm (——), 4.7 mm (– – –), and 9.4 mm (••••••••) and Re = 10,000.

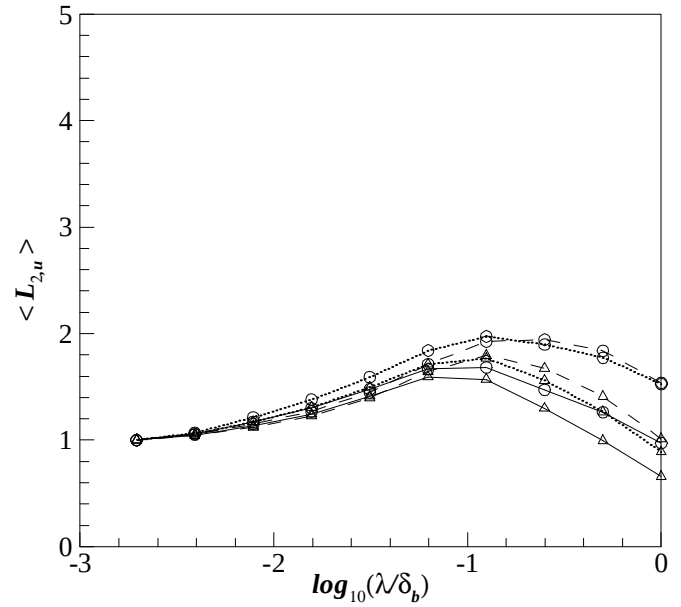

Figure 5.26 Coverage length underestimate as a function of source nozzle diameter. Data plotted versus normalized scale, λ/δ_b, for the passive scalar iso-surface at a concentration m times the local standard deviation above the local mean, for m = 3 (○) and 5 (△), at x = 4 m; for D = 2.2 mm (——), 4.7 mm (– – –), and 9.4 mm (••••••••) and Re = 10,000.

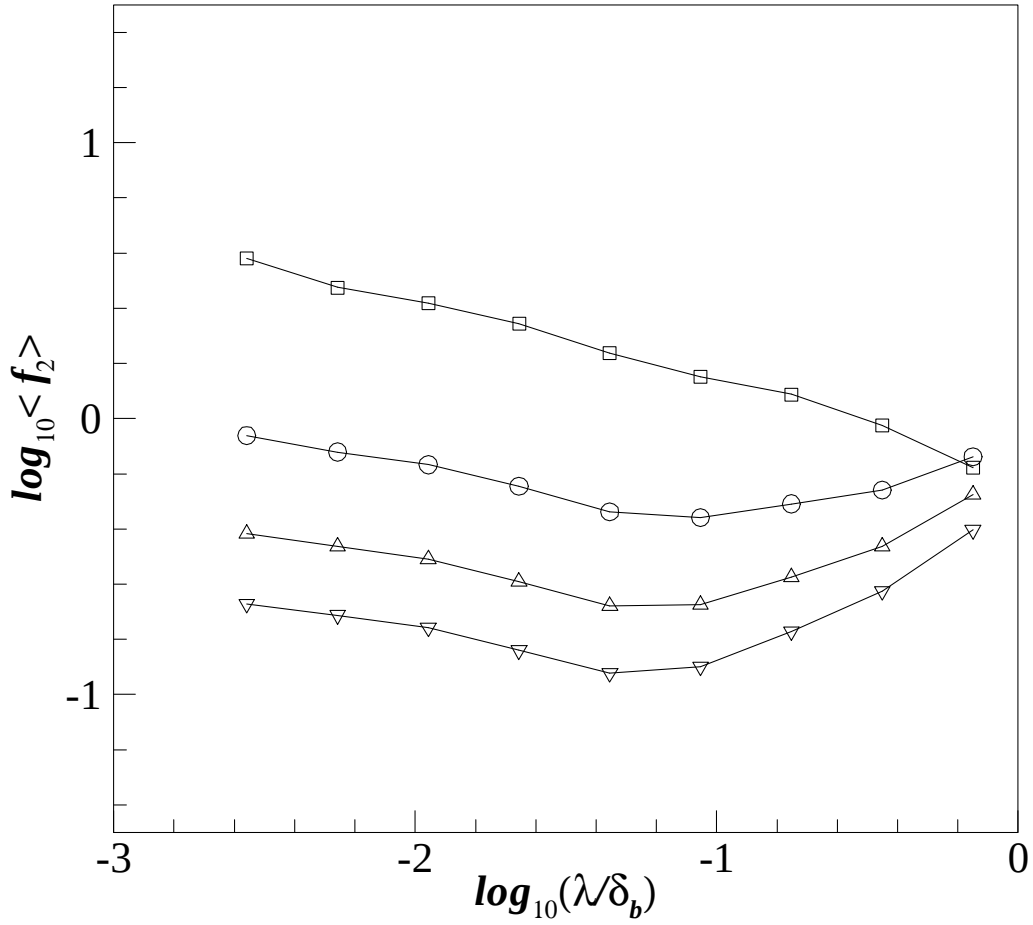

Figure 5.27 LEB-scale PDF as a function of concentration threshold. Data plotted versus normalized scale, λ / δ_b, for the passive scalar iso-surface at a concentration m times the local standard deviation above the local mean, for m = 1 (□), 3 (○), 5 (△), and 7 (▽), at x = 4 m; for D = 4.7 mm and Re = 10,000.

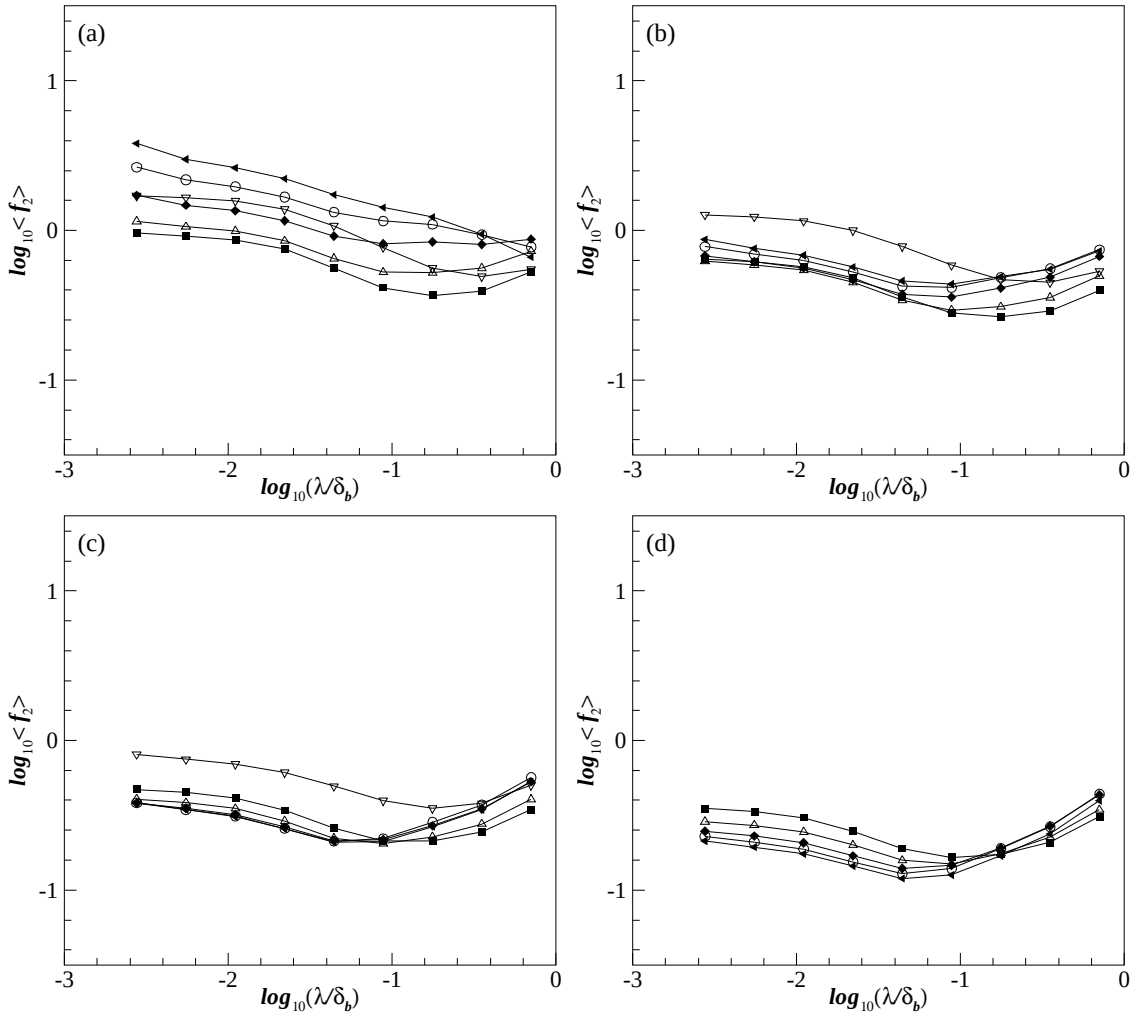

Figure 5.28 LEB-scale PDF as a function of distance from the source. Data plotted versus normalized scale, λ/δ_b, for the passive scalar iso-surface at a concentration m times the local standard deviation above the local mean, for (a) m = 1, (b) 3, (c) 5, and (d) 7, at x = 0.1 m (▽), 0.25 m (■), 0.5 m (△), 1 m (♦), 2 m (○), and 4 m (◀); for D = 4.7 mm and Re = 10,000.

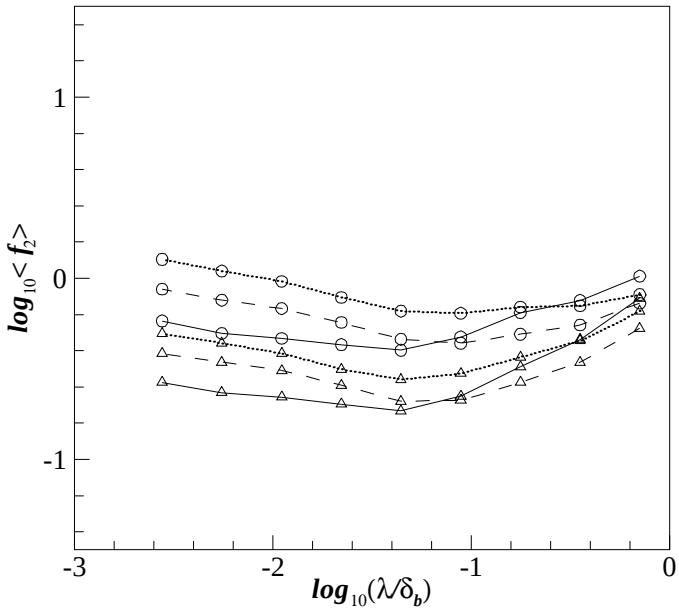

Figure 5.29 LEB-scale PDF as a function of Reynolds number. Data plotted versus normalized scale, λ / δ_b, for the passive scalar iso-surface at a concentration m times the local standard deviation above the local mean, for m = 3 (○) and 5 (△), at x = 4 m; for D = 4.7 mm and Re = 5000 (——), 10,000 (– – –), and 20,000 (••••••••).

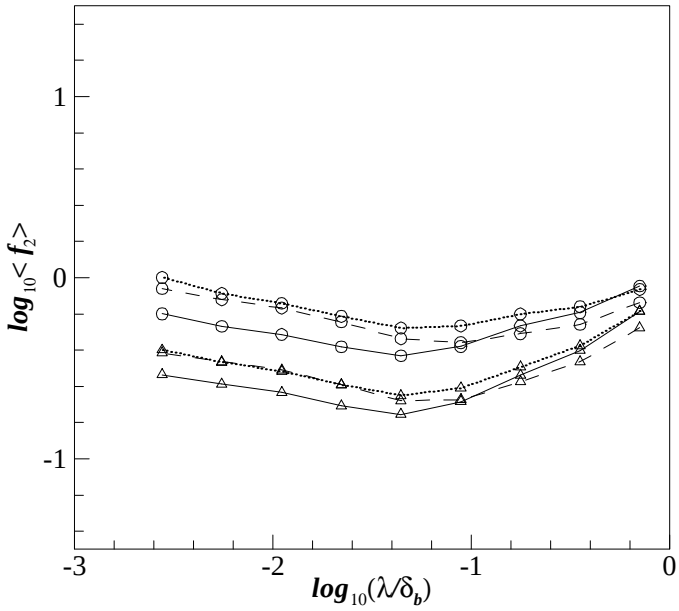

Figure 5.30 LEB-scale PDF as a function of source nozzle diameter. Data plotted versus normalized scale, λ / δ_b, for the passive scalar iso-surface at a concentration m times the local standard deviation above the local mean, for m = 3 (○) and 5 (△), at x = 4 m; for D = 2.2 mm (——), 4.7 mm (– – –), and 9.4 mm (••••••••) and Re = 10,000.

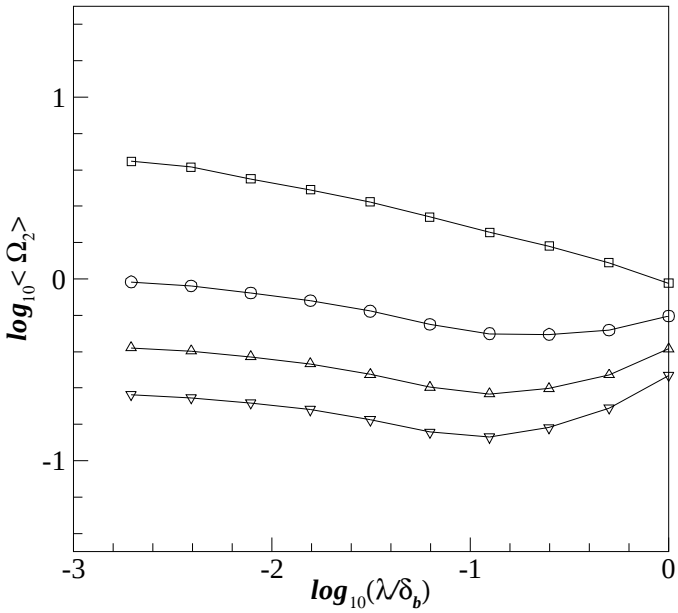

Figure 5.31 Scale-cumulative length-area ratio as a function of concentration threshold. Data plotted versus normalized scale, λ/δ_b, for the passive scalar iso-surface at a concentration m times the local standard deviation above the local mean, for m = 1 (□), 3 (○), 5 (△), and 7 (▽), at x = 4 m; for D = 4.7 mm and Re = 10,000.

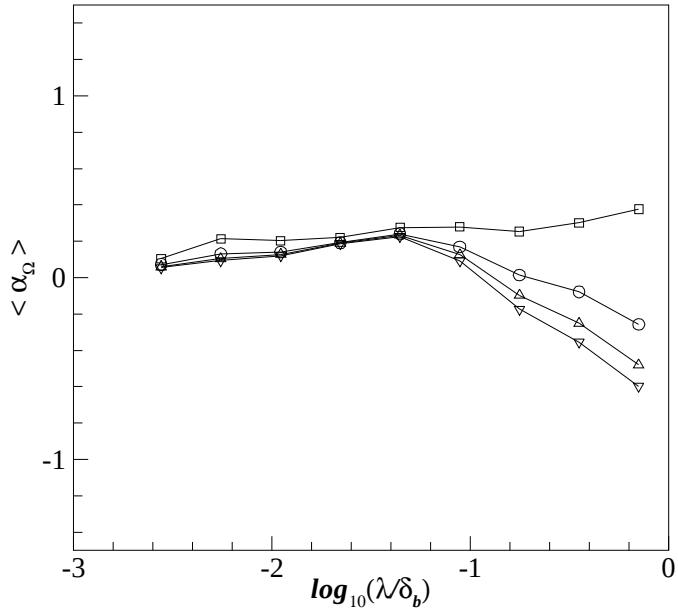

Figure 5.32 Scale-cumulative length-area ratio exponent as a function of concentration threshold. Data plotted versus normalized scale, λ/δ_b, for the passive scalar iso-surface at a concentration m times the local standard deviation above the local mean, for m = 1 (□), 3 (○), 5 (△), and 7 (▽), at x = 4 m; for D = 4.7 mm and Re = 10,000.

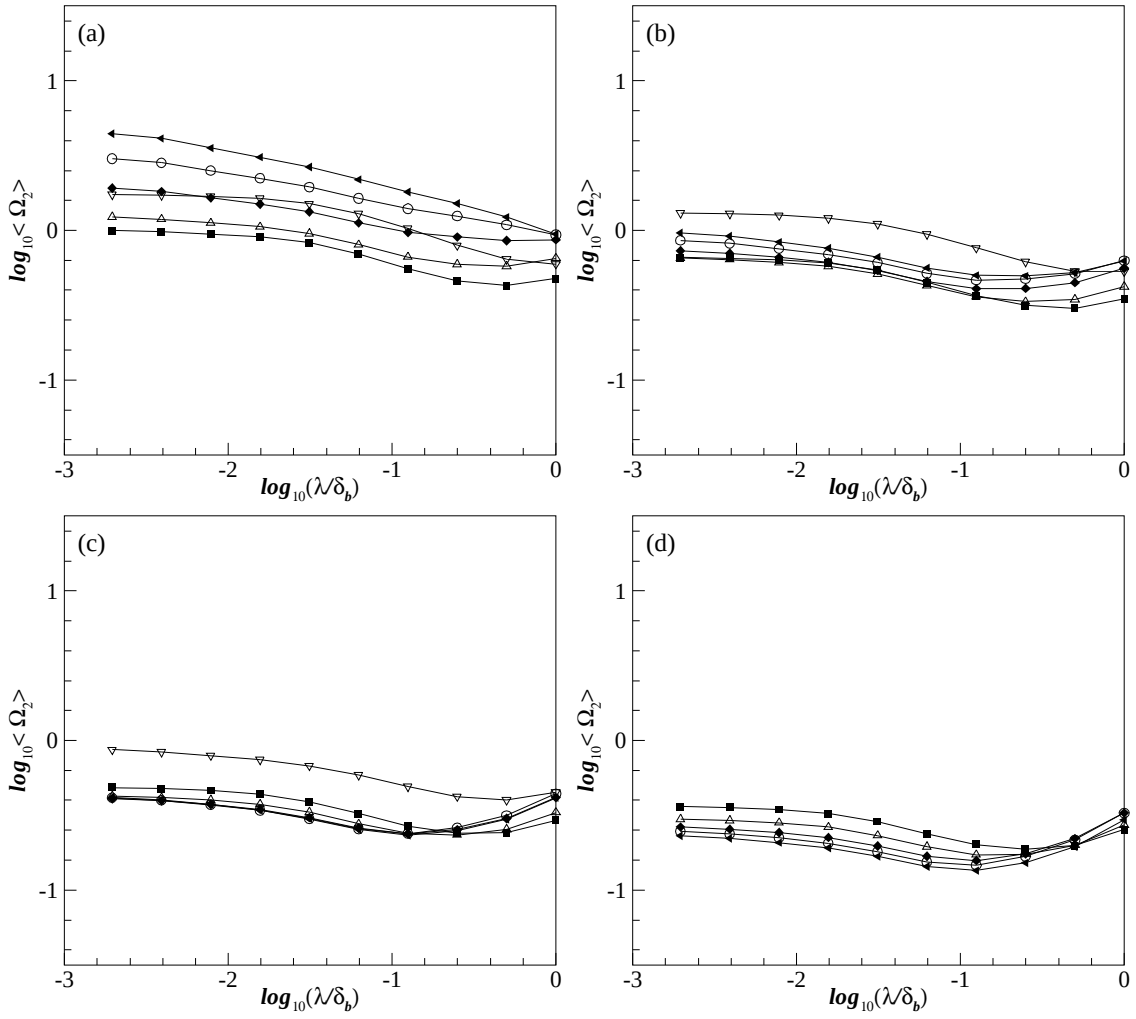

Figure 5.33 Scale-cumulative length-area ratio as a function of distance from the source. Data plotted versus normalized scale, λ/δ_b, for the passive scalar iso-surface at a concentration m times the local standard deviation above the local mean, for (a) m = 1, (b) 3, (c) 5, and (d) 7, at x = 0.1 m (▽), 0.25 m (■), 0.5 m (△), 1 m (♦), 2 m (○), and 4 m (◀); for D = 4.7 mm and Re = 10,000.

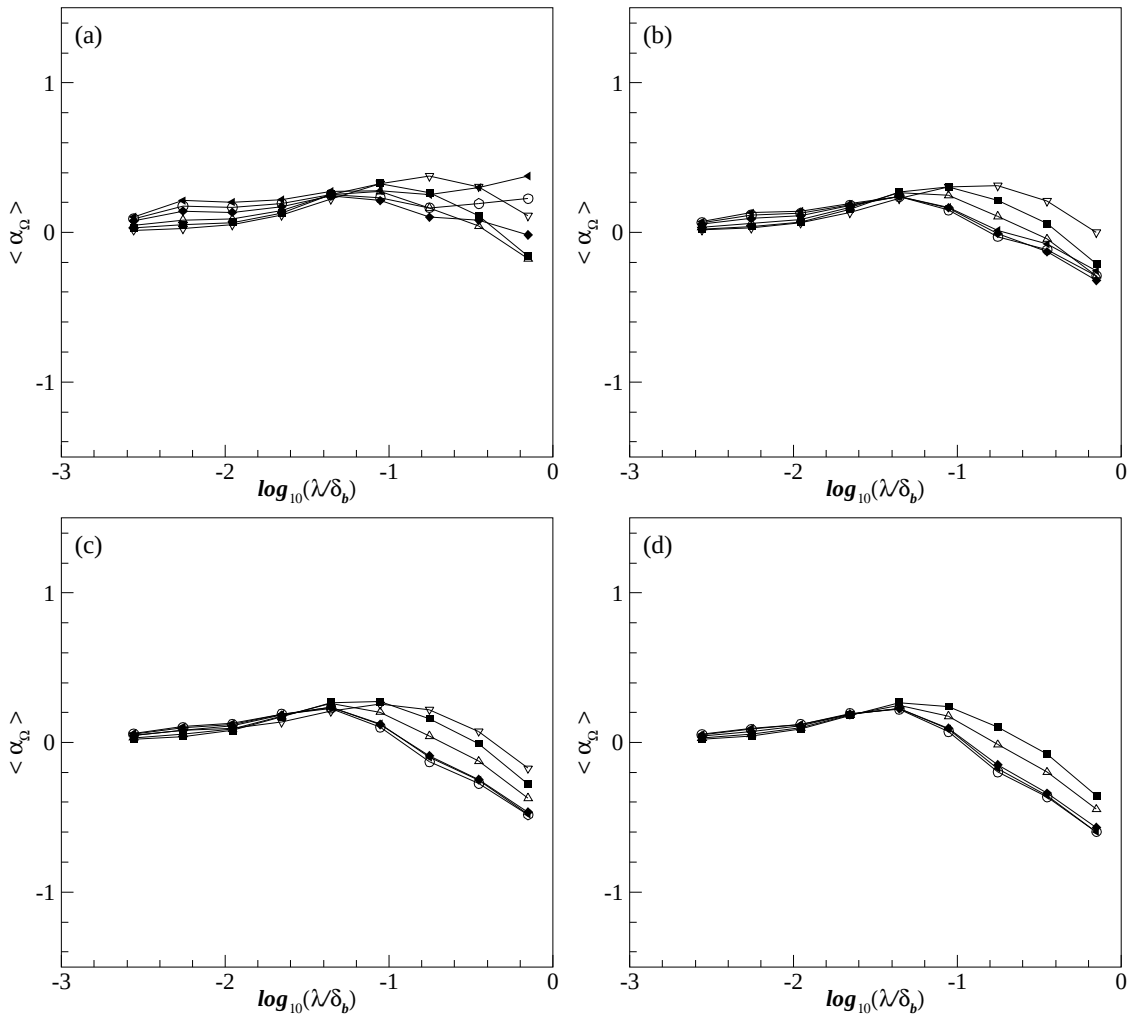

Figure 5.34 Scale-cumulative length-area ratio exponent as a function of distance from the source. Data plotted versus normalized scale, λ/δ_b, for the passive scalar iso-surface at a concentration m times the local standard deviation above the local mean, for (a) m = 1, (b) 3, (c) 5, and (d) 7, at x = 0.1 m (▽), 0.25 m (■), 0.5 m (△), 1 m (♦), 2 m (○), and 4 m (◀); for D = 4.7 mm and Re = 10,000.

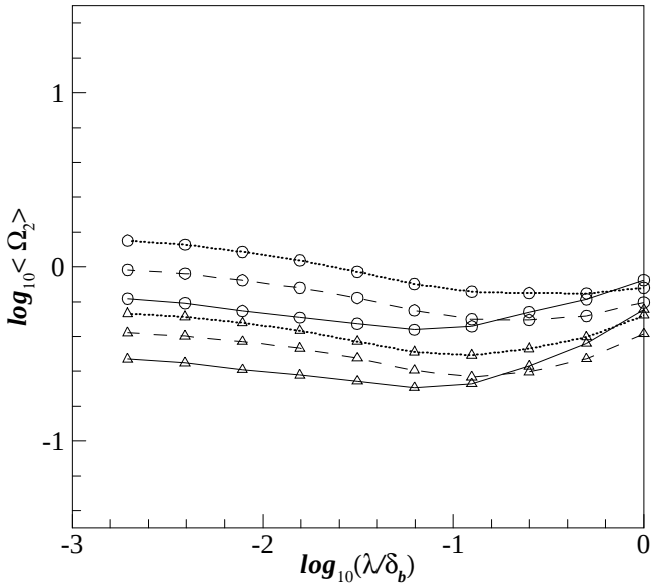

Figure 5.35 Scale-cumulative length-area ratio as a function of Reynolds number. Data plotted versus normalized scale, λ/δ_b, for the passive scalar iso-surface at a concentration m times the local standard deviation above the local mean, for m = 3 (○) and 5 (△), at x = 4 m; for D = 4.7 mm and Re = 5000 (——), 10,000 (– – –), and 20,000 (••••••••).

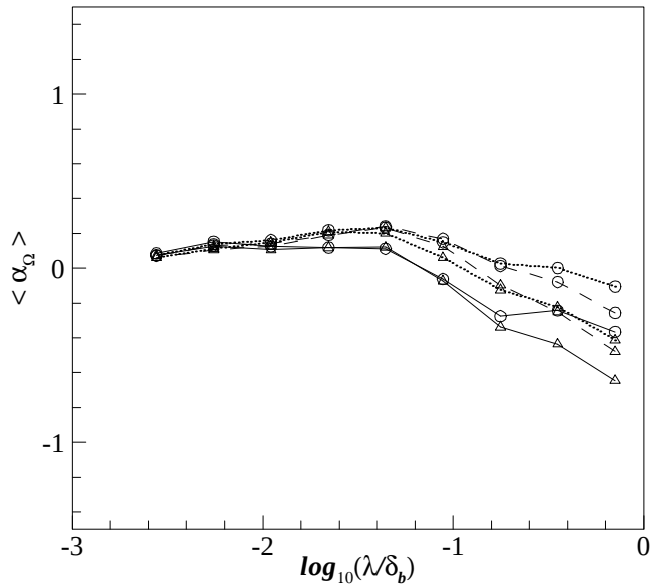

Figure 5.36 Scale-cumulative length-area ratio exponent as a function of Reynolds number. Data plotted versus normalized scale, λ/δ_b, for the passive scalar iso-surface at a concentration m times the local standard deviation above the local mean, for m = 3 (○) and 5 (△), at x = 4 m; for D = 4.7 mm and Re = 5000 (——), 10,000 (– – –), and 20,000 (••••••••).

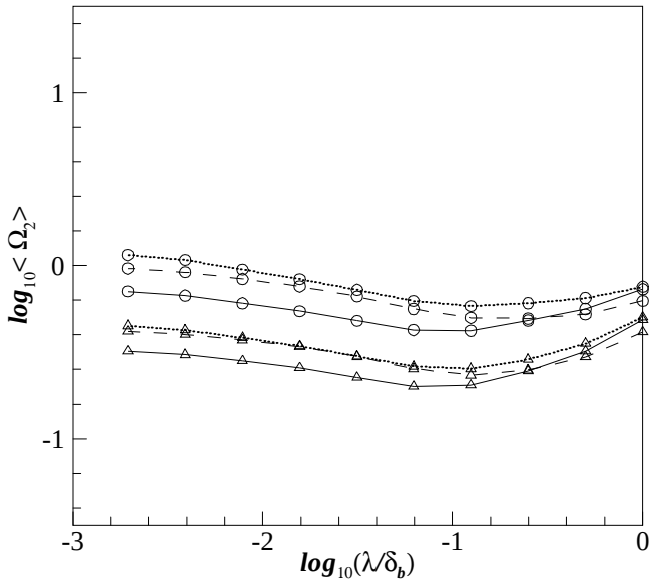

Figure 5.37 Scale-cumulative length-area ratio as a function of source nozzle diameter. Data plotted versus normalized scale, λ / δ_b, for the passive scalar iso-surface at a concentration m times the local standard deviation above the local mean, for m = 3 (○) and 5 (△), at x = 4 m; for D = 2.2 mm (——), 4.7 mm (– – –), and 9.4 mm (••••••••) and Re = 10,000.

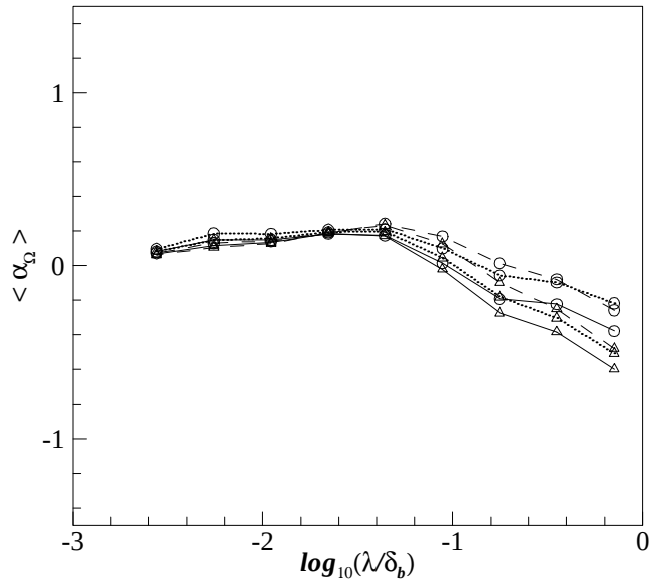

Figure 5.38 Scale-cumulative length-area ratio exponent as a function of source nozzle diameter. Data plotted versus normalized scale, λ / δ_b, for the passive scalar iso-surface at a concentration m times the local standard deviation above the local mean, for m = 3 (○) and 5 (△), at x = 4 m; for D = 2.2 mm (——), 4.7 mm (– – –), and 9.4 mm (••••••••) and Re = 10,000.

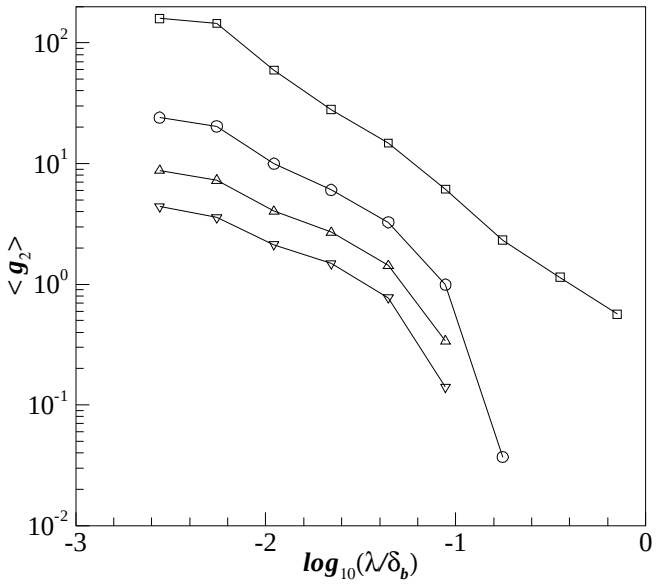

Figure 5.39 Scale-local length-area density as a function of concentration threshold. Data plotted versus normalized scale, λ/δ_b, for the passive scalar iso-surface at a concentration m times the local standard deviation above the local mean, for m = 1 (□), 3 (○), 5 (△), and 7 (▽), at x = 4 m; for D = 4.7 mm and Re = 10,000.

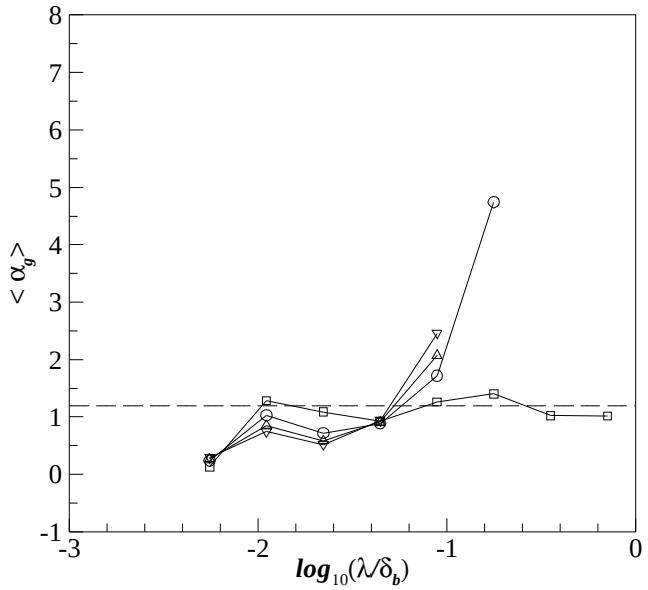

Figure 5.40 Scale-local length-area density exponent as a function of concentration threshold. Data plotted versus normalized scale, λ/δ_b, for the passive scalar iso-surface at a concentration m times the local standard deviation above the local mean, for m = 1 (□), 3 (○), 5 (△), and 7 (▽), at x = 4 m; for D = 4.7 mm and Re = 10,000. Long dashed line represents $\langle \alpha_g \rangle = 1.2$.

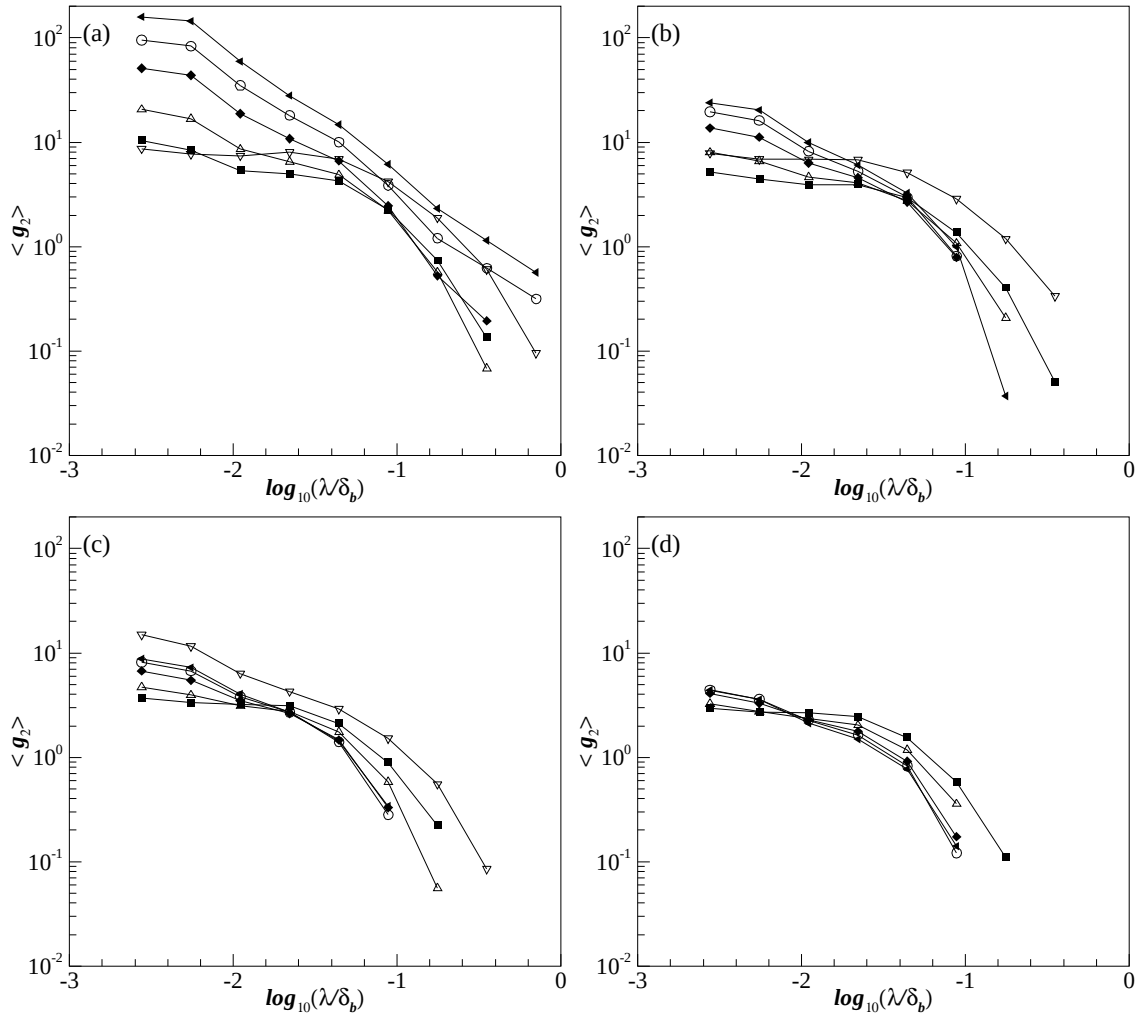

Figure 5.41 Scale-local length-area density as a function of distance from the source. Data plotted versus normalized scale, λ/δ_b, for the passive scalar iso-surface at a concentration m times the local standard deviation above the local mean, for (a) m = 1, (b) 3, (c) 5, and (d) 7, at x = 0.1 m (▽), 0.25 m (■), 0.5 m (△), 1 m (♦), 2 m (○), and 4 m (◀); for D = 4.7 mm and Re = 10,000.

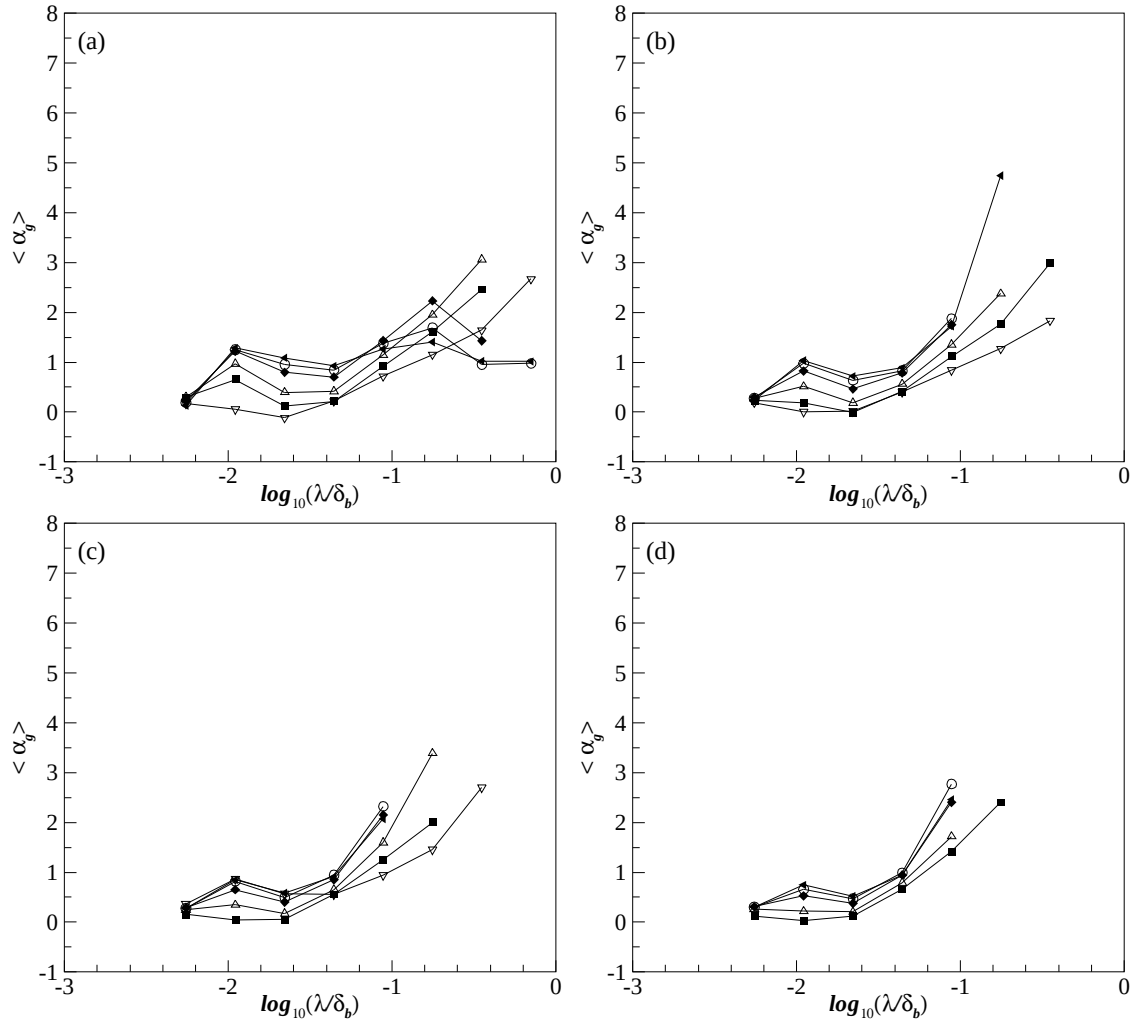

Figure 5.42 Scale-local length-area density exponent as a function of distance from the source. Data plotted versus normalized scale, λ / δ_b, for the passive scalar iso-surface at a concentration m times the local standard deviation above the local mean, for (a) m = 1, (b) 3, (c) 5, and (d) 7, at x = 0.1 m (▽), 0.25 m (■), 0.5 m (△), 1 m (♦), 2 m (○), and 4 m (◀); for D = 4.7 mm and Re = 10,000.

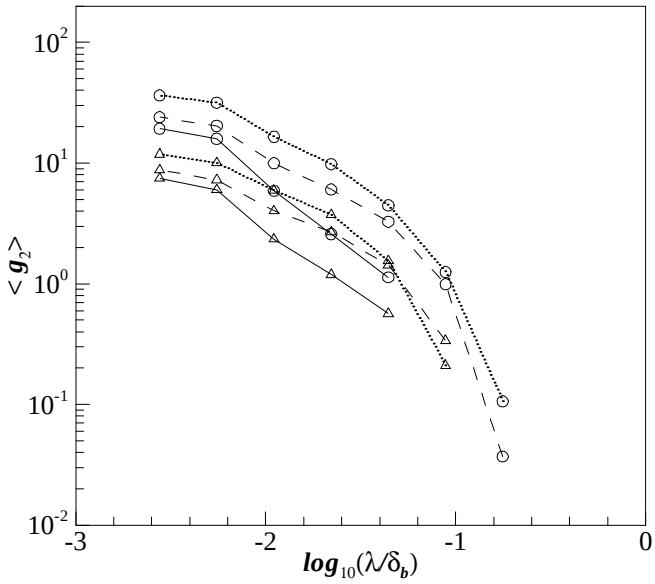

Figure 5.43 Scale-local length-area density as a function of Reynolds number. Data plotted versus normalized scale, λ/δ_b, for the passive scalar iso-surface at a concentration m times the local standard deviation above the local mean, for m = 3 (○) and 5 (△), at x = 4 m; for D = 4.7 mm and Re = 5000 (——), 10,000 (– – –), and 20,000 (••••••••).

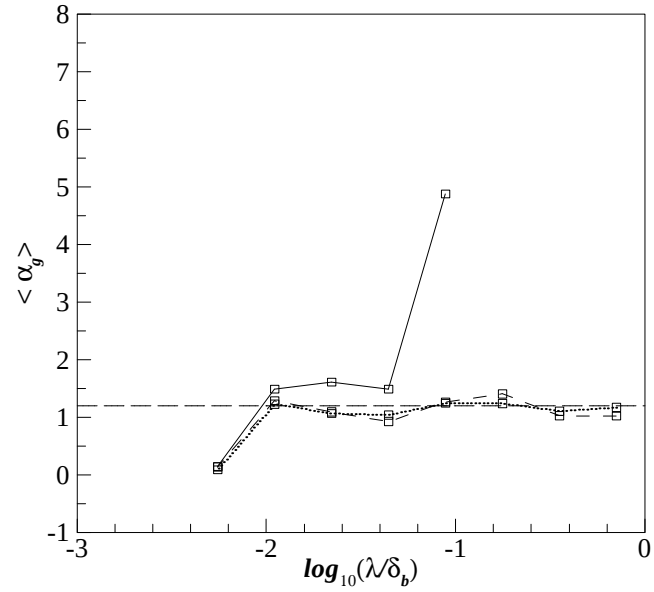

Figure 5.44 Scale-local length-area density exponent as a function of Reynolds number. Data plotted versus normalized scale, λ/δ_b, for the passive scalar iso-surface at a concentration m times the local standard deviation above the local mean, for m = 1 (□), at x = 4 m; for D = 4.7 mm and Re = 5000 (——), 10,000 (– – –), and 20,000 (••••••••). Long dashed line represents $\langle \alpha_g \rangle = 1.2$.

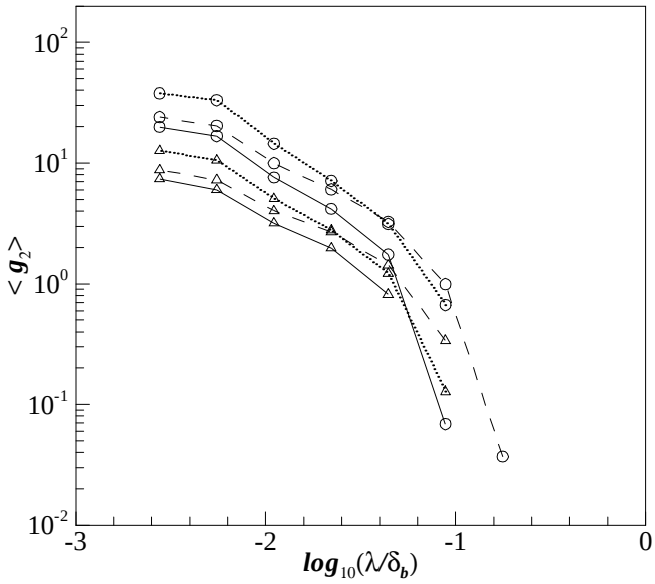

Figure 5.45 Scale-local length-area density as a function of source nozzle diameter. Data plotted versus normalized scale, λ/δ_b, for the passive scalar iso-surface at a concentration m times the local standard deviation above the local mean, for m = 3 (○) and 5 (△), at x = 4 m; for D = 2.2 mm (——), 4.7 mm (– – –), and 9.4 mm (••••••••) and Re = 10,000.

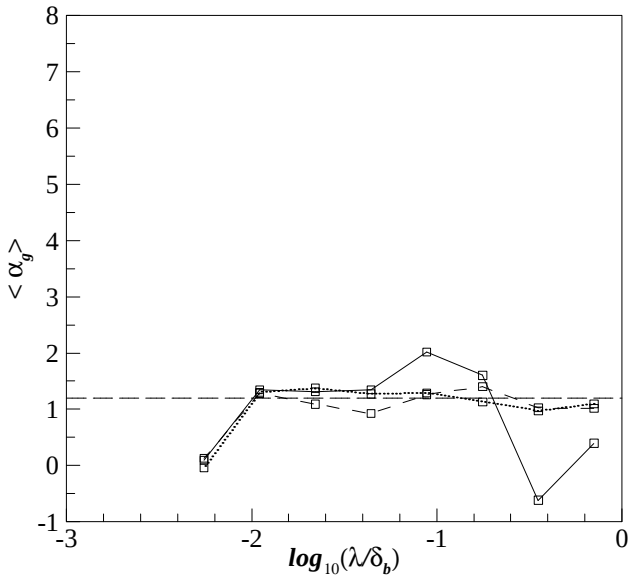

Figure 5.46 Scale-local length-area density exponent as a function of source nozzle diameter. Data plotted versus normalized scale, λ/δ_b, for the passive scalar iso-surface at a concentration m times the local standard deviation above the local mean, for m = 1 (□), at x = 4 m; for D = 2.2 mm (——), 4.7 mm (– – –), and 9.4 mm (••••••••) and Re = 10,000. Long dashed line represents $\langle \alpha_g \rangle = 1.2$.

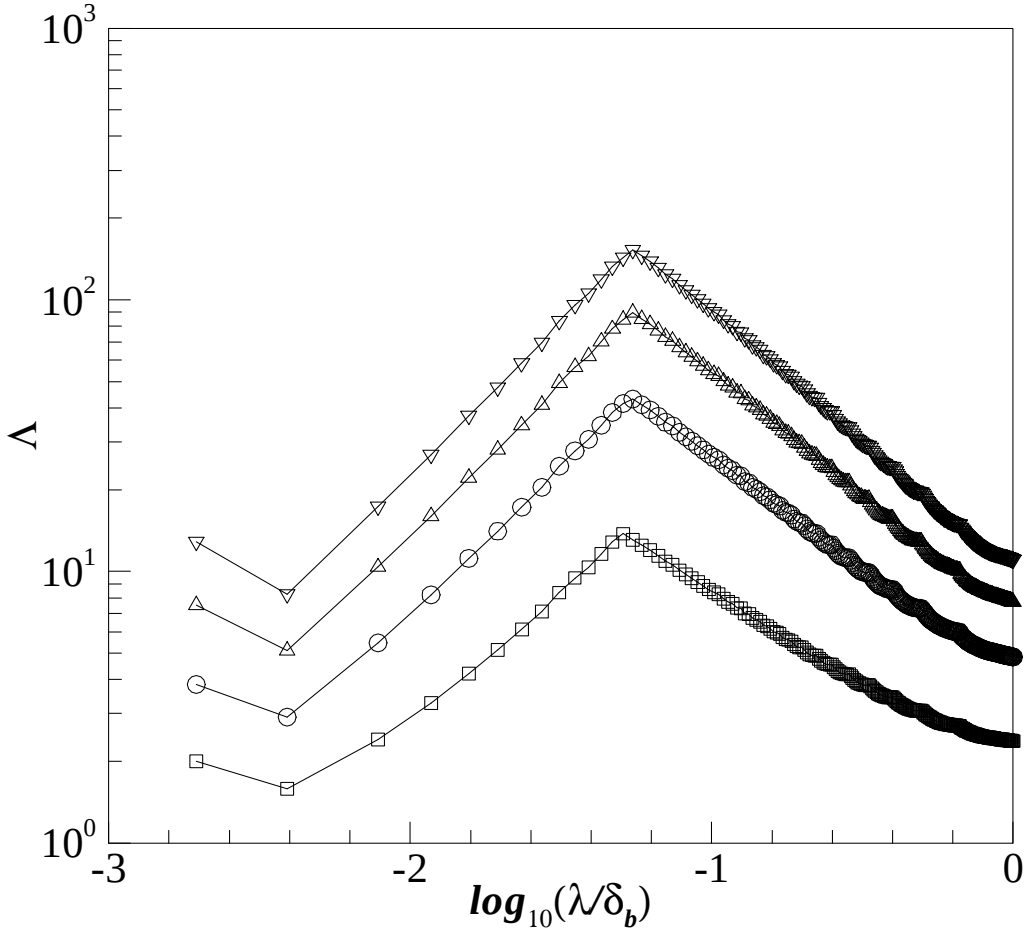

Figure 5.47 Lacunarity as a function of concentration threshold. Data plotted versus normalized scale, λ/δ_b, for the passive scalar iso-surface at a concentration m times the local standard deviation above the local mean, for m = 1 (□), 3 (○), 5 (△), and 7 (▽), at x = 4 m; for D = 4.7 mm and Re = 10,000.

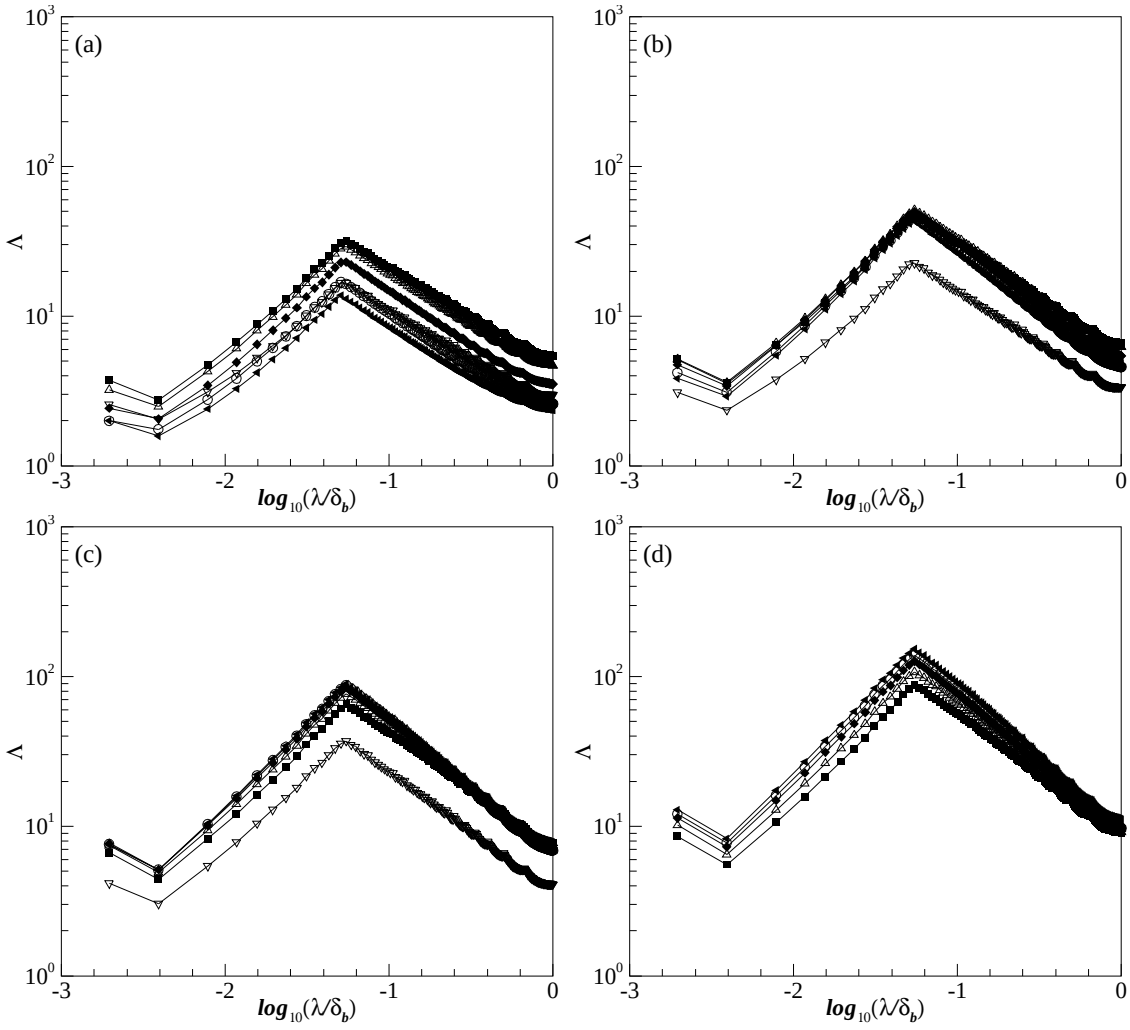

Figure 5.48 Lacunarity as a function of distance from the source. Data plotted versus normalized scale, λ/δ_b, for the passive scalar iso-surface at a concentration m times the local standard deviation above the local mean, for (a) m = 1, (b) 3, (c) 5, and (d) 7, at x = 0.1 m (▽), 0.25 m (■), 0.5 m (△), 1 m (♦), 2 m (○), and 4 m (◀); for D = 4.7 mm and Re = 10,000.

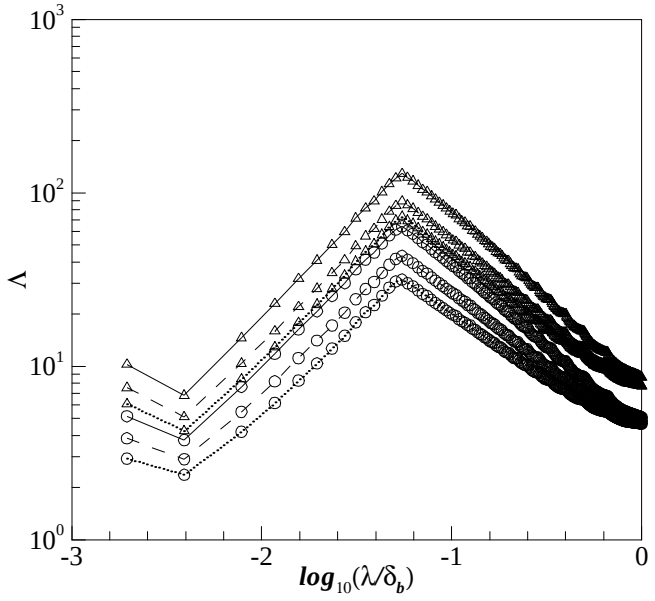

Figure 5.49 Lacunarity as a function of Reynolds number. Data plotted versus normalized scale, λ/δ_b, for the passive scalar iso-surface at a concentration m times the local standard deviation above the local mean, for m = 3 (○) and 5 (△), at x = 4 m; for D = 4.7 mm and Re = 5000 (——), 10,000 (– – –), and 20,000 (••••••••).

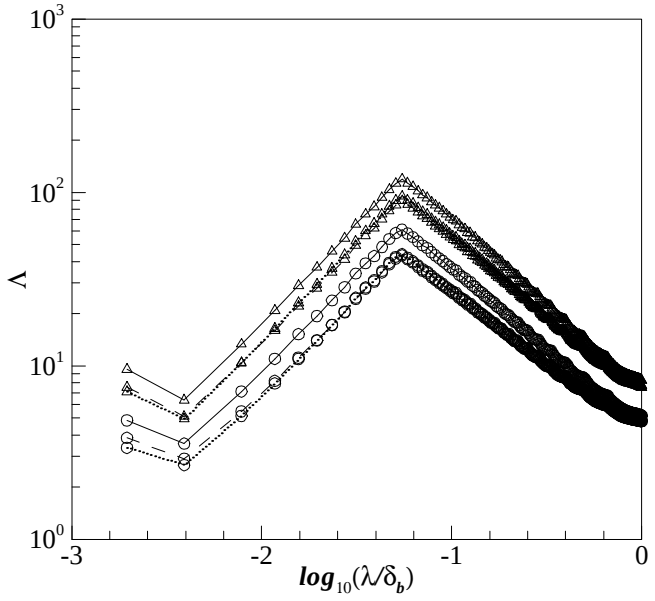

Figure 5.50 Lacunarity as a function of source nozzle diameter. Data plotted versus normalized scale, λ/δ_b, for the passive scalar iso-surface at a concentration m times the local standard deviation above the local mean, for m = 3 (○) and 5 (△), at x = 4 m; for D = 2.2 mm (——), 4.7 mm (– – –), and 9.4 mm (••••••••) and Re = 10,000.

Chapter 6

Summary and Discussion

Chapters 4 and 5 present a detailed analysis of the local-structure of the passive scalar field generated by an iso-kinetic release of a high Schmidt number dye into a turbulent boundary layer. The analysis mainly focused on the effects of velocity characteristics, large-scale anisotropy of the scalar field, external intermittency, and initial injection length scale on the local structure and highlighted the deviations from the theoretical predictions based on self-similarity hypotheses and other classical arguments as a consequence of these effects. In particular, Chapter 4 presents a statistical analysis of the local structure via statistical quantities such as moments, probability density functions, power spectra, structure functions, and correlation functions of the small-scale structure of the scalar field. Chapter 5 presents an analysis of the local-structure from a more applied view point via the tools of fractal geometry namely: the fractal dimension and other coverage statistics along with newer measures such as the coverage length underestimate and lacunarity. This chapter aims to draw important conclusions from Chapters 4 and 5, discuss the significance of these results in the "big-picture" of the current state of research on passive scalars in turbulent flows, and make suggestions for future research.

6.1 Summary

6.1.1 The passive scalar probability density functions (PDFs)

As seen in Chapter 4, the PDF of the passive scalar fluctuations is obviously non-Gaussian. The results are more supportive of the existence of elongated exponential-like tails as predicted in the PSS argument (Pumir et al. 1991) for scalar fields in the presence of a mean gradient. This study also shows that the tail of the PDF is sensitive to initial conditions with the steepness of the tail decreasing with increasing injection length scale.

The characteristics of the PDF of the fluctuating scalar gradients are observed to be consistent with Monin & Yaglom (1975). In particular, these PDFs have tails that are much broader than a corresponding Gaussian tail due to internal intermittency of the scalar dissipation field. The small-scale structure has preferential orientation with the presence of ramp-cliff structures aligning with the mean gradient. This is indicated by the $O(1)$ skewness observed for the PDFs of both longitudinal and vertical scalar gradients. The PDFs possess tails that are asymmetrically flared. Also, the tails of the PDFs grow broader with distance from the source indicating an increase in the internal intermittency. Moreover, far from the source the scalar gradient PDFs are practically unaffected among the studied Reynolds numbers. Most importantly, these PDFs are sensitive to initial conditions with the tails less broad for the larger injection length scales. In conclusion, the scalar gradient PDF is strongly influenced by large-scale anisotropies, Reynolds number, and initial conditions.

The PDF of scalar differences is also non-Gaussian for large separation distance in odds with the classical theoretical assumptions. The mean scalar gradients are observed to skew these PDFs for all separation distances.

6.1.2 Spectrum of the passive scalar field

The present study addresses the characteristics of the passive scalar power spectrum in the inertial-convective and viscous-convective regimes. The scaling-exponent in the inertial-convective regime was found to be dependent on Reynolds number in agreement with Sreenivasan (1996). The exponent increased in magnitude with increasing Reynolds number. The scaling exponent was found to be more sensitive to the intermittency factor and scalar gradients in agreement with Dowling & Dimotakis (1990). The exponent increased in magnitude with the presence of stronger mean gradients and intermittency factor. The inertial-convective scaling exponent, in general, was not $-5/3$ and varied strongly with large-scale anisotropy in violation of local-isotropy assumptions. The effect of initial conditions was evident when the size of the nozzle diameter was in the range of dissipative scales. For this case, the inertial-convective range scaling exponent deviated from $-5/3$ and showed k^{-1} scaling far downstream where the effects of large-scale anisotropies were minimal. This observation is consistent with the cascade-bypass scenario suggested by Villermaux et al. (2001). In this scenario, the presence of a strong stretching rate at the scale of the nozzle diameter bypasses the traditional cascade picture.

The viscous-convective scaling behavior deviated significantly from Batchelor's k^{-1} scaling law, clearly disputing the generality of Batchelor's arguments. The observations

agreed with the scaling behavior in Miller & Dimotakis (1996) where a log-normal spectral decrease was observed. The steepness of the log-normal decrease for the vertical power spectrum was found to be sensitive to the presence of a vertical mean velocity gradient.

6.1.3 Passive scalar structure and correlation functions

Even-ordered structure functions of the passive scalar field were calculated with the highest order of $n = 12$. The exponents were found to deviate from the KOC prediction and appeared to saturate with increasing order. The deviation, however, was sensitive to large-scale anisotropy. The longitudinal exponents were higher in magnitude than the KOC prediction near the source due to the mean scalar gradient and intermittency. With increasing downstream distance, the exponents decreased in magnitude below the KOC predication and then increased slowly appearing to asymptote to their respective isotropic values for $x \to \infty$. The variation of these exponents inversely correlated with the variation of skewness and kurtosis of the scalar fluctuations. Another interesting result is that the exponents of the vertical structure functions were quite different in magnitude than their longitudinal counterparts. The exponents for the vertical structure functions showed strong saturation when plotted against n due to the stronger mean gradient in the vertical direction. Both the longitudinal and vertical exponents increased in magnitude with Reynolds number and injection length scale.

Scaling behavior was also noted for the two-point correlation functions and the defined triangular three-point correlation functions. The variation of these scaling exponents with

different experimental parameters agreed well with the variations of the structure function exponents.

6.1.4 Fractal geometry of passive scalar iso-surfaces

The passive scalar iso-surfaces were analyzed by the box-counting algorithm to generate various scale-dependent coverage statistics of the iso-surfaces including the fractal dimension. The raw iso-surface images are qualitatively different from those reported in the archival literature for the case of scalar fields generated via high-momentum jets. Here, the scalar field is highly intermittent and consists of sparse filaments in the measurement plane. The fractal measures of the iso-surfaces were found to be scale dependent with Level 3 complexity.

The fractal dimension (of two-dimension transects of passive scalar iso-surfaces) was observed to be close to 1.0 at scales near the Batchelor length scale and increased with increasing scale, which indicates that the interfaces are smooth at the smallest scale. For the higher concentration thresholds the fractal dimension reached a maximum around the Kolmogorov length scale indicating maximum convolution at this scale. Fractal dimension values below the topological dimension were observed for higher thresholds due to the sparseness of the filaments. The fractal dimension was sensitive to all experimental parameters. However, in the viscous-convective regime the fractal dimension appeared to follow a universal behavior. The fractal dimension at larger scales decreased with increasing concentration threshold and distance from the source, and it

increased with increasing Reynolds number. The dependence with respect to nozzle diameter was not clear.

Other fractal measures collectively known as the coverage statistics were also examined and showed significant dependence on intermittency factor, Reynolds number, and nozzle diameter. Most importantly, new measures called the coverage length underestimate and lacunarity were calculated for the passive scalar iso-surfaces. The coverage length underestimate is a useful measure for modeling because it provides information for the true interfacial length given a course observation or simulation of the passive scalar field. It is easy to show that the coverage length underestimate at a given scale is purely a function of the coverage dimension at lower scales. Using Equations 5.21 and 5.20 and the fact that $L_{d,u} = \Omega_{d,tot} / \Omega_d$ it can be shown that:

$$L_{d,u}(\lambda) = \exp\left(\int_0^{\lambda} \tfrac{1}{\tilde{\lambda}} \left(D_d\left(\tilde{\lambda}\right) - d_t \right) d\tilde{\lambda} \right) \tag{6.1}$$

The integrand in the above equation is integrable in the given limits as Catrakis (2002) showed that $g_d(\lambda \to 0) = 0$. From the above equation, it is clear that a universal variation of the fractal dimension in the viscous-convective regime corresponds with universal behavior of the coverage length underestimate in the viscous-convective regime. Consequently, one may estimate the true interfacial length based on the variation of the fractal dimension in the viscous-convective regime. The lacunarity of the iso-surfaces increases with scale in the viscous-convective regime, which suggests increasing

in-homogeneity and intermittency. The fluctuating iso-surfaces appear to be most inhomogeneous around the Kolmogorov length scale due to a local maximum of lacunarity.

6.2 Conclusions

It is clear from this study that the large-scale anisotropy of the scalar field, the initial conditions for a point-source release, and the boundedness of the scalar deviate the characteristics of local structure from the isotropic expectations.

The PDFs of concentration fluctuations are influenced by the fluctuation boundedness and deviate significantly from Gaussian distributions. The injection length scale influences the slope of the exponential-like tails of the scalar fluctuation PDF and scalar gradient PDF. The mean gradient influences the skewness of the scalar gradient PDF, and the external intermittency greatly increases the kurtosis. The inertial-convective scaling of the scalar spectra depends on the external intermittency, mean scalar gradient, and injection length scale. The cascade-bypass scenario appears to be valid for injection length scales in the inertial-convective regime. The viscous-convective regime shows an approximately log-normal spectral decrease, at least over the first half of the regime, with the decrease faster than Batchelor's k^{-1} scaling. The data also suggests that Batchelor's scaling is not attained over the unresolved portion of the viscous-convective regime. Also, the mean shear appears to influence the slope of the log-normal spectral decrease for the one-dimensional spectra. Further study is needed on the influence of the boundedness of the scalar variance on the energy contained in the wave-number range

$k > \frac{1}{\eta}$ because the k^{-1} scaling implies that $\left\langle \theta^2 \right\rangle \to \infty$ as $Sc \to \infty$, which is inconsistent. The structure function exponents deviate from the local-isotropy expectation and depend on the mean gradient and external intermittency. These exponents are inversely correlated with the kurtosis of the PDF of scalar fluctuations. Two- and three-point correlation functions also show scaling behavior with exponents well correlated with those of the structure functions.

The fractal geometry analysis provides valuable insights on the geometry of the scalar boundary. The coverage dimension varies with scale in a universal form over the viscous-convective range. The coverage length underestimate reflects this universal behavior and forms an important measure for practical applications. The lacunarity of the passive scalar iso-surfaces shows that the passive scalar field is most in-homogenous around the Kolmogorov length scale.

6.3 Unique contributions and applications

The following is a brief list of unique contributions:

- Demonstrated the dependence of the tails of the PDFs of scalar fluctuations and scalar gradient on the initial conditions of the plume (i.e. injection size).
- Established the dependence of the inertial-convective scaling of the scalar power spectrum on large-scale anisotropy.
- Independently confirmed the cascade-bypass phenomena.
- Established the absence of Batchelor scaling in the viscous-convective regime for the current flow conditions.

- Established the correlation between the structure function scaling exponents and kurtosis of scalar fluctuations.
- Established the universality of the coverage dimension and coverage length underestimate in the viscous-convective regime.
- Introduced lacunarity to quantify the in-homogeneity of the instantaneous passive scalar fields.

The following is a brief list of applications of this research:

- The research may be applied to develop new models of small-scale structure that are non-universal and depend on local characteristics of the mean passive scalar field.
- The data may be used to develop plume source tracking strategies for autonomous robots by assessing cues present in the field.

6.4 Future directions

The current research opens the possibility of additional analysis of the data as well as new ideas to conduct future research in the area of passive scalar mixing in turbulent flows. A brief description of ideas and directions are presented in this section.

The experiment configuration in this research is limited in the sense that there is minimal control on the mean velocity shear via Reynolds number variation and the scalar is released with a fixed injection mechanism. Novel techniques need to be developed with the aim of producing a uniform scalar gradient non-invasively in a homogeneous

turbulent shear flow. Developing such experimental facilities is key to addressing the issue of effects of large-scale anisotropy on the local structure of velocity and scalar fields.

Multi-point correlation functions need to be addressed in a more detail to investigate if these functions provide additional insights into the local structure compared to the traditional structure functions. In particular, characterizing the multi-point joint probability density function will be a useful because any structure function or multi-point correlation function may be derived from this distribution. There is strong indication that this distribution possesses quasi-universal behavior for separations in the inertial-convective regime. Characteristics of the joint probability density function may be studied as a function of Sc, Re, large-scale anisotropy, and intermittency.

Understanding the dynamics of the scalar variance dissipation field is critical to understanding the turbulence of passive scalars in turbulent flows. Effects of large-scale anisotropy, Schmidt number, and initial-conditions need to be addressed on the scalar dissipation field to better understand the dynamics of realistic anisotropic scalar fields. It is possible to extend the current study by analyzing the dissipation field approximated by a two-dimensional surrogate. It will be useful to analyze the PDF, and multifractal characteristics of the dissipation field for the current study for modeling purposes.

New experiments are needed to couple the effects of the velocity field via simultaneous velocity and passive scalar measurements. Such an approach will provide information on

the velocity structure and the joint velocity and passive scalar structure via joint structure functions and cross-correlation functions.

The fractal geometry analyzed is clearly limited by the embedding dimension of the measurements. This study may be extended via three-dimensional imaging of the small-scale structure to provide the actual multi-fractal behavior of the scalar field. Such an approach to plume dispersion problems has immense significance in the field of design of hydraulic structures built for waste-water or pollutant disposal in the natural environment.

References

Anselmet, F., Gagne, F., Hopfinger, E. J., and Antonia, R. A. (1984) "High-order velocity structure functions in turbulent shear flows," J. Fluid Mech., 140, 63-89.

Antonia, R. A., Browne, L. W. B., Britz, D., and Chambers, A. J. (1984) "A comparison of properties of temporal and spatial temperature increments in a turbulent plane jet," Phys. Fluids, 27(1), 87-93.

Antonia, R. A., Satyaprakash, B. R., Hussain, A. K. M. F. (1982) "Statistics of fine-scale velocity in turbulent plane and circular jets," J. Fluid Mech., 119, 55-89.

Arad, I., Biferale, L., Mazzitelli, I., and Procaccia, I. (1999) "Disentangling scaling properties in anisotropic and inhomogeneous turbulence," Phys. Rev. Letters, 82, 5040-5043.

Arad, I., Dhruva. B., Kurien, S., L'vov, V. S., Procaccia, I. and Sreenivasan, K. R. (1998) "Extraction of anisotropic contributions in turbulent flows," Phys. Rev. Letters, 81, 5330-5333.

Arad, I., L'vov, V. S., and Procaccia, I. (1999) "Correlation functions in isotropic and anisotropic turbulence: The role of the symmetry group," Phys. Rev. E, 59, 6753-6765.

Arcoumanis, C., McGuirk, J. J., and Palma, J. M. L. M. (1990) "On the use of fluorescent dyes for concentration measurements in water flows," Exp. Fluids, 10, 177-180.

Batchelor, G. K. (1959) "Small-scale variation of convected quantities like temperature in turbulent fluid. Part 1. General discussion and the case of small conductivity," J. Fluid Mech., 5,113-133.

Bergstrom, D. J., Tachie, M. F., and Balachandar, R. (2001) "Application of power laws to low Reynolds number boundary layers on smooth and rough surfaces," Phys. Fluids, 13(11), 3277-3284.

Biferale, L., and Vergassola, M. (2001) "Isotropy vs. anisotropy in small-scale turbulence," Phys. Fluids, 13, 2139-2141.

Castaing, B. (1989) "On the shape of histograms in turbulence, " Comptes Rendus De L Academie Des Sciences Serie II, 309(6), 503-506.

Catrakis, H. J. (2000) "Distribution of scales in turbulence," Phys. Rev. E, 62, 564-578.

Catrakis, H. J., Aguirre, R. C., and Ruiz-Plancarte, J. (2002) “Area-volume properties of fluid interfaces in turbulence: scale-local self-similarity and cumulative scale dependence,” J. Fluid Mech., 462, 245-254.

Catrakis, H. J., Aguirre, R. C., Ruiz-Plancarte, J., and Thayne, R. D. (2002) “Shape complexity of whole-field three-dimensional space-time fluid interfaces in turbulence,” Phys. Fluids, 14(11), 3891-3898.

Catrakis, H. J., and Bond, C. L. (2000) “Scale distributions of fluid interfaces in turbulence,” Phys. Fluids, 12(9), 2295-2301.

Catrakis, H. J., and Dimotakis, P. E. (1996) “Mixing in turbulent jets: scalar measures and isosurface geometry,” J. Fluid Mech., 317, 369-406.

Catrakis, H. J., and Dimotakis, P. E. (1998) “Shape complexity in turbulence,” Phys. Rev. Letters, 80(5), 968-971.

Celani, A., Lanotte, A.,. Mazzino, A., and Vergassola, M. (2000) “Fronts in passive scalar turbulence,” Phys. Fluids, 13(6), 1768-1783.

Chatwin, P. C., and Sullivan, P. J. (1989) “The intermittency factor of scalars in turbulence,” Phys. Fluids A, 1(4), 761-763.

Chen, S., Sreenivasan, K. R., Nelkin, M., and Cao, N. (1997) “Refined similarity hypothesis for transverse structure functions in fluid turbulence,” Phys. Rev. Letters, 79, 2253-2256.

Chen, S. Y., and Kraichnan, R. H. (1998) “Simulations of a randomly advected passive scalar field,” Phys. Fluids, 10(11), 2867-2884.

Chow, V. T., (1988) “Open Channel Hydraulics,” McGraw-Hill.

Constantin, P., and Procaccia, I. (1991) “Fractal geometry of isoscalar surfaces in turbulence: Theory and experiments,” Phys. Rev. Letters, 67, 1739-1742.

Corrsin, S. (1951) “On the spectrum of isotropic temperature fluctuations in an isotropic turbulence,” J. Applied Physics, 22(4), 469-473.

Cowen, E. A., and Monismith, S. G. (1997) “A hybrid digital particle tracking velocimetry technique,” Exp. Fluids, 22(3), 199-211.

Dimotakis, P. E., and Miller P. L. (1990) “Some consequences of the boundedness of scalar fluctuations,” Phys. Fluids A, 2(11), 1919-1920.

Dowling, D. R., and Dimotakis, P. E. (1990) “Similarity of the concentration field of gas-phase turbulent jets,” J. Fluid Mech., 218, 109-141.

Eswaran, V., and Pope, S. B. (1988) “Direct numerical simulations of the turbulent mixing of a passive scalar,” Phys. Fluids, 31(3), 506-520.

Favre, A., Gaviglio, J., and Dumas, R. (1967) “Structure of velocity space-time correlations in a boundary layer,” Phys. Fluids, 10, S138.

Ferchichi, M., and Tavoularis, S. (2002) “Scalar probability density function and fine structure in uniformly sheared turbulence,” J. Fluid Mech., 461, 155-182.

Ferrier, A. J., Funk, D. R., and Roberts, P. J. W. (1993) “Application of optical techniques to the study of plumes in stratified fluids,” Dyn. of Atm. and Oceans., 20, 155-183.

Frederiksen, R. D., Dahm, W. J. A., and Dowling, D. R. (1997) “Experimental assessment of fractal scale-similarity in turbulent flows. Part 2. Higher-dimensional intersections and non-fractal inclusions,” J. Fluid Mech., 338, 89-126.

Gargett, A. E. (1985) “Evolution of scalar spectra with the decay of turbulence in a stratified fluid,” J. Fluid Mech., 159, 379-407.

Gibson, C. H., and Masiello, P. J. (1972) “Observations of the validity of dissipation rates of turbulent velocity and temperature fields,” Lecture Notes Phys. Stat. Models Turbul., 12, 427-453.

Gibson, C. H., and Schwarz, W. H. (1963) “The universal equilibrium spectra of turbulent velocity and scalar fields,” J. Fluid Mech., 16(3), 365.

Gollub, J. P., Clarke, J., Gharib, M., Lane, B., and Mesquita, O. N. (1991) “Fluctuations and transport in a stirred fluid with a mean gradient,” Phys. Rev. Letters, 67(25), 3507-3510.

Grant, H. L., Hughes, B. A., Vogel, W. M., and Moilliet, A. (1968) “Spectrum of temperature fluctuations in turbulent flow,” J. Fluid Mech., 34, 423.

Grossmann, S., Heydt, A. V. D, and Lohse, D. (2001) “Scaling exponents in weakly anisotropic turbulence from the Navier-Stokes equation,” J. Fluid Mech., 440, 381-390.

Gui, L. and Wereley, S. T. (2002) “A correlation-based continuous window-shift technique to reduce the peak-locking effect in digital PIV image evaluation,” Exp. Fluids, 32(4), 506-517.

Gurvich, A. S., and Yaglom, A. M. (1967) “Breakdown of eddies and probability distributions for small-scale turbulence,” Phys. Fluids, 10, 559-565.

Hentschel, H. G. E., and Procaccia, I. (1983) "The infinite number of generalized dimensions of fractals and strange attractors," Physica D, 8, 435-444.

Holmes, P. J., Lumley, J. L., Berkooz, G., Mattingly, J. C., and Wittenberg, R. W. (1997) "Low-dimensional models of coherent structures in turbulence," Physics Reports-Review Section of Physics Letters, 287(4), 338-384.

Holzer, M., and Siggia., E. D. (1994) "Turbulent mixing of a passive scalar," Phys. Fluids, 6, 1820-1837.

Hosokowa, I. (1991) "Turbulence models and probability distributions of dissipation and relevant quantities in isotropic turbulence," Phys. Rev. Letters, 66, 1054-1057.

Jayesh and Warhaft, Z. (1991) "Probability-distribution of a passive scalar in grid-generated turbulence," Phys. Rev. Letters, 67(25), 3503-3506.

Jayesh and Warhaft, Z. (1992) "Probability-distribution, conditional dissipation, and transport of passive temperature-fluctuations in grid-generated turbulence," Phys. Fluids A, 4(10), 2292-2307.

Jayesh, Tong, C. N., and Warhaft, Z. (1994) "On temperature spectra in grid turbulence," Phys. Fluids, 6(1), 306-312.

Kolmogorov, A. N. (1941). "The local structure of turbulence in incompressible viscous fluid for very large Reynolds numbers," Dolk. Akad. Nauk SSSR, 30, 301.

Kolmogorov, A. N. (1962) "A refinement of previous hypotheses concerning the local structure of turbulence in a viscous incompressible fluid at high Reynolds number," J. Fluid Mech., 13, 82-85.

Koochesfahani, M. M., and Dimotakis, P. E. (1986) "Mixing and chemical reactions in a turbulent liquid mixing layer," J. Fluid Mech., 170, 83-112.

Kovasznay, L. S. G., Kibens, V., and Blackwelder, R. F. (1970) "Large-scale motion in intermittent region of a turbulent boundary layer," J. Fluid Mech., 41, 283.

Kraichnan, R. H. (1968) "Small-scale structure of a scalar field convected by turbulence," Phys. Fluids, 11, 945-63.

Kraichnan, R. H. (1994) "Anomalous scaling of a randomly advected passive scalar," Phys. Rev. Letters, 72, 1016-1019.

Kurien, S., Alivalis, K. G., and Sreenivasan, K. R. (2001) "Anisotropy of small-scale scalar turbulence," J. Fluid. Mech., 448, 279-288.

Kurien, S., and Sreenivasan, K. R. (2000) “Anisotropic scaling contributions to high-order structure functions in high-Reynolds-number turbulence,” Phys. Rev. E, 62, 2206-2212.

Kurien, S., L’vov, V. S., Procaccia, I., and Sreenivasan, K. R. (2000) “Scaling structure of the velocity statistics in atmospheric boundary layers,” Phys. Rev. E, 61, 407-421.

Liepmann, H.W. (1952) Z. Angew. Math. Phys., 3, 321.

Mandelbrot, B. B. (1967) “How long is the coast of Britain? Statistical self-similarity and fractional dimension,” Science, 155, 636-638.

Mandelbrot, B. B. (1974) “Intermittent turbulence in self-similar cascades: divergence of high moments and dimension of the carrier,” J. Fluid Mech., 62, 331-358.

Mandelbrot, B. B. (1975) “Stochastic-models for earths relief, shape and fractal dimension of coastlines, and number-area rule for islands,” Proc. Natl. Acad. Sci. USA, 72(10), 3825-3828.

Meneveau, C., and Sreenivasan, K. R. (1987) “Simple multifractal cascade model for fully-developed turbulence,” Phys. Rev. Letters, 59(13), 1424-1427.

Meneveau, C., Sreenivasan., K. R., Kailasnath, P., and Fan, M. S. (1990) “Joint multifractal measures: Theory and applications to turbulence,” Phys. Rev. A, 41, 894-913.

Mestayer, P. (1982) “Local isotropy and anisotropy in a high-Reynolds-number turbulent boundary-layer,” J. Fluid Mech., 125, 475-503.

Mi, J., and Antonia, R. A. (2001) “Effect of large-scale intermittency and mean shear on scaling-range exponents in a turbulent jet,” Phys. Rev. E, 6402(2), 026301-1 - 026302-8.

Miller, P. L., and Dimotakis P. E. (1991). “Reynolds-number dependence of scalar fluctuations in a high Schmidt number turbulent jet,” Phys. Fluids A, 3(5), 1156-1163.

Miller, P. L., and Dimotakis, P. E. (1991) “Stochastic geometric-properties of scalar interfaces in turbulent jets,” Phys. Fluids A, 3(1), 168-177.

Miller, P. L., and Dimotakis, P. E. (1996) “Measurements of scalar power spectra in high Schmidt number turbulent jets,” J. Fluid Mech., 308, 129-146.

Monin, A. S., and Yaglom, A. M. (1975) “Statistical fluid mechanics: Mechanics of turbulence,” Vol 2., MIT Press.

Mydlarski, L., and Warhaft, Z. (1998) “Three-point statistics and the anisotropy of a turbulence passive scalar,” Phys. Fluids, 10, 2885-2894.

Nezu, I., and Rodi, W. (1986) “Open-channel flow measurements with a laser Doppler anemometer,” J. Hydr. Engng., 112(5), 335-355.

Novikov, E. A. (1971) “Intermittency and scale similarity in the structure of a turbulent flow,” Prikl. Math. Mech., 35, 266-277.

Obukhov, A. M. (1949) “Strucktura temperaturengo polya v turbulentnom potoke,” Izvestiya akademii nauk SSSR Seriya. Geograficheskaya i Geofizicheskaya, 13(1), 58-69.

Obukhov, A. M. (1962) “Some specific features of atmospheric turbulence,” J. Fluid Mech., 13, 77-81.

OuldRouis, M., Anselmet, F., Legal, P., and Vaienti, S. (1995) “Statistics of temperature increments in fully-developed turbulence. 2. Experiments,” Physica D, 85(3), 405-424.

Overholt, M. R., and Pope, S. B. (1996) “Direct numerical simulation of a passive scalar with imposed mean gradient in isotropic turbulence,” Phys. Fluids, 8(11), 3128-3148.

Prasad, R. R., and Sreenivasan, K. R. (1990) “Quantitative three-dimensional imaging and the structure of passive scalar fields in fully turbulent flows,” J. Fluid Mech., 216, 1-34.

Press, W. H., Flannery, B. P., Teukolsky, S. A., and Vetterling, W. T. (1992) “Numerical recipes in C: The art of scientific computing,” Second Edition, Cambridge Univ. Press.

Pumir, A., Shraiman, B., and Siggia, E. D. (1991) “Exponential tails and random advection,” Phys. Rev. Letters, 66(23), 2984-2987.

Rehab, H., Antonia, R. A., and Djenidi, L. (2001) “Streamwise evolution of a high-Schmidt-number passive scalar in a turbulent plane wake,” Exp. Fluids, 31(2), 186-192.

Reynolds, O. (1883) “An experimental investigation of the circumstances which determine whether the motion of water shall be direct or sinuous, and the law of resistance in parallel channels,” Philos. Trans. R. Soc. London Ser. A, 174, 935-982.

Reynolds, O. (1894) "On the dynamical theory of incompressible viscous flows and the determination of the criterion," Philos. Tans. R. Soc. London Ser. A, 186, 123-161.

Richardson, L. F. (1922) "Weather prediction by numerical process," Cambridge University Press.

Schuerg, F. (2003) "Fractal geometry of iso-surfaces of a passive scalar in a turbulent boundary layer," M.S. Thesis, Georgia Institute of Technology.

Schumacher, J., and Sreenivasan, K. R. (2003) "Geometric features of the mixing of passive scalars at high Schmidt numbers," Phys. Rev. Letters, 91(17), 174501-1 - 174501-4

Shen, X., and Warhaft, Z. (2000) "The anisotropy of the small scale structure in high Reynolds number - $Re_\lambda \sim 1000$ – turbulent shear flow," Phys. Fluids, 12, 2976-2989.

Shraiman, B. I., and Siggia, E. D. (1995) "Anomalous scaling of a passive scalar in turbulent-flow," Comptes Rendus De L Academie Des Sciences Serie II Fascicule B-Mecanique Physique Chimie Astronomie, 321(7), 279-284.

Shraiman, B. I., and Siggia, E. D. (1996) "Symmetry and scaling of turbulent mixing," Phys. Rev. Letters, 77(12), 2463-2466.

Shraiman, B. I., and Siggia, E. D. (2000) "Scalar turbulence," Nature, 405, 639-646.

Spalart, P. R. (1988) "Direct simulation of a turbulent boundary-layer up to $Re_\theta = 1410$," J. Fluid Mech., 187, 61-98.

Sreenivasan, K. R. (1991) "Fractals and multifractals in fluid turbulence," Annu. Rev. Fluid Mech., 23, 539-600.

Sreenivasan, K. R. (1991) "On local isotropy of passive scalars in turbulent shear flows," Proc. Royal Soc. London Series A, 434, 165-182.

Sreenivasan, K. R. (1996) "The passive scalar spectrum and the Obukhov-Corrsin constant," Phys. Fluids, 8, 189-196.

Sreenivasan, K. R. (1998) "An update on the energy dissipation rate in isotropic turbulence," Phys. Fluids, 10, 528-529.

Sreenivasan, K. R. (1999) "Fluid turbulence," Rev. Modern Phys., 71, S383-S395.

Sreenivasan, K. R., and Antonia, R. A. (1997) "The phenomenology of small-scale turbulence," Annu. Rev. Fluid Mech., 29, 435-472.

Sreenivasan, K. R., Antonia, R. A., and Danh, H. Q., (1977) "Temperature dissipation fluctuations in a turbulent boundary-layer," Phys. Fluids, 20(8), 1238-1249.

Sreenivasan, K. R., Danh, H. Q., and Antonia, R. A. (1977) "Temperature dissipation fluctuations in a turbulent boundary-layer," Phys. Fluids, 20(10), S288-S288.

Sreenivasan, K. R., and Kailasnath, P. (1993) "An update on the intermittency exponent in turbulence," Phys. Fluids A, 5(2), 512-514.

Sreenivasan, K. R., and Meneveau, C. (1986) "The fractal facets of turbulence," J. Fluid Mech., 173, 357-386.

Sreenivasan, K. R., Prasad, R. R., Meneveau, C., and Ramshankar, R. (1989) "The fractal geometry of interfaces and the multifractal distribution of dissipation in fully turbulent flows," Pure and Applied Geophysics, 131, 43-60.

Tachie, M. F., Balachandar, R., and Bergstrom, D. J. (2003) "Low Reynolds number effects in open-channel turbulent boundary layers," Exp. Fluids, 34(5), 616-624.

Tavoularis, S., and Corrsin, S. (1981) "Experiments in nearly homogenous turbulent shear-flow with a uniform mean temperature-gradient. Part 1," J. Fluid Mech., 104, 311-347.

Tavoularis, S., and Corrsin, S. (1981) "Experiments in nearly homogeneous turbulent shear-flow with a uniform mean temperature-gradient. Part 2. The fine-structure," J. Fluid Mech., 104, 349-367.

Taylor, G. I. (1935) "Statistical theory of turbulence: Parts I-III," Proc. R. Soc. London A, 151, 421-464.

Thoroddsen, S. T., and Van Atta, C. W. (1992) "Exponential tails and skewness of density-gradient probability density-functions in stably stratified turbulence," J. Fluid Mech., 244, 547-566.

Tong, C. N., and Warhaft, Z. (1994) "On passive scalar derivative statistics in grid turbulence," Phys. Fluids, 6(6), 2165-2176.

Villermaux, E., and Innocenti, C. (1999) "On the geometry of turbulent mixing," J. Fluid Mech. 393, 123-147.

Villermaux, E., Innocenti, C., and Duplat, J. (1998) "Scalar fluctuation PDF's in transient turbulent mixing," Comptes Rendus De L Academie Des Sciences Serie Ii Fascicule B-Mecanique Physique Astronomie, 326(1), 21-26.

Villermaux, E., Innocenti, C., and Duplat, J. (2001) “Short circuits in the Corrsin-Obukhov cascade,” Phys. Fluids, 13(1), 284-289.

Wang, L. P., Chen, S., and Brasseur, J. G. (1999) “Examination of hypotheses in the Kolmogorov refined turbulence theory through high-resolution simulations. Part 2. Passive scalar field,” J. Fluid. Mech., 400, 163-197.

Wang, L. P., Chen, S., Brasseur, J. G., and Wyngaard, J. C. (1996) “Examination of hypotheses in the Kolmogorov refined turbulence theory through high-resolution simulations. Part 1. Velocity field,” J. Fluid. Mech., 309, 113-156.

Warhaft, Z. (2000) “Passive scalars in turbulent flows,” Annu. Rev. Fluid Mech., 32, 203-240.

Watanabe, T., and Gotoh, T. (2004) “Statistics of a passive scalar in homogeneous turbulence,” New Journal of Physics, 6, 1-36.

Webel, G. and Schatzmann, M. (1984) “Transverse mixing in open channel flow,” J. Hydr. Engng., 110(4), 423-435.

Webster, D. R., Rahman, S., and Dasi, L. P. (2003) “Laser-induced fluorescence measurements of a turbulent plume," J. Engng. Mech., 129, 1130-1137.

Welander, P. (1955) “Studies on the general development of motion in a 2-dimensional, ideal fluid,” Tellus, 7(2), 141-156.

Wereley, S. T., and Meinhart, C. D. (2001) “Second-order accurate particle image velocimetry,” Exp. Fluids, 31(3), 258-268.

Williams, B. S., Marteau, D., and Gollub, J. P. (1997) “Mixing of a passive scalar in magnetically forced two-dimensional turbulence,” Phys. Fluids, 9(7), 2061-2080.

Yee, E., Wilson, D. J., and Zelt, B. W. (1993) “Probability-distributions of concentration fluctuations of a weakly diffusive passive plume in turbulent boundary-layer,” Boundary-Layer Meteorology, 64, 321-354

Yeung, P. K., Xu, S., and Sreenivasan, K. R. (2002) “Schmidt number effects on turbulent transport with uniform mean scalar gradient,” Phys. Fluids, 14(12), 4178-4191.

Yeung, P. K., Xu, S., Donsis, D. A., and Sreenivasan, K. R. (2004) “Simulation of three-dimensional turbulent mixing for Schmidt numbers of the order 1000,” Flow, Turbulence and Combustion, in press.

Zabusky, N. J., and Kruskal, M. D. (1965) “Interaction of solitons in a collisionless plasma and recurrence of initial states,” Phys. Rev. Letters, 15, 240.